

TAILORING THE GROWTH AND ELECTRONIC STRUCTURE
OF ORGANIC MOLECULAR HETEROINTERFACES

By

Andrew WJ Tan

A DISSERTATION

Submitted to

Michigan State University

in partial fulfillment of the requirements

for the degree of

Physics – Doctor of Philosophy

2019

ABSTRACT

TAILORING THE GROWTH AND ELECTRONIC STRUCTURE OF ORGANIC MOLECULAR HETEROINTERFACES

By

Andrew WJ Tan

In the rapidly developing electronics industry, it has become increasingly necessary to explore materials that are cheap, flexible and versatile which have led to significant research efforts towards organic molecular thin films. Understanding and control of heterointerface between highly ordered organic molecular thin films with extended π systems and inorganic materials are therefore of critical importance for the development of modern organic electronics. Organic molecules are unique compared to their inorganic atomic counterparts as their properties can be tuned drastically through chemical functionalization, offering versatility, though their extended shape and weak intermolecular interactions bring significant challenges to the control of both the growth and the electronic structures of molecular thin films. This is further complicated by interaction between organic molecules and the underlying substrate which can lead to interfacial effects such as charge transfer, chemical interaction and electrostatic screening, all of which can significantly impact device performance and/or the characteristic of the organic thin film.

This dissertation will first focus on a systematic review of the growth and electronic structure of organic molecular thin films, particularly on weakly interacting substrates. The self-assembly process and how long-range ordered organic molecular thin films are established will be discussed. We will also discuss how the electronic structures of thin films are impacted by the molecule's local electrostatic environment and its interaction with the substrate, within the context of controlling interfacial energy level alignment between organic semiconductors and electrodes in electronic devices.

Employing scanning tunneling microscopy and spectroscopy, experimental studies focusing on characterizing the growth and electronic structure of organic molecules on weakly interacting substrates were carried out and discussed. Studies focusing on the electronic structure of zinc phthalocyanine (ZnPc) and its fluorinated counterpart $F_{16}ZnPc$ were carried out on the deactivated Si(111)-B surface and h-BN/Cu(111). We show that interfacial charge transfer occurs between the deactivated Si(111)-B substrate and the $F_{16}ZnPc$ monolayer, which gives rise to a pronounced spatial variation of the occupied molecular state across the molecular assembly attributed to the inhomogeneous electrostatic screening of the intra-orbital Coulomb interaction in molecular adsorbates arising from the substrate boron distribution in the deactivated Si(111)-B substrate. To circumvent this inhomogeneous effect, the donor-acceptor molecular pair was studied on weakly interacting hexagonal boron nitride (h-BN)/Cu(111) which possesses a periodic electronic corrugation. We show that the formation of the lateral heterostructure drastically increases the charge transfer between $F_{16}ZnPc$ molecules and the substrate, which is attributed to the greater electrostatic stability of the heterostructure compared to that of the pure phase. This study highlights the importance of the substrate, even a weakly interacting one, such as h-BN/metal, can still perturb the intermolecular charge transfer and thereby the heterostructure behaviors via interfacial processes.

The focus of a secondary study was to initiate preliminary experimentation towards understanding the substrate's influence on the exotic properties of a class of organic-based systems known as charge transfer complexes (CTC). By utilizing the unique modulation properties of various weakly-interacting substrates, control of the properties of CTCs could be attained allowing for a better understanding of their fundamental physical mechanism to be developed and a new class of thin-film CTCs which will be highly relevant towards organic electronics to be developed.

This thesis is dedicated to
Jeff Kaplan and the Overwatch team

ACKNOWLEDGEMENTS

The work presented in this dissertation was supported by the U.S. Department of Energy (DOE) Office of Science Early Career Research Program (Grant No. DE-SC0006400 and DE-SC0019120) through the Office of Basic Energy Science.

There were a lot of people who played a significant role in the works detailed in this thesis as well as my life throughout my Ph.D. career. I would like to take this opportunity to acknowledge and thank those who supported me through the years.

First, I would like to thank my advisor, Professor Pengpeng Zhang, for taking me on as a student and allowing me to experience the challenges of a budding scanning probe microscopy research laboratory. My time in her research group was an incredibly prosperous one as I was given the opportunity to combine my interests in physics and chemistry in the study of organic molecular thin films. With her incredibly helpful guidance, I was able to bring many projects to fruition and lay the foundation for many projects to come. This has equipped me with a host of valuable skills and experiences that I am sure will prove very useful for the rest of my scientific career.

Over the years, I have had the pleasure of working with a lot of excellent people in the lab. Sean Wagner, Jiagui Feng, Xi Dong, Chuanpeng Jiang, Justin Lane and Timofey Golubev were excellent labmates and I thank them for all of their help and discussion. Sean, in particular, whose work served as the foundation of my dissertation, proved to be an invaluable mentor and I am very happy that I had the opportunity to work with him. It was also my pleasure to help train Ian Neuhart who joined the group while this dissertation was written and his help alongside Xi Dong in acquiring some of the data in Chapter 9 were invaluable and I wish them the best of luck in their

future endeavors. In addition, my fellow physics compatriots like Xingze Mao, Bryan Isherwood and John Bower were great to talk to and hang out with.

I would also like to thank the Department of Physics and Astronomy and the people therein. Kim Crosslan, Baokang Bi, Jessica and Cathy Cords and the staff of the Physics and Astronomy Machine Shop were always so friendly and helpful, and it was a pleasure to work with them. To Reza Loloee, who kept the basement from going up in flames, your help could never be overstated, and I am so thankful for all the discussions and assistance that you have provided over the years. To the members of my thesis committee, Philip Duxbury, Kirsten Tollefson, Johannes Pollanen and Stuart Tessmer, I thank you for serving on my committee. I would like to thank Stuart Tessmer, in particular, for his mentorship and for inviting me over for all those thanksgiving dinners.

I would like to acknowledge Professor Richard Lunt for his help with the sublimation process to purify the phthalocyanine molecules used in this study. I would like to thank Sahar Sharifzadeh for the helpful discussions on finite element simulation. I would also like to acknowledge Professor Shenqiang Ren and his group where our collaborative work will hopefully bring forth new and exciting new insights in the exciting field of organic charge transfer complexes. I would also like to acknowledge the Institute for Cyber-Enabled Research for providing the computational resources needed for the study detailed in Chapter 8.

Special thanks goes out to Ron Southwick and the MSU Taekwondo Club. It was my absolute honor to train under him and his mentorship was something I will never forget. Victoria Breeze, Jia-Yi Chan, Susan Little and the MSU Taekwondo Club were instrumental in keeping me sane over the years of my Ph.D. work and I could never have done it without them and their constant companionship and support.

I would be negligent if I did not also thank Jeff Kaplan and the Overwatch team. They made such an incredible game that absolutely changed my life and served as a bedrock for my life over the years of my degree. Through the game, I enjoy the company of so many wonderful people and incredible experiences and I am so thankful for its creation. To you all, I dedicate this dissertation.

I wanted to thank my friends and family who lived so far away but were always there for me and supported me over the years. My family, Tan Lye Cheng, Yeow Seok Yean, Amy and Alan Tan, your love and support kept me strong. To my brother, in particular, his constant advice and companionship was very much appreciated. To my close friends, Wong Wei Mei, Ang Kai Chian and Felicia Poh, thank you so much for all of the conversations and for putting up with all kinds of nonsense ideas and adventures that I came up with. To my other group of close friends, the Nuts, even though we met and talked so rarely, every time I had the opportunity to come home to Malaysia and meet you all, I would leave with a renewed sense of purpose and identity and I thank you all for that. And finally, I wanted to thank Ashleigh Cushman, her love and support were so important in helping me chug through the final leg of my Ph.D. journey and I am so thankful we met.

Thank you all.

TABLE OF CONTENTS

LIST OF TABLES	xi
LIST OF FIGURES	xii
1 Introduction	1
1.1 Motivation	1
1.2 Content and Layout of this Work.....	2
2 Growth of Organic Molecular Thin Films	5
2.1 Generic kinetic and thermodynamic considerations	5
2.2 Molecule-molecule and molecule-substrate interactions	8
2.3 Characterization Techniques	9
2.4 Case studies of organic molecular thin film growth on weakly interacting and strongly interacting substrates	12
2.4.1 Molecule on Silicon Oxide	12
2.4.2 Molecule on Metals.....	15
2.5 Long-range ordered growth in both in-plane and out-of-plane directions demonstrated using ZnPc on deactivated Si(111)-B.....	18
2.5.1 Step-flow growth of ZnPc on deactivated Si(111)-B	19
2.5.2 Out-of-plane ordering of ZnPc on deactivated Si(111)-B	22
2.6 Organic-inorganic van der Waals heterostructures: a promising template for device applications.....	22
3 Electronic Structures of Organic Molecular Thin Films	27
3.1 Dependence of Electronic Structures of Organic Molecules on Electrostatic Screening and Molecular Orientation	29
3.2 General consideration of the interfacial effects arising from the molecule-substrate interaction on metals or strongly interacting substrates	38
3.3 Impacts of molecule-substrate interaction on molecular electronic structures and interfacial energy level alignment in the integer charge transfer regime	40
3.3.1 Introduction of the integer charge transfer (ICT) model	40
3.3.2 Recent development of the ICT model and its implications on molecular electronic structures and molecular thin film growth.....	43
3.3.3 Revisit the interfacial energy level alignment in the ICT regime and its impacts on the charge injection behaviors in organic electronic devices	49
4 Charge Transfer Complexes.....	56
4.1 Introduction to Charge Transfer Complexes.....	56
4.2 Organic ferroelectricity	59
4.3 Properties of a ferroelectric monolayer: An STM study	61

5	Experimental and Computational Methods.....	64
5.1	Ultra-high vacuum system	64
5.2	Scanning tunneling Microscopy and Spectroscopy	69
5.2.1	Scanning Tunneling Microscopy	69
5.2.2	Scanning Tunneling Spectroscopy.....	75
5.2.3	Considerations of Scanning Tunneling Spectroscopy on Organic Molecules on Weakly Interacting Substrates	78
5.2.4	Differential Conductance Mapping.....	81
5.3	Computational Methods	82
5.3.1	MATLAB Processing of Scanning Tunneling Spectroscopy Data.....	82
5.3.2	Epitaxial registration analysis	83
5.3.3	COMSOL finite element simulation.....	88
5.4	Sample Preparation	90
5.4.1	Chemical and thermal processing of highly boron doped silicon.....	90
5.4.2	Metal preparation and Chemical Vapor Deposition of Boron Nitride.....	92
5.4.3	Organic Molecule Deposition.....	95
6	Self-Assembly of F₁₆ZnPc and ZnPc/F₁₆ZnPc heterostructures on the Deactivated Si(111)-B Surface	98
6.1	Self-Assembly of F ₁₆ ZnPc on deactivated Si(111)-B	99
6.2	Growth of F ₁₆ ZnPc-ZnPc heterojunctions on the deactivated Si(111)-B	105
6.3	Conclusion.....	109
7	Electrostatic Screening Mediated by Interfacial Charge Transfer of Metal Phthalocyanine Molecules on the Deactivated Si(111)-B Surface	110
7.1	Geometric Structures of Molecular Overlayers	110
7.2	Electronic Structure of the deactivated Si(111)-B surface and molecular assemblies.	112
7.2.1	STS of the deactivated Si(111)-B surface.....	112
7.2.2	Electronic Structures of Molecular Assemblies.....	114
7.3	Inhomogeneous substrate screening.....	120
7.4	Discussion	124
7.5	Conclusion.....	128
8	Interfacial Charge Transfer Enhancement via Molecular Heterostructures Formation on Electronically Corrugated Boron Nitride.....	129
8.1	Growth of ZnPc and F ₁₆ ZnPc on h-BN/Cu(111)	131
8.2	Electronic Structure of ZnPc and F ₁₆ ZnPc on h-BN/Cu(111).....	134
8.3	Electronic Structure of the binary ZnPc/F ₁₆ ZnPc layer on h-BN/Cu(111)	142
8.4	Discussion	147
8.5	Conclusion.....	150
9	Growth and Electronic Structure of TCNQ and K-TCNQ Charge Transfer Complexes on Cu(111).....	152

9.1	Growth and Electronic Structure of TCNQ on Cu(111)	153
9.2	Growth and Electronic Structure of K-TCNQ on Cu(111)	156
9.3	Electronic Structure of K-TCNQ on Cu(111)	161
9.4	Conclusion and Future Studies	165
10	Conclusion and Future Prospects	167
10.1	TTF-CA: A Novel Organic Ferroelectric	167
10.1.1	Introduction to TTF-CA	167
10.1.2	Preliminary Data on the Growth of TTF-CA	168
10.2	Summary of Results and Future Work	170
	BIBLIOGRAPHY	174

LIST OF TABLES

Table 1: Summary of molecular lattice parameters for structure A and structure B and their corresponding transformation matrix with respect to the lattice of the deactivated Si surface. . 105

Table 2: Averaged Gaussian-fit peak positions of the unoccupied DOS feature of Si, ZnPc and F₁₆ZnPc. 119

Table 3: Lattice parameters and averaged Gaussian-fit peak positions of the unoccupied density of state features in the STS spectra taken on the pure and mixed molecular layers. 144

LIST OF FIGURES

Figure 2-1: Growth Processes	7
Figure 2-2: X-ray scattering and LEED geometries	12
Figure 2-3: Growth of DIP on SiO ₂	15
Figure 2-4: Growth of organic molecules on metals	18
Figure 2-5: Growth of ZnPc on deactivated Si(111)-B	21
Figure 2-6: Growth and Device Application of Organic Molecules on 2D Materials.....	26
Figure 3-1: Dependence of organic molecular electronic structure on local electrostatic environment	32
Figure 3-2: Orientation Dependent Electronic Structure	35
Figure 3-3: Comparison between physisorbed and chemisorbed organic molecular systems.....	40
Figure 3-4: Integer Charge Transfer Model.....	42
Figure 3-5: UPS and IPES spectra of C ₆₀ on MoO ₃ /Au(111), an integer charge transfer system	45
Figure 3-6: Effects of ICT detected by STM/STS	49
Figure 3-7: Contact properties of weakly interacting organic systems.....	52
Figure 3-8: Evolution of energy level alignment at weakly interacting heterointerfaces.....	55
Figure 4-1: Charge transfer complex packing and energy diagram.....	58
Figure 4-2: Organic ferroelectrics.....	61
Figure 4-3: Ferroelectric properties of SnTe as determined by STM/STS	63
Figure 5-1: Scienta Omicron LT and Preparation UHV Chamber	65
Figure 5-2: Image of the Scienta Omicron STM scanning stage in the LT UHV chamber. Image courtesy of Sean Wagner	67
Figure 5-3: SEM images of tungsten and Pt-Ir STM tips	69
Figure 5-4: Tunneling Mechanisms	70

Figure 5-5: Schematic of STM Operation in constant current mode. Image courtesy of Sean Wagner.....	74
Figure 5-6: Schematic of Negative Differential Resistance (NDR) and Example Spectra	80
Figure 5-7: Schematic representation of different epitaxial relations between overlayer and substrate. Image courtesy of Sean Wagner.....	85
Figure 5-8: Example result of the geometric phase coherence model where the epitaxial registration of the molecular overlayer lies between incommensurate and POL coincidence epitaxy.....	86
Figure 5-9: Example of a moiré pattern formed by rotated periodic lattices.....	87
Figure 5-10: Geometric setup for finite element analysis.....	90
Figure 5-11: Geometric and Electronic Properties of the Deactivated Si(111)-B Surface.....	91
Figure 5-12: Picture of Ion Gun Setup and Borazine Leak Valve and Ion Gun Ionization Module	93
Figure 5-13: Boron Nitride Deposition Sources, borazine liquid vessel and ammonia borane powder vessel. Chemical structure of borazine and ammonia borane are drawn out.....	95
Figure 5-14: Low temperature effusion cell with shutter and Knudsen cell and structure of organic molecules studied in this dissertation.	97
Figure 6-1: Apparent height measurement of F ₁₆ ZnPc and ZnPc assemblies on deactivated Si(111)-B.....	100
Figure 6-2: RT and ET structures of F ₁₆ ZnPc on deactivated Si(111)-B	102
Figure 6-3: Geometric and lattice simulation of F ₁₆ ZnPc on deactivated Si(111)-B	104
Figure. 6-4: STM images of F ₁₆ ZnPc-ZnPc heterostructures on deactivated Si(111)-B.....	108
Figure. 7-1: Structure of deactivated Si(111)-B, ZnPc and F ₁₆ ZnPc molecular layers	111
Figure 7-2: Electronic Structure of ZnPc and F ₁₆ ZnPc on deactivated Si(111)-B	114
Figure 7-3: dI/dV Maps of LUMO+1 of ZnPc overlayer and Si(111)-B Surface State.	116
Figure 7-4: Gaussian Fitting of Unoccupied Spectral Feature of ZnPc, F ₁₆ ZnPc and deactivated Si(111)-B STS spectra	117
Figure 7-5: Reproducibility of ZnPc and F ₁₆ ZnPc spectra taken on deactivated Si(111)-B	119
Figure 7-6: Additional STS data taken on ZnPc and F ₁₆ ZnPc on deactivated Si(111)-B	120

Figure 7-7: Electronic Structure of subsurface boron defects on deactivated Si(111)-B	122
Figure 7-8: Coulomb-potential induced band bending analysis	123
Figure 7-9: STS taken on areas of different contrast variation in the F ₁₆ ZnPc overlayer	124
Figure 7-10: Comparison of Subsurface Boron Distribution to Filled-State Images of F ₁₆ ZnPc	126
Figure 8-1: STM Images of h-BN and Pristine Orbitals of ZnPc, F ₁₆ ZnPc and the Binary ZnPc/F ₁₆ ZnPc Structure.	133
Figure 8-2: Growth of ZnPc and F ₁₆ ZnPc Organic Assemblies	134
Figure 8-3: Electronic Perturbation of h-BN Moiré Pattern on Organic Assemblies.....	138
Figure 8-4: Gaussian Fits of pure and mixed ZnPc/F ₁₆ ZnPc STS Spectra.....	139
Figure 8-5: Energy-band diagrams illustrated for ZnPc (right) and F ₁₆ ZnPc (left) at valley locations.	142
Figure 8-6: Finite element electrostatic simulations using COMSOL.....	145
Figure 8-7: COMSOL Simulation of the dependence of the vacuum level shift on the size of the molecular layer relative to the distance probed.	146
Figure 9-1: STM Image of TCNQ on Cu(111).....	154
Figure 9-2: Electronic Structure and dI/dV maps of TCNQ on Cu(111)	156
Figure 9-3: STM images showing the growth of K-TCNQ on Cu(111) at low and moderate K doping.	158
Figure 9-4: Assignment of the condensed stripe phase of K-doped TCNQ	160
Figure 9-5: Structure of K ₂ -TCNQ at high K doping.	161
Figure 9-6: Heterojunction of TCNQ/K-TCNQ	164
Figure 9-7: Electronic Structure of stripe phase K-TCNQ	164
Figure 10-1: Properties of TTF-CA	168
Figure 10-2: Growth of pure CA and TTF molecules grown on Cu(111).....	170

1 Introduction

1.1 Motivation

The demand for materials that are cheap, flexible and versatile has been growing in the ever-evolving electronics industry which has led to the significant investment of resources into the development of organic molecular thin film technology for use in devices and optoelectronics.[1-5] Conjugated organic molecules, in particular, have received significant attention due to the high charge carrier mobility established in their thin film form with extended π systems.[6-9] However, organic molecules bring forth their own unique advantages and challenges that differ from their inorganic counterparts.[8,10,11] Through the power of synthetic chemistry, organic molecules can be functionalized, thereby allowing viable changes to the steric shape and/or electronic character of the molecule.[12-16] However, the extended nature of organic molecules also results in an increase in the degrees of freedom, which complicates the thermalization of molecules mediated by their interaction with each other and with the substrate surface, leading to complex growth mechanisms.[17-20] The crystallinity and ordering of molecular thin films will be critically important to device operations as defects such as grain boundaries can lead to formation of trap states that can severely hinder the transport of charge carriers and/or excitons.[21-24] Furthermore, the anisotropic nature of organic molecules often leads to a correspondingly anisotropic carrier mobility in molecular thin films, i.e., higher mobility along the face-to-face π - π intermolecular bonding direction. Therefore, orientational/tilting degrees of freedom of molecules need to be considered for the development of thin films targeted at specific device applications.[21,25] For instance, while organic field-effect transistors (OFETs) require good in-plane carrier mobility promoted by standing-up conjugated molecules with respect to the substrate surface, organic photovoltaics (OPVs) and organic light emitting diodes (OLEDs) demand high out-of-plane carrier

mobility aided by flat-lying conjugated molecules. It is also important to note that while device application will typically utilize multi-layered molecular films, the precise interface between the film and the substrate, i.e. the first monolayer, will often dictate the growth of the subsequent layers and impact the electronic behaviors of the whole system.[26]

Beyond the control of morphology, the electronic properties of thin films also need to be thoroughly examined. One major limiting factor in many organic devices lies in the contact resistance that occurs at the interface between the metal electrodes and the organic semiconducting thin film. This resistance is tied closely to the specific energy level alignment that occurs at the interface. However, due to the anisotropic shape of organic molecules, the ionization potential and electron affinities are directly linked to the specific molecular orientation within the thin film.[27-31] In addition, the same mechanism that gives organic thin films their mechanical flexibility, i.e., the weak non-covalent intermolecular interaction and low wavefunction overlap, is also responsible for a strong charge localization in the molecules, yielding a pronounced sensitivity of molecular electronic structures, and thereby the position of the molecular orbitals, to the local electrostatic environment.[32-39] The presence of a supporting substrate or a metal electrode near the molecular overlayer necessitates the examination of the electrostatic influence of the substrate such as the image-charge screening and the interfacial effects including charge transfer while analyzing the energy level alignment of the system.[40-44]

1.2 Content and Layout of this Work

In this dissertation, a systematic and detailed review of organic molecule self-assembly will be discussed in Chapter 2. Growth of organic molecules on amorphous weakly interacting substrates, strongly interacting metallic substrates will first be reviewed followed by a discussion

of anisotropic step flow growth behavior of ZnPc on deactivated Si(111)-B pioneered by Dr. S. Wagner, whose work served as the basis for this dissertation. This is followed by a discussion of organic molecule growth on weakly interacting, highly crystalline two dimensional materials such as HOPG and h-BN. Chapter 3 will then discuss the electronic structure of organic molecules and the relevant energy level alignment effects. The influence of substrate electrostatic screening and molecular orientation on the electronic structure of organic molecules will be explored. This is followed by a detailed review of the energy level alignment and general considerations of organic molecules on metals and weakly interacting substrates. In Chapter 4, a brief discussion on the properties of donor-acceptor mixtures known as charge transfer complexes (CTC) that exhibit unique physical behavior, different from that of its constituting semiconducting components will be had, with a review of monolayer ferroelectricity as observed by STM/STS included in this discussion.

The experimental and computational methodologies used in this dissertation shall be discussed in Chapter 5. This includes a brief description of the experimental setup, a discussion on the operating principles of scanning tunneling microscopy (STM) and considerations for studying organic molecule systems. Sample preparation techniques and theoretical calculations used in this body of work will also be discussed. The growth and electronic structure of donor and acceptor organic molecules on weakly-interacting deactivated Si(111)-B have been studied and discussed in Chapter 6 and Chapter 7. In Chapter 6, the growth of F₁₆ZnPc and ZnPc-F₁₆ZnPc heterojunctions on the deactivated Si(111)-B surface are characterized where it is discovered that F₁₆ZnPc possesses a stronger molecule-substrate interaction in comparison to ZnPc. Chapter 7 discusses the electronic structure of both ZnPc and F₁₆ZnPc and how they are influenced by the deactivated Si(111)-B surface. Particularly, it is demonstrated here that the thermally induced subsurface boron

defects in the deactivated Si(111)-B substrate results in a perturbation of $F_{16}ZnPc$ occupied orbitals. This is the result of the increased sensitivity of $F_{16}ZnPc$ occupied orbitals due to the charge transfer interaction between the acceptor molecule and Si. With that understanding in hand, we then moved on to study the characteristics of a binary donor-acceptor molecular layer, comprising of $ZnPc$ and $F_{16}ZnPc$, molecules whose growth and electronic properties have been well discussed, on a weakly-interacting substrate, h-BN, in Chapter 8. Here, we will discuss STS studies of a mixed donor-acceptor system which reveals the substrates influence on the intermolecular charge transfer. Chapter 9 discusses preliminary data taken on the K-TCNQ on Cu(111) system where the geometric and electronic structure of TCNQ assemblies are altered by the introduction of K atoms. Chapter 10 which serves as the conclusion of this dissertation will summarize the results presented in this dissertation and will also include preliminary studies done on the TTF-CA CTC system on Cu(111) that shall serve as the launch bed for future studies into the exotic CTC systems. The challenges of growing TTF-CA assemblies will be discussed followed by a brief discussion on the structures that were observed on the surface. Optional research projects will also be discussed in this chapter.

2 Growth of Organic Molecular Thin Films

In this chapter, a thorough discussion of the growth of organic molecule systems on various types of substrates of varying degrees of crystallinity and interaction strength. In Section 2.1, the basic kinetic and thermodynamic considerations of organic thin film growth are discussed. This is followed by an additional discussion on the energetic considerations for molecular systems pertaining to the intermolecular and molecule-substrate interactions in Section 2.2. Section 2.3 discusses typical characterization techniques that are used to analyze the growth morphology of organic molecular thin films as well as relevant deposition methodologies. In Section 2.4, specific case studies of the growth of organic molecules on weakly interacting amorphous substrates and strongly interacting metallic substrates are discussed. Section 2.5 will discuss the unique anisotropic step-flow growth behavior of zinc phthalocyanine (ZnPc) on deactivated Si(111)-B which was discovered by Dr. S. Wagner. Finally, in Section 2.6, we will discuss the growth and device performance advantages of long-range ordered organic molecule thin films on highly crystalline and weakly interacting two-dimensional materials. This review was adapted from Reference [45,46]: *A. Tan et al., Encyclopedia of Interfacial Chemistry 267 (2018), A. Tan et al., Journal of Physics: Condensed Matter (2019) (Manuscript In-Review).*

2.1 Generic kinetic and thermodynamic considerations

The self-assembly and growth of organic molecular thin films on surfaces is often governed by the intermolecular and molecule-substrate interactions. Although the self-assembly process driven by intermolecular interactions such as hydrogen bonding, van der Waals interaction, and dipole-dipole interaction can be well controlled and predictable, making it immensely useful for the development of molecular thin films, the influence of the substrate on the as-grown structures

can also be critical.[47-53] Organic molecular systems share many fundamental processes with inorganic atomic systems during the initial stage of the thin film growth such as adsorption, diffusion and nucleation, as illustrated in Figure 2-1a. [11,26,45,54-60] After being adsorbed onto the surface, molecules will explore the surface energy landscape, through the process of diffusion, to find energetically favorable sites for nucleation and growth. Diffusion is a thermally activated process which can be manifested through various means such as edge diffusion, surface diffusion and interlayer diffusion, each of which is associated with an activation barrier. The activation barrier for surface diffusion, E_d , one of the most basic pathways, is illustrated in the surface potential landscape in Figure 2-1b.

Whether a growth is limited by kinetics or thermodynamics will be primarily dictated by the diffusivity of adsorbates and the deposition flux.[56,61] Under the scenarios of high deposition flux and low diffusivity, adsorbates will not be able to fully explore the surface potential landscape to reach the minimum energetic state before aggregation occurs, rendering the growth kinetically limited. Substrate temperature becomes a useful knob to tune the diffusivity and thus the growth regimes. However, in molecular systems with weak interactions to the substrate, the window of the viable substrate temperature for establishing a high molecular diffusivity, and meanwhile preventing molecular desorption from the substrate surface, can be quite limited. Failure to surmount the various diffusion barriers will have unique effects on the growth process such as scattered cluster formation for limited surface diffusion and diffusion-limited aggregation (DLA) for hindered edge diffusion.[19,62,63] Finally, interlayer diffusion allows for adsorbates to diffuse down across the substrate or self-edges. This diffusion process is dictated by the activation barrier known as Ehrlich-Schwöebel barrier (ESB), which arises from the loss of coordination during interlayer mass transport (Figure 2-1c).[18,64-68] Overcoming the ESB

barrier will help prevent the formation of a rather rough film with 3D island growth. The ESB becomes far more complex when considering organic molecular systems due to their extended nature, which necessitate the consideration of molecular orientation, bending, and the specific pathways in which molecules descend the edges.[18,20,69,70]

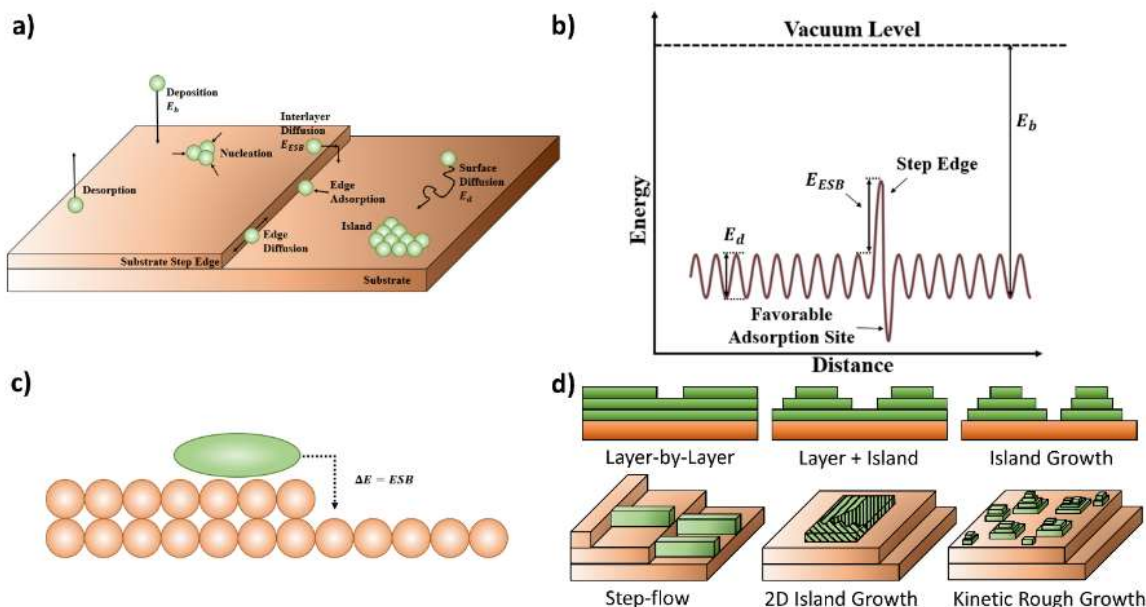


Figure 2-1: Growth Processes

(a) Basic processes shared between inorganic thin film growth and organic molecular self-assembly on a substrate surface. (b) Surface potential landscape with the surface diffusion barrier, E_d , interlayer diffusion barrier, E_{ESB} and binding energy, E_b illustrated. The favorable adsorption site at the bottom of a step edge is also indicated. (c) Illustration of the interlayer diffusion process with the consideration of the Ehrlich-Schwöebel barrier (ESB). (d) Thin film thermodynamic growth modes (top): layer-by-layer, layer-plus-island, and island growth; and kinetic growth modes (bottom) with special consideration with regards to organic molecular assemblies: anisotropic step-flow, 2D island growth showing polycrystallinity as one of the potential consequences of such growth, and kinetic rough growth.

If the kinetic limitations of a system are overcome, the growth of the thin film can proceed near thermodynamic equilibrium. The classical thermodynamic growth modes in inorganic systems are determined by the surface energy of the overlayer, the surface energy of the substrate,

and the interface energy between the film and substrate. Depending on the balance between these three energy parameters, layer-by-layer (Frank-van der Merwe), layer-plus-islands (Stranski-Krastanov) or island growth (Volmer-Weber) can be observed (Figure 2-1d). It is worth emphasizing that there are also three kinetic growth modes, i.e., step-flow growth, 2D island growth, and kinetic rough growth, as drawn in Figure 2-1d. For instance, the 3D island growth could be fundamentally determined by the energetics, it could also simply result from the kinetic rough growth. Thus, it is important to distinguish the near equilibrium growth modes from those dominated by kinetics.[61]

2.2 Molecule-molecule and molecule-substrate interactions

As discussed earlier, what complicates the growth of organic molecular thin films as compared to their inorganic counterparts are the extended shape of molecules and the interaction scheme in organic molecular systems. For ordered molecular structures to form, a delicate balance between the molecule-molecule and molecule-substrate interactions needs to be established.[45,47,55-57,71,72] While the intermolecular interactions in organic systems are often dictated by weak interactions such as Van der Waals or dipole-dipole interactions, the strength of the molecule-substrate interactions can be significantly varied depending on the supporting substrate. If this interaction is too strong, diffusion of molecules could be hindered. Furthermore, molecules may be forced into highly strained structures that deviate significantly from their bulk phase.[73-77] In fact, most conjugated molecules will adopt a flat-lying configuration on metals, driven by the hybridization between the molecule's π -system and the continuum states of the metal substrate.[43,78,79] When the molecular assembly is extended beyond the first monolayer, the exponentially decayed molecule-substrate interaction in subsequent layers will inevitably lead to a relaxation of the molecular film back into its bulk structure, resulting in a loss of out-of-plane

ordering.[80-82] In the case of pentacene on Au(111), the molecules first form a wetting layer of flat-lying configuration before reverting to the formation of 3D crystallites, yielding an overall rough film.[74] On the other hand, if the molecule-substrate interaction is too weak, the substrate's crystalline symmetry will not be imposed onto the thin film, resulting in randomly oriented molecular domains and correspondingly the formation of high-angle grain boundaries that serve as strong scattering and trapping sites for charge carriers or excitons.[21-24,64,69,83-85] A delicate balance therefore needs to be struck, where the molecule-substrate interaction is strong enough such that symmetry of the crystalline substrate can be imposed onto the molecular thin film but weak enough so that it does not force the molecules to pack into highly strained configurations.

2.3 Characterization Techniques

With these challenges in mind, it is therefore necessary to discuss the right tools needed for the characterization of organic molecular assembly and thin film growth. Since exposure to ambient conditions can introduce defects or induce de-wetting processes that are not inherent in the as-grown organic thin films, *in-situ* characterizations are necessary. Techniques such as x-ray scattering, low energy electron diffraction (LEED) and scanning probe microscopies (SPM) are commonly employed. X-ray scattering techniques are very powerful as an *in-situ* probe, and the experimental geometry also makes it capable of *real-time* measurements that allow for the observation of the evolution of the growth structures and intermediate states. [17,69,70,80,82,86] X-ray experiments are characterized by the change in momentum between the incident and scattered beams upon diffraction. Specifically, in x-ray reflectivity (XRR) experiments, as illustrated in Figure 2-2a, layered structures, such as organized molecular thin films, create an oscillation in intensity as a function of q_z , allowing for the measurement of the interlayer distance

and film thickness. while $q_{||}$ can be probed by the grazing incidence diffraction (GID) experiments, as shown in Figure 2-2b, allowing for the measurement of the in-plane lattice parameters.[11,17,64,70,82,86,87] Similarly, LEED, whose experimental setup is drawn in Figure 2-2c, is also capable of measuring the in-plane lattice parameters by projecting the reciprocal space of the periodic two-dimensional surface onto a screen where well defined diffraction spots represent periodic components of the real-space lattice. [88-92] However, a significant drawback of these techniques is the averaging effect over large areas of the sample, therefore lacking fine spatial resolution. Scanning probe techniques like STM offer the ability to identify the local ordering of the molecular thin film, allowing for the precise determination of the nature of defects within the film. Furthermore, STM, when used in conjunction with STS, enables the simultaneous measurement of the geometric and electronic structure of the thin film, which will be discussed in Chapter 5.[37,93-96]

Methodologies of organic molecular thin film growth can typically be classified into vacuum deposition and solution processing, which were initially encouraged by the difference in the solubility between polymers and small molecules.[97,98] Small molecules, especially ones with the flat or nearly flat structure, do not easily dissolve in most solvents and therefore require vacuum deposition in order to create the molecular thin film. Polymers, however, due to their larger molecular weight, have much higher sublimation temperatures, often to the point that the polymer will decompose before sublimation occurs which results in the need for solution processing. Numerous innovative solution processing techniques have been invented in recent years and demonstrated the ability to tailor the morphology of thin films through the use of kinetic, electrical or magnetic forces.[99] One such example, the off-center spin coating method (OCSC), utilizes the increased centripetal acceleration to align the molecular thin films in specific directions

and allow for non-equilibrium structures to form such as molecular thin films with closer intermolecular spacing.[9,100] This has the intriguing advantage of increasing the charge carrier mobility through increased intermolecular wavefunction overlap. On the other hand, vacuum deposition methodologies have the benefit of being capable of precisely controlling the film thickness, permitting the formation of heterostructures with a sharp interface. Furthermore, vacuum deposition methodologies are intrinsically compatible with many surface sensitive probing techniques such as ultraviolet photoemission spectroscopy (UPS), scanning tunneling microscopy/spectroscopy (STM/STS) and x-ray spectroscopies, allowing for in-situ probing of the molecular thin film's electronic and geometric structures. Both growth methodologies have their place, however due to the focus of this dissertation being on the fundamental properties of organic molecular thin films and their tie to device characteristics studied by the surface sensitive probing techniques, a larger emphasis will be put on the vacuum deposition methodologies. Discussions more dedicated to solution processing can be found in other reviews.[99-101]

Numerous vacuum deposition techniques can be exploited to grow organic molecular thin films, with the most common methodology based on simple thermal evaporation. [102-110] Other techniques, including pulse-injection and electrospray ionization, have been developed to provide a greater range of depositable molecules, for instance, macromolecules.[102,103,106,107] Electrospray ionization, in particular, also allows for the control of the kinetic energy of impinging molecules through the use of an electrostatic quadrupole deflector.[106,107] Another technique that enables the tuning of kinetic energy (from ~ 200 meV to 40 eV) by an isentropic expansion of a carrier gas is termed supersonic molecular beam epitaxy (SMBE). [109,110] The increased kinetic energy, at its simplest form, can be treated like a local annealing effect without the

drawbacks of traditional substrate annealing, within certain extent, such as molecular desorption or dewetting of existing organized assemblies.

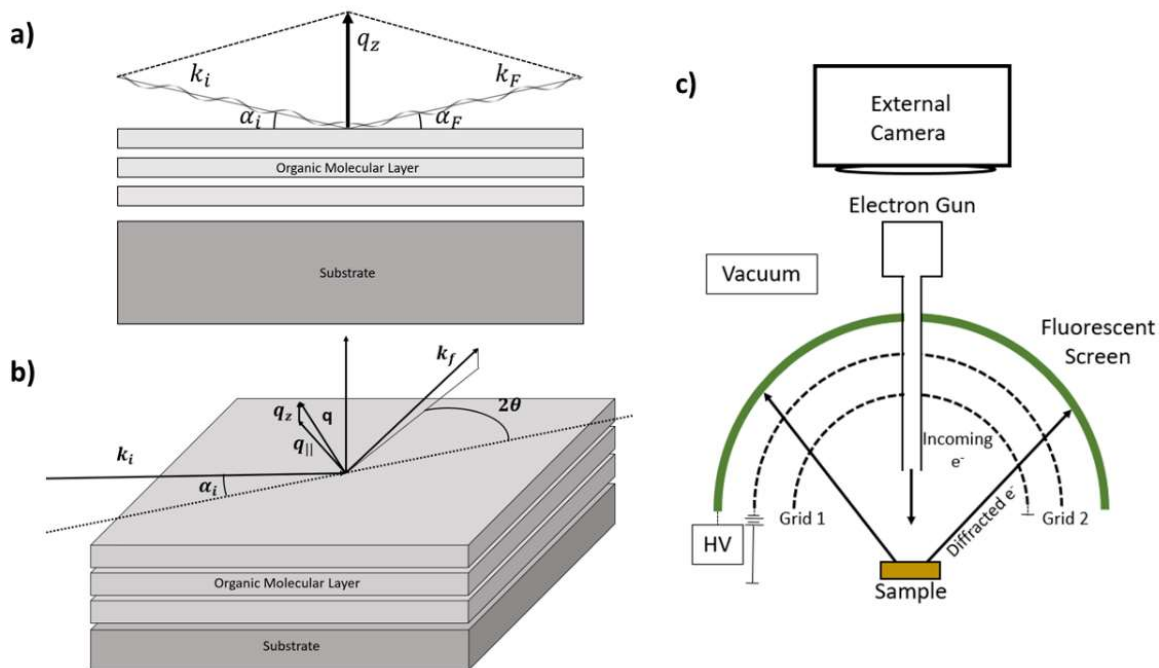


Figure 2-2: X-ray scattering and LEED geometries

X-ray scattering geometries for (a) x-ray reflectivity (XRR) and (b) grazing incidence diffraction (GID). XRR is capable of providing information on the surface/interface roughness, interlayer distance and film thickness. GID can provide information on the in-plane lattice parameters. (c) Schematic of a low energy electron diffraction (LEED) setup. Diffracted electrons are accelerated towards the fluorescent screen where a periodic lattice will be represented by well defined diffraction spots on the screen.

2.4 Case studies of organic molecular thin film growth on weakly interacting and strongly interacting substrates

2.4.1 Molecule on Silicon Oxide

Armed with these experimental techniques, researchers have explored different combinations of molecules and substrates. As we have mentioned before, the molecule-molecule and molecule-substrate interaction is of paramount importance to the development of a well-organized film. The amorphous and insulating nature of silicon oxide (SiO_2) make it a prime

candidate for studying the growth of organic molecular assembly in the low molecule-substrate interaction scenario. In Figure 2-3, we present the results of a study of di-indenoperylene (DIP) on SiO₂ using AFM, XRR and GID performed by Dosch, *et. al.*[70] AFM images of DIP films at different thicknesses grown at room temperature are shown in Figure 2-3. In the initial stages of growth, DIP grows in a layer-by-layer-fashion with the first monolayer completed before the second layer begins to grow. This behavior appears to continue until roughly around the formation of the 3rd monolayer where this layer-by-layer growth devolves into island growth with the 4th monolayer beginning to grow before the completion of the 3rd monolayer. The behavior continues at even higher coverage, translating to a 3D growth and an overall rough film.[70]

X-ray scattering experiments have also been conducted to provide further insights into the mechanisms of the growth mode transition. It is known that the intensity of X-ray reflectivity depends on surface/interface roughness. Therefore, if being monitored *real-time* at chosen q_z -points, X-ray reflectivity measurements will provide information on the evolution of film roughness from which the growth mode transition can be derived. For instance, well defined reflectivity oscillations with respect to growth time or film thickness will indicate layer-by-layer growth, while the damping of the oscillation can be attributed to the transition towards the island growth. In details, in the layer-by-layer growth, upon completion of a full monolayer, film roughness reaches to minimum, corresponding to the maximum reflectivity. Figure 2-3b reveals three growth oscillations as expected for the layer-by-layer growth, followed by the damping of the oscillation which is associated with the increase in film roughness. This observation is in agreement with the AFM results. As discussed previously, XRR is also capable of measuring the interlayer distance in organic thin films. Figure 2-3c illustrates that this distance decreases initially until it reaches to a constant value beyond a few monolayers, evidencing a change in the molecular

tilting angle with respect to the surface normal from 3° (at 2ML) to 21° (at 4ML). These changes in the growth behavior and molecular tilting angle are further accompanied by the relaxation of the compressively strained in-plane molecular unit cell (probed by GID), primarily along the b-vector, towards its bulk configuration, as shown in Figure 2-3d. The compressive strain in the initial few layers was suggested to originate from the amorphous nature of the SiO_2 substrate. Due to the lack of epitaxial relationship between the molecular overlayer and the substrate surface, molecules are able to adopt denser unit cells in order to maximize their intermolecular interaction.[70]

Thus, the comprehensive X-ray reflectivity and GID studies clearly show that the shift of the roughness behavior occurs in the 3-4 monolayer regime, which is associated with the change in the molecular tilting and unit cell relaxation.[70] Such phenomenon can be explained by the interlayer mass transport of organic molecules. As has been mentioned before, the downward interlayer mass transport is dictated primarily by the downward ESB. However, this system is complicated further by the introduction of a sizable upward interlayer mass transport. The increase of the molecular tilting angle with respect to the surface normal leads to an increasing downward ESB and a decreasing upward ESB, and the combination of the two effects leads to the collapse of the layer-by-layer growth and the emergence of the island growth.[70] Lastly, it is worth pointing out that due to the lack of the epitaxial relationship between the molecular overlayer and the substrate surface randomly oriented molecular domains are formed, leading to a high density of large-angle grain boundaries to scatter or trap charge carriers. It is therefore necessary to explore the growth of molecular thin films on substrates that offer a stronger molecule-substrate interaction and a high degree of crystallinity to enable the epitaxial registration to molecular overlayers.

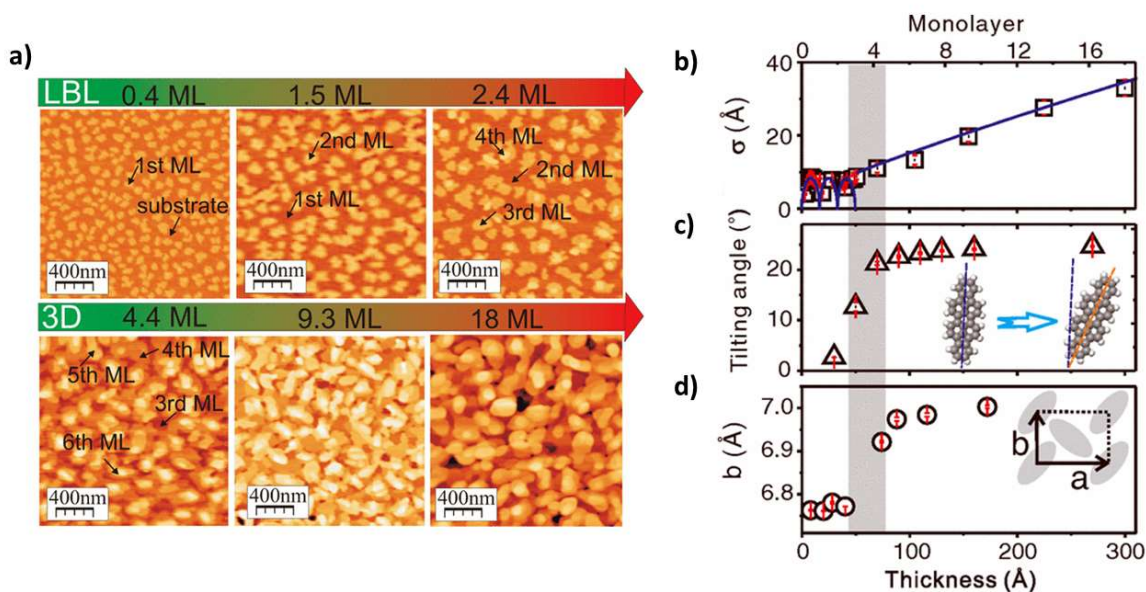


Figure 2-3: Growth of DIP on SiO₂

Growth of DIP on SiO₂ reprinted with permission from [70]. (a) AFM images at different film thicknesses showing a transition from layer-by-layer growth to 3D island growth. Summary of data gathered from XRR and GID showing the evolution of (a) root mean square roughness (correlated to reflectivity intensity), (b) tilting angle with respect to the surface normal (correlated to interlayer distance), (c) b-vector of the DIP in-plane unit cell, with respect to the film thickness. All parameters seem to demonstrate a similar transition in the 3-4 monolayer regime denoted by a shaded area.

2.4.2 Molecule on Metals

Exploring the higher molecule-substrate interaction, researchers have naturally turned to the growth behavior of organic molecules on metal surfaces. These surfaces also offer the benefit of being highly crystalline as compared to the amorphous SiO₂. As seen in Figure 2-4a, pentacene molecules form organized structures on the Au(111) surface, where they adopt a flat lying configuration in the wetting layer driven by the strong molecule-substrate interaction.[74] However, upon further deposition, molecules were found to form localized 3D crystallites. The tilting herringbone structures as that of the bulk were observed with different facets of the molecular crystals being exposed, as illustrated in Figure 2-4b. It should be noted that the

molecular packing of pentacene in the wetting layer on Au(111) is different from any (hkl) slice of the reported bulk structure, therefore, the reversion to the bulk structure in thicker films can be attributed to the relaxation of the strain built up in the first monolayer.[74]

To circumvent this problem that commonly happens in molecular growth on metal surfaces, it will be beneficial if the molecular entity utilized possesses a crystal facet in its bulk structure that is comprised of flat-lying molecules as those displayed in the wetting layer. This could potentially reduce the degree of molecular reorientation in thicker films and the amount of strain introduced by the strong molecule-substrate interaction. Perylenetetracarboxylic dianhydride (PTCDA) is a rational choice as its crystal structure is comprised of layered molecular stacks.[17] Specifically, the (102) plane is constructed of approximately coplanar molecules. To investigate the evolution of the PTCDA growth on Ag(111), XRR data taken on thin films grown at different substrate temperatures will be discussed. Oscillating XRR signal at the anti-Bragg point, $q = \frac{1}{2} \cdot q_{Bragg}$, and the corresponding roughness measurement as shown in Figure 2-4c, d reveal an initial layer-by-layer growth followed by an eventual collapse into the island growth with temperature dictating the rate of collapse.[17] This suggests that the wetting layers of PTCDA are still strained, and the growth mode evolves despite that molecules remain the flat-lying configuration through the entire film. Unlike the case of DIP on SiO₂ where the growth mode transition is attributed to the changing molecular tilting angle and the associated variation in ESB, the transition of PTCDA is due to the competition between the wetting-favored molecule-substrate interaction and the island-favored relaxation of strain.[17]

Lastly, we will discuss the impacts of the stronger molecule-substrate interaction and the high crystallinity of metal surfaces on the epitaxial registration of the molecular films. As presented in the STM images in Figure 2-4e, PTCDA molecules deposited on the Ag(111) surface

prefer to adsorb to the step edges of the substrate, arising from the enhanced coordination of molecules at the step edge.[78] Unit cell measurements from LEED and STM indicate that PTCDA molecules adopt a rectangular commensurate structure with the metal substrate. LEED simulation of the PTCDA monolayer, as shown in Figure 2-4f, further reveals the presence of multiple molecular domains with one of them illustrated by filled circles. This indicates that the step-phase is short-ranged, likely due to the low molecular diffusivity on a strongly interacting surface. 6 molecular domains, i.e., three rotational domains and their corresponding mirror domains, exist on the wide Ag(111) terraces, originating from the symmetry mismatch between the molecular unit cell and that of the metal substrate.[78] As discussed earlier, this is problematic because the presence of these different domains will lead to the formation of domain boundaries which could effectively scatter charge carriers.

To summarize, molecules deposited on SiO₂ and Ag(111) form initial wetting layers, followed by a collapse into the island growth at higher film thicknesses, leading to the lack of out-of-plane ordering. On the other hand, the in-plane growth of molecules on silicon dioxide lacks epitaxial guidance and thus cannot form long-range ordered structures due to the amorphous nature of the substrate. Molecular growth on metal surfaces, however, can lead to the formation of multiple rotational/mirror domains on the surface. The demonstration of long-range ordered and single crystalline organic thin film is thus highly desirable.

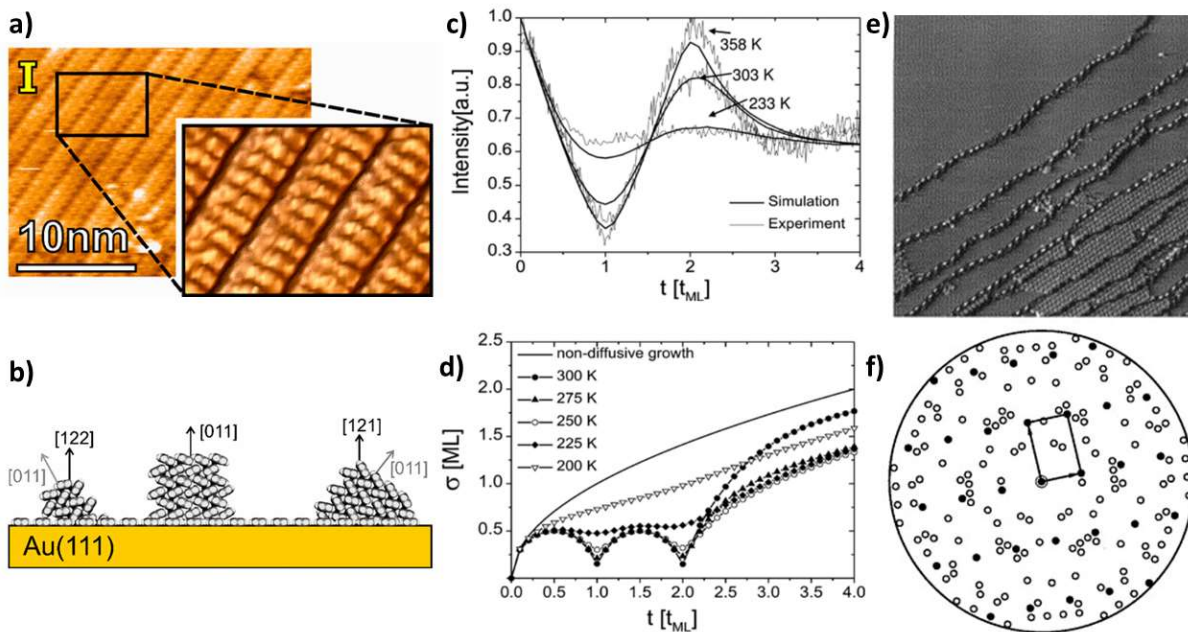


Figure 2-4: Growth of organic molecules on metals

(a) STM image of pentacene monolayer on Au(111). (b) Schematic of the growth of pentacene on Au(111). Pentacene initially forms a flat-lying wetting layer before relaxing into its bulk crystal with different facets of the crystal exposed. Reprinted with permission from [74]. (c) XRR data of PTCDA on Ag(111) at the anti-Bragg point demonstrating growth oscillations at substrate temperatures of 233K, 303K and 358K. Monte Carlo simulation results are also plotted which fit well to the experimental observation. (d) Film roughness, σ , which also shows growth oscillation with minima occurring upon completion of a layer. Reprinted with permission from [17]. (e) STM image of PTCDA on Ag(111) showing step edge nucleation and molecular assembly structures. Width of image represents 70.4nm. (f) LEED Simulation pattern of PTCDA monolayer on Ag(111) that agrees with experiment showing 3 rotational domains and their corresponding mirror domains. One of the domains is indicated by filled dots and the unit cell is illustrated. Reprinted from [78].

2.5 Long-range ordered growth in both in-plane and out-of-plane directions demonstrated using ZnPc on deactivated Si(111)-B

Next, we use specific examples to illustrate the kinetics and thermodynamics considerations for attaining long-range ordered organic molecular assemblies. Zinc phthalocyanine (ZnPc) grown on the deactivated Si(111)-B $\sqrt{3} \times \sqrt{3}$ surface is an example of such a system.[88,111-113] The deactivation of the Si(111) surface is established via thermally

segregating substrate boron dopants to the third atomic layer which deplete electrons from the Si adatoms, leading to a highly-crystalline, atomically flat and “chemically inert” surface.[114-118] The deactivated surface shows a clean band gap in the STS spectrum, in comparison to the metallic surface states observed on the 7×7 reconstructed Si(111), as seen in Figure 2-5a. The lack of density of states at the Fermi level contributes to the suppressed orbital hybridization between molecular adsorbates and the deactivated Si(111)-B surface, particularly when ZnPc molecules with the central metal ion of fully occupied d -orbitals are concerned. This relatively weak molecule-substrate interaction enables a large molecular diffusivity, allowing ZnPc ad-molecules to fully explore the surface potential landscape at room temperature to find energetically favorable nucleation sites at the bottom of Si step edges. ZnPc molecules then assemble outwards across the Si terraces in a highly ordered, anisotropic stripe structure (Figure 2-5b), i.e., step-flow growth, followed by termination upon reaching the upper end of the following Si step edge due to the large ESB involved in molecules descending the edge.[111]

2.5.1 *Step-flow growth of ZnPc on deactivated Si(111)-B*

Owing to the hexagonal symmetry of the deactivated Si(111)-B surface, if the ZnPc growth proceeds with the 2D island nucleation on the middle of the Si terraces, all six molecular domains allowed by the substrate symmetry, i.e., three from rotational symmetry of the substrate and two from the mirror reflection symmetry for each rotational domain, would be present. This is indeed what was observed (Figure 2-5c) when the deposition was carried out on a highly defected Si(111)-B surface. In contrast, on a surface with low defect density the flux accumulation on terraces can be suppressed, and the step-flow growth is almost entirely dominated by an exclusive in-plane orientation that provides the shortest path between step edges, which essentially reduces the substrate symmetry and eliminates rotational domains. Although mirror domains (Figure 2-5d)

still exist within the system leading to the creation of low-angle twin boundaries, it has been shown that trapping and scattering of charge carriers is not nearly as detrimental as at large-angle grain boundaries.[21,23] This study marks the first observation of step-flow growth of organic molecules on a semiconducting substrate.[113]

Through differential conductance mapping and apparent height measurement of the ZnPc assembly, molecules were found to tilt at $\sim 30^\circ$ with respect to the surface. The tilting configuration originates from the large lattice constant of the deactivated Si(111)-B surface ($6.65 \pm 0.01 \text{ \AA}$), two or three times larger than those of metallic surfaces typically utilized in ZnPc studies, resulting in a more corrugated potential energy landscape of ZnPc on the surface.[112] As discussed earlier, molecular adsorption and nucleation occur at local energetic minima on the surface potential energy landscape. With increasing molecular coverage, the additional energy gain from the intermolecular interaction can be fully achieved on a metallic surface due to its flat potential energy landscape, driving the formation of close-packed flat-lying molecular structures on the surface. However, on the deactivated Si(111)-B with high surface potential corrugation, rather than occupying many energetically unfavorable sites for incoming molecular adsorbates, it is energetically more beneficial to maximize the intermolecular attraction at the cost of a portion of surface adsorption energy when the molecule-substrate interaction is comparable to or weaker than the molecule-molecule interaction, leading to a structural transition of molecular aggregates from the flat-lying configuration to a tilted one at higher coverages (Figure 2-5e).[112] This tilting configuration allows for good molecule-molecule coupling through the overlapping π -systems, favoring superior electrical conduction along both the molecular stripes (in-plane direction) and between the molecular layers (out-of-plane direction).[88]

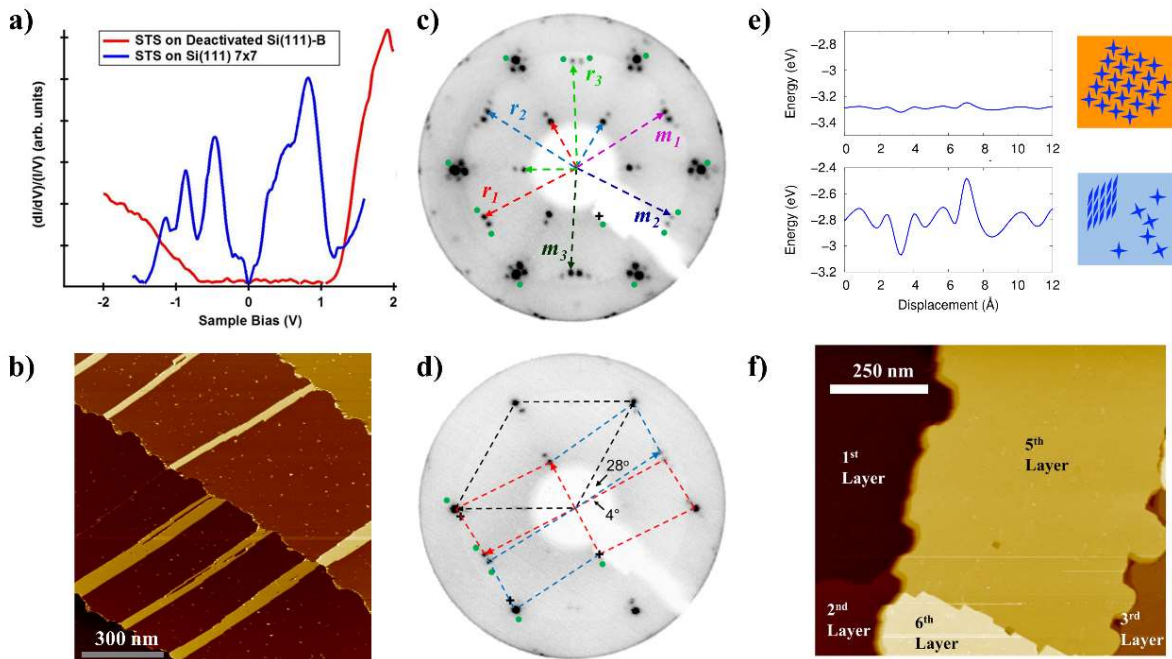


Figure 2-5: Growth of ZnPc on deactivated Si(111)-B

(a) STS spectra of the 7×7 reconstructed Si (blue) and the deactivated Si(111)-B surface (red), demonstrating the emergence of a clean band gap in the latter. Reprinted from [88]. Copyright 2014 American Chemical Society. (b) STM image of ZnPc (the parallel stripes) deposited on Si(111)-B (a vicinal surface) that exhibits the anisotropic step-flow growth. Once the molecular stripes are terminated by upper Si step edges due to the large ESB barrier associated with the interlayer mass transport, they will expand laterally to complete the monolayer. Reprinted from [113]. LEED images of ZnPc molecular structures grown on Si(111)-B with (c) a defected surface and (d) a pristine surface, demonstrating the reduction in the number of molecular domains through step-flow growth on the pristine surface. Six colored domains of ZnPc are depicted in (c) with the lattice vectors of the rotational domains and their corresponding mirror domains denoted by r and m , respectively. Unit cells of the Si(111)-B surface (dotted black) and the two mirror domains of ZnPc (dotted blue and red) in the reciprocal space are indicated in (d) to illustrate the specific azimuthal registration of the molecular overlayer to the substrate surface. Note that the black crosses indicate the location of expected ZnPc diffraction peaks while the green dots indicate the location of expected satellite peaks from the Moiré patterns that were not intense enough to be observed in experiments. Reprinted from [88]. Copyright 2014 American Chemical Society. (e) Potential energy landscapes (left panels) of a CuPc molecule on Au(111) (top) and Si(111)-B (bottom), and the resulting morphologies (right panels) of CuPc aggregates (blue stars). Molecules on the corrugated Si(111)-B surface sacrifice a portion of the molecule-substrate interaction in favor of the greater intermolecular interaction, leading to a tilted molecular configuration at higher coverages. Reprinted from [112]. (f) STM image of few-layer ZnPc on Si(111)-B, which illustrates the ability of ZnPc to grow in a layer-by-layer fashion within Si terraces. Reprinted from [111].

2.5.2 *Out-of-plane ordering of ZnPc on deactivated Si(111)-B*

Lastly, with increasing film thickness, the ZnPc growth is able to maintain the same molecular packing beyond 40 monolayers.[88] Although molecular packing of ZnPc film is different from any (*hkl*) slice of the reported bulk structure, no significant structural relaxation or molecular reorientation has been noticed with the increase of film thickness, likely due to the favorable π - π interaction between molecular layers afforded by the tilting molecular configuration. Consequently, the layer-by-layer growth of ZnPc molecular thin films within individual Si terraces is established, as shown in Figure 2-5f. However, it should be noted that film roughness still increases with coverage due to the inability of ZnPc to diffuse down the Si step edges. This can be mitigated, in part, through the use of substrates with lower miscut angles allowing for larger terraces for molecular growth. Nevertheless, the demonstration of long-range ordering of an organic molecular system both in and out-of-plane with uniform molecular orientation will be highly pertinent to the creation of high-performance organic electronic devices.

2.6 Organic-inorganic van der Waals heterostructures: a promising template for device applications

Recently, the combined hybrid systems of 2D inorganic materials and organic thin films have attracted intense research interest for their potential electronic and optoelectronic applications.[42,92,119-132] 2D inorganic materials can exhibit widely varying properties, from semimetallic graphene and its insulating isomorph hexagonal boron nitride (h-BN) to certain semiconducting transition metal dichalcogenides (TMD). The corresponding bulk materials, such as graphite, have the inherent benefit of being cleavable, meaning that their interlayer interaction is governed by van der Waals force and their surfaces lack dangling bonds.[92,122,124] This,

coupled with the high degree of crystallinity, makes 2D layered atomic crystals suitable candidates for supporting the growth of organic thin films.

The integration of these two different classes of materials opens the possibility of developing flexible (opto)electronic devices with novel architectures where important device components such as gate dielectric, contact electrodes and active semiconducting layer can all be constructed using a combination of atomically thin 2D crystals and highly functionalized organic molecular assemblies.[124,125,132-136] The specific role of the organic molecular component depends on the desired applications. For instance, the large light absorption cross section of organic molecules makes them excellent sensitizers, paving the way for inorganic-organic photovoltaic devices.[119,132,137] Gate-tunable organic-inorganic (graphene/TMD) Schottky junctions that afford a high rectifying ratio and photovoltaic responses have been explored.[119,137-139] Additionally, organic molecules with strong electron-withdrawing/-donating or dipole groups self-assembled on the surface of 2D electronic materials can effectively introduce doping or exert a periodic surface potential modulation to the 2D material.[129,140,141] Such chemical doping methodology has shown promise in modulating the optical and optoelectronic characteristics of 2D van der Waals crystals. [142-144]

In the context of forming well-ordered organic molecular assemblies on 2D materials for the development of high-performance OFETs, C8-BTBT (2,7-dioctyl[1]benzothieno[3,2-*b*][1]benzothiophene), a molecular system with large charge carrier mobility, stands out for showing encouraging results with regards to growth and device characteristics.[139,145] As shown in Figure 2-6a,d, C8-BTBT films demonstrate decent crystallinity on 2D materials, however, the growth of C8-BTBT starts with nucleation at areas of high surface energy, i.e., grain boundaries or wrinkles for the case of graphene and h-BN and atomic defects resulting from sulfur vacancies

in the case of MoS₂.^[139,145] This puts a stringent requirement on the defect-control of the 2D material, necessitating large single-crystalline grains with minimal surface defects in order to maximize the domain size and the long-range ordering of the molecular overlayer. Significant research efforts are being put towards this issue with recent advances in the growth of large-scale single-crystalline h-BN and graphene.^[119,124,145-151] Furthermore, C8-BTBT on 2D materials undergoes a structural transition with increasing film thickness as seen in Figure 2-6b,c,e. As an example, the initial C8-BTBT wetting layer on graphene adopts a flat-lying molecular configuration originating from the interaction between the π -systems of C8-BTBT and graphene or h-BN before quickly transitioning into a more standing orientation in subsequent layers.

While further improvements of this broad class of organic-inorganic hybrid structures could likely be attained through controlling the quality of the associated interfaces and the morphologies of organic molecular thin films, devices fabricated from such systems have already demonstrated impressive performance. For instance, OTFTs fabricated with crystalline C8-BTBT monolayers (excluding the initial interfacial layer with the flat-lying molecular configuration) on h-BN exhibit intrinsic hole mobility over 30 cm²/Vs, which is among some of the highest in OTFT devices, and Ohmic contact with laminated Au top electrodes.^[152] Furthermore, the adoption of the tilted molecular configuration in the C8-BTBT channel results in a favorable intermolecular interaction which leads to band-like transport down to 150K. Strikingly, the efficient charge injection is only observed in the monolayer devices. For devices made of bilayer or thicker C8-BTBT films, Schottky contact with large contact resistance dominates. Measurements of the drain-source current, I_{ds} vs. temperature, T show the temperature-independent trend in monolayer devices associated with the tunneling charge injection process, while the I_{ds} of bilayer devices decreases with temperature suggesting charge injection occurs through thermionic emission as

seen in Figure 2-6f. Here, the Ohmic contact was attributed to the direct tunneling of electrons between the non-invasive laminated Au contacts and the monolayer transport channel (Figure 2-6g), along with the close alignment of C8-BTBT's valence bands of high density of states (DOS) with Au Fermi level which further enhances the tunneling probability at the interface. This tunneling mechanism is suppressed in thicker films, partly due to the greater separation between Au electrodes and the charge-transporting layer adjacent to the h-BN dielectric interface.

This example also indicates that the structural relaxation from monolayer to bi-layer, again excluding the initial interfacial layer, with C8-BTBT molecules adopting a completely standing orientation, gives rise to an alteration of the intermolecular orbital overlap, which results in charge localization of the molecular valence states, detrimental to charge transport and device performance.[152] As shown in the ZnPc growth on the deactivated Si(111)-B surface, the large surface potential corrugation and the realization of the step-flow growth help support long-range ordering of the film with uniform molecular orientation both in-plane and out-of-plane.[112,113] However, creating long-range ordered thin films in larger molecular systems, like C8-BTBT, will likely require the discovery of different innovative mechanisms for controlling the thermodynamic and/or kinetic parameters during the growth process.

In summary, the growth of organic molecular thin films has undergone substantial development in recent years with the demonstration of anisotropic step-flow growth with outstanding ordering both in-plane and out-of-plane. Electronic devices based on hybrid organic-inorganic 2D heterostructures have shown great promise, however, the precise control of long-range ordering and molecular orientations within such films, in order to optimize device performance, is still under development. Nonetheless, the growth of organic molecular thin films

only represents one aspect of the device design, the electronic structures of these films and how they are perturbed by the heterointerfaces must also be considered.

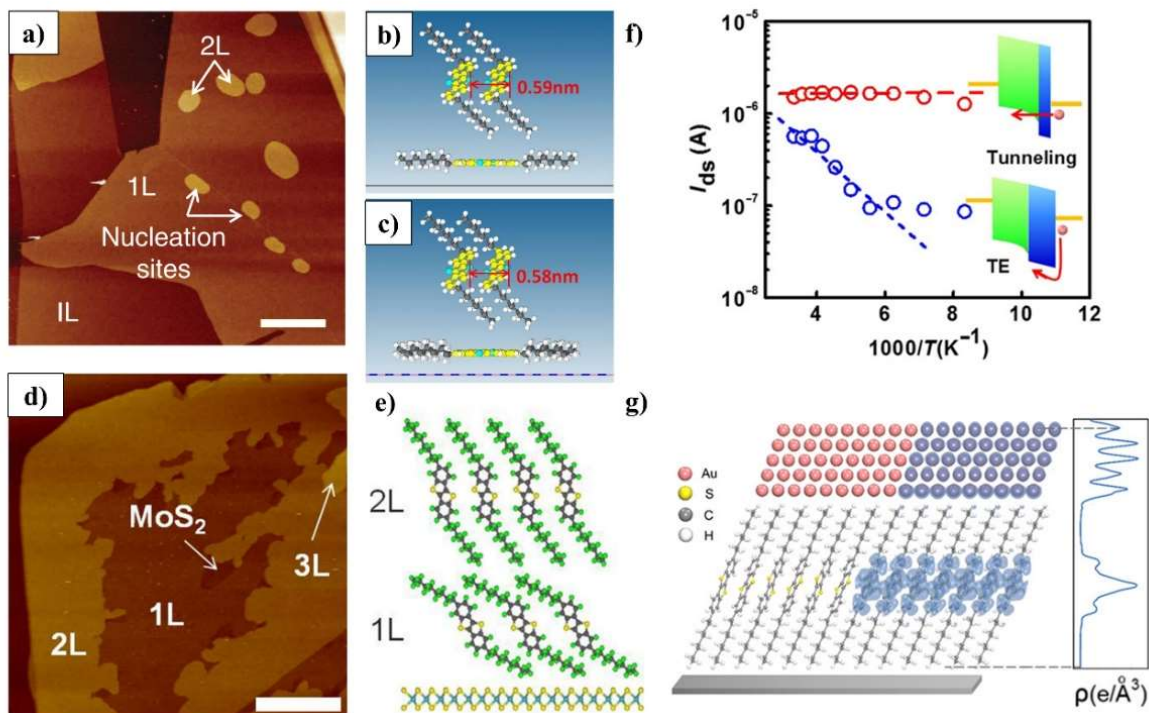


Figure 2-6: Growth and Device Application of Organic Molecules on 2D Materials

AFM images of the growth of C₈-BTBT on (a) graphene and (d) MoS₂. Molecules grow in a layer-by-layer fashion on graphene with nucleation occurring at wrinkles of the graphene substrate, while a layer-plus-island growth mode is observed on MoS₂. Molecules adopt a flat-lying configuration in the initial interfacial layer on (b) graphene and (c) h-BN, while on (e) MoS₂ they adopt a tilted configuration. Subsequent layer growth results in the structural relaxation towards a standing configuration in all systems. Reprinted from [139,145] (f) Arrhenius plot of I_{ds} ($V_g = -70$ V, $V_{ds} = -1$ V) of C₈-BTBT monolayer (red) and bilayer (blue) devices on h-BN. The initial interfacial layer with the flat-lying molecular configuration is not taken into account. Inset shows the band diagram and the relevant charge injection process with TE referring to thermionic emission. The temperature independence of I_{ds} of monolayer C₈-BTBT devices is indicative of a tunneling charge injection process, while the significant decrease of the bilayer I_{ds} with temperature demonstrates a thermally activated charge injection process and the presence of a sizable energy barrier. (g) Illustration of the atomically sharp C₈-BTBT / Au interface. The right side of the graph is overlaid with the charge density in the energy range from the Fermi level to 0.5eV below, with the distribution along the z direction plotted in the inset. The tunneling distance is attributed to the side carbon chain which separates the metal contact from the conducting benzothiophene core. Reprinted from [152]

3 Electronic Structures of Organic Molecular Thin Films

OFETs constructed of crystalline C8-BTBT monolayers provide a great example of the importance of contact optimization on device performance. In OLEDs and OPVs, charge injection from electrodes to organic semiconductors or charge collection by electrodes are also crucial to the operation of devices. Electronic structures of organic molecular thin films, specifically its energy level alignment with electrodes at the interface, are of primary concern.[153,154]

Metal-semiconductor contacts are typically categorized into two different conduction mechanisms, thermionic emission and tunneling with the latter providing a feasible route to form Ohmic contact. In order to favor the tunneling process, the width of the tunneling barrier needs to be minimized. This can be achieved, for instance, by inserting a contact doping layer between metal and organic semiconductor, where the doping of the organic film results in a narrowed space charge layer.[153,154] For devices made of monolayer organic films such as C8-BTBT as discussed previously, the width of the barrier is physically reduced to less than 1nm. Alternatively, decreasing the Schottky barrier, ϕ_B , will lead to the exponential decrease in the contact resistance.[154] However, in order to minimize the Schottky barrier, the specifics of the interfacial electronic structure need to be considered.

The charge injection barriers, in the simple case of vacuum level alignment (the Schottky-Mott limit), are defined as the energetic separation between the Fermi level of the metal contact and the charge transport levels of the organic semiconducting film, typically derived from the highest occupied molecular orbital (HOMO) and lowest unoccupied molecular orbital (LUMO) positions of the organic molecule. In the Schottky-Mott limit, the contact injection barrier can be effectively tuned by modulating the metal work function using self-assembled monolayers, metal

oxides, inorganic salts, or 2D materials such as graphene.[154-157] It is worth noting that the presence of these insertion layers between metal contact and organic film may perturb the substrate image-charge screening as well as the molecular orientation.[42,139,145] These electronic and structural changes can have profound impacts on the energetic positions of the relevant frontier molecular orbitals.

However, the Schottky-Mott limit is a scenario that cannot always be attained. In many cases, the formation of chemical bonds, the weak hybridization between organic molecular orbitals and the metal continuum states, or the emergence of defects at metal-organic interfaces give rises to gap states and/or the broadening of molecular orbitals, which can pin the Fermi level and limit the tuning of the injection barrier.[40,43] Even at weakly interacting interfaces where chemical interaction or orbital hybridization is absent, Fermi level pinning can still occur when there is charge transfer between the contact and the organic layer.[155,158,159] In the scenarios of weakly interacting interfaces, energy level alignment is typically dictated by the integer charge transfer model (ICT).[40] In the following sections, we will first discuss the general influence of electrostatic screening and molecular orientation on organic molecular electronic structures, followed by a discussion on the different energy level alignment regimes that are highly dependent on the nature of the interaction at interface. A greater emphasis will be placed on the weakly interacting regime, particularly the ICT system, due to the improvement in ordering demonstrated on weakly interacting surfaces shown earlier in Chapter 2.

In this chapter, we will discuss the various factors that can influence the electronic structure of organic molecules and the resulting energy level alignment. In Section 3.1, the general effects of electrostatic screening and molecular orientation on the molecule's electronic structure are discussed. Section 3.2 will discuss the effects on the electronic structure and energy level

alignment for molecules adsorbing onto metal or strongly interacting surfaces. Weakly-interacting molecule-substrate interfaces will be discussed within the context of the integer charge transfer model in Section 3.3. This review was adapted from Reference [46]: *A. Tan et al., Journal of Physics: Condensed Matter (2019) (Manuscript In-Review)*.

3.1 Dependence of Electronic Structures of Organic Molecules on Electrostatic Screening and Molecular Orientation

The first step in determining the energy level alignment and the relevant charge injection barriers is the accurate determination of the molecular electronic structure. As mentioned before, the weak wavefunction overlap and non-covalent intermolecular interaction are typically involved in organic molecular systems, which results in band structures with very little dispersion and small bandwidths compared to their covalently bound inorganic counterparts.[43,160,161] Rubrene, a benchmark molecular system, shows a bandwidth of 0.4eV, while most other organic systems exhibit even smaller dispersion width.[160] As a result, energy states in molecular films or crystals are more akin to discrete and localized levels than delocalized bands. The associated strong charge localization can further complicate the electronic structure measurements. For instance, molecular band gaps measured by techniques such as UPS and STS, which involves the injection or extraction of an electron from the film, is always larger than that derived from the single-particle or mean-field theory.[34,39] Furthermore, the molecular band gap is not rigid. Instead, it varies significantly with the electrostatic environment.[32-36] These phenomena can be attributed to the charging energy (U), an additional energy term that originates from the strong Coulomb repulsion between the localized excess charge created by the electronic-structure-probing technique and other molecular charges, which enlarges the band gap (Figure 3-1a).[33,37-39,162,163] For the

case of an N-electron molecule, with the consideration of U, the total energy can be approximated as

$$E_N = \sum_{i=1}^N (\epsilon_i - \mu) + \frac{\Delta N(\Delta N - 1)}{2} U \quad (3-1)$$

where ΔN represents the net charge of the molecule, ϵ_i the mean-field molecular energy levels and μ the chemical potential of the underlying substrate if present.[37] This charging energy can be attenuated through a variety of means in molecular crystals or molecular assemblies on a supporting substrate (Figure 3-1a). For instance, the polarization of neighboring molecules and the formation of image charges in the substrate will contribute to the screening of U, resulting in a significantly reduced band gap in molecular condensates as compared to that of the gas-phase molecules. [33,34,38,42,162,164] The various screening effects render the molecular electronic structures sensitive to the local electrostatic environment. Necessarily, due to the different screening contributions, the observed band gap of organic molecules in their bulk structure and thin-film phases can be different (Figure 3-1a).[39,165] It is worth noting that due to the anisotropic nature of organic molecules and their complex packing in molecular thin films, the polarization response of neighboring molecules and their resulting contribution to the screening of U can be complicated (Figure 3-1b).[164]

$$E_{polarization} = \frac{e^2}{16\pi^2\epsilon_0^2} \sum_{i=1}^{N-1} \frac{(\alpha_{MM} \sin^2 \beta_i + \alpha_{LL} \cos^2 \beta_i)}{R_i^4} \quad (3-2)$$

where R_i represents the distance between the considered pair of molecules, β_i is the angle between the pair-connecting vector and the long-axis of the molecule, α_{MM} and α_{LL} represent the polarizability of the molecule with respect to the short and long axis, respectively. This equation can be simplified for a symmetric system like C₆₀ or Pc molecules to:

$$E_{polarization} = \frac{Ne^2\alpha}{2R^4} \quad (3-3)$$

N is the number of closest molecular neighbors, α is the polarizability of the molecular species and R is the intermolecular distance. Molecules adopting different packing via adsorption on different substrates could lead to significant alterations in their HOMO/LUMO positions due to the polarization response of neighboring molecules as well as the substrate screening.[34,137,166-169]

Since charge injection barrier and contact resistance in electronic devices are most directly related to the electronic structures of organic molecules near the contact interface, we discuss the effects of substrate electrostatic screening quantitatively. As shown in Figure 3-1c, the substrate screening effect can be estimated by the classical image-charge model equation:

$$E = \frac{qq'}{4\pi\epsilon_0 \cdot 2(d - z_0)} \quad (3-4)$$

where d is the molecule-substrate distance, $q' = q(\epsilon - 1)(\epsilon + 1)$ is the effective image charge, and z_0 the effective position of the image plane.[42,93,170-172]

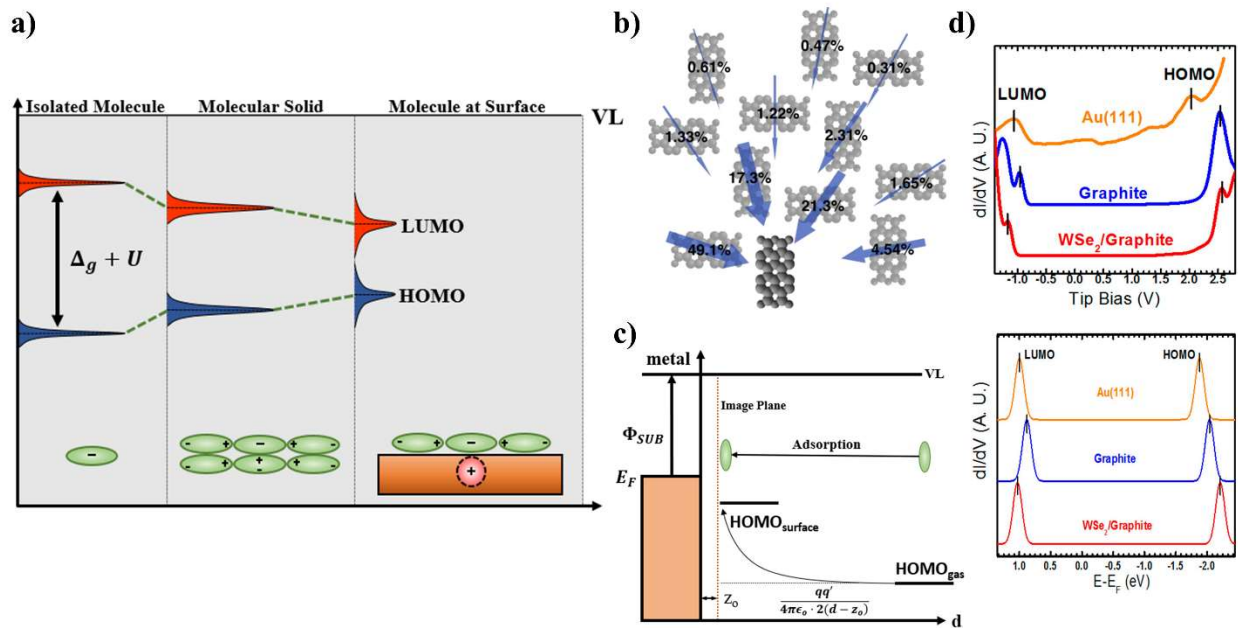


Figure 3-1: Dependence of organic molecular electronic structure on local electrostatic environment

(a) Diagram summarizing the influence of the charging energy on the measured molecular band gap and the subsequent screening of this energy through neighboring polarization and image charge formation within the substrate. Δ_g is the molecular electronic gap derived from the single-particle or mean-field description. U is the charging energy. The charging energy, once attenuated by the substrate screening and/or polarization of neighboring molecules, can result in molecular electronic structures that are highly susceptible to electrostatic environments and molecular packing. Adapted from [39] (b) Percentage contribution of neighboring PTCDA (perylene-tetracarboxylic dianhydride) molecules to the screening of U on the molecule drawn in solid grey. Arrows represent induced dipole direction with the width of arrows representing induced dipole strength. Reprinted from [164] (c) Organic molecular adsorption on a supporting substrate results in the formation of an image charge in the substrate, leading to the screening of U and an upshift in the HOMO of the molecule. (d) Top: STS spectra of PTCDA on Au(111), graphite, and WSe₂/graphite, revealing the HOMO-LUMO gap variations on the different substrates. Bottom: Theoretical predictions of the HOMO and LUMO positions of PTCDA on different substrates after considering the GW approximation (for electron-electron correlation) and the image-charge model. Reprinted from [42]. Copyright 2016 American Chemical Society.

Metals, for example, typically have more protruding image planes, and when considered in conjunction with the enormous collection of free charge carriers, results in a very large screening capability. Experimentally, the influence of the image charge and the resulting screening on U has

been verified in numerous systems.[39,42,137,173-175] For example, molecular assemblies of PTCDA (perylene-tetracarboxylic dianhydride) on Au(111), graphite, and WSe₂/graphite represent three different systems relevant to contact interfaces.[42] In these scenarios, PTCDA molecules all adopt a lying-down configuration on the surfaces with similar lattices. As a result, the polarization response of neighboring molecules and its contribution to the reduction/screening of U are expected to be similar among the three systems. However, due to the varying position of the image charge plane, the substrate screening on U differs drastically. For example, Au(111), graphite, and WSe₂/graphite have image planes that protrude 0.9Å, 0.7Å and 0.1Å above the surface atomic layer, respectively. As a result, PTCDA molecules adsorbed on the Au(111) surface show a molecular band gap of 3.1 eV. In contrast, gaps of 3.49 eV and 3.73 eV are observed for molecules on the graphite and WSe₂/graphite surfaces, respectively, as seen in Figure 3-1d. A sizable difference of ~0.6 eV in molecular bandgap between the extreme cases of this example could have huge consequences for interfacial energy level alignment and thus the charge injection barriers in organic electronic devices. One common methodology of lowering the contact resistance between metal electrode and organic semiconducting film is the insertion of an intermediate layer which can serve to tune the work function of the metal electrode and/or to dope the organic layer.[154,157] Inevitably, this approach may result in the alteration of the frontier molecular orbitals, as shown in the case of WSe₂/graphite. Naturally, this image charge effect will decay with increasing film thickness, which often leads to the widening of the band gap in thicker molecular films.[165,176,177] It should be noted that the image charge plane position can also be adjusted by variations in the surface or even the sub-surface features of the same substrate.[93,178]

Beyond its influence on substrate screening, the insertion layer can also alter the orientation of organic molecules with respect to the substrate surface. The extended nature of organic

molecules and the associated quadrupoles will play a role in determining the energetic positions of frontier molecular orbitals in a molecular thin film. Conjugated molecules typically possess permanent quadrupolar charge distributions with negative charge density (π -electrons) above and below the molecular plane and positive charge density (nuclear charges) in the molecular plane.[31] These local variations from the quadrupole field have no significant influence on the ionization potential (IP) and electron affinity (EA) of free isolated molecules as the electrostatic potential arising from the local charge distribution decays quite rapidly to a common vacuum level within a few angstroms as seen in Figure 3-2a.[29,31] Here, IP and EA refer to the amount of energy required/released when an electron is removed from/added to a neutral molecule, respectively. However, in the case of a molecular thin film in contact with the underlying substrate, the *local vacuum level* defined as the electrostatic potential energy for electrons near the molecular film, will be of more relevance for the purpose of interfacial energy level alignment. In thin films composed of flat-lying molecules, the π -electron cloud now spans across the entire surface of the film, leading to an extended region of greater electrostatic potential energy for electrons above the film as seen in Figure 3-2b. Similarly, a film composed of standing-up molecules with their π -electron clouds pointed at each other and their hydrogen terminated ligands facing towards vacuum will see a lower electrostatic potential energy for electrons above the film as seen in Figure 3-2c. In this context, the effective IP and EA can be defined with respect to the local vacuum level (Figure 3-2d), which leads to an orientation-dependent HOMO and LUMO.[27-31,172,179-182]

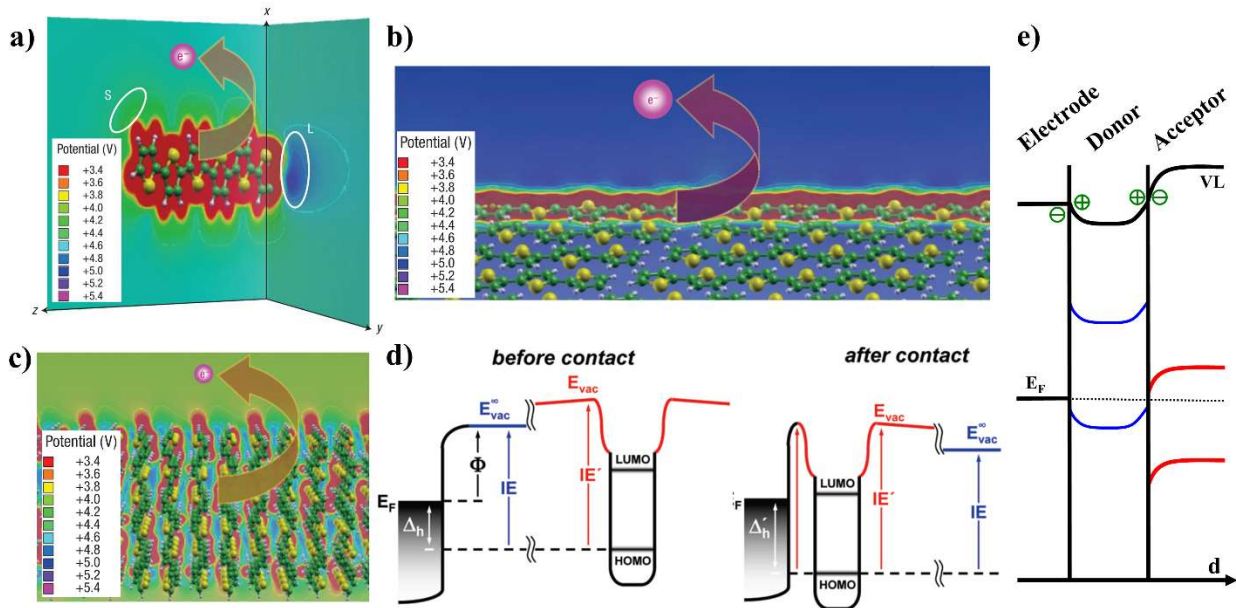


Figure 3-2: Orientation Dependent Electronic Structure

(a) Electrostatic potential around a single sexithiophene (6T) molecule where the higher potential is located over the π -conjugated molecular backbone (blue, in the x-y plane that is perpendicular to the molecule) and the lower potential is located around the hydrogen ligands (green, in the x-z molecular plane). Films assembled to expose the (b) π -electron system as in the case of a flat-lying 6T film or (c) hydrogen end groups as in the case of a standing 6T film see a higher or lower electrostatic potential for electrons above the molecular film, respectively. The origin of the energy scale in each plot is the respective HOMO energy. Reprinted from [29] (d) Energy level alignment diagram between a layer of flat-lying conjugated organic molecules and a metal surface. E_F and the Φ define the Fermi level and the work function of the metal substrate with respect to the global vacuum level, while IE and IE' define the ionization potential energy of the molecules with respect to the global and local vacuum levels denoted by E_{vac}^{∞} and E_{vac} , respectively. The local vacuum level is elevated due to the exposed π electron system of the flat-lying molecules and its associated molecular quadrupole field, and upon contact the HOMO and LUMO positions shift down in energy with respect to E_F , aligning the vacuum levels. Δ_h and Δ_h' defines the energy difference between E_F and the molecular HOMO before and after contact, with the latter corresponding to the hole injection barrier. It should be noted that infinitely far away, E_{vac}^{∞} is unperturbed by the interfacial energy level alignment. Reprinted from [31] (e) Energy level alignment diagram of a vertical organic-organic (CuPc-F₁₆CuPc of the edge-to-edge mutual molecular orientation) heterojunction in contact with a weakly-interacting electrode such as PEDOT:PSS (poly(3,4-ethylenedioxythiophene)-poly(styrenesulfonate)). Charge accumulation in donor and acceptor layers near the interfaces is indicated by the plus and minus symbols on the top side of the diagram, respectively. Adapted with permission from [183]

α -Sexithiophene (6T) molecule and its derivatives have been demonstrated to adopt different molecular orientations depending on the strength of their interaction with the substrate. [184] Deposition of 6T on either the flat-lying or the standing-up α,ω -dihexyl-sexithiophene (DH6T) films results in 6T molecules adopting the same matching orientation to the underlying DH6T molecules, which allows for UPS studies of the orientation dependence of IP of both molecular species in the thin film form.[29] Upon the initial deposition of DH6T monolayer that adopt a flat-lying molecular configuration on the Ag(111) surface, a lowering of the vacuum level (~ 0.7 eV) was observed which can be attributed to the ‘push-back’ effect, which will be discussed in more detail later, leading to the reduction of the metal work function. DH6T molecules in the subsequent layers are relaxed into a standing orientation, accompanied by a decrease of the IP by ~ 0.6 eV as a result of the molecular quadrupole field. Similarly, 6T film of the standing molecular orientation displays a lower IP (by ~ 0.4 eV) in comparison to that of the lying 6T film. While this study exemplified the orientation dependence of IP of a molecular thin film, the question of the quadrupole’s influence on the EA of the film had yet to be verified.

More recently, using both inverse photoemission spectroscopy (IPES) and UPS techniques the orientation dependence of IP and EA of DIP (diindenoperylene) molecular thin films assembled on HOPG and SiO₂ was investigated.[30] DIP molecules on SiO₂ adopt a standing-up configuration with C-H bonds exposed to the vacuum, while DIP molecules on HOPG adopt a flat-lying configuration with the exposed π electron system. Consequently, a ~ 0.4 eV difference in both IP and EA is observed between the two molecular thin films of the varying orientation with respect to the substrate surface. While it is expected that standing molecules with hydrogen-terminated ends have lower IP and EA values compared to their flat-lying counterparts, fluorination of molecules, a very common methodology to alter the electronic character of a

molecule from donor-like to acceptor-like, leads to an opposite trend due to the opposite polarity of the C-F bond.[179,180] For example, F₁₆CuPc and CuPc show opposite orientation-dependent energy shifts with an IP of 6.5 eV and 4.75 eV for their standing-up configuration, and 5.65 eV and 5.15 eV for their lying-down configuration, respectively.[28] Necessarily, such an orientation shift will have a significant impact when considering the problems of contact resistance and charge injection barriers. As illustrated in Figure 3-2d, the energy level alignment at the interface directly determines the hole injection barrier, which can be modulated by the orientation of molecules with respect to the surface of the metal electrode within the molecular assembly.

Furthermore, in donor-acceptor heterojunctions, this opposite movement of IP and EA can significantly alter the relative positions of the donor HOMO and the acceptor LUMO, which could either favor intermolecular charge transfer or inhibit it.[27,185,186] In the case of F₁₆CuPc and CuPc, a stronger ground-state intermolecular charge transfer is expected at the standing (edge-to-edge) organic-organic heterointerface relative to the interface comprised of flat-lying (face-to-face) donor-acceptor Pc molecules. [186] The donor-acceptor heterojunctions with the edge-to-edge mutual molecular orientation could be beneficial to the operation of ambipolar OFETs, however, the charge accumulation and the associated energy level bending in both the donor and acceptor films near the interface, as seen in Figure 3-2e, arising from the ground-state intermolecular charge transfer inevitably reduce the upper limit of the open circuit voltage and pose an energy barrier for the transport of photo-generated carriers from the heterointerface to the corresponding electrodes, thus detrimental to the OPV performance.[27,183] Molecular orientations within the film can be modulated, to certain extent, by substrate templating layers for targeted device applications. For instance, a recent study comparing the edge-on (standing) and face-on (lying) orientations of ZnPc in a ZnPc/C60 OPV bilayer heterojunction showed a nearly

doubled power conversion efficiency in the face-on ZnPc solar cells, where this face-on molecular orientation was induced by adopting CuI, a hole-conducting templating layer on top of the ITO (indium tin oxide) electrode.[187,188]

As the examples illustrate, this orientation dependent IP and EA will be especially important when considering the energy level alignment and charge transfer processes at both the molecule-substrate and donor-acceptor hetero-interfaces which can drastically influence the performance of organic electronic devices.

3.2 General consideration of the interfacial effects arising from the molecule-substrate interaction on metals or strongly interacting substrates

It is clear, at this point, that the positions of HOMO and LUMO, which are often complicated by the interdependency of the molecular growth, e.g., defect control and molecular orientation, and the local electrostatic environment, are important considerations when designing organic molecular devices. In this section, we will briefly discuss the different models, typically categorized by the nature of the molecule-substrate interaction, for describing/predicting the interfacial energy level alignment. We will then focus the discussion on recent developments of the integer charge transfer (ICT) model in weakly interacting systems.

The first step when considering heterointerfaces between metal electrodes and organic semiconducting films is the ‘push-back’ or ‘pillow’ effect. Most clean metal surfaces have part of the electron wavefunction tail off into vacuum. This charge density is pushed back into the metal upon adsorption of organic molecules, which leads to the reduction of the metal work function.[40,43,179] It is necessary to note that the different surface orientations of the substrate have different work functions, correlating to the openness of the surface. When considering the heterointerface of clean metal and organic molecular overlayers, the orientation and openness of

the surface plays a role in determining molecular packing, molecular adsorption height, and molecule-substrate interaction, thus impacting the electrostatic screening of U by both the substrate and neighboring molecules, the reduction of the substrate work function by molecular adsorption, as well as the interfacial charge transfer and orbital hybridization.[189-192] All these factors contribute to the energy level alignment at the heterointerface, as revealed in a recent study of PTCDA on Ag(111), Ag(100), and Ag(110).[189,193]

The interaction between PTCDA and the different crystal planes of Ag also demonstrates the strong possibility that the molecule-substrate interaction can go beyond van der Waals forces at these organic/metal interfaces. If chemical bonds are formed between the adsorbed molecules and the surface of a clean metal, it can sometimes lead to a geometric distortion of the organic molecule known as Jahn-Teller distortion and oftentimes, the formation of a density of interface states, D_{is} , which, if significant, will cause the pinning of Fermi level. [43,94,112,194-196] In some cases, a physisorbed system can be transitioned into a chemisorbed system through temperature treatment, such as cysteine on Au(111) where the covalent sulfur-Au bond is thermally activated, as seen in Figure 3-3a.[55,197,198] In the absence of specific chemical pathways, weak hybridization may still occur, for instance, between molecular orbitals and the continuum states of the metal substrate.[43,199] Hybridization with this broad density of states feature will lead to the broadening of molecular orbitals as seen in Figure 3-3b.[40,43,96,200,201] The energy level alignment of these weakly hybridizing systems is typically described using the induced density of interface states (IDIS) model.[40,43] It is worth emphasizing that the hybridization process, being strong or weak, can be accompanied by a charge imbalance between the molecules and the substrate, typically characterized as partial or fractional charge transfer.[94,202-204] Interface dipoles arising from this charge transfer will drive the system to depart from the vacuum level

alignment or Schottky-Mott limit, and charge neutrality level (CNL) of the interface states is often invoked when analyzing the charge equilibrium at such interfaces. [40,43] While interfacial hybridization can be useful for engineering the electronic characteristics of the interface states, establishing long-range ordered growth of organic molecular thin films in both the lateral and vertical directions, as we have discussed previously, usually involves physisorbed systems.

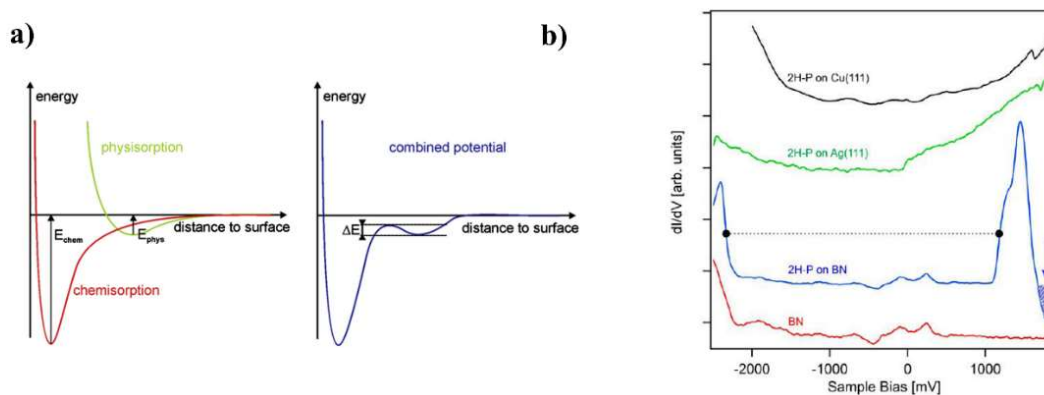


Figure 3-3: Comparison between physisorbed and chemisorbed organic molecular systems

(a) Physisorption and chemisorption are sometimes separated by a small energy barrier (ΔE), resulting in a thermally-activated transition from a physisorbed molecular system to a chemisorbed one. Reprinted from [55] (b) STS spectra of free-base porphine (2H-P) on Cu(111), Ag(111), and h-BN/Cu(111), along with the spectrum on bare h-BN/Cu(111) as the reference. Weak hybridization between metal density of states and molecular orbitals results in significantly broadened spectral features. In contrast, the spectrum of 2H-P on h-BN, an insulating monolayer that decouple molecules from the metal substrate, shows sharp and well-defined signatures for the molecular orbitals. Reprinted from [205]

3.3 Impacts of molecule-substrate interaction on molecular electronic structures and interfacial energy level alignment in the integer charge transfer regime

3.3.1 Introduction of the integer charge transfer (ICT) model

As mentioned earlier, numerous methodologies have been developed to tune the charge injection barriers whilst simultaneously providing a weakly interacting template.[154-157,205] Owing to the lack of chemical interaction, pristine molecular orbitals are typically preserved in

weakly interacting physisorbed systems such as a molecular overlayer on passivated or contaminated metal surfaces (intentional or otherwise).[43] The details of the interfacial energy level alignment and charge transfer, however, can be fairly complex. On the one hand, charge transfer should be energetically favored if the frontier molecular orbitals, i.e., LUMO/HOMO, sits below/above the substrate Fermi level, resulting in the formation of an interface dipole. As a consequence of the dipole formation, the energy offset between LUMO/HOMO and the substrate Fermi level and thereby the driving force for the charge transfer decreases, which eventually should lead to Fermi-level pinning at frontier orbitals. On the other hand, experimental observation has shown that charge transfer can still occur when the substrate Fermi level sits within the molecular bandgap.[40,175,202,206] To explain this behavior, the ICT model was developed. This model predicts the existence of integer charge transfer states, ICT⁺ and ICT⁻, that lie up to several hundred meV within the bandgap from their derived molecular orbitals.[40,44,186] It should be noted that these ICT states will necessarily vary with the orientation of the molecule within the molecular film.[186] Experimental observations of the energy-level alignment between molecular species and substrates of different work functions demonstrate that the previously mentioned criteria for charge transfer should be described with respect to the ICT⁻ and ICT⁺ states rather than to the LUMO and HOMO, and charge transfer is not observed if the substrate Fermi level lies between the ICT⁻ and ICT⁺ states.[40] This overall trend can be illustrated in a “Mark of Zorro” type shape as seen in Figure 3-4a. It should be noted again that the ICT model was developed to describe physisorbed systems, such as molecule-substrate pairs with minimal chemical interaction or systems with a decoupling layer between molecular adsorbates and substrate. As a result, charge transfer, if it occurs, is via the tunneling mechanism, and the transferred charges are in integer

quantities rather than the fractional charge transfer observed in the strongly interacting systems.[37,94,96,202,204]

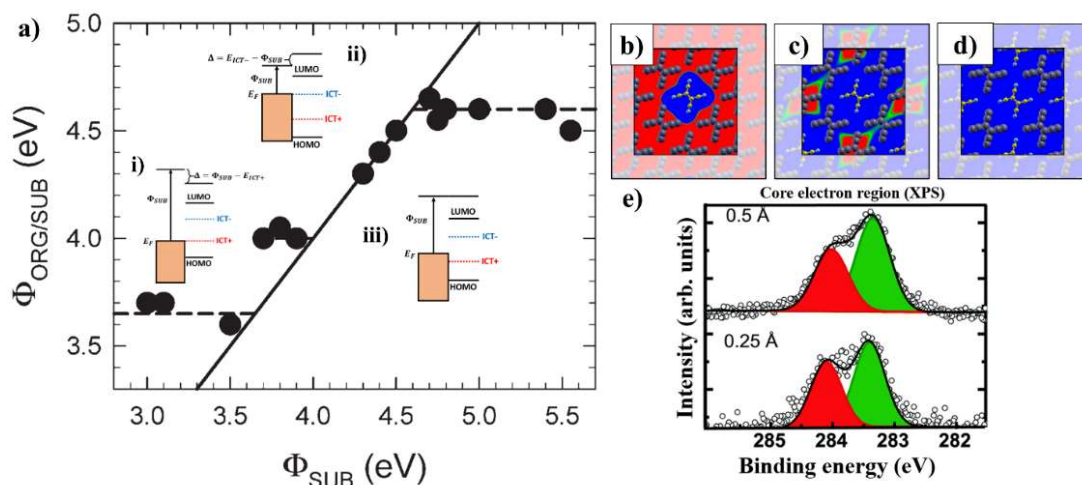


Figure 3-4: Integer Charge Transfer Model

(a) Dependence of the work function of organic/substrate heterojunction, $\Phi_{ORG/SUB}$, on the work function of supporting substrate, Φ_{SUB} , with insets depicting the energy level alignment regimes according to the ICT model. (i) $\Phi_{SUB} > E_{ICT+}$ where electrons are transferred from molecules to the substrate, (ii) $\Phi_{SUB} < E_{ICT-}$ where electrons are transferred from substrate to molecules. Due to Fermi-level pinning to E_{ICT+} and E_{ICT-} , respectively, $\Phi_{ORG/SUB}$ is independent of the substrate work function in (i) and (ii). (iii) $E_{ICT-} < \Phi_{SUB} < E_{ICT+}$ where no charge transfer occurs between molecules and substrate, leading to vacuum level alignment at the interface. $\Phi_{ORG/SUB}$ thus linearly depends on Φ_{SUB} with slope of 1. A low-band gap alternating polyfluorene was spin-coated as the organic layer, which allows all the three energy level alignment regimes to be assessed. Substrates with passivated surfaces were chosen and the role of the substrate screening is likely minimal in this study. Adapted from [40]. (b-d) Adsorption induced alteration in electron potential energy as the number of charged molecules (yellow) within a fixed area (the inner square outlined in black) increases from (b) one, (c) two, to (d) three. Gray molecules indicate hypothetical adsorption sites at full coverage. Charging of a single molecule with an electron increases the electron potential energy of the adjacent area. As a result, additional molecules adsorbed in blue regions (CER) remain charge neutral as the relevant molecular orbital levels are elevated above the E_F of the substrate. Here, the molecule is tetracyanoethene (TCNE) and the substrate is NaCl/Cu(100). Reprinted from [202] (e) XPS spectra showing C1S core-levels of C_{60} on $MoO_3/Au(111)$ at different nominal coverage in the sub-monolayer regime. The experimental data (black circles) can be fitted by the superposition of two peaks associated with the charged (red) and neutral (green) species. The fraction of charged molecules decreases with increasing coverage due to the existence of CER. Reprinted from [207]

The origin of the ICT states has been a topic of debate over the past decade or so. Initially, the ICT model was derived in polymer systems. It was claimed that the lattice-charge coupling and the associated geometric relaxation of charged molecules is the origin of the deviation between the ICT states and the HOMO/LUMO measured by electron-structure-probing techniques such as UPS.[43] However, when this model was extended to small conjugated molecules it was found that the related relaxation/reorganization energy, typically $\sim 0.1-0.2$ eV, appears to be too small to account for the energy offsets between the ICT states and the associated frontier molecular orbitals.[43,44,159].

3.3.2 Recent development of the ICT model and its implications on molecular electronic structures and molecular thin film growth

One of the more recent interpretations of the ICT model is based on the concept of the coexistence of charged and neutral molecular species within the thin film.[202,207-210] The reorganization energy, the on-site Coulomb interaction in charged molecules (anion/cation), and the inter-site Coulomb interaction between molecular charges distributed in the anion/cation and their adjacent neutral species, will likely need to be considered together in describing the energy diagram in weakly-interacting systems.[202,207] To understand this coexistence of neutral and charged molecules, one can examine the scenario of charging a molecular island as seen in Figure 3-4b-d. Within this island, the charging of a single molecule with an electron, i.e., anion formation, will result in the increase of electrostatic potential energy for electrons around the molecule which will discourage the charging of neighboring molecules in the local area, described as the charge exclusivity region (CER). [202] Naturally, the electrostatic potential energy for an electron decays with distance away from the charged molecule, allowing for the charging of additional molecules sufficiently far away.[207] This process will continue until an equilibrium is reached in the

molecular island, i.e., the density of formed interface dipoles and the associated vacuum level shift compensate the initial energy level offset between the ICT states and the substrate Fermi level. Experimentally, this coexistence of charged and neutral molecules has been verified by core-level spectroscopy such as x-ray photoelectron spectroscopy (XPS) where the binding energies of specific core levels are sensitive to the charge state of the adsorbed species as seen in Figure 3-4e.[207,209] Note that ICT implies a reversible and dynamic charging process. The charge state of each individual molecule is strongly dependent on those of the nearby molecules at any given moment in time. Overall, this ICT process, through the dynamic coexistence of charged and neutral molecules, renders the averaged charge transfer per molecule within the island fractional, though it is important to note the distinction between the ICT charge transfer and the fractional/partial charge transfer in strongly interacting systems.

The integer charging of organic molecules has a profound effect on the electronic structure measurements. The act of charging a molecule through ICT renders the involved molecular orbital singly-filled. Probing of this orbital either through the extraction or injection of an electron will lead to the splitting of the molecular level into a singly occupied molecular orbital (SOMO) and a singly unoccupied molecular orbital (SUMO), separated energetically by the intra-orbital Coulomb repulsion.[96,163,164,175,211-213] Such orbital splitting has been observed in multiple systems by photoemission techniques.[175,207,210,214] For example, in the case of C_{60} adsorbed on $MoO_3/Au(111)$, the ultrathin insulator layer was introduced to decouple the molecules from the underlying metal substrate, inhibiting interfacial hybridization and confining the system to the weakly-interacting physisorption scenario.[207] Since the work function of $MoO_3/Au(111)$ is larger than the IP of C_{60} , electrons are expected to transfer from the molecules to $Au(111)$ via tunneling through the MoO_3 layer until an equilibrium is reached. UPS data measured in this

system shows the coexistence of neutral and cationic C_{60} species (Figure 3-5a), in agreement with the ICT model. Intriguingly, a HOMO-derived unoccupied spectral feature of cations was revealed by IPES, which, combined with theory, provides a strong evidence for the SOMO-SUMO splitting of charged molecules. This orbital splitting and the electrostatic effects of cations on neighboring molecules are illustrated in Figure 3-5b.[207]

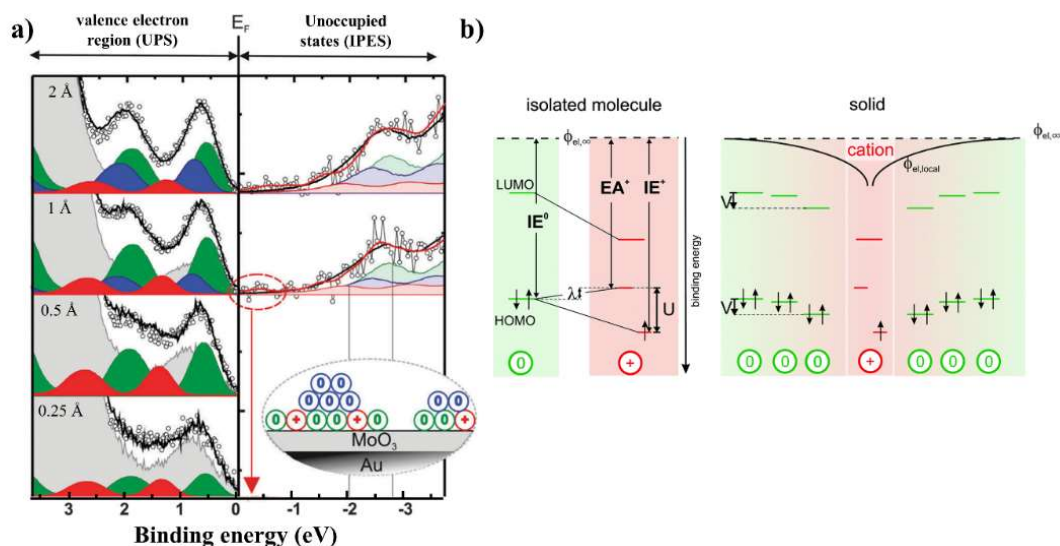


Figure 3-5: UPS and IPES spectra of C_{60} on $MoO_3/Au(111)$, an integer charge transfer system

(a) Three different sets of spectral features associated with the first layer charged (red), first layer neutral (green), and subsequent layer neutral (blue) molecules, as illustrated in the inset diagram. The grey curve represents the background contribution from the bare $MoO_3/Au(111)$ substrate. Owing to the existence of C_{60} cations, a unique HOMO-derived unoccupied spectral feature (circled in red) is detected near Fermi level in IPES spectra, providing a strong evidence for the SOMO-SUMO splitting of charged molecules. (b) Energy level diagram of the ICT charging of molecular semiconductors. The existence of charged molecules, in the case of cation, in proximity to neutral molecules results in a distance-dependent downshift of the vacuum level as well as the HOMO and LUMO positions of the neutral molecules due to the inter-molecular Coulomb interaction, V . The splitting of the two HOMO-derived orbitals of the cations, i.e., SOMO and SUMO, are represented by IE^+ and EA^+ , respectively, with an energetic separation between the two determined by the intra-orbital Coulomb repulsion, U . The reorganization energy, λ , determines the separation between IE^0 , i.e., the energy cost to remove an electron from neutral molecules, and EA^+ , i.e., the energy gain of returning this electron to the fully relaxed cation. Reprinted from [207]

Fitting of the experimental data in Figure 3-5a also reveals the decay in intensity of the cationic spectral features with increasing molecular layer thickness, suggesting that the relative fraction of charged molecules to neutral molecules decreases with increasing coverage. The propagation of ICT effects into thicker films is a question of great relevance to device applications. In similar systems, thorough thickness dependent studies have been performed and it was found that subsequent deposition of C₆₀ at a fixed thickness of the insulating decoupling layer witnessed a nearly exponential decline (Debye length of $\sim 2\text{nm} \approx 2.5$ C₆₀ layers) in the fraction of charged molecules, in agreement with the decreased tunneling probability from the metal substrate. Meanwhile, the fraction of charged molecules necessarily decreases with increasing thickness of the insulating decoupling layer.[210] The decay rate of the fraction of charged molecules with molecular layer thickness is an important factor in determining the spatial confinement of the space charge region. The associated band bending behavior at the interface is important towards device application. For instance, in contrast to the localized interface dipoles arising from the formation of gap states at electrodes without the insulating decoupling layer, the built-in electric field in the extended band bending region of the molecular film, as illustrated in Figure 3-8, can help facilitate the collection of photo-generated charge carriers by the respective electrodes in OPV devices.[210]

ICT implies a reversible and dynamic charging of molecules where the charge state of each individual molecule is strongly dependent on the arrangement and charge states of neighboring molecules at any given moment in time. While ensemble averaging techniques such as photoemission spectroscopy have been able to detect the coexistence of neutral and charged molecules in organized molecular assemblies, STM/STS has primarily verified the electronic effects of the charged states of individual molecules.[93,164,175,207-209] STM/STS has shown compelling evidence on the SOMO-SUMO splitting, for instance, of individual pentacene

molecules adsorbed on top of NaCl/Cu(111) with the charge state of molecules controlled through side attachment of Au atoms (Figure 3-6a).[211] These integer charged pentacene molecules exhibit pronounced peak features on both sides of the substrate Fermi level in STS. Typically, these features would be associated with the molecular LUMO and HOMO, however, STM imaging reveals the same nodal-structured density-of-states distribution for both of the peaks, indicating that they originate from the same intrinsic molecular orbital. Despite the evidence of SOMO-SUMO splitting of individual charged molecules, STS's lack of temporal resolution and the strong electric field between the tip and sample makes the measurement of the reversible and dynamic charging behavior in molecular assemblies extremely difficult.[208] To the best of our knowledge, scanning probe experiments performed on organic molecule assemblies on weakly interacting substrates have either revealed the presence of neutral molecular systems or fully charged assemblies, in which all the molecules appear similar regardless of their initial charge state.[42,93,164,175,205,208,215] As an example, spatially resolved mapping of apparent barrier height, determined by the local work function of the sample, is performed using dI/dS (S : tip-sample distance) STM/STS technique on the TBP (tetra[1,3-di(tert-butyl)phenyl]pyrene) assemblies on Au(111) and Cu(111), respectively.[208] Due to the geometric shape of the molecule, its adsorption to the metal surfaces does not alter the intrinsic molecular orbitals, representing physisorbed systems. Furthermore, dictated by the relative positions of the molecular states to the substrate Fermi level, there is no charge transfer at the TBP-Cu(111) interface, while TBP-Au(111) can be characterized as an ICT system. It can be seen that in this ICT system, all molecules within a given island appear identical in the local work function map which shows the variation in $\Delta\Phi$ with respect to the bare metal substrate (Figure 3-6b). While the coexistence of charge states through STM/STS was not demonstrated, the influence of ICT on the modulation of

the local work function should still be observed. When compared to the case of TBP on Cu(111), a system with no charge transfer, a $\Delta\Phi$ drop of $\sim 0.2\text{eV}$ is observed on TBP/Au(111) due to the electron transfer from molecules to the substrate.

The ICT charging of TBP also demonstrates a profound influence on the growth of the molecular overlayer. It is known that molecules such as F₄TCNQ (2,3,5,6-Tetrafluoro-7,7,8,8-tetracyanoquinodimethane) do not tend to assemble into organized structures due to the strong electrostatic repulsion that originates from the terminating F groups.[216] A similar observation is expected for charged molecules, e.g., a thin film that is charged completely positive would experience strong intermolecular electrostatic repulsion. Indeed, STM measurements and Monte Carlo simulations have shown that the introduction of a mixture of charged and neutral molecules, as in the ICT model, allows for the formation of compact assemblies, while fully charging all molecules on the surface will lead to scattered molecular clusters as seen in Figure 3-6c.[208] This is because neutral molecules in the CER act essentially as dielectric spacers that can serve to mitigate the Coulomb repulsion between charged molecules, and large scale self-assembly will be established if a balance is reached between the Coulomb repulsion, the energy gain from the interfacial charge transfer and the attractive van der Waals intermolecular and molecule-substrate interactions.

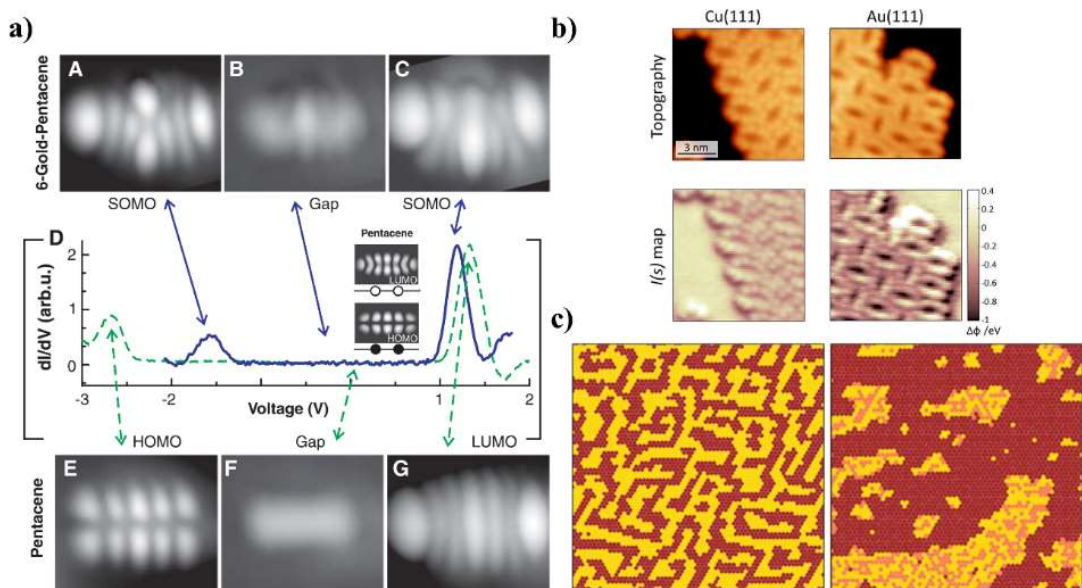


Figure 3-6: Effects of ICT detected by STM/STS

(a) Bias-dependent STM images and dI/dV spectra for a 6-gold-pentacene complex (a Au atom attached to the central ring of pentacene) and an isolated pentacene molecule on NaCl/Cu(100). 6-gold-pentacene complex shows similar molecular features at occupied and unoccupied state imaging as seen in A and C, respectively, while isolated pentacene molecules show clearly different nodal structures in its occupied and unoccupied states as seen in E and G, respectively. The spatial distribution of the 6-gold-pentacene orbitals appear similar to that of the LUMO of isolated pentacene molecules, suggesting that the LUMO peak has been singly occupied and split into SOMO and SUMO (referred to as two SOMOs in this work). Reprinted from [211] (b) STM topologies and simultaneously obtained local work function maps of a TBP assembly on Cu(111) and Au(111) showing the spatial variation in $\Delta\Phi$ with respect to the bare metal substrate, respectively. A difference in work function, $\Delta\Phi$, can be observed between the TBP molecules and the supporting substrate, but molecules appear homogenous within the same assembly. (c) Monte Carlo simulation of TBP/Au(111) where all molecules are irreversibly ionized (left) and reversibly charged via ICT (right). Large compact structures are unable to form in the fully ionized case due to the strong Coulomb repulsion that exists between molecules, while the reversible charging of the molecules allows for the formation of compact assemblies. Yellow and pink dots represent charged and neutral molecules while the substrate is depicted as brown dots. Reprinted from [208]

3.3.3 Revisit the interfacial energy level alignment in the ICT regime and its impacts on the charge injection behaviors in organic electronic devices

With these recent developments of the ICT model, it is imperative to revisit the interfacial energy level alignment in the ICT regime. As discussed previously, Fermi level pinning can occur

in a variety of different scenarios. If E_F is pinned by traps or localized interface states originating from the formation of chemical bonds, metal-organic weak hybridization (IDIS model), or defect/disorder-induced tail states, a finite Schottky barrier will emerge which becomes difficult to reduce further. Alternatively, the ICT model introduces the possibility to pin the E_F at the charge transport levels of organic molecules, i.e., the ICT states, which should, in principle, result in a minimized Schottky barrier and the establishment of Ohmic contact. This is indeed observed in numerous organic polymer systems.[217-219] Small organic molecules, however, with polaron energies that are typically quite small, have been a question of intense debate with regards to the nature of the ICT states that the model predicts. The notion of charge transfer states derived from the fully relaxed HOMO/LUMO are often cited as the origin of the ICT pinning levels, while other groups have attributed the pinning to be a natural consequence of the Fermi-Dirac distribution and the DOS distribution of the organic molecular system.[40,155,158,159,186,220-222] Even the notion of Ohmic contact in ICT systems composed of small organic molecules is a point of open debate as some groups have reported Ohmic contact while others insist that an injection barrier exists.[159,220,223,224]

Recently, a Universal energy-level alignment with a minimum of ~ 0.3 eV charge injection barrier has been identified among about 40 interfacial systems composed of different metal oxide/organic molecule combinations.[155] As discussed previously, tuning the metal work function with an insertion layer is a common approach for adjusting the contact injection barrier with organic semiconducting films. Metal oxides are often used for this purpose due to the wide range of work function ($\sim 2 - 7$ eV) they offer. Oxides-terminated metal, if weakly interacting with organic molecules, is compatible with the ICT model. In the multiple organic donor/n-type oxide systems investigated by Greiner et al., though the transition between the regimes of vacuum level

alignment and Fermi level pinning does occur when the work function of the substrate (ϕ_{sub}) equals the ionization potential of organic molecules (IE_{org}), UPS results indicate the formation of a minimum hole injection barrier of ~ 0.3 eV, as displayed in Figure 3-7a. In this work as well as the follow-up theoretical study by Ley et al., molecular energy levels, e.g., HOMO, are treated as discrete charge-transfer states rather than with a DOS distribution, and the offset of the pinning position from HOMO was attributed to the charge equilibrium of the system expressed by the Fermi-Dirac distribution function.[220] Specifically, only a small fraction of molecules needs to be charged at the interface to satisfy the charge equilibrium of the entire system, which brings HOMO to the steep tail of the Fermi-Dirac distribution function. Since E_F cannot cross the molecular charge-transfer levels, a finite charge injection barrier is created. These studies demonstrate that the energy level alignment does not rely on the formation of the ever-elusive interfacial ICT states.[158,159,220,225]

Realistically, many factors could give rise to the broadening of molecular orbitals at the interface. Some recent studies have attributed the pinning mechanism in weakly interacting systems to the energetic disorder at the interface represented by the width of the DOS distribution of the involving molecular orbitals.[158,224] Charges populated in the tail states of the broadened interface DOS prevent the Fermi level from approaching the HOMO/LUMO onsets, giving rise to a charge injection barrier, ΔE_H . Figure 11 illustrates the broadening of interface DOS by morphological disorder, etc., while the decay of the attractive image-charge potential and the fraction of charged molecules with film thickness result in the band bending-like feature in the film which further magnifies ΔE_H . In a recent study, ΔE_H was shown to be tunable by the introduction of an organic interlayer between the electrode and the active organic film. This new interlayer serves to further decouple the film from the electrode electrostatically, minimizing the

energetic disorder and image charge effects within the film. ΔE_H was thus reduced by about 50%, which led to significantly improved IE_{org} charge conduction with devices exhibiting the Ohmic contact behavior (Figure 3-7b).[224]

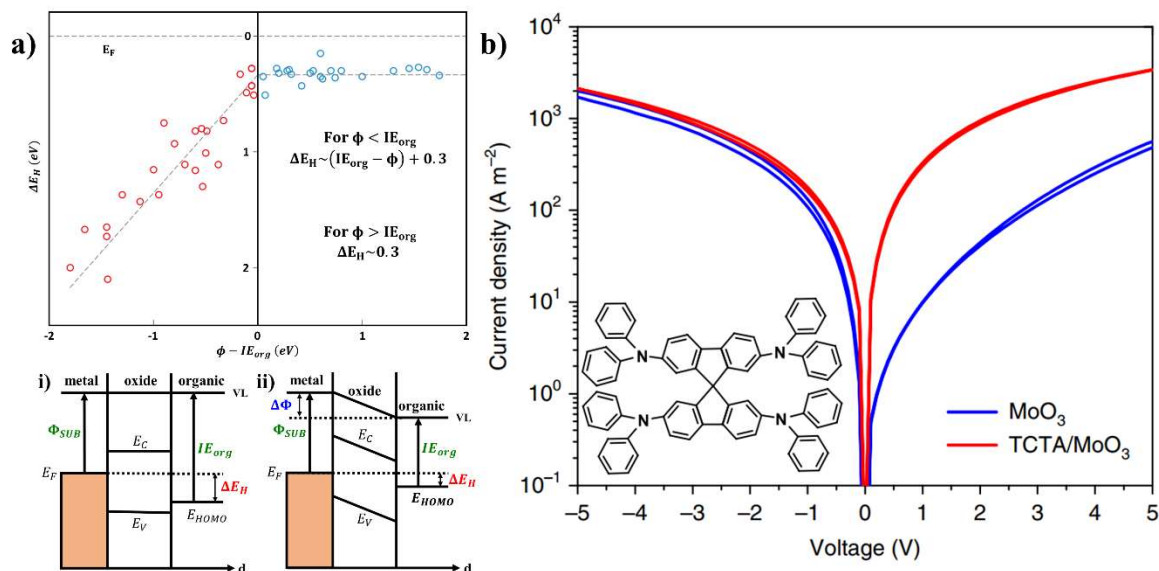


Figure 3-7: Contact properties of weakly interacting organic systems

(a) Plot of the HOMO offset, ΔE_H , corresponding to the hole injection barrier, versus the difference between the substrate work function (ϕ_{sub}) and the organic ionization potential (IE_{org}), summarized from the various metal oxide/organic molecule systems. The dashed lines in the linear regime ($\phi < IE_{org}$) and the pinning regime ($\phi > IE_{org}$) were determined by the calculated average of ΔE_H over the different molecule-substrate combinations and a least-squares regression fit, respectively, with the restriction that the boundary of the two regimes ($\phi = IE_{org}$) has ΔE_H equals 0.3 eV. Bottom panels denote the band diagrams in the linear (i) Schottky-Mott regime and the (ii) pinning regime with the potential drop across the oxide dielectric ($\Delta\phi$) as a result of the integer charge transfer between metal electrode and organic adlayer. Adapted with permission from [155,220] (b) Current density-voltage characteristics of a device comprised of PEDOT:PSS/Spiro-TAD (2,2',7,7'-tetrakis(N,N-diphenylamino)-9,9-spirobifluorene)/MoO₃ with and without a 5nm TCTA (tris(4-carbazoyl-9-ylphenyl)amine) interlayer between the transport layer (Spiro-TAD) and MoO₃. Inset shows the molecular structure of Spiro-TAD. Introduction of the TCTA interlayer yields an improvement in the current density by over an order of magnitude at positive bias due to the reduction in the hole injection barrier from MoO₃ to Spiro-TAD. Reprinted from [224].

Based on the recent investigations, it becomes increasingly clear that the ICT states, at least for the case of small organic molecules, are more representative of an empirical energy level alignment reference rather than a unique interfacial state with distinct chemical or physical origin. The energy level alignment at weakly interacting interfaces is strongly dependent on the DOS distribution of the HOMO/LUMO orbitals, which, coupled with the Fermi-Dirac statistics and the electrostatic considerations, gives rise to an offset between the substrate Fermi level and the molecular transport states.[155,158,159,220,224] While the energetic disorder that causes the broadening of DOS has been commonly attributed to the structural disorder within the organic film, the coexistence of charge states as shown in Figure 3-5b should also contribute to the overall broadening of the frontier molecular orbitals.

Thus far, the discussion has been focused on the properties of organic molecular thin films that have been primarily characterized in highly controlled environments such as films grown under vacuum conditions. However, in order for organic molecular electronics to be operated and deployed en-masse, harsher operation conditions need to be considered with devices likely seeing some level of exposure to potentially-detrimental factors including light, moisture, oxygen, heat and other chemicals.[226] Important device parameters such as the charge injection barrier could be significantly altered as a result.[226-231]

Heat generated during device operation could result in an annealing effect on the molecular thin film which, as described earlier in this review, may lead to the formation/migration of morphological defects and the loss of ordering.[226] Ambient air exposure, mainly water and oxygen, is an additional factor that is difficult to avoid. A study on the effects of ambient air exposure on the injection barrier was conducted across a series of organic molecules on the MoO₃ substrate.[230] It was shown that molecules with a sufficiently high IP would undergo a significant

increase in the hole injection barrier as a result of the oxidative adsorption of water molecules at the organic/MoO₃ interface. Additionally, oxidation of organic molecules could lead to chemical alterations in the molecule.[226,231] For example, the oxidation of pentacene results in the formation of double bonded oxygen which can lead to a collapse of the π -conjugation and an overall drop in thin-film conductivity.[231] In order to alleviate these degradation effects on organic molecular electronics, numerous techniques are under development to protect the sensitive organic film from exposure to moisture, oxygen and chemicals via processes like thin-film encapsulation (TFE) and lamination.[232] Alternatively, studies are being conducted to understand the reaction pathways and degradation mechanisms that occur in organic electronics, which will help guide the tailoring and optimization of the chemical functionality of organic molecules, their morphology and their thin-film preparation processes to improve their resistance to environmental factors.[226]

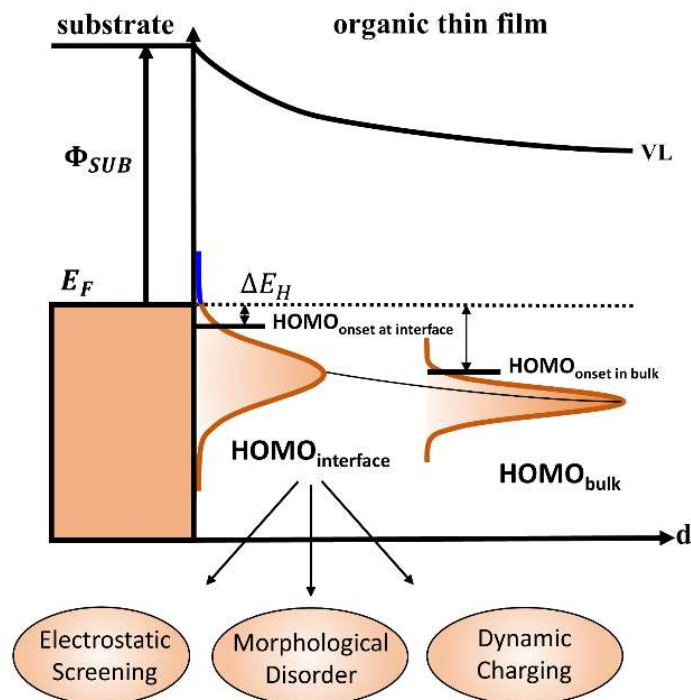


Figure 3-8: Evolution of energy level alignment at weakly interacting heterointerfaces

The DOS of the frontier molecular orbital (in this case the HOMO) is broadened at the interface as the result of morphological disorder and the dynamic coexistence of neutral and charged molecules arising from the interfacial integer charge transfer which renders the consideration of inter-molecular (V) and intra-orbital (U) Coulomb interactions on the distribution of molecular levels as illustrated in Figure 3-5 (b). Charges populated in the tail states (blue line) of the broadened interface DOS prevent the Fermi level from approaching the HOMO/LUMO onsets, giving rise to a charge injection barrier, ΔE_H . Due to the stabilizing force of the substrate image charge, the average energetic position of the HOMO is shifted upwards at the interface. As the film thickness increases, electrostatic screening from the substrate and the percentage of charged molecules per layer decrease, resulting in a band bending-like feature. Note that, depending on the growth mode, morphological disorder can either increase or decrease as the molecular assembly transitions into a bulk crystalline structure, while the energetic disorder is depicted as decreasing here in consideration of the readily reduced distribution of charged molecules.

4 Charge Transfer Complexes

4.1 Introduction to Charge Transfer Complexes

Thus far, most of the discussion of organic molecule growth and electronic structure has been focused on single-component organic molecular films. Mixed blends of donor and acceptor species that exhibit unique physical behavior that go beyond the uni-polar, semiconducting behavior of typical single-component organic molecular systems are known as charge transfer complexes (CTCs). These compounds, typically consisting of inorganic/organic donor and acceptor species, have been demonstrated to exhibit metal-like conduction, superconductivity, anti-ferromagnetism, ferromagnetism, ferroelectricity and more.[233-237] Many applications can be outlined with the introduction of such a rich class of systems. As discussed in earlier chapters, the use of metal substrates for molecular growth can be quite challenging due to the typically strong molecule-substrate interaction which inhibits long-range ordered growth, particularly in the out-of-plane direction. On the other hand, the growth on weakly interacting substrates can be difficult with regards to the in-plane ordering due to the prevalence of rotational domains. Utilizing an organic metal as the supporting substrate which weakly interacts with molecular adlayers, could therefore lead to better symmetry and lattice matching and/or better charge injection efficiency.[154,224] CTCs, with their rich array of physical properties could be used to develop devices such as organic-based superconductors, ferroelectric devices or devices where critical device components are built almost entirely from organic molecules.

The physical properties of a CTC are highly dependent on the intermolecular interaction, intermolecular charge transfer and the molecular packing. The intermolecular charge transfer can be characterized by the comparison between the difference in the donor IP (E_D), the acceptor EA (E_A), and the Madelung energy of the resulting crystal (E_M). It is important to note that the E_M

describes the electrostatic interaction of a charged lattice, weaker short-ranged interactions such as van der Waals interactions, $\pi - \pi$ bonding and the different variants of dipole-dipole interactions are not accounted for which separates E_M from general lattice energy. E_M can be described by the equation:[238,239]

$$E_M = \frac{1}{2} M \sum_i \frac{z_i e^2}{4\pi\epsilon_0 l_o} \quad (4-1)$$

where z_i refers to the charge at site i and M , describing the Madelung constant, can be described by the equation:

$$M = \sum_{ij} \frac{z_j}{l_{ij}/l_o} \quad (4-2)$$

where l_{ij} refers to $|\vec{l}_i - \vec{l}_j|$ and l_o refers to a chosen reference distance, such as a unit cell parameter. From these equations, E_M represents the degree in which a lattice of ions is stabilized by their collective electrostatic interaction and if E_M is unable to stabilize a possible ionic lattice, such a lattice will necessarily be disfavored. Three different regimes can therefore be defined: the neutral regime ($E_D - E_A < E_M$), the ionic regime ($E_D - E_A > E_M$) and the mixed valence regime ($E_D - E_A \approx E_M$). [235,240] CTCs in the neutral and ionic regime typically exhibit non-conductive properties as illustrated in Figure 4-1. For the case of neutral molecules, free charge carriers are minimal, limiting conductivity. In the ionic regime, charge transfer approaches 1e per molecule resulting in most donor molecules charged +1e while acceptor molecules are charged -1e. Charge conduction from donor/acceptor to donor/acceptor sites becomes quite difficult due to the need to overcome the large on-site Coulomb repulsion. The mixed valence regime, however, represents an interesting scenario. Due to charge transfer being in-between the neutral and ionic regimes, not all molecular sites are charged which results in a reduced intra-orbital Coulomb repulsion allowing

for metal-like conduction.[240] On the other hand, CTCs that do not exhibit metallic conductivity are capable of other interesting physical behavior such as ambipolar transport, magnetoresistance and so on.[233-237,240]

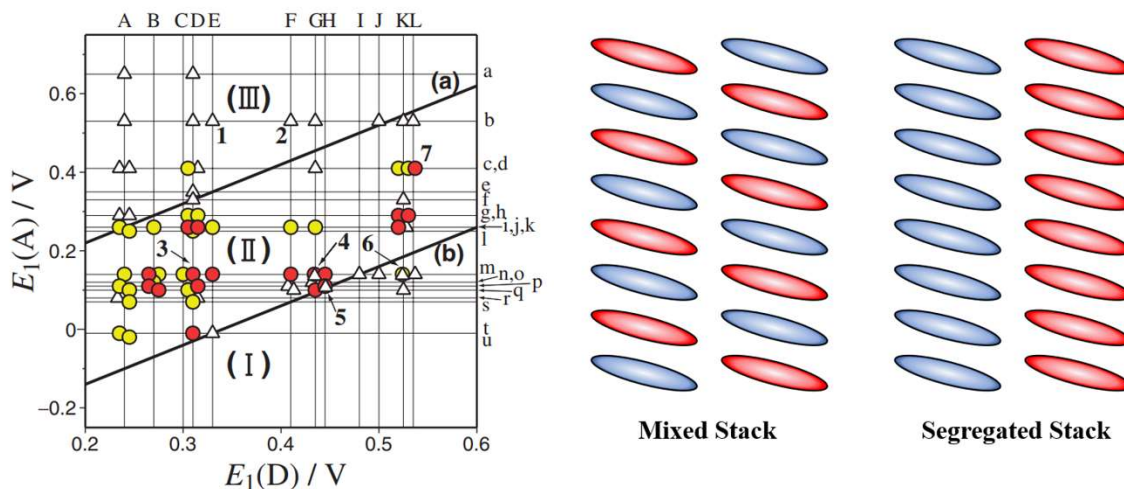


Figure 4-1: Charge transfer complex packing and energy diagram

(a) Ionicity diagram for TTF-TCNQ systems and their derivatives denoted by various markers. Triangles denote classes of materials that are insulators, yellow circles denote highly conductive CTCs and red circles denote organic metals. The three ionicity regimes are denoted by (I) neutral, (II) mixed valence defined by the range $-0.02 V \leq E_M \leq 0.34 V$ and (III) ionic. The compounds denoted by lower-case and upper-case letters can be found in [234,240] Reproduced with permission from [234]. (b) The two common stacking types for 1:1 organic CTC systems with blue and red molecules representing donor and acceptor molecules respectively.

However, the degree of intermolecular charge transfer alone is not enough to determine the CTCs physical properties. The molecular packing must also be considered.[234,235,240] This is illustrated by the example of phenazine-TCNQ. While the degree of intermolecular charge transfer should be sufficient to allow for metal-like conduction, this CTC adopts a mixed-stack packing which limits metallic conductivity along the stacks due to the minimum orbital overlap between adjacent donor and acceptor molecules.[240] Two typical packing types are considered as illustrated in Figure 4-1b. Mixed-stack packing has donor and acceptor molecules mixing within an individual stack. Necessarily, charge conduction along the stacking direction would be highly

impeded in a mixed-stack CTC crystal. In segregated stack packing, on the other hand, donor and acceptor molecules are segregated into individual stacks with only one molecular species, typically in the direction of strongest intermolecular interaction such as $\pi - \pi$ interaction, thereby facilitating charge conduction.[234,240] While mixed-stack CTCs are unlikely to display metallic conductivity, this class of CTCs are known to be capable of exhibiting other exotic physical properties such as ferroelectricity. [233-237,240]

4.2 Organic ferroelectricity

Ferroelectrics are described as materials with the ability to retain a reversible spontaneously generated electric polarization upon application of an external electric field. The critical electric field required to reverse this polarization is known as the coercive field. Ferroelectricity is typically characterized by mapping the electric displacement (D) of the material as a function of the applied field strength (E). This results in a hysteresis profile in the D-E loop, resulting from the ordering of dipole moments within the material similar to how ferromagnetic materials and their magnetic dipoles respond to an applied magnetic field as seen in Figure 4-2. Such a hysteresis loop allows for memory capabilities, and for the development of ferroelectric random-access memory and field effect transistors.[241-245]

The manner in which the electric dipoles in a ferroelectric material are varied and, for the case of CTCs, the type of ferroelectricity is defined by how the dipoles are created as depicted in Figure 4-2. A regular intermolecular separation exists within a typical mixed-stack donor-acceptor crystal and a negligible intrinsic dipole moment. This regular lattice spacing can be symmetry broken as the result of strong donor-acceptor interaction such as intermolecular charge transfer, resulting in the formation of dipolar donor-acceptor dimers. This kind of spontaneously formed

dipole moment, resulting from the displacement of the donor/acceptor molecules is known as ionic ferroelectricity.[241,243,244] It should be noted that for this kind of displacement to spontaneously form, a degree of structural instability needs to exist resulting from a delicate balance between the attractive electrostatic force between donor/acceptor molecules and the short-range repulsive force between ions. This instability further aids the realization of smaller coercive fields needed to switch the polarization of the device. While this type of ferroelectric behavior is typically observed in inorganic systems, it is significantly less effective in organic ferroelectric systems due to the low ionic charge, as noted earlier in Section 4.1, and dipole density compared to their inorganic counterparts. An alternative scenario is the formation of electronic ferroelectricity. In this case, a convolution between increased charge transfer and ionic displacement results in the formation of a significantly larger dipole moment, net polarization and a much stronger ferroelectric behavior. [241,243,244] This behavior was observed in the most systematically studied bulk organic ferroelectric crystal, TTF (tetrathiafulvalene)-CA (p-chloranil).[241-245]

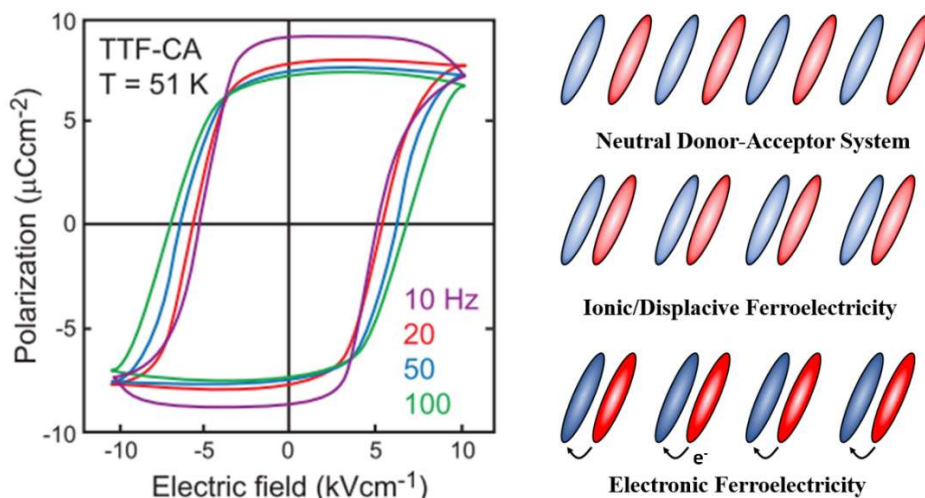


Figure 4-2: Organic ferroelectrics

(a) P-E hysteresis loop observed in the TTF-CA system at 51K measured with different frequencies. Reproduced with permission from [244] (b) Origin of organic ferroelectricity with blue and red molecules representing donor and acceptor molecules respectively. Ionic ferroelectricity originates from the simple dimerization of donor-acceptor molecules while electronic ferroelectricity involves the spontaneous dimerization and increased charge transfer.

4.3 Properties of a ferroelectric monolayer: An STM study

In order to determine the properties of an organic ferroelectric material, it is necessary to understand how ferroelectric behavior manifests in a monolayer film. Ferroelectric materials, as discussed, are characterized by structural distortion, the presence of an internal electric polarization field and the ability to switch the polarization direction through the application of an electric field. STM, therefore, makes an excellent characterization tool for ferroelectric thin films due to its high spatial resolution and electric field-based measurements. SnTe on a weakly-interacting graphene substrate represents an excellent system to illustrate how the properties of a ferroelectric monolayer are investigated by an STM.[246]

STM images of SnTe show the presence of two types domains as seen in Figure 4-3a. Lattice-resolved images, as seen in the inset of Figure 4-3a, show that the lattice is continuous

along the same domain, however the two domains are distorted from the expected square unit cell to a parallelogram of mirrored orientation as seen in Figure 4-3b. The observation of domain boundary formation and lattice distortion could have several different explanations, and alone, are insufficient evidence for the existence of ferroelectricity. To analyze the polarization effects of a ferroelectric material, the island edges were observed more closely. A difference in perceived height was observed on opposite sides of a single domain, as seen in Figure 4-3c, and is attributed to the presence of a band bending effect resulting from the existence of an in-plane polarization (evidenced from the position-dependent STS spectra in Figure 4-3d). The perceived height in an STM image is a convolution between the morphological structure of the film and its electronic structure as will be discussed in more detail in Section 5.2. Due to the weak interaction between graphene and SnTe, the film remains geometrically flat. The height variation is thereby originated from the band bending effect. Specifically, this effect results in a shift of the band edges of the material and consequently the integrated DOS between the scanning sample bias and the Fermi level. Owing to the opposite directions of the shifts caused by the charges built at the two edges of the domain, an oppositely altered apparent step height emerges as seen in Figure 4-3c.

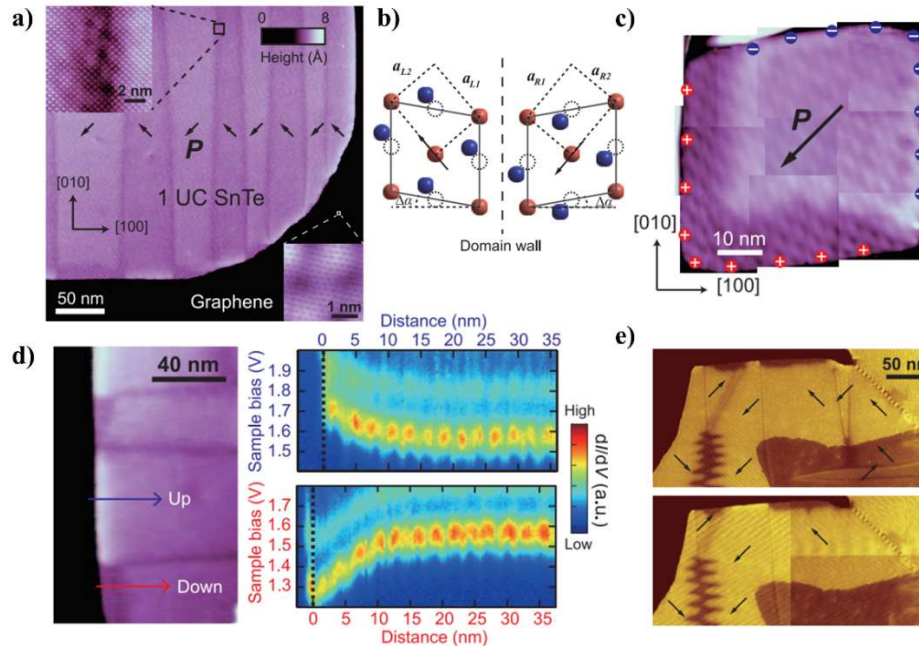


Figure 4-3: Ferroelectric properties of SnTe as determined by STM/STS

(a) Domain boundaries observed in SnTe (b) Schematic diagram of the unit cells of the two different domains. Polarization direction of the domain is indicated by the arrow. (c) Isolated SnTe island with opposite height variations occurring on opposite sides of the island. (d) Position-dependent STS taken along the height variation direction indicated by the blue and red arrows with STS spectra (right) indicating the existence of band bending. (e) STM images of an SnTe island taken before (top) and after (bottom) a 5 V electric pulse is applied. Arrows denote the polarization direction of the domains with some domains merging as a result of the electric pulse. Reproduced with permission from [246].

The final requirement that we have discussed for a ferroelectric material, is the ability to manipulate the polarization direction by means of an electric field. By using an electric field pulse from the STM tip, Chang et al. was able to alter the domain direction, resulting in the merging of several domains as seen in Figure 4-3e. In combination, these different observations make for a compelling case for ferroelectric behavior in a thin film. It is then the hope that upon formation of a thin-film phase of an organic ferroelectric material, it would be possible to apply this knowledge to identify and characterize the behavior of the organic CTC.

5 Experimental and Computational Methods

In order to facilitate the growth and study of organic molecular thin films, it is necessary to understand the tools and techniques that were used. This chapter will discuss important experimental apparatuses as well as experimental and computational techniques needed to acquire, analyze and interpret data utilized throughout this dissertation. Section 5.1 will discuss ultra-high vacuum technology, the main environment for which the organic molecular thin films are grown and studied in. Section 5.2 will discuss the main principles of STM/STS. Section 5.3 will discuss the computational methods used in this dissertation: data analysis of the STS spectra and epitaxial registration of a molecular overlayer with respect to the underlying substrate lattice and the finite element simulations conducted in COMSOL while section 5.4 will discuss the various sample preparation techniques.

5.1 Ultra-high vacuum system

Growth and characterization of organic molecular thin films were carried out in an ultra-high vacuum (UHV) chamber which is commercially available through Scienta Omicron GmbH as seen in Figure 5-1. The base operating pressures within the UHV system are maintained below 1×10^{-10} mbar through a combination of titanium sublimation pumps (TSP) and ion pumps which removes the influence of ambient conditions on the preparation and measurement of samples.[247,248] The UHV chamber rests upon vibrational dampeners to vibrationally isolate the entire system from the mechanical vibrations of the building. This particular UHV setup is comprised of three UHV chambers, separated by gate valves, and load-lock ports which allowed sample to be introduced into the UHV without compromising the vacuum condition. Additionally,

layered materials such as HOPG and TMDs could be cleaved in the load-lock under vacuum conditions before being introduced into the UHV.

Samples introduced from the load-lock reach the preparation chamber through a combination of magnetically coupled transfer arms. Here samples are typically treated through a variety of methodologies to make them suitable for measurement. A sample manipulator arm housed within this chamber allows for linear travel and full 360° rotation, allowing for samples to be positioned and angled to face the different ports throughout the length of the preparation chamber for processing. The manipulator is also equipped with two sample stages that allow for direct current heating and indirect radiative resistive heating depending on the nature of the sample. Semiconducting samples such as the deactivated Si(111)-B, when mounted on a specialized sample plate, can be used with direct current heating to reach extremely high temperatures of ~1400°C. Metallic or conductive samples, due to their low resistance, are typically heated via resistive heating, allowing for processing temperatures up to ~1100°C.

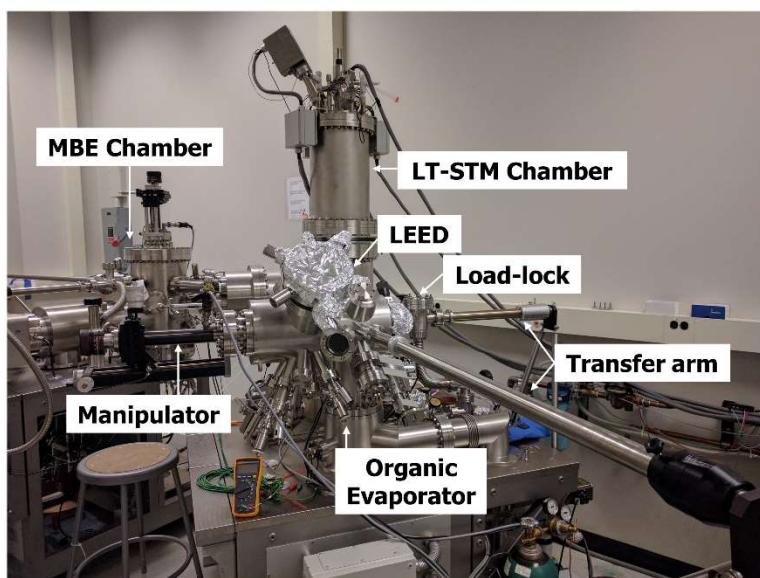


Figure 5-1: Scienta Omicron LT and Preparation UHV Chamber

Over the years, the preparation chamber has housed low-temperature effusion cells with Knudsen based boron-nitride crucibles designs from Createc Fischer and Co GmbH, capable of evaporating purified organic molecules to a manipulator-held substrate sample. A series of leak valves have also been installed throughout the chamber allowing for controlled introduction of chemical vapors for boron nitride growth or high vapor pressure organic molecules. (See Section 5.4.3 for additional discussion on organic molecule deposition methods) An additional filament evaporator is also available for samples that require the evaporation of Si or K depending on the mounted source. An ion gun source from SPECS Surface Nano Analysis GmbH is attached to the chamber along with a leak-valve controlled argon gas line which is routinely baked to ensure cleanliness and a differential turbomolecular pumping system to control ion source chamber pressure. Typical ion gun sputtering conditions hover around 20-30 uA beam currents, 2 keV beam energy and $\sim 1 \times 10^{-6}$ mbar chamber pressure. (Discussed in more detail in Section 5.4.2) Beyond the sample preparation equipment, a multi-channel plate (MCP) LEED apparatus from Scienta Omicron GmbH is mounted in the preparation chamber allowing for electron diffraction measurements of the lattice parameters of the various samples. The setups of the optics of this LEED are capable of producing low energy electron beam currents down to the pico-ampere range which helps to preserve the integrity of the molecular structures during measurement. Furthermore, a molecular beam epitaxy (MBE) chamber is available for *in situ* growth of TMDs and metal thin films.

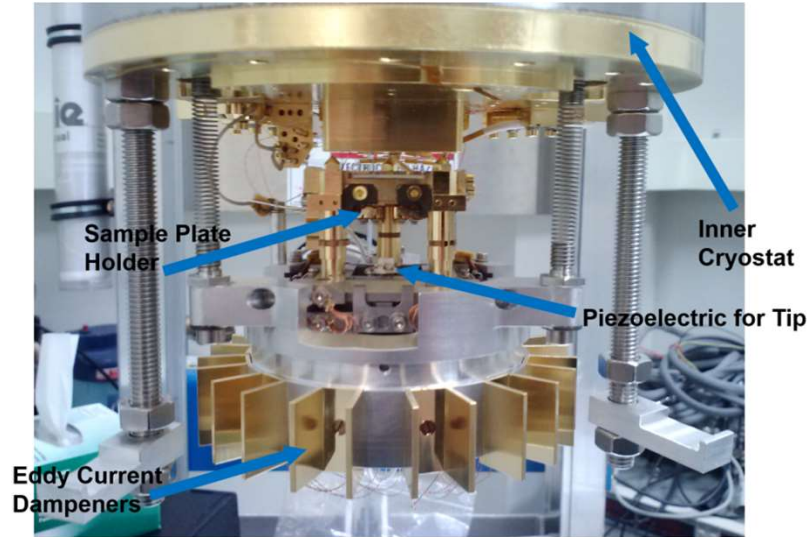


Figure 5-2: Image of the Scienta Omicron STM scanning stage in the LT UHV chamber. Image courtesy of Sean Wagner

Once sample processing has been completed in the preparation chamber, the sample is transferred *in situ* to a sample carousel in the low-temperature chamber (LT), which can hold up to six different samples or tip holders, before being ultimately loaded into the low-temperature scanning tunneling microscope (LT-STM) and Q-Plus atomic force microscope (Q-Plus AFM) for surface measurements. An excellent vibration decoupling system is used to mechanically isolate the scanning stage from the rest of the chamber, allowing for high-resolution scanning probe microscopy images to be acquired. This decoupling system includes three soft springs that are used to freely suspend the stage during measurement and an array of metal plates and permanent magnets which produces Eddy currents to further damp any residual mechanical noise from the stage as seen in Figure 5-2. The sample and stage are housed inside two concentric copper shields that are in direct contact with two cryostats. The inner cryostat can be filled with either liquid helium or liquid nitrogen while the outer cryostat is typically only filled with liquid nitrogen to thermally shield the inner cryostat, which is indirect contact with the stage and therefore determines the stage's ultimate temperature. The spring system can be locked, resulting in the

stage making thermal contact with the inner cryostat, allowing for faster cooling and the copper shields which surround the stage provide thermal isolation for the STM system, allowing the stage to be maintained at low temperature for scanning probe measurements.

In the center of the STM stage lies a piezoelectric scanner where a STM or Q-Plus AFM tip is magnetically mounted. A coarse motor is connected to the piezoelectric, allowing for quick repositioning of the tip relative to the sample surface. The piezoelectric tube is controlled by a series of electronics that are connected to a control box responsible for computer communication and feedback loop management necessary for scanning probe microscopy measurements. The loaded tip can be conditioned using these electronics by applying a high voltage electric pulse between the tip and sample which results in either the collection or expulsion of material to or from the tip. This is a necessary step to quickly and consistently attain the atomically sharp, metallic tip needed for STM/STS. In the scenario where the tip is damaged or otherwise unrecoverable by STM conditioning techniques, it can be extracted from the piezoelectric tube and exchanged with a new tip. The scanning probe tips are typically made of electrochemically etched tungsten wire or mechanically sheared platinum iridium (Pt-Ir) wire of appropriate sharpness. The sharpness of the tip can be determined by either scanning electron microscopy (SEM) or through optical microscopy. SEM images of a tungsten and Pt-Ir tip can be seen in Figure 5-3. When an adequately sharp tip has been produced, it is cut down to size and mechanically mounted to the tip carrier which will be later be mounted to the STM stage. Both tungsten and Pt-Ir tips were used throughout this dissertation.

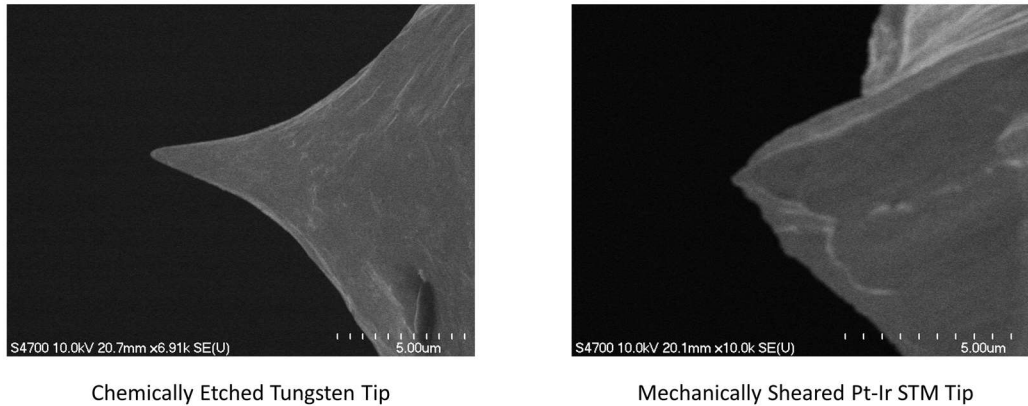


Figure 5-3: SEM images of tungsten and Pt-Ir STM tips

5.2 Scanning tunneling Microscopy and Spectroscopy

5.2.1 Scanning Tunneling Microscopy

Based on the principle of quantum mechanical tunneling, scanning tunneling microscopy (STM) was pioneered by Binnig and Rohrer in the 1980s where the first observation of an electron tunneling signal led the pair to demonstrate that this mechanism could be applied to produce topographical images of conductive samples with atomic resolution.[249,250] As noted earlier in Chapter 2, STM is commonly utilized to acquire atomically resolved images of the surface morphology and local electronic structure.

The basic mechanism of STM is relatively straightforward. When an STM and a sample are within a few angstroms of each other, electrons can tunnel through the vacuum gap between the two.[251-253] Initially, an electronic equilibrium is reached between the tip and sample where the Fermi levels of the two conducting materials are in alignment. However, upon application of a bias voltage, V , between the tip and sample, the Fermi levels of the two materials become separated by an energy eV where e refers to the elementary charge of an electron. This allows for the controlled direction of electron tunneling as shown in Figure 5-4. Under these conditions, electrons

flow from the occupied states of the sample, which has a higher Fermi level, into the unoccupied states of the tip, which has a lower Fermi level, thereby establishing a tunneling current. It should be noted that such a technique necessitates the use of conducting or semiconducting materials due to the need to maintain a tunneling current signal. The surface of insulators cannot be studied due to their wide band gap which offers no available density of states for electrons to tunnel into or out of.

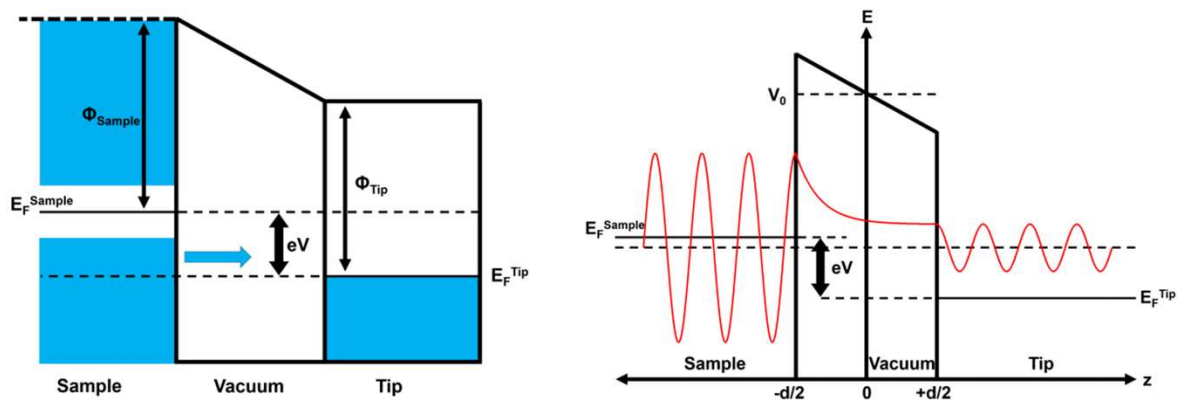


Figure 5-4: Tunneling Mechanisms

(a) Diagram representation of directed electron tunneling between tip and sample through a vacuum gap. An applied tip-sample bias of V results in an energetic separation of eV between the tip and sample Fermi levels. (b) Schematic diagram of an electron wavefunction moving between tip and sample through a vacuum barrier of width, d . The electron wavefunction first appear sinusoidal in the sample before assuming an exponentially decay form inside the vacuum barrier followed by a transition back to a sinusoidal form in the STM tip region. Images courtesy of Sean Wagner

A more complete understanding of the quantum mechanical tunneling can be garnered from the discussion of the Tersoff-Hamnn model and Bardeen's tunneling matrix which describes the tunneling process of an arbitrary three-dimensional geometry. First consider that the tunneling barrier that represented the vacuum gap, can be described by a rectangular potential barrier of finite width and height so long as the applied bias voltage between the tip and sample is small in

comparison the work functions of the STM tip and sample. The work function ϕ_o can be described by the equation:

$$\phi = V_o - E_F \quad (5-1)$$

Where V_o defines the barrier height and E_F is the Fermi level. For simplicity, a one-dimensional tunneling barrier can be assumed. Due to the common STM setup geometry and orientation, the barrier width is denoted by the displacement z . The Schrödinger equation defines the quantum mechanical motion of electrons and, in this case, can be described using the time independent equation:

$$-\frac{\hbar^2}{2m_e} \frac{d^2\psi}{dz^2} + V_o\psi = E\psi \quad (5-2)$$

Where \hbar is the Plank constant, m_e is the mass of the electron, E is the energy of the electron and ψ is the wavefunction of the electron. Assuming a plane-wave wavefunction and a vacuum barrier of thickness d centered on the origin, from equation (5-2), generalized solutions will take the form:

$$\psi = \left\{ \begin{array}{ll} Ae^{ikz} + Be^{-ikz}, & z < -\frac{d}{2} \\ Ce^{kz} + De^{(-kz)}, & -\frac{d}{2} < z < \frac{d}{2} \\ Fe^{ik(z-d)}, & z > \frac{d}{2} \end{array} \right\} \quad (5-3)$$

Where k and κ are defined as:

$$k = \frac{\sqrt{2mE}}{\hbar} ; \kappa = \frac{\sqrt{2m(V_o - E)}}{\hbar} \quad (5-4)$$

From this solution, the wavefunction assumes a sinusoidal form in the sample region ($z < -\frac{d}{2}$), initially. Upon entering the vacuum barrier ($-\frac{d}{2} < z < \frac{d}{2}$), the wavefunction decays exponentially before transitioning to a sinusoidal form, albeit with a reduced amplitude due to the electron transmission amplitude through the vacuum barrier τ , in the STM tip region ($z > \frac{d}{2}$). (See Figure 5-4) Due to the need for a continuous wavefunction at the sample-vacuum and vacuum-tip interface, the free parameters of A, B, C, D and F are constrained. Using these constraints, the system of equations can be solved where τ can be derived noting that the coefficient A can be represented in terms of F giving the equation:

$$\tau = \frac{|F|^2}{|A|^2} = \frac{1}{1 + \left[1 + \left(\frac{\kappa^2 - k^2}{2k\kappa} \right)^2 \right] \sinh^2(kd)} \quad (5-5)$$

Equation (5-5) can be simplified further in the scenario where the potential barrier of the vacuum gap is large in comparison to the energy of electrons, $V_o \gg E$ leading to then $\kappa d \gg 1$. This results in the following equation:

$$\tau \Rightarrow \frac{16k^2\kappa^2}{k^2 - \kappa^2} e^{-2\kappa d} \quad (5-6)$$

As the tunneling current I is proportional to τ , the critical relation that grants STM atomic scale resolution is therefore: [251-253]

$$I \propto \tau \propto e^{-2\kappa d} \quad (5-7)$$

Where a change in the tip-sample distance as derived from equation (5-7) will result the tunneling current signal changing by the factor:

$$\frac{I_{final}}{I_{initial}} = e^{-2\kappa\Delta d} \quad (5-8)$$

Since the work functions of most typical STM investigated surfaces span a range of around 4-5 eV, $\kappa \approx 1 \text{ \AA}^{-1}$. A tip-sample distance increase of 1 \AA will therefore result in the tunneling current signal decreasing by a factor of ≈ 0.135 . This means that the tunneling current will primarily flow between the tip and the atom or molecule with the smallest tip-sample distance and that variations in this distance as small as 1 \AA results in an order of magnitude alteration or more in the tunneling current signal. This relation gives STM the power to routinely resolve the atomic corrugation of the underlying sample. [251-253]

In order to form an atomically resolved image of a sample surface, it is necessary to have extremely precise control of the STM tip's position relative to the sample. This degree of control is typically accomplished through the use of a piezoelectric material. By applying a voltage to this material, its shape can be altered with angstrom level precision via the piezoelectric effect. An STM system will therefore have piezoelectric elements that control movement of the STM tip in the x,y and z directions. As noted before, due to the common orientation of most STM systems, movement in the xy plane is considered parallel to the sample while movement in the z direction is orthogonal to the surface and will dictate the important tip-sample distance. The piezoelectric tube used in this study consist of four electrodes, two for x and y directions, surrounding an inner z electrode. Electronic signals can be applied to these electrodes to induce a bending motion in the xy plane and allow the piezoelectric tube and the STM tip, which is mounted to the end of the tube, to raster across the sample surface with fine precision. The tip-sample distance is controlled by the inner z-electrode where an applied voltage signal drives the z-motion of the STM tip.

Typical STM images at 77 K are acquired in constant-current mode. In order to maintain a constant tunneling current, the STM tip is controlled by a feedback loop where the tip-sample distance is electronically controlled in order to minimize variations in the tunneling current. The feedback loop is a relatively straightforward mechanism. Tunneling current values are typically in the picoampere to nanoampere range which necessitates the use of a high gain amplifier to convert the signal into a voltage. This voltage is compared to a preset value which corresponds to the desired scanning tunneling current. The difference between the two is sent to a feedback circuit and a feedback voltage is subsequently sent to the piezoelectric which corrects the tip position and correspondingly, the tip-sample distance to yield the desired tunneling current. The change in z position of the STM tip is then plotted with respect to its position in the xy plane as the tip rasters across the surface, producing an STM image. [251-253] A detailed schematic of STM operation is shown in Figure 5-5: Schematic of STM Operation.

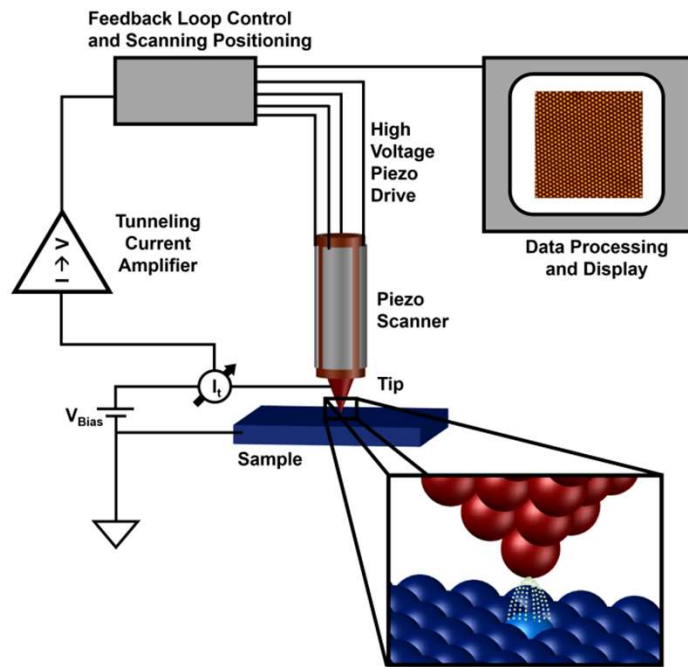


Figure 5-5: Schematic of STM Operation in constant current mode. Image courtesy of Sean Wagner.

5.2.2 Scanning Tunneling Spectroscopy

Scanning tunneling spectroscopy (STS) is a process where the STM tip is parked at a specified x-y location on the sample and the applied sample bias (V) is swept across a pre-defined range and the resulting response in the tunneling current (I) is measured leading to the acquisition of an $I(V)$ curve. Necessarily, the feedback loop that regulates the z-position of the tip and the tunneling current is disabled during this data acquisition. By taking the derivative of the $I(V)$ curve, a differential conductance spectrum is acquired which is known as an STS spectrum. These spectra are typically acquired either by taking the derivative of the tunneling current mathematically or by the use of lock-in detection techniques. [251-253] To perform the latter experimental technique, an modulating AC voltage is applied to the bias voltage resulting in the applied sample bias assuming the form of:

$$V = V_o + \delta V \cos \omega t \quad (5-9)$$

Thus, the resulting tunneling current response $I(V)$ to first order in δV will be given by:

$$I(V) = I(V_o) + \left(\frac{dI}{dV} \right)_{V=V_o} \delta V \cos \omega t \quad (5-10)$$

This response can be divided into a DC response, which is the baseline $I(V)$ response before the modulating voltage is applied and an AC response which can be isolated and detected using a lock-in amplifier. An STS spectrum is acquired when this AC signal is measured across a range of V , typically concurrently with the acquisition of the $I(V)$ curve.

STS spectra are of interest due to its ability to garner information about the electronic structure of the examined surface. Under the assumption that all tunneling transitions between tip and sample occur at constant energy, the tunneling signal will be primarily comprised of the states

between the relative Fermi levels of the tip and sample, separated by eV . The number of occupied states of the sample n_{sample} at a particular energy, E is given by the following equation for temperatures $T > 0$:

$$n_{sample} = D_s(E)f(E) \quad (5-11)$$

Where $D_s(E)$ is the density of states (DOS) of the sample and $f(E)$ is the Fermi function (which shares a very similar form to Fermi-Dirac distribution that has been mentioned in Chapter 3 and is given by the following equation:

$$f(E) = \frac{1}{e^{\frac{E}{k_B T}} + 1} \quad (5-12)$$

Similarly, the number of unoccupied states in the STM tip n_{tip} in which electrons from the sample tunnel into is described by the equation:

$$n_{tip} = D_t(E - eV)(1 - f(E - eV)) \quad (5-13)$$

Where $D_t(E - eV)$ is the DOS of the tip. The generalized tunneling current from tip to sample, $I_{s \rightarrow t}$ is therefore the integral of these expressions and the previously described transmission coefficient (Equation (5-5)):

$$I_{s \rightarrow t} \propto \int_{-\infty}^{\infty} \tau D_s(E)f(E)D_t(E - eV)(1 - f(E - eV))dE \quad (5-14)$$

When $T > 0$, thermal excitations can result in the reverse flow of tunneling current $I_{t \rightarrow s}$ described by the equation:

$$I_{t \rightarrow s} \propto \int_{-\infty}^{\infty} \tau D_t(E - eV)f(E - eV)D_s(E)(1 - f(E - eV))dE \quad (5-15)$$

The total tunneling current is therefore the difference between equation (5-14) and equation (5-15) which results in the following equation:

$$I \propto \int_{-\infty}^{\infty} \tau D_s(E) D_t(E - eV) (f(E) - f(E - eV)) dE \quad (5-16)$$

The transmission coefficient τ , due to the fixed tip-sample distance and the reasonable assumption that $E \sim E_F$, can be assumed to be constant and therefore can be incorporated into the proportionality constant of I . Typically, the STM tip is comprised of a noble metal, such as tungsten and Pt-Ir, which possesses a constant DOS near the tip's Fermi level. Using this, we can simplify equation (5-16) by setting D_t to be a constant value and incorporate it into the proportionality constant of the tunneling current as well. By taking the derivative of the tunneling current I with respect to V , a relation of the AC component of the tunneling current captured by the lock-in technique can be expressed as:

$$\frac{dI(V)}{dV} \propto \int_{-\infty}^{\infty} D_s(E) \left(-\frac{\partial f(E - eV)}{\partial(eV)} \right) dE \quad (5-17)$$

In the relation that $T \rightarrow 0$, the behavior of the Fermi function simplifies to the following expression:

$$\frac{\partial f(E - eV)}{\partial(eV)} \Rightarrow \delta(E - eV) \quad (5-18)$$

Substituting this into equation (5-17), results in the key relation:

$$\frac{dI(V)}{dV} \propto D_s(eV) \quad (5-19)$$

Therefore, by measuring the derivative of the $I(V)$ signal at low temperatures, mathematically or experimentally via the lock-in technique, a signal proportional to the DOS of the sample is acquired allowing for the determination of the electronic structure of the sample. However, an additional complication must be considered with regards to the previously simplified transmission coefficient.

For simplicity, we regarded the coefficient τ as a constant, however, in scenarios where significant

band dispersion is present such that the parallel momentum $k_{||}$ is non-negligible, the following form of the effective tunneling decay constant must be considered:

$$\kappa = \sqrt{\left(\frac{2m_e\Phi}{\hbar^2} + k_{||}^2\right)} \quad (5-20)$$

m_e is the electron mass, and Φ the tunneling barrier height. It is expected that the larger the $k_{||}$, the weaker its contribution to the overall tunneling spectra.[254-256] By combining the two equations (5-7) and equation (5-20), it can be noted that states that have minimal $k_{||}$ will contribute more significantly to the overall tunneling current, i.e. near the $\bar{\Gamma}$ point and will therefore affect the observed magnitude of the spectral features in STS spectra.

5.2.3 *Considerations of Scanning Tunneling Spectroscopy on Organic Molecules on Weakly Interacting Substrates*

Further considerations are needed when analyzing STS spectra taken on organic molecules on weakly interacting substrates. Organic molecules tend to have localized Gaussian spectral features associated with the molecular orbitals which are visible when the molecular orbitals overlap with available DOS in the substrate, through the principle of resonant tunneling. These features tend to be well preserved when molecules are adsorbed onto weakly interacting substrates.[205,257,258] Due to the fact that molecular orbitals typically occupy well defined energetic positions, clear inter-orbital energy gaps are typically observed where no DOS from the molecules are present. This is illustrated in Figure 5-6. In the acquisition of an STS spectra over an electronically well-preserved organic molecule, a negative differential resistance (NDR) regime is often observed.[205,257,258] This region manifests as a dip in the measured tunneling current and dI/dV signal in a certain region despite the increase of the applied sample bias as seen in Figure 5-6. This is often associated with the voltage dependence of the tunneling barrier height.[258]

The voltage dependence of the tunneling barrier height can be described by revisiting the equation for the transmission amplitude τ in Equation (5-6) where it can be rewritten as:

$$\tau \propto e^{-k \int_0^{z_0} dz \sqrt{\Phi_0 - E + eV \frac{z}{z_0}}} \quad (5-21)$$

where z_0 is the tip-sample distance and Φ_0 is the work function. This equation can then be simplified to give:

$$\tau \propto e^{-kz_0 \sqrt{\Phi_0 - E + \frac{eV}{2}}} \quad (5-22)$$

This equation then intuitively indicates that the applied sample bias, $V \ll \Phi_0$ and $E \approx 0$ referring to the Fermi level being set to the origin in STS spectra, the equation reduces back to Equation (5-6). Consider then, the comparison of the tunneling current when the Fermi level of the tip is aligned with a localized molecular resonance at energy $E_L = eV_L$ and when the Fermi level of the tip is shifted such that $V > V_L$. The ratio of $\frac{I(V)}{I(V_L)}$ can then be expressed by using Equation (5-22) and Equation (5-6) to give the expression:

$$\frac{I(V)}{I(V_L)} = e^{-kz_0 \left(\sqrt{\Phi_0 - \frac{E_L}{2} + \frac{eV}{2}} - \sqrt{\Phi_0 - \frac{E_L}{2}} \right)} \quad (5-23)$$

From this, it can be concluded that the ratio will always be less than 1 and therefore NDR will be observed for $V > V_0$. [258] Necessarily, if a sufficiently large constant DOS is present, such as that of a metal substrate which possesses a large metallic continuum of states, the NDR will be eliminated. This is the result of the NDR being overpowered by the tunneling processes to the highly conductive underlying metal substrate. [205,257,258] The effect of the metal, as mentioned earlier, can be suppressed by the addition of a decoupling layer, such as a wide band gap inorganic salt or even another molecular layer, where the increased height of the molecular layer will result in a significantly reduced tunneling signal from the metal directly.

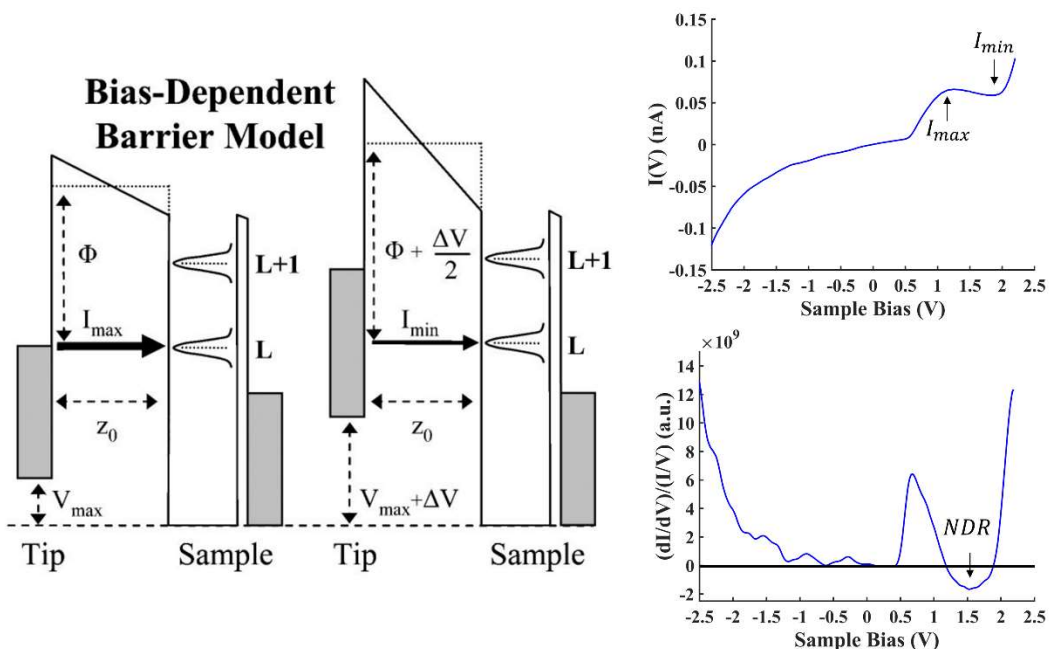


Figure 5-6: Schematic of Negative Differential Resistance (NDR) and Example Spectra

(a) Schematic diagram of the tunneling junction of a C_{60} bilayer where the probed top layer represents molecules sitting on a weakly-interacting substrate (the bottom molecule layer). Tip-sample distance is kept at a constant z_0 , with left and right panels indicating different applied sample bias, with the difference denoted by ΔV . I_{max} and V_{max} correspond to the maximum tunneling current and sample bias seen in (b) whereas I_{min} corresponds to the minimum current in the NDR regime (when the tunneling current dips with increasing sample bias). L and L+1 refer to the molecule's LUMO and LUMO+1 orbitals. Reproduced with permission from [258]. (b) Example $I(V)$ and STS spectra of organic molecules on weakly interacting substrates. I_{max} and I_{min} are labelled on the $I(V)$ curve and the NDR region is indicated in the STS spectra, noting that the dI/dV signal dips below the zero-point as a result of the NDR.

An additional consideration involves the vibrational modes of an organic molecule. As noted earlier in Section 5.2.1, the tunneling process is considered elastic where electrons tunnel between tip and sample without loss of energy and is reflective of the DOS of the tip and sample. However, when the energy of the tunneling electron exceeds that of the molecular orbital energy, it could result in the excitation of phonons within the molecule. This leads to the opening of additional conductance channels which show up in the STS spectrum as peaks and/or bumps.[259-261] These new features can be deconvoluted into well-defined peaks through software fitting

showing the emergence of a progression of additional resonance peaks with spacing comprised of the excited vibrational modes $\hbar\omega_i$ where ω_i corresponds to the frequency of the vibrational mode.[259-261]

The spacing between these peaks is typically quite small, in accordance with the energy of molecular vibrational modes which typically discounts higher order molecular orbitals.[259] In the case of molecules on weakly interacting substrates such as a metal oxide or inorganic salts, a double-barrier molecular junction is formed with the two barriers referring to the tip-molecule gap and the decoupling layer.[260] As a result of this problem, a correction factor needs to be applied to the measured spacing of the vibronic peaks to account for the potential drop across the decoupling layer. For the case of electron tunneling from tip to sample, the correction to the applied sample bias is given as:

$$|V| = \frac{E_{0 \rightarrow -1}}{e(1 - \alpha)} \quad (5-24)$$

where α is the correction factor such that αV gives the potential drop across the decoupling layer.

The vibrational mode energy is then corrected using the following equation:

$$V_{vib_{corrected}} = V_{vib}(1 - \alpha) \quad (5-25)$$

The corrected value can then be compared to phonon-measurement spectroscopies to determine the nature of the vibrational mode. The determination of which vibrational mode is selected during the tunneling process is a complicated combination of molecule adsorption geometry and coupling between the molecule and the substrate.[260,261]

5.2.4 *Differential Conductance Mapping*

Differential Conductance mapping is a technique that combines the topographical imaging capabilities of STM with the electronic structure measurement of STS. To carry out this technique,

the STM is once again operated in constant current mode and an STM image is acquired. Concurrently, the AC modulation voltage is applied as the STM tip rasters across the surface at a pre-set sample bias and the differential conductance signal (dI/dV) is measured using the lock-in amplifier. This signal is sent to the computer and plotted vs the STM tip's location in the xy -plane creating the differential conductance map. The chosen pre-set sample bias is based upon STS features of interest obtained previously on the surface. By measuring the differential conductance signal at a set bias while acquiring an STM image allows for direct comparisons to be made between the observed surface topography and the spatial distribution of the DOS at a specific bias. The speed in which a differential conductance map is limited to the time constant of the lock-in amplifier and the pixel resolution of the image. The averaging time of each individual pixel in the image should ideally be integer multiples of the lock-in amplifier's time constant to enhance the resolution of the image with slower scan rates typically resulting in higher signal to noise ratio. This tends to lead to differential conductance maps taking longer to acquire due to longer scan times requiring more extensive sample-noise isolation, STM tip position drift minimization and sufficiently low temperatures to minimize thermal contributions to tip drift.

5.3 Computational Methods

5.3.1 *MATLAB Processing of Scanning Tunneling Spectroscopy Data*

Processing of STS spectra is typically done through the use of a MATLAB program. Initially, $I(V)$ and signals acquired from the lock-in amplifier, henceforth to be known in this chapter as the dI/dV signal, are imported into MATLAB. STS data are acquired with the feedback loop disabled and the tip-sample distance fixed. This tip-sample distance is determined by the preset sample bias V and tunneling current I . In order to better compare STS data, the dI/dV signal is normalized by the $|I(V)|$ signal so as to minimize contribution from the tip-sample distance.

However, in situations where a substrate band gap is present, such as is the case with the deactivated Si(111)-B surface, or when the I(V) sweeps through the Fermi level, denoted by the origin in STS spectra, a singularity will occur during normalization. To counter this, an offset is applied to allow the normalization to occur. Once the normalization is completed, the spectra are averaged. In addition, due to the existence of electronic noise in the system, a baseline offset can occur in the intensity of STS spectra. This leads to scenarios where parts of a spectrum where no DOS is available, such as the Si bandgap, does not lie at 0. To avoid confusion, most spectra are shifted such that the minimum intensity location near the Fermi level is shifted to 0. As mentioned in Section 5.2.3, STS spectra of organic molecules can often be a convolution of multiple different peaks. In order to properly ascertain their energetic position, STS spectra are fitted with a series of Gaussian peaks using the built-in MATLAB fitting function.

5.3.2 *Epitaxial registration analysis*

The epitaxial registration of organic molecular thin films requires special consideration apart from their well-studied inorganic counterparts. Due to the delicate balance that exist in self-assembled organic monolayers between the intermolecular and molecule-substrate interactions, it is often difficult to predict the organization or epitaxial registration of an organized molecular overlayer. As such, modeling methodologies have been developed to analyze the epitaxial registration of an organic overlayer with respect to a substrate. The geometric phase coherence model will be the model of focus due to its ability to describe the epitaxy of organic molecules on weakly-interacting substrates. Before this model can be described, a brief discussion of the different epitaxial modes must be had.

The epitaxial registration of a molecular overlayer with respect to a substrate surface can be defined by considering the lattice parameters of the two structures and the azimuthal rotation between the two lattices. These key parameters are defined as: \vec{a}_1 and \vec{a}_2 define the lattice vectors of the substrate with α referring to the angle between \vec{a}_1 and \vec{a}_2 ; \vec{b}_1 and \vec{b}_2 define the lattice vectors of the molecular overlayer with β being the angle between \vec{b}_1 and \vec{b}_2 ; θ refers to the angle between a_1 and b_1 . Using these lattice parameters, a structure transformation matrix in real space can be defined:

$$[M] = \begin{bmatrix} M_{11} & M_{12} \\ M_{21} & M_{22} \end{bmatrix} = \begin{bmatrix} \frac{b_1 \sin(\alpha - \theta)}{a_1 \sin(\alpha)} & \frac{b_1 \sin(\theta)}{a_2 \sin(\alpha)} \\ \frac{b_2 \sin(\alpha - \theta - \beta)}{a_1 \sin(\alpha)} & \frac{b_2 \sin(\theta + \beta)}{a_2 \sin(\alpha)} \end{bmatrix} \quad (5-26)$$

where a_1, a_2 and α are the substrate lattice parameters, b_1, b_2 and β molecular lattice parameters, and θ the azimuthal angle between b_1 and a_1 , the reciprocal unit cell vectors can be transformed via

$$\begin{bmatrix} b_1^* \\ b_2^* \end{bmatrix} = (M^{-1})^T \begin{bmatrix} a_1^* \\ a_2^* \end{bmatrix} \quad (5-27)$$

From the matrix elements of $[M]$, the type of epitaxy can be determined. If all matrix elements are integer numbers, all lattice points of the molecular overlayer correspond to a lattice point of the substrate. This is known as a commensurate epitaxy relationship, which typically results from common lattice parameters between molecule and substrate and/or a stronger molecule-substrate interaction. Alternatively, if only a single column of matrix elements consists of integers, then specific lines of the molecular overlayer will coincide with lines in the underlying substrate. This is known as point-on-line (POL) coincidence epitaxy. The matrix element requirement of this kind of epitaxy generates another condition where $b_1^* = ma_1^*$ will therefore be

satisfied in the case of a properly constructed unit cell.[262,263] This means that, in reciprocal space, one of the reciprocal lattice vectors of the molecular overlayer will coincide with a reciprocal lattice vector of the substrate. These structures can be seen in Figure 5-7. The final scenario occurs when one of the matrix elements of $[M]$ is irrational and/or no columns is made of integers. In this scenario, no specific registration is made with the surface resulting in an incommensurate structure. This structure is typically the least favored and is indicative of a weaker molecule-substrate interaction as compared to the POL coincidence epitaxy and commensurate epitaxy.

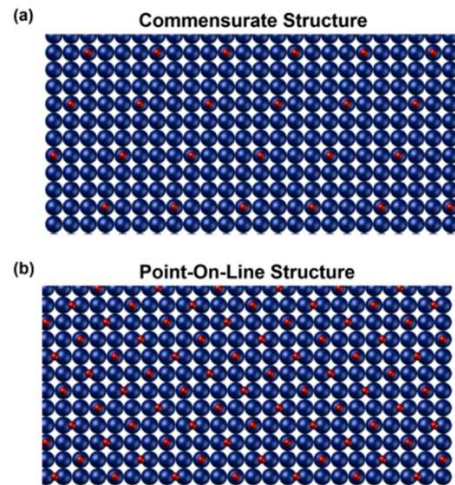


Figure 5-7: Schematic representation of different epitaxial relations between overlayer and substrate. Image courtesy of Sean Wagner.

These epitaxial relations can be further be illustrated by the geometric phase coherence model.[263] This model describes the surface potential landscapes of the substrate lattice and molecular overlayer with plane waves. The discrete ratio of the two plane wave potentials (V/V_0) that corresponds to the lattice mismatch is then calculated as the molecular overlayer is azimuthally rotated with respect to the substrate lattice. V/V_0 is defined using parameters from Equation (5-26):

$$\frac{V}{V_o} = \left(\frac{1}{2N^2} \right) \left[2N^2 - \frac{\sin(\pi NM_{11}) \sin(\pi NM_{21})}{\sin(\pi M_{11}) \sin(\pi M_{21})} - \frac{\sin(\pi NM_{12}) \sin(\pi NM_{22})}{\sin(\pi M_{12}) \sin(\pi M_{22})} \right] \quad (5-28)$$

where N is related to the size of the molecular overlayer. An example plot of V/V_o with respect to the azimuthal rotation is shown in Figure 5-8. The lattice parameters can be determined using experimental techniques such as STM or LEED. This calculation yields values of $V/V_o = 0$ for lattices with the lowest amount of lattice mismatch corresponding to a commensurate epitaxy relationship while POL coincident epitaxy gives a $V/V_o = 0.5$ and $V/V_o = 1$ for the largest degree of lattice mismatch indicating the molecular overlayer is incommensurate to the substrate. This methodology is useful for searching through the different possible epitaxial configurations between the molecular overlayer and substrate to determine optimal epitaxial relationships. Furthermore, matching between the geometric phase coherence model and experimental measurements suggests that the molecular assembly is dominated not by local chemical potentials but rather the overall phase coherence between the two lattices.[263]

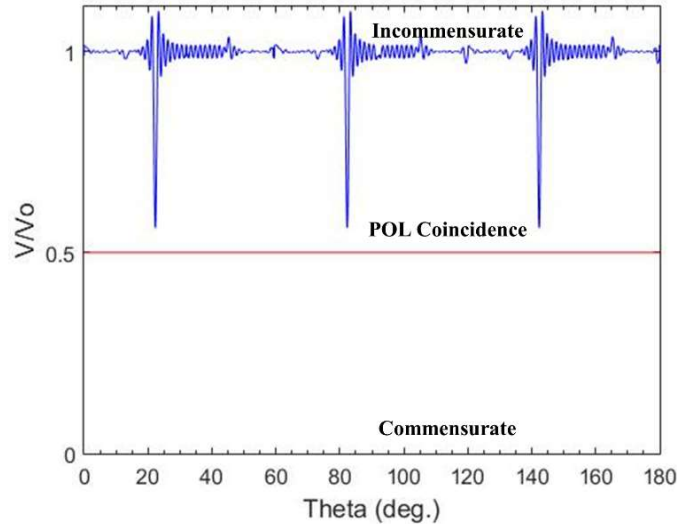


Figure 5-8: Example result of the geometric phase coherence model where the epitaxial registration of the molecular overlayer lies between incommensurate and POL coincidence epitaxy.

Periodic superstructures known as moiré patterns are described by many of the same traits that characterize epitaxy in terms of phase coherence between molecular overlayer and the substrate lattice. These patterns emerge when two periodic patterns are overlaid and rotated with respect to each other, the pattern of a superstructure as seen in Figure 5-9. Mathematically, the moiré pattern is described similarly to the description of matching plane-waves of an overlayer and substrate. Various moiré patterns can emerge depending on the epitaxial registration such as one-dimensional periodic patterns in the case of POL coincidence epitaxy. These patterns have been observed in STM measurements of molecular overlayers on crystalline substrates as seen in the case of ZnPc on deactivated Si(111)-B described in Section 2.5. Using software lattice generation methodologies in combination with the results of the geometric phase coherence model, visualizations of the moiré pattern and the lattice matching can be created such as was shown in Figure 5-7. The resulting lattice and moiré superstructure can then be compared to experimentally obtained STM images.

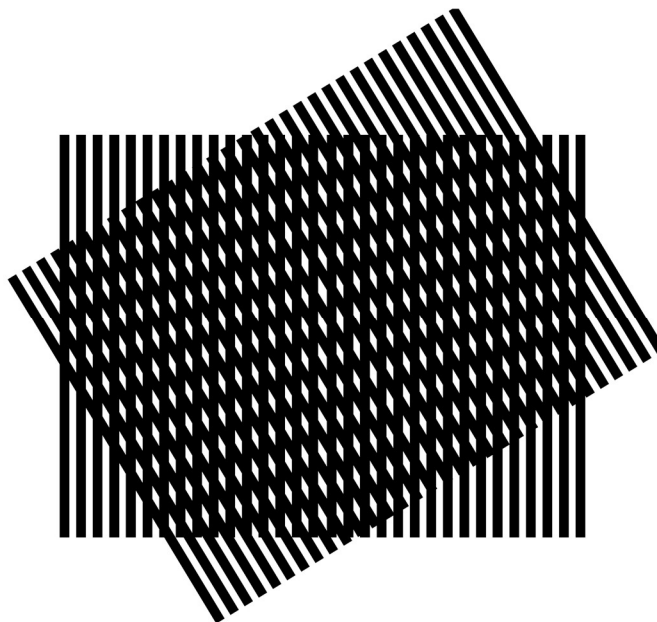


Figure 5-9: Example of a moiré pattern formed by rotated periodic lattices

5.3.3 COMSOL finite element simulation

Due to the complexity of organic molecular systems, it is often extremely difficult to analytically solve the electrostatic problems that concern these systems. Finite element analysis is a methodology that involves the discretization of the large complex system into a mesh consisting of smaller, simpler pieces known as finite elements. These elements can then be solved given initial starting values and any available boundary condition when the problem was defined. The solution to these simple equations is then systematically reassembled to generate the overall solution. This initial solution, however, is far from perfect. Variational methods, where small changes are applied to parameters, are then utilized to minimize a related error function or energy parameter in order to arrive at a solution. The COMSOL software is utilized for the finite element analysis in this dissertation and was supported by computational resources provided by the Institute for Cyber-Enabled Research.

The primary application of the finite element analysis in this body of work is the consideration of the electrostatics of charged organic molecules on a metallic substrate, such as Cu, with a decoupling dielectric layer, such as h-BN. In order to set up this problem, the size of the system L is defined such that the intermolecular distance $r \ll L$. This allows for the definition of a simple boundary condition where the outer bounds of the system can be set to 0 V. The organic molecules are defined as simple cuboids whose lateral dimensions are determined by the unit cell parameters of the molecular overlayer and thickness is defined by two times the typical van der Waals binding distance (0.3 nm) to account for the protruding π orbitals of the molecule. The thickness of the decoupling layer is defined by the specific layer-metal distance. As noted from Section 3.1, the image charge plane of a metal can extend some distance above the metal's surface. As such, we allow this plane to extend into the thickness of the decoupling layer, effectively

reducing the thickness of the decoupling layer and bringing the metal plane closer to the molecular adsorbates. When molecules are charged, an initial uniform charge density is applied to the molecule.

After the electrostatics of this simple model have been solved, the evolution of the potential energy for electrons above the molecule surface, which relates to the local vacuum level shift, are recorded. In order to ascertain the stabilization of the charged organic molecules due to the polarization of its local electrostatic environment, the total electrostatic energy of a molecule in its particular configuration is calculated using the equation:

$$E = \int_0^V \frac{1}{2} \rho \Phi dV \quad (5-29)$$

where Φ refers to the electrostatic potential and ρ is the charge density distribution. The results of this energy are then compared when the charged molecule is in free space, where there is no polarization effects surrounding the molecule, as a charged molecule within a neutral layer of molecules adsorbed on top of the decoupling layer and metal substrate and finally as a charged molecule that is part of a matrix of other charged molecules in the same system. This comparison allows the extraction of the relative polarization energy and the e-e repulsion energy between adjacent, similarly charged molecules which can provide information about the relative stability of different charging configurations. A 2D representation of the geometric setup is given in Figure 5-10

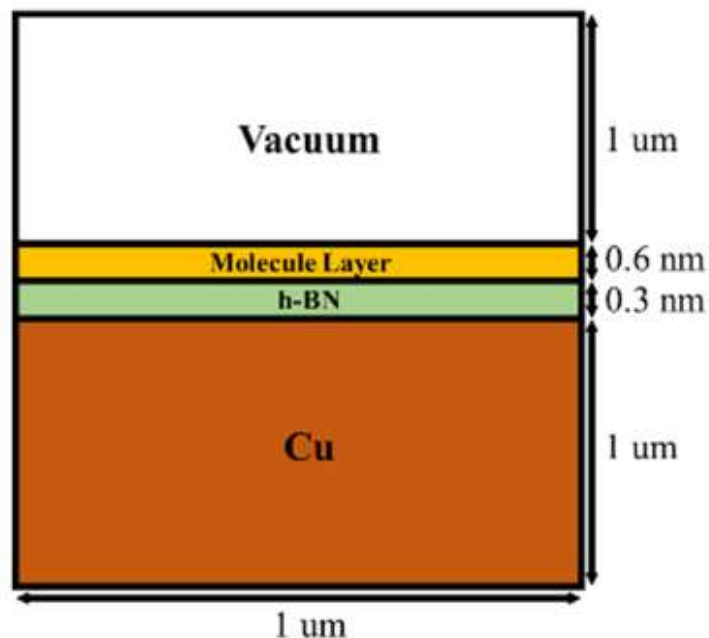


Figure 5-10: Geometric setup for finite element analysis

5.4 Sample Preparation

5.4.1 Chemical and thermal processing of highly boron doped silicon

In order to prepare the Si (111)-B $\sqrt{3} \times \sqrt{3}$ -R30° surface, we used degenerately boron-doped Si(111) wafers with 0.01 – 0.001 $\Omega \cdot \text{cm}$ resistivity. These silicon samples can be cut to the typical 1 cm x 1 mm sample size by hand with a diamond-tipped pen or diced with a diamond coated blade using a dicing saw. The use of non-metallic tools is important to prevent nickel contamination which can hinder the reconstruction of the deactivated Si(111)-B surface. The substrate was first cleaned via RCA1 and RCA2 procedures, leaving behind a thin oxide layer (1-2 nm). The sample was then loaded into the preparation chamber of the UHV system via the preparation chamber's load-lock. The sample was flashed at 1200°C to remove the surface oxide and establish a fresh clean Si interface surface, followed by annealing at 800°C to induce subsurface boron migration into the third atomic layer. The presence of trivalent boron atoms at

this location results in bond formation between four neighboring Si atoms which results in the depletion of the dangling bond of the Si adatom as seen in Figure 5-11a. The depletion of the surface Si dangling bonds results in the creation of a clean band gap with no available DOS near the Fermi level as compared to that of the Si(111) 7×7 reconstruction where dangling bonds are not deactivated as seen in Figure 5-11b. When the sub-surface boron reaches $\approx 1/3$ monolayer, an atomically smooth and deactivated Si(111)-B surface is formed.[115,116,264,265] It is important to note that the deactivation process which creates the Si(111)-B $\sqrt{3} \times \sqrt{3}$ surface could result in an inhomogeneous subsurface boron distribution beyond the third atomic layer, potentially influencing the electrostatic environment and thus the electronic structure of the molecular overlayer.[266] (See Chapter 7)

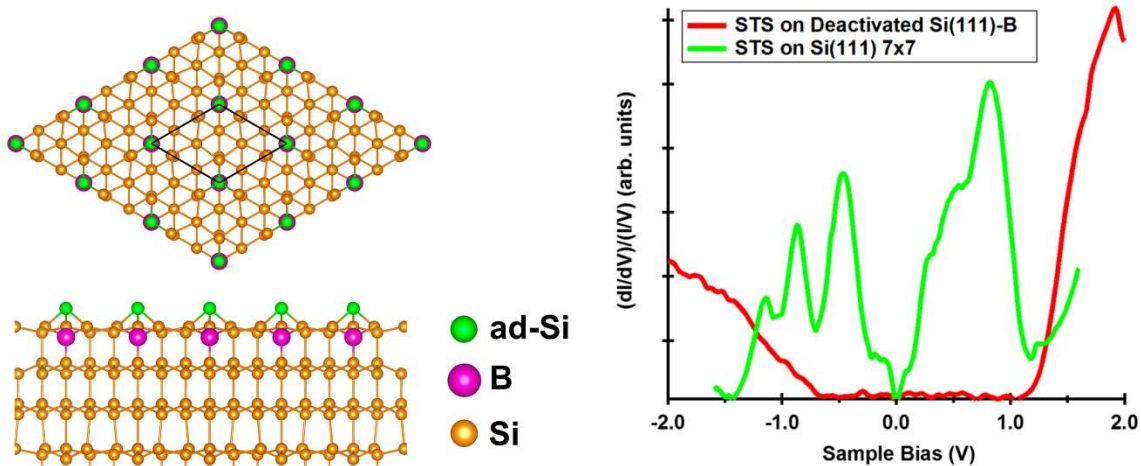


Figure 5-11: Geometric and Electronic Properties of the Deactivated Si(111)-B Surface

(a) Simulated structure diagram of the deactivated Si(111)-B surface lattice in top down view (top panel) and side view (bottom panel). (b) STS taken on Deactivated Si(111)-B and Si(111) 7×7 . The emergence of a clean band gap is observed for the deactivated Si(111)-B surface as the result of boron dopants migrating to the third atomic layer to deactivate the Si dangling bond.

5.4.2 *Metal preparation and Chemical Vapor Deposition of Boron Nitride*

Single crystalline, atomically flat metal substrates are a commonly used supporting substrate for the growth of organic molecules and inorganic 2D thin films such as TMD and HOPG. The commonly used metal substrates in this lab are Cu(111), Ag(111) and Ir(111) which were purchased from Princeton Scientific. However, the exposure of metal substrates to air inevitably leads to the formation of a surface oxide. In order to form the pristine atomically flat metal surface, ion gun sputtering is utilized. Argon gas, a typically chosen inert gas, is flowed into the ionization chamber of our SPECS Surface Nano Analysis ion gun. Here, electrons emitted from the ion gun filament are accelerated to a cathode cage in the presence of argon atoms at about 100 eV. The electrons collide with the argon gas at high energy, thereby ionizing them. The argon ions are then accelerated by an electric field of 0-5000V, focused and directed at the metal substrate. The impinging argon ions collide with the surface of the metal where the kinetic energy of the argon ions is absorbed by surface adatoms, giving them enough kinetic energy to leave the surface. Typical sputtering conditions include an acceleration voltage of 2 keV, ~20-30 μA beam current. Pressure in the preparation chamber during sputtering procedures are typically around $1-2 \times 10^{-6}$ mbar. This process, while capable of removing the metal oxide and/or molecular adsorbates, leaves behind a relatively rough surface. An annealing procedure, where the metal is taken up to a high temperature, ~500° C for Ag(111) and Cu(111), enhances surface diffusion allowing for an atomically flat surface to once again be established.

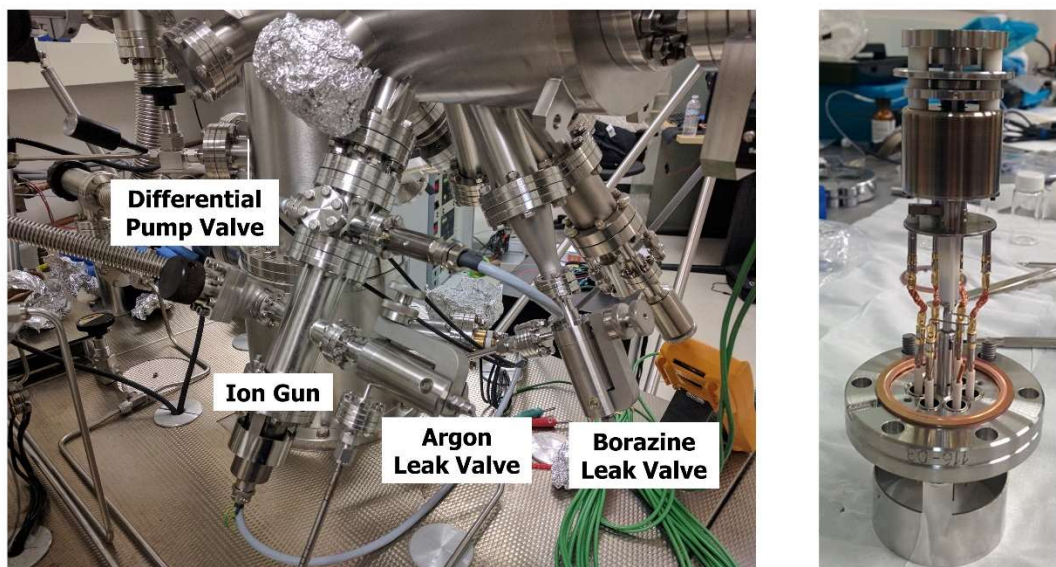


Figure 5-12: Picture of Ion Gun Setup and Borazine Leak Valve and Ion Gun Ionization Module

As noted in earlier chapters, a decoupling layer is very useful to decouple the organic molecule from the metal substrate. Hexagonal boron nitride (h-BN) is a wide bandgap, highly crystalline insulator and serves as the supporting substrate for the study discussed in Chapter 8. h-BN can be grown on a suitable metal substrate, typically Ir(111) or Cu(111) by means of UHV-chemical vapor deposition. Borazine molecules, the typical precursor molecule, are flowed onto the metal substrate heated at very high temperatures, $\sim 820^\circ\text{C}$ for Cu via a leak valve at a pressure of $\sim 1 \times 10^{-6}$ mbar. The borazine molecules are catalytically dissociated by the metal surface into constituting hydrogen, boron and nitrogen atoms. The hydrogen atoms evaporate at the high substrate temperature with boron and nitrogen atoms organizing into a hexagonal lattice in the form of h-BN.[267] This growth is a self-limiting process since the catalytic activity of Cu(111) is drastically reduced once the surface is passivated by a complete h-BN monolayer.[267]

The precursor borazine molecules can typically be attained by two different means, evaporation of pure borazine liquid or decomposition of ammonia borane. Handling of the

borazine liquid can be quite challenging as the liquid degrades when held at room temperature over time. As a result, the liquid needs to be detached from the chamber and stored in a fridge at below 5° C to slow down the degradation process. Exposure of borazine molecules to air can also result in the formation of an oxidized borazine which leaves behind a white powder residue which can be detrimental to vacuum and pump integrity. Deriving borazine from the thermal decomposition of ammonia borane, however, is a much simpler process. Ammonia borane is typically loaded into a stainless-steel vessel where it is pumped and degassed. The temperature of the vessel is then raised to 150° C to trigger the slow decomposition of ammonia borane which releases borazine and hydrogen gas, leaving behind a polymer residue. This process is much more convenient compared to borazine liquid as the ammonia borane powder and its residue can be left for weeks/months within the stainless-steel vessel without noticeable issue. Images of the vessels used to house the borazine sources and their chemical structure can be found in Figure 5-13: Boron Nitride Deposition Sources, borazine liquid vessel and ammonia borane powder vessel Figure 5-13.

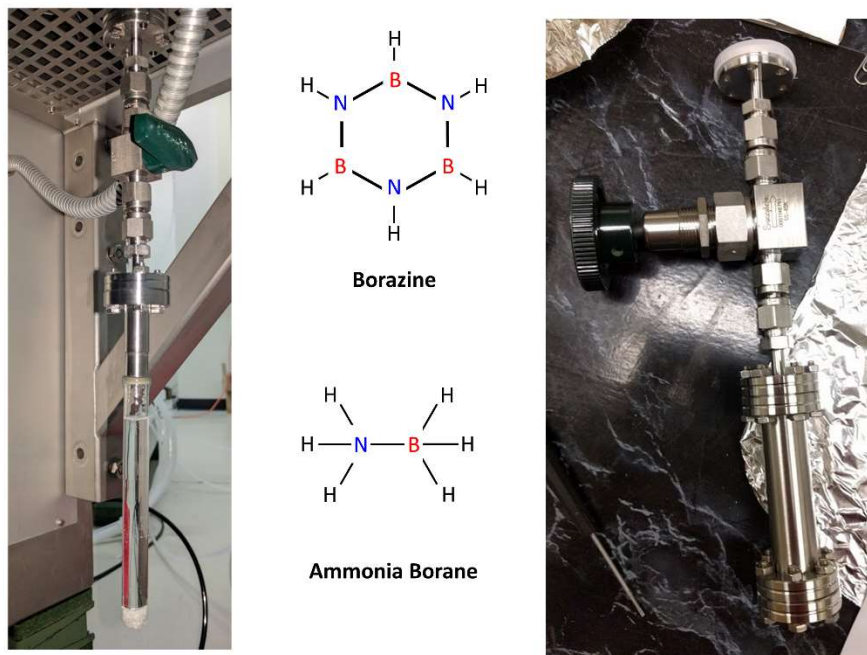


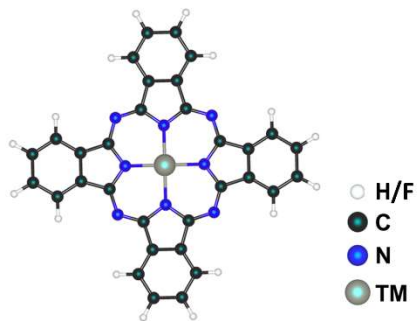
Figure 5-13: Boron Nitride Deposition Sources, borazine liquid vessel and ammonia borane powder vessel. Chemical structure of borazine and ammonia borane are drawn out.

5.4.3 Organic Molecule Deposition

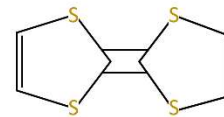
The growth and electronic structure of organic molecules are often very sensitive to impurities and foreign molecules. To minimize their effects, deposition sources for organic molecules are typically highly purified. Most of the organic molecules used in this study are purified by vacuum sublimation purification.

In order to deposit the organic molecules used in this study, two evaporator setups are utilized. A Createc Fisher and Co GmbH low temperature effusion cell with a Knudsen based boron nitride crucible was the primary evaporator used in most of these studies. It allows for accurate temperature control and superior cleanliness due to mounting of the evaporator to the UHV system directly. Molecules are typically baked to $\sim 140^{\circ}\text{C}$ for 3 days before additional degassing at higher temperatures is performed to allow the molecular source to be heated to the

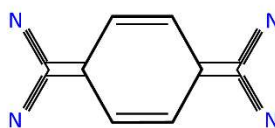
necessary sublimation temperature without compromising the pressure of the chamber. A simple mechanical shutter is used to shield most of the chamber and the sample from unwanted deposition as the source temperature is ramped up or during degassing. Phthalocyanine molecules and potassium-doped-TCNQ molecules were deposited using this evaporator design. When different molecules are needed for deposition, the crucibles are emptied and taken through a series of ultrasonicated trichloroethylene, acetone and isopropyl-alcohol baths to remove left-over organic molecule powder. The empty crucibles are then loaded into the chamber and taken through an extensive degassing procedure, significantly above the molecule's sublimation temperature. The second molecular evaporator designed is termed the valved evaporator. The source of this evaporator is segmented from the rest of the preparation chamber by a leak valve which allows for controlled leakage of molecular vapors into the chamber, similar to how borazine gas is introduced in Section 5.4.2, albeit at significantly lower pressures. The vessel that contains the source molecular material is connected a small mechanical pump and a separately backed small turbomolecular pump. This setup allows molecular powder to be separately loaded, pumped and baked without influencing the vacuum of the main sample preparation chamber. Molecules with high vapor pressure at low temperatures such as TTF and CA, are deposited using this evaporator as they cannot be loaded into the UHV. Molecule deposition from either evaporator typically occurs in the 10^{-9} to 10^{-10} mbar range. Image of the low temperature effusion cell and the molecular structure are shown in Figure 5-14. For the purpose of studying CTC systems as noted in Chapter 4, a potassium dispenser from SAES was installed to allow for controlled doping of potassium atoms to our samples. The potassium dispenser is heated by a DC power supply with ~ 5 A of current to trigger the decomposition of potassium-carrying salt in the dispenser, releasing potassium atoms into the chamber.



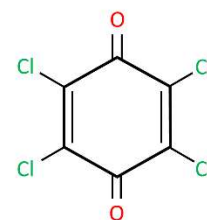
Metal Phthalocyanine (MPc)



Tetrathiafulvalene (TTF)



Tetracyanoquinodimethane (TCNQ)



p-chloranil (CA)

Figure 5-14: Low temperature effusion cell with shutter and Knudsen cell and structure of organic molecules studied in this dissertation.

6 Self-Assembly of F₁₆ZnPc and ZnPc/F₁₆ZnPc heterostructures on the Deactivated Si(111)-B Surface

The demonstration of anisotropic step-flow growth and long range order of ZnPc on the deactivated Si(111)B was a major step forward for organic thin films as noted in Section 2.5. Growth behavior is further enriched by the ability to functionalize organic molecules. Functionalization is a very useful attribute of organic molecules because it provides a pathway to tune the electronic properties of molecules as well as the molecule-substrate and molecule-molecule interactions with relative ease. For instance, fluorination of zinc phthalocyanine (ZnPc) will lead to the withdrawal of electrons from the conjugated π plane of the molecule to the highly electronegative fluorine atoms.[268] This process results in deeper highest occupied molecular orbital (HOMO) and lowest unoccupied molecular orbital (LUMO) levels, making fluorinated ZnPc (F₁₆ZnPc) useful as an electron acceptor in device application. F₁₆ZnPc along with ZnPc, thus, become viable candidates for the construction of donor-acceptor heterojunctions. As mentioned earlier, ZnPc assemblies on the deactivated Si(111)-B surface are highly ordered. Furthermore, this growth is particularly attractive for the study of heterojunctions since ZnPc forms parallel anisotropic molecular stripes on the surface,[269] suggesting that phase-segregated donor and acceptor domains that are laterally or vertically stacked may be readily created if F₁₆ZnPc grows in a similar fashion to ZnPc.

In this chapter, we utilize scanning tunneling microscopy (STM) to explore the local ordering and epitaxial relation of F₁₆ZnPc, a prototypical acceptor organic molecule, molecular assemblies on the deactivated Si surface (Section 6.1). Although F₁₆ZnPc is still adopting the tilted molecular configuration comparable to ZnPc, it forms two morphologically distinct self-assembled structures of similar epitaxial registration with the substrate surface which reflects the interplay

between the molecule-substrate interaction, π - π intermolecular interaction, and side-to-side intermolecular repulsion originating from the fluorine groups. Furthermore, we demonstrate that the formation of F₁₆ZnPc-ZnPc heterojunction is possible (Section 6.2). Various relative molecular orientations are exposed at the heterojunction, allowing for future spectroscopy investigation of molecular electronic structures at the single molecule level. This chapter is adapted from the References [71,93] *A. Tan et al., The Journal of Chemical Physics* **146** 052809 (2017) and *A. Tan et al., Physical Review B* **96** 035313 (2017).

6.1 Self-Assembly of F₁₆ZnPc on deactivated Si(111)-B

As shown in Figure 6-1a, when F₁₆ZnPc molecules are evaporated onto the surface of the deactivated Si(111)-B held at RT, they self-assemble into an ordered structure which we term, simply, as structure A. The apparent height of the molecular stripe is 0.54 ± 0.04 nm, which is comparable to that of ZnPc indicating a similar molecular tilting angle of $\sim 30^\circ$ with respect to the surface as noted in Figure 6-1ab. Figure Figure 6-2b illustrates the fast Fourier transform (FFT) pattern of the STM image presented in Figure 6-2a, where four distinct peaks beyond that of the molecular and Si reciprocal lattices are circled in black. To determine the nature of these peaks, a low energy electron diffraction (LEED) pattern is simulated using LEEDLab (Figure 6-2c). The simulation indicates that these diffraction spots originate from multi-scattering between the molecular lattice and the substrate surface. Normally, multi-scattering peaks that arise from LEED patterns can manifest themselves as a Moiré superstructure in STM images,[270-275] however, we were not able to discern the corresponding Moiré pattern in Figure 6-2a. The detailed morphological features will be discussed later. Under the ET growth condition, a new structure of distinct packing morphology emerges (Figure 6-2d), which we term as structure B. Molecules in structure B adopt a slightly larger tilting angle leading to an increased apparent height of the

molecular stripe ($0.66 \pm 0.07 \text{ nm}$) as noted in Figure 6-1c. Additionally, the b_1 lattice parameter is larger compared to that of structure A, while b_2 remains approximately the same in magnitude. This is likely due to the strong F-F repulsion between the side-to-side packed $F_{16}\text{ZnPc}$ molecules, which relax themselves into a more stable configuration at elevated temperature. Nevertheless, structure A is not completely suppressed as we often observe the co-existence of the two structures in STM images, suggesting that there are likely two local minima on the free energy curve representing the two structures. Again, to explain the FFT features of structure B shown in Figure 6-2e, we include a simulated LEED pattern (Figure 6-2f) for comparison. Circled diffraction spots originate from the multi-scattering process.

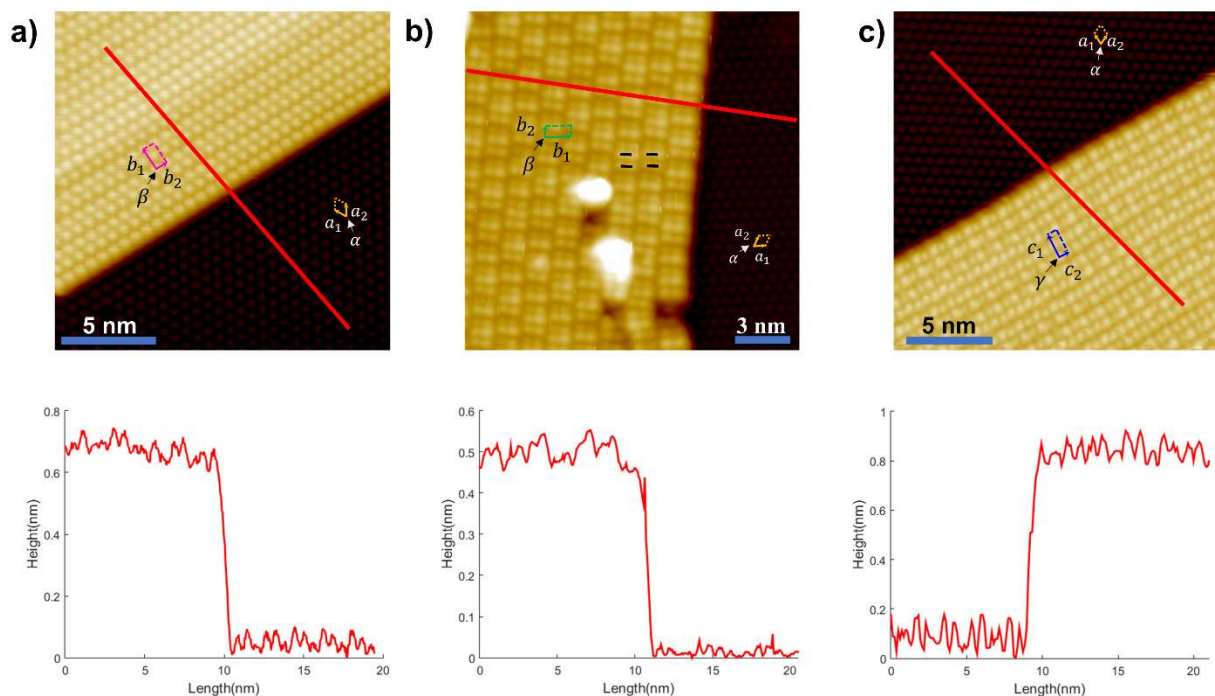


Figure 6-1: Apparent height measurement of $F_{16}\text{ZnPc}$ and ZnPc assemblies on deactivated $\text{Si}(111)\text{-B}$

STM topography images taken at 77K of (a) ZnPc ($V_s = 1.8\text{V}$, $I_t = 60\text{pA}$) with a step height of $0.55 \pm 0.02 \text{ nm}$ (b) $F_{16}\text{ZnPc}$ (structure A) ($V_s = 2\text{V}$, $I_t = 5\text{pA}$) with a step height $0.54 \pm 0.04 \text{ nm}$ (c) $F_{16}\text{ZnPc}$ (structure B) ($V_s = 2\text{V}$, $I_t = 5\text{pA}$) with a step height $0.66 \pm 0.07 \text{ nm}$ with their corresponding line profiles marked by the red line shown in the bottom panels. This suggests that the molecules are tilted on the surface, similar to the case of ZnPc .

With the packing morphologies of F₁₆ZnPc presented, we would like to comment on the role of fluorination on the self-assembly process. The lattice parameter of the F₁₆ZnPc assemblies, in either structure A or B, is larger along the b_1 direction compared to that of ZnPc, which we attribute to the significantly stronger F-F repulsion between the side-to-side packed F₁₆ZnPc molecules. Meanwhile, the spreading of the electron cloud along the molecular backbone originating from the fluorination of the molecule[268] allows for a closer π - π stacking corresponding to the shorter b_2 vector. Regarding the molecule-substrate interaction, F₁₆ZnPc molecules exhibit significant charge transfer with the Si(111)-B substrate.[33] This is expected to introduce electrostatic interaction between the substrate and the molecular overlayer, which is in sharp contrast to the scenario of ZnPc where charge transfer with the substrate is negligible.[276] To explore the impact of the stronger molecule-substrate interaction, we first examine the epitaxial registration of the molecular overlayer with the substrate surface. As seen in the FFT patterns shown in Figure 6-2b and Figure 6-2e, the reciprocal lattice of the molecular overlayer, in either A or B structure, shares a common lattice vector with that of the Si(111)-B surface, i.e., b_2^* equals a_2^* within measurement uncertainty. This means that b_1 must be parallel to a_1 in real space. This relation should have profound implications in the epitaxial relation. The fact that the molecular b_2^* vector equals the Si a_2^* vector indicates that M_{12} and M_{22} from Equation (5-26) must be 0 and 1, respectively. By inputting experimentally determined unit cell values of the two F₁₆ZnPc assembly structures, the matrices are derived, as listed in Table 1. Within experimental uncertainty, the transformation matrices indeed contain the predicted integer values in the second column. The confinement of two integers in a column is regarded as the evidence of point-on-line (POL) coincident epitaxial relation.[262,263] Therefore, compared to ZnPc growth, the stronger

molecule-substrate interaction seems to have driven the molecular assembly of F₁₆ZnPc into a more favorable registration with the substrate.

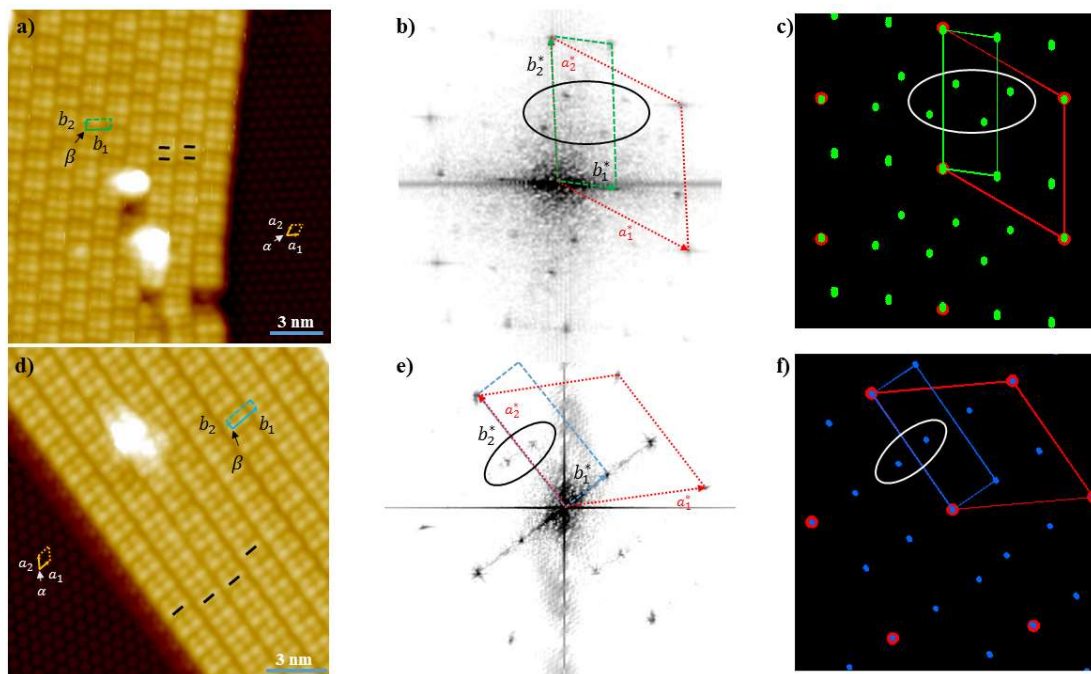


Figure 6-2: RT and ET structures of F₁₆ZnPc on deactivated Si(111)-B

(a) STM topography image ($V_s = 2V$, $I_t = 5pA$) of F₁₆ZnPc assembly (structure A) on the deactivated Si(111)-B surface obtained at 77K reproduced from Figure 6-1b, and the corresponding FFT pattern (b). The substrate surface is hexagonal with lattice parameter $a = 0.665 \pm 0.005 \text{ nm}$. Unit cell of the molecular overlayer given by: $b_1 = 1.49 \pm 0.06 \text{ nm}$, $b_2 = 0.59 \pm 0.02 \text{ nm}$, $\beta = 82^\circ \pm 1$. (c) Simulated LEED pattern of F₁₆ZnPc (structure A) on the Si(111)-B surface using the unit cell parameters determined from STM. (d) STM topography image ($V_s = 2V$, $I_t = 5pA$) of F₁₆ZnPc assembly (structure B) on the deactivated Si(111)-B surface obtained at 77K, and the corresponding FFT pattern (e). Unit cell of the molecular overlayer given by: $b_1 = 1.56 \pm 0.02 \text{ nm}$, $b_2 = 0.58 \pm 0.01 \text{ nm}$, $\beta = 89 \pm 1^\circ$. (f) Simulated LEED pattern of F₁₆ZnPc (structure B) on the Si(111)-B surface using the unit cell parameters determined from STM. In STM images: Black lines define individual molecules. In FFT and simulated LEED patterns: Reciprocal space unit cells of the molecular overlayer and the Si surface are marked in red (Si), green (structure A), and blue (structure B). Circled diffraction spots originate from multi-scattering. No rotational domains were included in LEED simulation.

This epitaxial relation can be further illustrated by the geometric phase coherence model described in Section 5.3.2. We are able to demonstrate the POL coincidence for both structures

using the lattice parameters that fall within the experimental range. As an example, Figure 6-3a displays V/V_0 as a function of θ that is performed on structure B. The first minimum in V/V_0 ($=0.5$) is observed when the azimuthal rotation angle is 0° , with the subsequent minima occurring at 60° intervals due to the C3 symmetry of the Si surface. Note that the calculated azimuthal angle is consistent with the experimental observation (Figure 6-2a, d), where the b_1 vectors of the A and B structures are both parallel to the C3 symmetry direction of the substrate. The validity of the model in describing the epitaxial relation of $F_{16}ZnPc$ assemblies on Si(111)-B suggests that, instead of local potential, it is the phase coherence between the molecular overlayer and the substrate surface that determines this registration.

Next, we simulate the overlayer – substrate geometric structures by superimposing the two lattices with 0° azimuthal rotation with respect to each other. The simulated results can be directly compared to the STM topography images (Figure 6-2a and Figure 6-2d). As shown in Figure 6-2d, there is a pronounced alternating contrast of molecules along the b_2 direction. Specifically, on the first four molecular rows next to the step edge, the 1st and the 4th rows share the same alternating pattern, while the 2nd and the 3rd rows have their patterns offset by one lattice constant with respect to row 1 and 4. As an observation guide, a molecule of the bright contrast is labeled on each row in Figure 6-2d. This exact pattern can be reproduced in the simulated geometric structure illustrated in Figure 6-2b, where the $F_{16}ZnPc$ overlayer lattices (blue dots) that sit above the Si adatoms (red circles outlined in black) correlate to the molecules that appear brighter in the STM image due to enhanced electron tunneling, while those positioned between the Si adatoms corresponding to the darker molecules. On the other hand, when the periodicity of structure A (Figure 6-2a) is examined, two characteristic contrast patterns along the molecular rows, i.e., bright-dark-bright-bright-dark and bright-dark-dark-bright, can be discerned. Again, such contrast patterns are duplicated in the

simulated geometric structure (Figure 6-3c). Finally, it is worthwhile to point out that the POL coincident registration can be clearly identified in the simulated geometric structures, in which the molecular overlayer lattices all lie on the lattice line of the substrate surface.

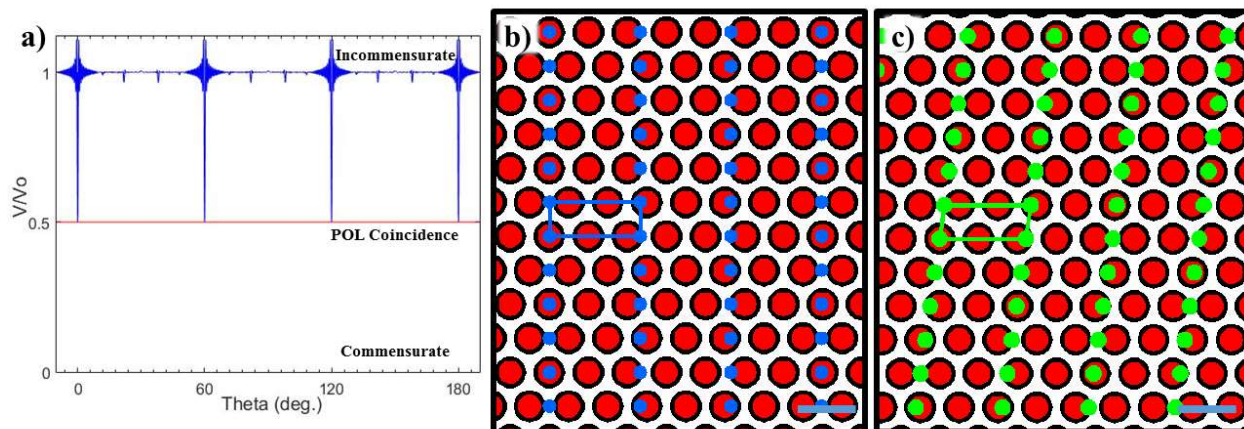


Figure 6-3: Geometric and lattice simulation of $F_{16}ZnPc$ on deactivated Si(111)-B

(a) Results of a geometric analysis as the $F_{16}ZnPc$ overlayer (structure B), extended to $N=30$ unit cells, is rotated azimuthally on the Si substrate with lattice parameters: $b_1 = 1.547 \text{ nm}$, $b_2 = 0.576 \text{ nm}$, $\beta = 90^\circ$. θ represents the angle between b_1 and a_1 defining the azimuthal rotation of the molecular overlayer with respect to the Si(111)-B surface. The first minimum in V/V_0 ($=0.5$), indicative of point-on-line coincidence, is observed at 0° with additional minima appearing in 60° increments due to the C3 symmetry of the substrate. (b-c) Simulated geometric layout of $F_{16}ZnPc$ overlayer in structure B (b), and structure A (c), on the Si(111)-B surface. The lattice parameters of structure B are listed above, and for structure A: $b_1 = 1.480 \text{ nm}$, $b_2 = 0.582 \text{ nm}$, $\beta = 82^\circ$. Red circles outlined in black represents Si adatoms. Blue and green dots represent the $F_{16}ZnPc$ overlayer lattice in structure B and A, respectively. Blue scale bars represent 1 nm.

Table 1: Summary of molecular lattice parameters for structure A and structure B and their corresponding transformation matrix with respect to the lattice of the deactivated Si surface.

Structure	Experiment	
	Lattice Parameters	Epitaxial Relation
A	$b_1 = 1.49 \pm 0.06 \text{ nm}$ $b_2 = 0.59 \pm 0.02 \text{ nm}$ $\beta = 82^\circ \pm 1$	$\begin{bmatrix} 2.24 \pm 0.09 & 0 \\ -0.38 \pm 0.03 & 1.01 \pm 0.04 \end{bmatrix}$
B	$b_1 = 1.56 \pm 0.02 \text{ nm}$ $b_2 = 0.58 \pm 0.01 \text{ nm}$ $\beta = 89 \pm 1^\circ$	$\begin{bmatrix} 2.35 \pm 0.03 & 0 \\ -0.49 \pm 0.02 & 1.01 \pm 0.02 \end{bmatrix}$

6.2 Growth of F₁₆ZnPc-ZnPc heterojunctions on the deactivated Si(111)-B

With the two characteristic structures of F₁₆ZnPc well defined, the next step becomes the development of an organic heterojunction. As has been previously discussed, F₁₆ZnPc could be used for a device's acceptor layer and ZnPc for the donor layer. It has been predicted that F₁₆ZnPc-ZnPc heterojunctions will exhibit equilibrium (under dark) charge transfer properties when packed side-to-side and no charge transfer properties when stacked face-to-face.[277] Two growth conditions were tested in the attempt to achieve controlled relative molecular orientation at the heterojunction. We first performed the F₁₆ZnPc/ZnPc growth where we grew F₁₆ZnPc under ET growth conditions on the deactivated Si(111)-B surface followed by the deposition of ZnPc at RT. By controlling the growth temperatures of the sequential deposition in this manner, we can maximize the phase-segregation of the two molecular assemblies. This process yielded a variety of interesting structures as seen in Figure. 6-4a-e. First of all, F₁₆ZnPc and ZnPc structures remain predominantly separate entities and they cannot grow exactly parallel to each other due to the fundamental difference in their azimuthal rotations with respect to the Si lattice (Figure. 6-4a).[269] However, when a ZnPc structure intersects an F₁₆ZnPc structure, ZnPc adopts a zigzag

pattern to maximize the contact, as shown in Figure. 6-4b. We hypothesize this behavior to be a result of Coulomb interaction originating from charge transfer, though further study will be needed to confirm this. During this behavior, scenarios can occur when ZnPc molecules are forced to conform to the edge of the F₁₆ZnPc assembly as seen in Figure. 6-4c. This leads to a well-ordered side-to-side heterojunction. ZnPc will adopt a similar structure when they are inserted in groups into the F₁₆ZnPc stripes as can be seen in Figure. 6-4d. This leads to a uniform face-to-face heterojunction.

Scattered second layer growth associated with the deposition of ZnPc is also observed. This is likely due to the corrugated potential energy landscape of the F₁₆ZnPc layer which hinders the diffusion of ZnPc molecules. However, molecular diffusion on this layer is not at all impossible. As seen in Figure. 6-4e, an organized ZnPc structure was able to form on top of the F₁₆ZnPc layer. This structure adopts a highly kinked pattern that is likely a result of an epitaxial registration effect to the underlying F₁₆ZnPc layer.

When F₁₆ZnPc molecules are deposited on the ZnPc structure, i.e. ZnPc/F₁₆ZnPc, however, the system appears quite different. Since ZnPc structures do not change with growth temperature, we choose to deposit ZnPc at RT followed by the RT deposition of F₁₆ZnPc. As previously mentioned, F₁₆ZnPc's corrugated surface potential energy suppresses the formation of long-range ordered ZnPc structures deposited on top, but ZnPc seems to have a much smoother potential energy landscape that allows for long range ordered F₁₆ZnPc structures to more easily occur. As shown in Figure. 6-4f, F₁₆ZnPc form stripe structures on top of the ZnPc underlying layer. There appears to be two distinct segments in these stripes, i.e., a highly corrugated segment where F₁₆ZnPc deviates from the ZnPc's growth direction, labeled as IC (incommensurate), and a smoother segment that is commensurate to the ZnPc lattice, labeled as C (commensurate). The

commensurate structure is relatively short ranged since the smaller lattice parameter of b_1 in ZnPc assembly leads to stronger intermolecular repulsion between the F groups. Eventually, the strained F_{16} ZnPc commensurate structure will relax into its more stable incommensurate form. This competing act between trying to match ZnPc's lattice and minimizing the F-F repulsion results in the alternating segments in the second layer F_{16} ZnPc, as observed in Figure. 6-4f.

These characteristics of the F_{16} ZnPc-ZnPc heterojunction provide numerous unique avenues for future research. The growth process not only exposes the vertical heterojunction (F_{16} ZnPc/ZnPc and ZnPc/ F_{16} ZnPc), but also the lateral heterojunction of two different relative molecular orientations, i.e., edge-to-edge and face-to-face. These results will provide the basis for detailed investigations of charge transfer behavior at donor-acceptor heterojunctions of well-controlled molecular configuration under equilibrium and photoexcitation conditions.

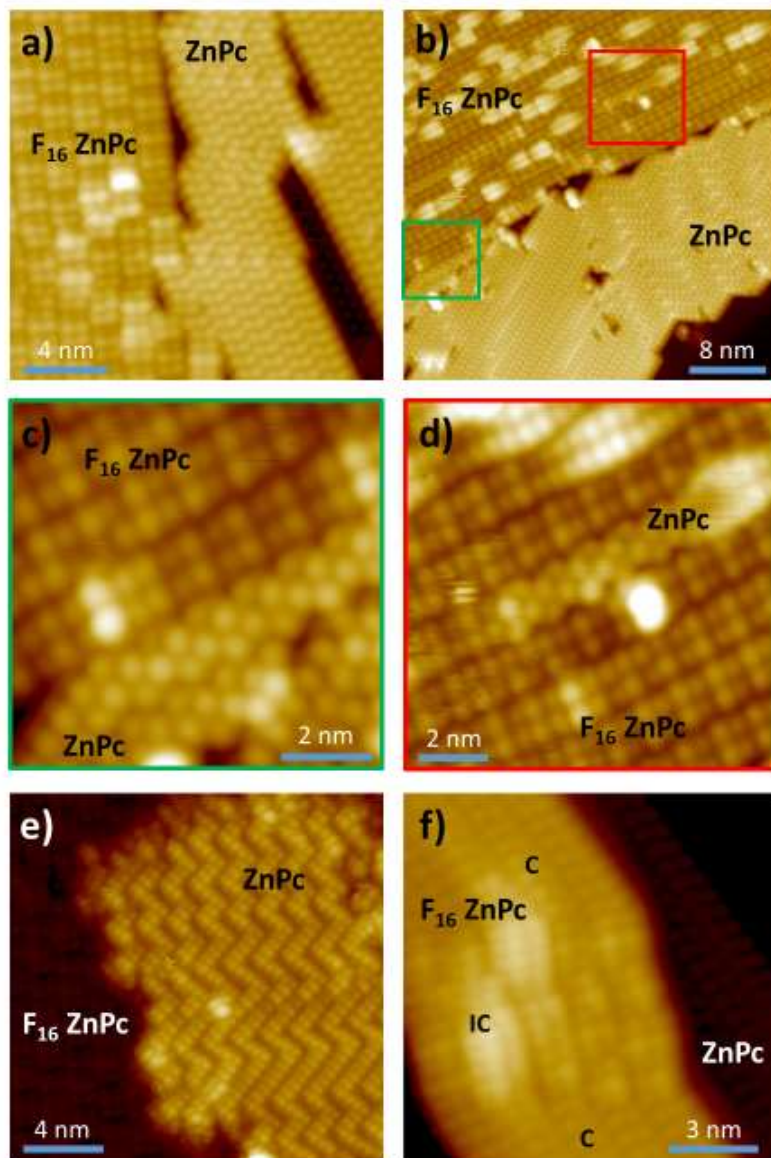


Figure. 6-4: STM images of F₁₆ZnPc-ZnPc heterostructures on deactivated Si(111)-B

(a-e) STM topography images ($V_s=2V$, $I_t=5pA$) of the F₁₆ZnPc/ZnPc heterostructures obtained at 77K. (a) ZnPc assemblies grow at an angle to F₁₆ZnPc assemblies due to the fundamental difference in their respective azimuthal rotation to the Si substrate. (b) ZnPc assemblies are observed to zigzag along the edge of the F₁₆ZnPc assembly. Two areas of interest are boxed in green and red which correspond to (c) and (d), respectively. (c) edge-to-edge F₁₆ZnPc/ZnPc heterojunction (d) face-to-face molecular heterojunction formed as a result of ZnPc insertion into the F₁₆ZnPc assembly. (e) Vertical heterojunction formed as a result of second layer growth of ZnPc on F₁₆ZnPc. (f) STM topography image ($V_s=2V$, $I_t=5pA$) of the ZnPc/ F₁₆ZnPc heterostructures obtained at 77K. Second layer F₁₆ZnPc is comprised of commensurate and incommensurate segments with respect to the underlying ZnPc.

6.3 Conclusion

In summary, we have demonstrated that $F_{16}ZnPc$ molecules exhibit self-assembling behavior on the deactivated Si (111)-B $\sqrt{3}\times\sqrt{3}$ surface similar to that of $ZnPc$. Different from $ZnPc$, $F_{16}ZnPc$ shows two different packing morphologies that can be described by the point-on-line coincident epitaxy with the substrate. The self-assembled behavior of $F_{16}ZnPc$ makes it a promising candidate for constructing the acceptor layer in OPV devices. We have presented results on the formation of vertical, face-to-face and edge-to-edge $F_{16}ZnPc$ - $ZnPc$ heterojunctions, which could be instrumental in developing a more thorough understanding of molecular electronic structure and charge transfer behavior at organic-organic heterointerfaces.

7 Electrostatic Screening Mediated by Interfacial Charge Transfer of Metal Phthalocyanine Molecules on the Deactivated Si(111)-B Surface

Despite the initial successes in the molecular growth of ZnPc and F₁₆ZnPc on deactivated Si(111)-B, molecular electronic structures and interfacial energy level alignment have not been well studied in these systems. In this chapter, using scanning tunneling microscopy and spectroscopy (STM/STS), we show that zinc phthalocyanine (ZnPc) and hexadecafluorinated zinc phthalocyanine (F₁₆ZnPc) both form ordered self-assemblies on the Si(111)-B $\sqrt{3} \times \sqrt{3}$ surface (Section 7.1), with the latter inducing a downward band bending in the bulk Si which is indicative of electron transfer from the F₁₆ZnPc molecules to the substrate. (Section 7.2). This charge transfer is further accompanied by a pronounced energy level variation of an occupied molecular state across the F₁₆ZnPc assembly, not observed in the unoccupied molecular orbital of F₁₆ZnPc nor in the molecular states of the ZnPc overlayer which does not undergo any charge transfer with the substrate. In Section 7.3, we attribute this observation to the inhomogeneous electrostatic screening of the intra-orbital Coulomb interaction in molecular adsorbates arising from the substrate boron distribution. This mechanism only impacts the molecular orbital that is directly involved in the interfacial charge transfer process discussed in Section 7.4. This chapter is adapted from the References [71,93] *A. Tan et al., The Journal of Chemical Physics* **146** 052809 (2017) and *A. Tan et al., Physical Review B* **96** 035313 (2017).

7.1 Geometric Structures of Molecular Overlayers

In the following discussion, the Si(111)-B $\sqrt{3} \times \sqrt{3}$ surface is abbreviated as Si(111)-B. Figure. 7-1 shows the STM topography images of the Si(111)-B, and the ZnPc and F₁₆ZnPc overlayers grown on this supporting substrate. As illustrated in Figure. 7-1a-b, the atomically smooth Si(111)-B surface is formed by the segregation of boron atoms in the third atomic layer

which substitute Si at the S_5 sites.[118] During this process, the trivalent boron atoms deplete electrons from the dangling bonds of the topmost Si adatoms, leading to a deactivated surface with large surface band gap as displayed in Figure 7-2a. The chemical inertness and atomic flatness of the surface makes Si(111)-B an ideal template for exploring the formation of organized organic molecular assemblies on inorganic substrates.

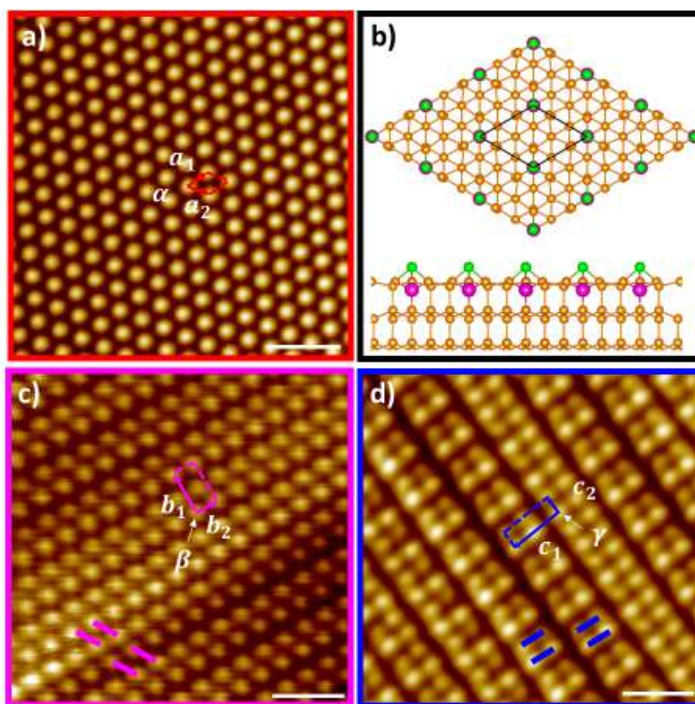


Figure. 7-1: Structure of deactivated Si(111)-B, ZnPc and F16ZnPc molecular layers

STM topography images of (a) Si(111)-B ($V_s = 2$ V, $I_t = 5$ pA), (c) ZnPc ($V_s = 1.8$ V, $I_t = 60$ pA), and (d) F₁₆ZnPc ($V_s = 2$ V, $I_t = 5$ pA) taken at 77K. Scale bars represent 2 nm. Lattice parameters of the three unit cells are given by: (a) $a_1 = a_2 = 0.665 \pm 0.005$ nm, $\alpha = 60^\circ$, (c) $b_1 = 1.23 \pm 0.01$ nm, $b_2 = 0.67 \pm 0.01$ nm, $\beta = 92 \pm 1^\circ$, (d) $c_1 = 1.56 \pm 0.02$ nm, $c_2 = 0.58 \pm 0.01$ nm, $\gamma = 89 \pm 1^\circ$. (b) Schematics of Si(111)-B in the top view (top) and side view (bottom), adapted from Ref. 30. The free radicals in the Si adatoms are deactivated by boron atoms located on the 3rd atomic layer directly beneath the adatoms.

Self-assembly of ZnPc and F₁₆ZnPc molecular adsorbates into monolayers with well-defined epitaxial registration to the Si(111)-B substrate is guided by the delicate balance between the molecule-molecule and molecule-substrate interactions.[71,113] As shown in Figure 7-3, both

assemblies adopt a tilted molecular configuration. This is owing to the corrugated surface potential landscape of Si(111)-B, born from the relatively large lattice constant of the surface, and the comparable strength of the molecule-molecule and molecule-substrate binding energies, leading to the molecules sacrificing a portion of the surface adsorption energy to maximize the $\pi - \pi$ intermolecular interaction with the increase of coverage.[112] Furthermore, geometric structures as illustrated in Figure 7-3 reveal that ZnPc overlayer adopts an incommensurate epitaxial registration to the Si(111)-B surface, while F_{16} ZnPc forms a point-on-line coincident structure. The distinct epitaxial relationship between the molecular overlayers and the substrate surface gives rise to the contrast variation observed in the STM topography images (Figure. 7-1c-d and Figure 7-3).[112] Lastly, as discussed earlier, molecular electronic structures are subjective to its electrostatic environment. The uniform molecular packing and molecular orientation as realized in the ZnPc and F_{16} ZnPc structures on the Si(111)-B surface, thus, uniquely allows for the disentanglement of the electrostatic effect of the substrate from that of the neighboring molecules.

7.2 Electronic Structure of the deactivated Si(111)-B surface and molecular assemblies

7.2.1 STS of the deactivated Si(111)-B surface

Figure 7-2(a) shows the characteristic STS curves taken on the ZnPc monolayer, the F_{16} ZnPc monolayer, and the Si(111)-B supporting substrate with colors corresponding to the outlines of the images shown in Figure. 7-1. To understand the STS curves and the associated molecular electronic features, we first look into the band structure of the Si(111)-B surface. The dangling bond deactivation process leads to the formation of two unoccupied surface states, SS1 and SS2, as well as occupied surface states that originate from the Si(adatom)-Si(second layer) and Si(second layer)-B(third layer) backbonds.[266,278-281] These backbond states are positioned at least 0.56 eV below the valence band maximum (at the Γ point), depending on the

location in k-space.[279] Thus, due to the overlap between the occupied surface states and the Si bulk valence states, the precise rise of the filled density of states is extremely sensitive to the STS set points and consequently the tip-sample distance. For instance, at a large tip-sample distance (controlled by the voltage and current set points before the STM feedback is disabled), we see a rise of the filled DOS at $\sim -0.5V$ (Figure 7-2a), suggesting that the surface states are the primary contributing factor to the STS spectra. However, when the tip-sample distance is small, the DOS of the bulk Si valence band becomes the predominant factor, causing the DOS to rise near the Fermi level which is expected for the degenerately boron-doped Si sample, as shown in Figure 7-7c. It is important to note, however, that the small tip-sample distance as established in Figure 7-7c is experimentally difficult to realize in molecular assembly studies. Because of the low electrical conductivity of the molecular overlayer, a relatively large tip-sample distance has to be utilized to prevent any damage to the molecular structures and the tip.

On the positive side of the spectrum, in contrast, we observe an overall consistent rise of the DOS features regardless of the tip-sample distance (Figure 7-2a vs. Figure 7-7c). To address the nature of these states, we first take a close look at the band structure calculated by density functional theory (DFT).[279] It shows that SS1 is the lowest lying state around the Γ point, followed by the SS2 state that is convoluted with the bulk conduction band. Since the effective tunneling decay constant described by Equation (5-20), is a function of the parallel momentum, it is expected that the larger the $k_{||}$, the weaker its contribution to the overall tunneling spectra.[254,255] Therefore, although the bulk states will be probed at the small tip-sample distance as we have discussed earlier, we still observe the rise of SS1 first, owing to the much stronger tunneling into the states around the Γ point where $k_{||}$ is minimum. This results in no noticeable change in the rise of the empty states between Figure 7-2a and Figure 7-7c. Furthermore,

Gaussian fitting of the spectral feature, shown in Figure 7-4, suggests that the SS1 and SS2 states are centered at $\sim 1.4\text{V}$ and $\sim 1.8\text{V}$, respectively, which is consistent with the previous report.[278]

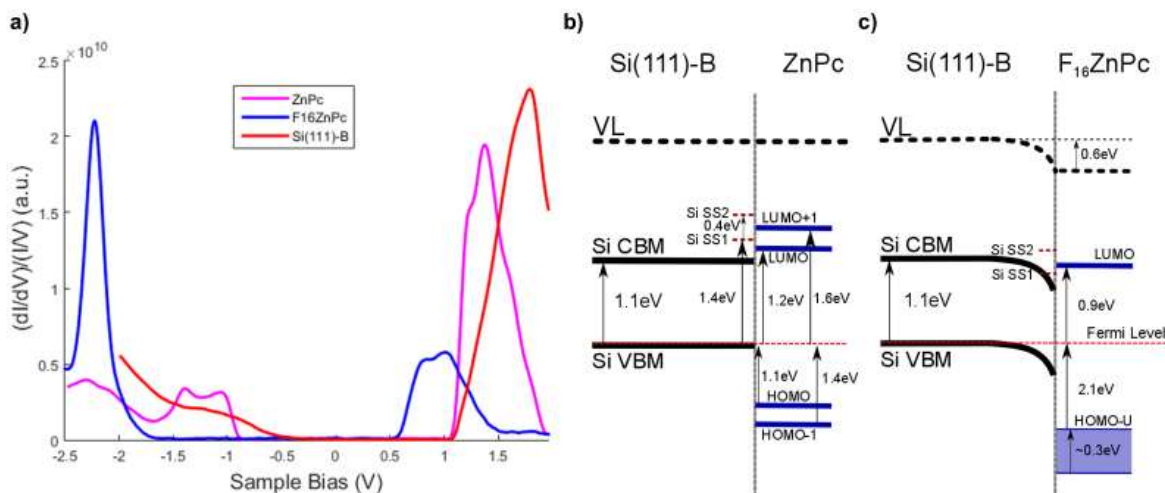


Figure 7-2: Electronic Structure of ZnPc and F₁₆ZnPc on deactivated Si(111)-B

(a) STS data taken on Si(111)-B (set point: $V_s = -2\text{ V}$, $I_t = 100\text{ pA}$, red), ZnPc molecular overlayer ($V_s = -2\text{ V}$, $I_t = 100\text{ pA}$, magenta) and F₁₆ZnPc molecular overlayer ($V_s = 2\text{ V}$, $I_t = 50\text{ pA}$, blue). Energy band diagram for (b) Si(111)-B/ZnPc and (c) Si(111)-B/F₁₆ZnPc. Energy levels are defined by STS peaks unless specified. For simplicity, it is assumed that there is no interface dipole so that the vacuum level is continuous at the F₁₆ZnPc/Si(111)-B hetero-interface. The energy range ($\sim 0.3\text{ eV}$) of the occupied molecular orbital of the F₁₆ZnPc overlayer, as provided in (c), is derived based on the analysis of Fig. 3(b).

7.2.2 Electronic Structures of Molecular Assemblies

When molecules are deposited on the Si(111)-B surface, however, electrons will tunnel into the molecular overlayer first then into the supporting substrate during the STM/STS measurements. Provided the surface states of the underlying Si(111)-B can be probed through the molecular layer, they will serve as the reference during the analysis of interfacial band alignment as the energy levels of these states are fixed relative to the band edges of the bulk Si. For the ZnPc spectrum displayed in Figure 7-2a, Gaussian analysis reveals four distinct peaks which altogether construct the main DOS feature on the positive sample bias as seen in Figure 7-4. The locations of

these unoccupied density of state peaks are summarized in Table 1. Specifically, those located at $1.37 \pm 0.04 V$ and $1.81 \pm 0.04 V$ align with the SS1 and SS2 surface states of the bare Si(111)-B substrate, suggesting that the adsorption of the ZnPc overlayer does not disturb the charge distribution in the substrate. This is consistent with the earlier DFT calculation which demonstrates a negligible charge transfer or charge redistribution between ZnPc and Si(111)-B.[112] Therefore, the ZnPc/Si(111)-B hetero-interface is anticipated to follow vacuum-level alignment, as depicted in Figure 7-2b. Additionally, with the aid of differential conductance (dI/dV) mapping which reveals the spatial distribution of the density of states, we attribute the other two peaks centered at $1.20 \pm 0.03 V$ and $1.59 \pm 0.06 V$ to the LUMO and LUMO+1 of the ZnPc molecular overlayer, respectively. The dI/dV map of the LUMO+1 molecular orbital is illustrated in the inset of Figure 7-5a, which shows distinctly different features from the DOS distribution of the SS1 and SS2 surface states (see Figure 7-3). The asymmetry appearance of molecular lobes in each individual ZnPc molecule is likely a result of the degeneracy lifting of the molecular orbitals, resulting in a C4 to C2 symmetry reduction.[94,95,282,283]. Note that due to the tilted molecular configuration where only the top two pyrrole rings are visualized, we do not expect to observe the nodal planes in the dI/dV map as for the flat lying molecules.

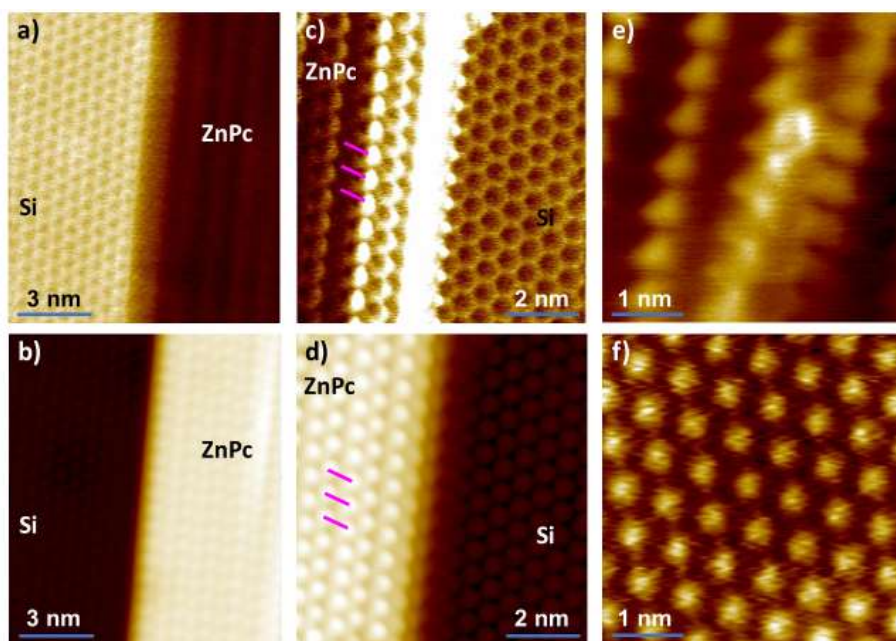


Figure 7-3: dI/dV Maps of LUMO+1 of ZnPc overlayer and Si(111)-B Surface State.

Simultaneously taken STM topography and dI/dV map of partially covered ZnPc areas obtained at 77K: (a,b) $V_s = 1.7$ V, $I_t = 100$ pA and (c,d) $V_s = 1.6$ V, $I_t = 50$ pA; dI/dV maps of (e) ZnPc overlayer ($V_s = 1.4$ V, $I_t = 100$ pA) and (f) bare Si ($V_s = 1.3$ V, $I_t = 30$ pA). Hexagonal features on the bare Si areas correspond to the spatial variation of Si SS1 and SS2. Alternating contrast patterns in the ZnPc areas correspond to the expected distribution of the molecular orbitals. Individual molecules has been marked in (c) and (d) for clarity. Due to the lack of hexagonal features on the ZnPc molecule overlayer, we conclude that the attenuated spatial DOS distribution of the Si SS1 and SS2 is overwhelmed by the spatial DOS distribution of the molecular orbitals themselves.

Regarding the $F_{16}\text{ZnPc}$ spectrum, the entire STS curve appears to be deviated to more negative energies (sample biases) in comparison to that collected on the ZnPc or the bare Si(111)-B surface. Similar to the previous discussion, we can apply a Gaussian analysis to deconstruct the unoccupied DOS feature residing within the Si(111)-B surface gap as seen in Figure 7-4. Among the three Gaussian-fit peaks centered at 0.73 ± 0.03 V, 0.94 ± 0.03 V, and 1.16 ± 0.05 V, peak 1 and 3 share the same separation in energy, within experimental error, as that observed between the SS1 and SS2 states of the bare Si(111)-B surface. If we assume that these two peaks are indeed associated with the surface states of the substrate, their shift towards the Fermi level (~ 0.6 eV)

provides direct evidence of downward band bending in the bulk Si, as illustrated in Figure 7-2c. Electron transfer from $F_{16}ZnPc$ molecules to the Si substrate is anticipated to be the origin of this band bending. It is worth pointing out that the Fermi level (at zero sample bias in the STS spectra) represents the charge equilibrium of the entire system and therefore is determined by the bulk Si regardless of molecular adsorption on the surface. Lastly, the electron density distribution of peak 2 as revealed in the dI/dV map (Figure 7-5b) displays an alternating contrast along the $F_{16}ZnPc$ molecular stripes, very much alike the topography of the overlayer discussed earlier in Chapter 6. This suggest that peak 2 corresponds to a molecular orbital, and the distinctive molecular registration to the Si(111)-B surface gives rise to the observed contrast in the dI/dV map.[71]

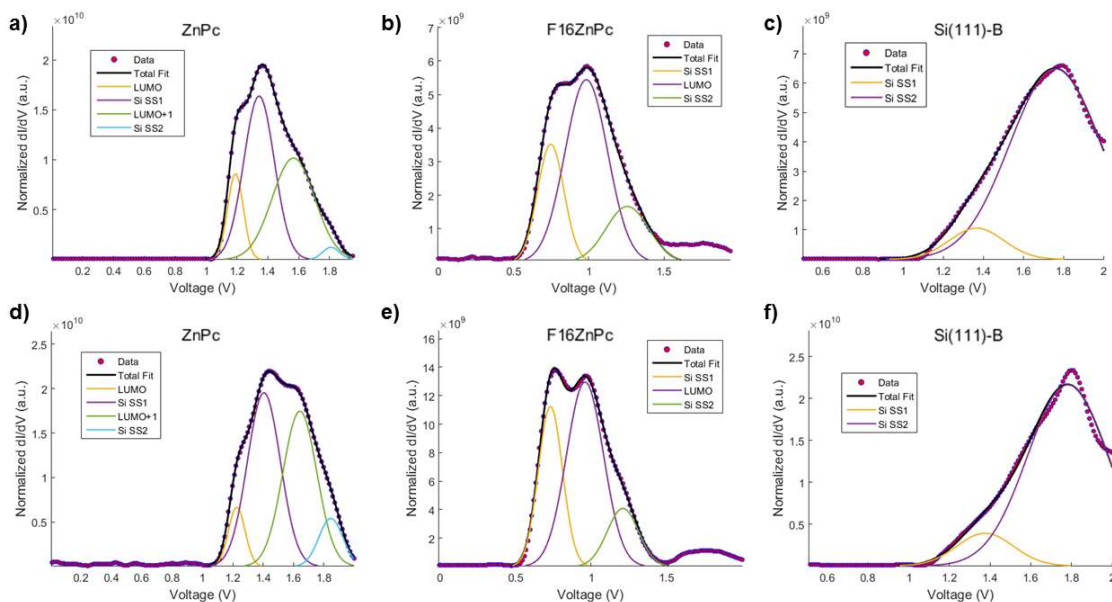


Figure 7-4: Gaussian Fitting of Unoccupied Spectral Feature of ZnPc, $F_{16}ZnPc$ and deactivated Si(111)-B STS spectra

Gaussian Peak fitting of the ZnPc spectrum (a,d), $F_{16}ZnPc$ spectrum (b,e), and the bare Si(111)-B spectrum (c,f), was done using the fitting function in MATLAB. The spectra used for the Gaussian fits in (a-c) and (d-f) are reproduced from Figure. 7-1 and Figure 7-6b respectively. The two sets of curves show good agreement with each other. Gaussian fitting of the Si curve was found to not be as good as that of ZnPc and $F_{16}ZnPc$ fits. This is likely a result of the convolution between the Si SS1, SS2 surface states and the bulk conduction band.

Thus far, our discussion has been concentrated on the band structure analysis guided by the SS1 and SS2 states of the Si(111)-B surface. Next, we will examine how the differentiating interfacial charge transfer behavior between ZnPc/Si(111)-B and F₁₆ZnPc/Si(111)-B impacts the occupied molecular states. The inset of Figure 7-5a shows the dI/dV maps of ZnPc taken at -1.0V and -1.5V, which illustrate asymmetric molecular features similar to those observed for the dI/dV map associated with LUMO+1. Figure 7-5a also illustrates the overlay of the STS curves taken on multiple locations of the ZnPc overlayer. Highly consistent features with the DOS peaks overlapping in energy positions and only differing slightly in intensity are observed. Intriguingly, when curves taken on the F₁₆ZnPc overlayer are put together, significant peak position variation as large as several hundred meV can be identified for the occupied molecular orbital displayed on the negative sample bias, whereas the empty states, *e.g.*, LUMO, SS1 and SS2, remain fixed (Figure 7-5b). More examples of this phenomenon can be found in Figure 7-6. It is worth mentioning that the STS curves are taken in areas away from the assembly edges to prevent the disturbance of the local electrostatic environment by the reduced molecular coordination at the edges.[39]

A natural question that arises is how to account for the spatial variation of the occupied molecular level in the F₁₆ZnPc monolayer which is not observed in the LUMO state or in the molecular states of the ZnPc layer. As discussed earlier, the electronic structure of organic molecular thin films can be modulated by the molecular orientation, packing, or local ordering.[29,30,33,162,284] However, as shown in the STM images (Figure. 7-1) as well as in an earlier study,[71] F₁₆ZnPc molecules are packed uniformly with a universal tilted orientation in the overlayer. Molecular orbital levels may also move relative to the substrate Fermi level by the formation of an interface dipole.[43,285] Nevertheless, if this would be the case, HOMO and

LUMO should shift rigidly together which is different from what has been observed in the STS spectra in Figure 7-5b.

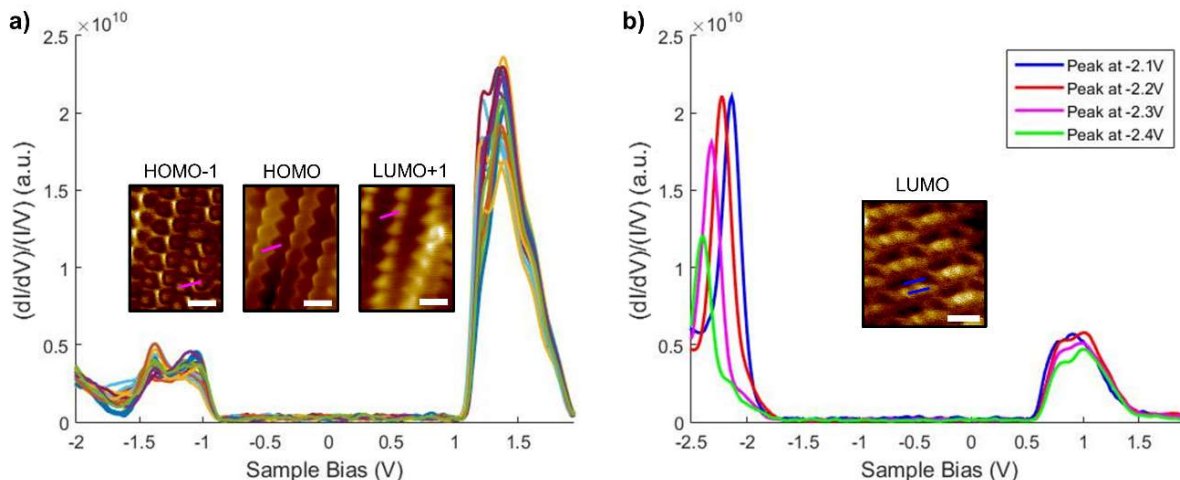


Figure 7-5: Reproducibility of ZnPc and F16ZnPc spectra taken on deactivated Si(111)-B

(a) Multiple STS spectra (set point: $V_s = -2$ V, $I_t = 100$ pA) taken on various locations of the ZnPc overlayer. No peak variation is observed among the curves. The positive DOS feature is a convolution of the LUMO, LUMO+1 and Si surface states. The two well resolved occupied molecular states are located at ~ -1.4 V and -1.1 V. Inset: dI/dV map of ZnPc obtained at ($I_t = 100$ pA): -1.5 V (left), -1 V (middle), 1.4 V (right). Magenta lines denote individual ZnPc molecules. (b) Four characteristic STS spectra (set point: 2 V, 50 pA) taken on multiple locations of the F₁₆ZnPc overlayer. The positive DOS feature that remains consistent (centered at ~ 1 V) is a convolution of the Si surface states and molecular LUMO. The occupied molecular orbital observed on the negative sample bias, however, is shifted in energy position. Inset: dI/dV map of F₁₆ZnPc at 1 V, 50 pA. Blue lines denote individual F₁₆ZnPc molecules. Scale bars represent 1 nm.

Table 2: Averaged Gaussian-fit peak positions of the unoccupied DOS feature of Si, ZnPc and F₁₆ZnPc.

Error bars are derived from the standard deviation of peak positions from multiple data sets, taking the lock-in modulation voltage (26 meV) as the lower bound.

Material	Molecular Peak (V)	Si SS1 (V)	Molecular Peak (V)	Si SS2 (V)
ZnPc	1.20 ± 0.03	1.37 ± 0.04	1.59 ± 0.06	1.81 ± 0.04
F ₁₆ ZnPc	-	0.73 ± 0.03	0.94 ± 0.03	1.16 ± 0.05
Si(111)-B	-	1.40 ± 0.04	-	1.79 ± 0.03

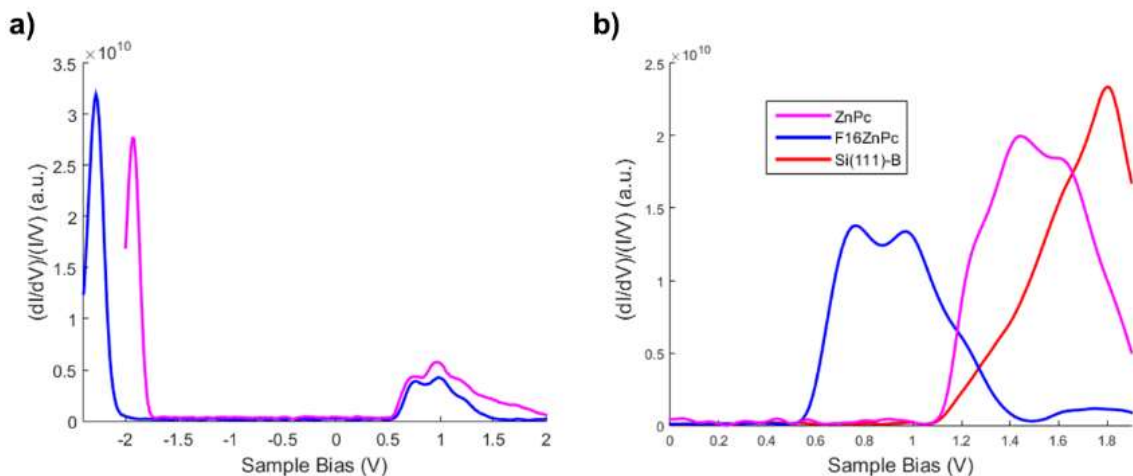


Figure 7-6: Additional STS data taken on ZnPc and F16ZnPc on deactivated Si(111)-B

(a) STS curves taken on multiple locations of the F₁₆ZnPc molecular overlayer under a different tip condition from the STS shown in Fig. 1 at the set point of $V_s = 1.8$ V, $I_t = 50$ pA. It can be seen that the HOMO-U peak exhibits significant spatial variation in energy position due to the inhomogeneous subsurface boron distribution, while the shape and peak position of the LUMO remains consistent. This is a universal phenomenon observed on the F₁₆ZnPc overlayer on Si(111)-B, which does not depend on the condition of the probing tip. (b) STS on the F₁₆ZnPc overlayer ($V_s = -2.5$ V, $I_t = 50$ pA), the ZnPc overlayer ($V_s = -2.5$ V, $I_t = 50$ pA), and the bare Si(111)-B surface ($V_s = -2$ V, $I_t = 50$ pA). The tip condition has remained the same on all three surfaces. The overall features are in agreement with those presented in Figure 7-2, but the relative peak intensity has been modulated by the lock-in amplifier sensitivity setting.

7.3 Inhomogeneous substrate screening

Another potential contribution to the tailoring of the molecular electronic structure is electrostatic screening from the substrate.[37-39,163] The thermal annealing process for creating the deactivated Si(111)-B surface inevitably introduces an inhomogeneous distribution of boron substituents in the bulk. Since the dielectric constant varies with doping concentration in degenerately doped Si,[286,287] the subsurface boron inhomogeneity can result in a modulated local electrostatic environment for molecular adsorbates which may consequently influence their electronic structures. To illustrate this correlation, we first explore the spatial variation of the subsurface boron distribution in the Si(111)-B substrate. Although STM is a surface sensitive

technique, imaging of subsurface dopants is feasible, especially when the surface states lie in energies that do not mask the bulk dopant states.[266,288-290]

Figure 7-7a and Figure 7-7b displays the STM topography image of the Si(111)-B surface taken at -0.1V and 1.3V, respectively. Hillocks as pointed by the red arrow are observed in the filled state image, which correspond to the more or less dimmer areas in the empty state image. To explain this contrast that is likely related to the boron distribution in the bulk, we further perform site-specific STS (Figure 7-7c) at a small tip-sample distance (set point: $V_s = -0.5$ V, $I_t = 300$ pA) where the tunneling current is more sensitive to the bulk states. The STS taken on the hillock in Figure 7-7a) displays an earlier rise of the filled state and a later rise of the empty state with respect to the Fermi level, in comparison to the spectrum on the dark area (blue arrow). This phenomenon is expected to arise from the Coulomb potential of the thermally ionized boron dopants which inhibit/enhance the downwards/upwards tip-induced band bending during the filled/empty state tunneling, as illustrated in the inset of Figure 7-7c. Consequently, areas with higher concentration of subsurface boron will appear brighter in the filled state images due to the larger integrated density of states, and vice versa. Since the Coulomb potential can be defined as:

$$V = \frac{q}{4\pi\epsilon_0\epsilon r} e^{-r/r_s} \quad (7-1)$$

where r_s is the screening length within the bulk. This potential is attenuated rapidly by the screening factor in degenerately doped Si,[291] the hillocks are expected to correspond to boron atoms near the surface, *e.g.*, in the fourth atomic layer, which will spread into more extended but less protruding regions when boron atoms are positioned in deeper layers. It should also be noted that due to the screening effect the magnitude of the band bending modulated by the Coulomb potential is rather small (shown in Figure 7-8), which falls within the uncertainty of the Gaussian fits as listed in Table 1. As a result, when the STS curves are taken on the Si(111)-B surface at a

large tip-sample distance and over a wide voltage span, no noticeable modulation on the apparent band gap or DOS features can be identified between the boron-rich and -deficient areas, as shown in Figure 7-7d.

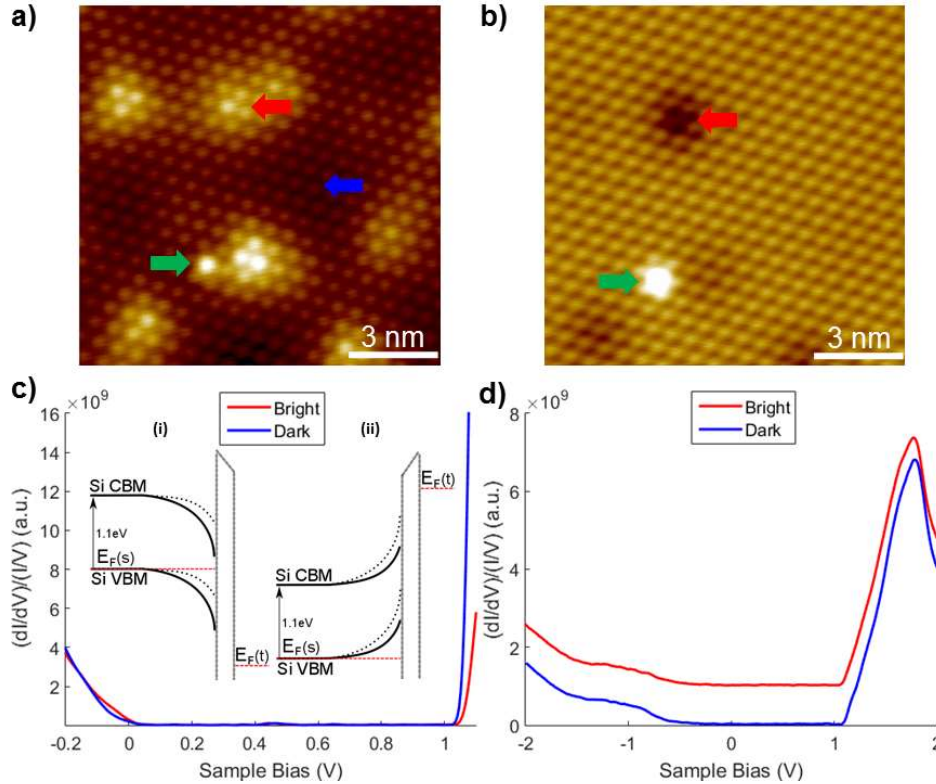


Figure 7-7: Electronic Structure of subsurface boron defects on deactivated Si(111)-B

STM topography image of Si(111)-B obtained at 77K at (a) $V_s = -0.1$ V, $I_t = 100$ pA and (b) $V_s = 1.3$ V, $I_t = 300$ pA. Subsurface boron dopant (beyond the 3rd atomic layer) and surface dangling bond defect are indicated by the red and green arrows, respectively. The blue arrow points to a region with low concentration of subsurface boron. (c) Averaged STS spectra taken at $V_s = -0.5$ V, $I_t = 300$ pA on the bright and dark regions indicated by the red and blue arrows in (a), respectively. Insets (i) and (ii) illustrate the tip induced band bending modulated by the Coulomb potential of thermally ionized boron dopants under the filled-state and empty-state tunneling conditions, respectively, where the dotted line in the schematics refers to the band structure on the bright areas (hillocks) with accumulated subsurface boron and the solid line refers to the dark areas where the boron accumulation is minimal. (d) STS taken at $V_s = -2$ V, $I_t = 100$ pA on bright (red) and dark (blue) areas as indicated by colored arrows in (a). The curves are vertically offset for clarity, and there is no noticeable modulation on the apparent band gap or density of states features.

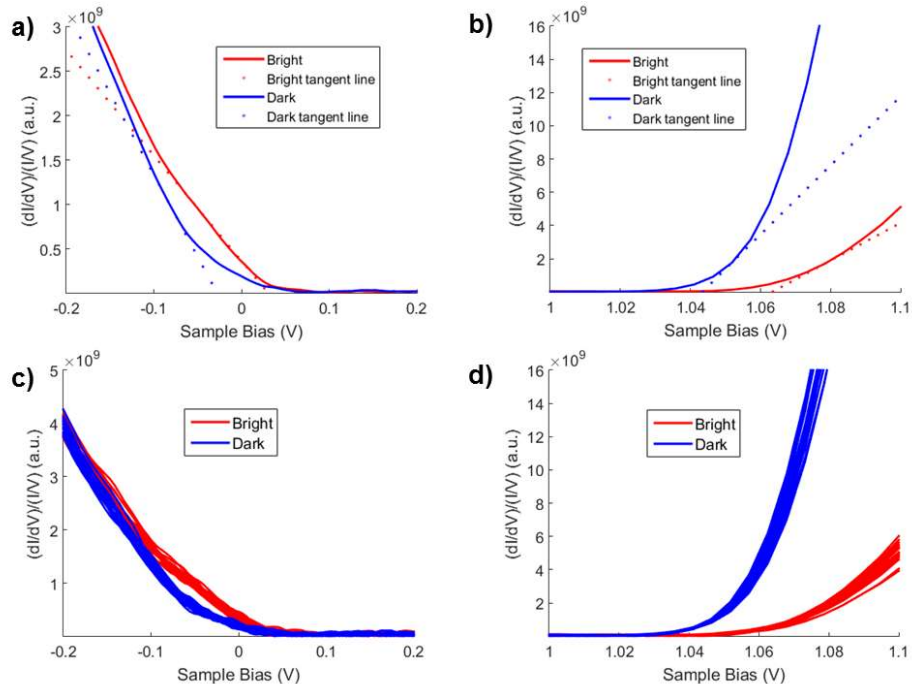


Figure 7-8: Coulomb-potential induced band bending analysis

Tangent line fitting of (a) filled states and (b) empty states of the STS shown in Figure 4(c). Red and blue lines correspond to the bright (hillock) and dark areas on the filled state image of the Si(111)-B surface, which represent subsurface boron-accumulated and -deficient regions, respectively. The dotted blue and red lines represent the tangent fitting to the solid curves, where the intercept points are at -0.03 V/1.04 V and 0.03 V/1.06 V for the negative/positive DOS rises, respectively. Individual curves that contribute to the averaged spectra presented in (a) and (b) are overlaid in (c) and (d) respectively, which shows that the magnitude of band bending induced by the Coulomb potential of subsurface boron, although small, is reliable.

In order to visualize the spatial variation of the occupied molecular level in the $F_{16}ZnPc$ overlayer, we image the $F_{16}ZnPc/Si(111)$ -B surface at -2.5V. As shown in Figure 7-9a, well-pronounced inhomogeneity is observed. This is strikingly different from the uniform features presented in the STM topography image of the same area at a positive sample bias shown in Figure 7-9b, which suggests that the contrast observed in Figure 7-9a is electronic in nature. We speculate that the inhomogeneous electrostatic screening by the Si(111)-B substrate is the origin of this phenomenon, as evidenced by the comparable length scale of the contrast variation between the filled-state image of the $F_{16}ZnPc$ overlayer and the bare Si(111)-B surface as seen in Figure 7-10.

Nevertheless, there is still one question that needs to be addressed. As depicted in Figure 7-5, the peak variation is neither observed in the LUMO of F₁₆ZnPc nor in the molecular states of the ZnPc overlayer which does not establish any charge transfer with the substrate. In order to reveal the underlying mechanism as to why the substrate screening only impacts the molecular orbital that is directly involved in the interfacial charge transfer process, a more thorough discussion on the charge transfer mechanism is required.

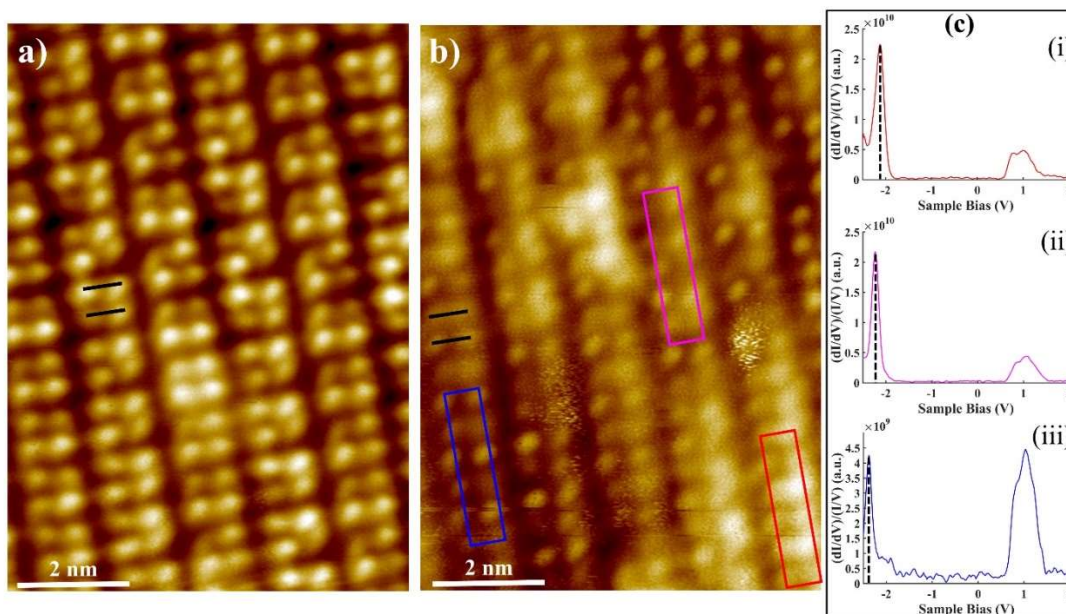


Figure 7-9: STS taken on areas of different contrast variation in the F₁₆ZnPc overlayer
 STM topography image of F₁₆ZnPc obtained at 77K at (a) $V_s = 2$ V, $I_t = 5$ pA and (b) $V_s = -2.5$ V, $I_t = 1$ pA. (c) Averaged STS spectra (setpoint: 2V, 50pA) taken on the corresponding color-outlined areas in (b). Brighter areas correspond to a SOMO/HOMO-U peak closer to the Fermi level. This corresponds to the enhanced image-charge screening as a result of the higher lying image-charge plane in areas of high subsurface boron density

7.4 Discussion

The interaction between metal phthalocyanine (MPc) and inorganic substrate can be mediated by the central transition-metal ion, which is typically very strong when the metal center possesses a singly-occupied d_z^2 orbital that can easily hybridizes with the protruding substrate

orbitals such as the $Ag-sp_z$ states or the p_z state of the Si adatoms on Si(111)-B.[96,112] Studies of the growth of CoPc on the Si(111)-B surface shows that this strong interaction leads to flat-lying molecules with limited assembly sizes. Owing to the fully filled d -orbitals associated with the Zn center, the formation of strong chemical bonds between molecule and substrate is prohibited in Zn-based Pc molecules as evidenced by the ability of ZnPc and $F_{16}ZnPc$ to form long-range ordered structures on the Si(111)-B surface. Note that the $F_{16}ZnPc$ overlayer displays a better epitaxial registration to the surface (point-on-line coincident in comparison to the incommensurate for the case of ZnPc) as a result of the additional electrostatic interaction due to interfacial charge transfer.[71,112,113,292,293] Nevertheless, the electronic characterization of the $F_{16}ZnPc$ overlayer has shown no indication of orbital hybridization such as the formation of interface states.[94,96,206,294] This leads us to conclude that $F_{16}ZnPc$ on Si(111)-B can be characterized as a weakly interacting system which is fundamentally different from a chemisorption scenario.

In weakly interacting systems, electrons tunnel in integer amounts between frontier molecular orbitals and the substrate states, typically described by the Integer Charge Transfer (ICT) model.[40,202,206] As the excess charge originating from the interfacial charge transfer results in the partial occupation of the specific molecular orbital involved in the ICT process, additional tunneling into this orbital, either by the extraction or injection of an electron, will lead to the splitting of the orbital into the singly occupied molecular orbital (SOMO), below the Fermi level, and the singly unoccupied molecular orbital (SUMO), above the Fermi level, that are energetically separated by the intra-orbital Coulomb repulsion.[96,163,164,202,211,213,295] It should be noted that the intra-orbital Coulomb repulsion will be necessarily larger than the intramolecular charging energy due to the more localized interaction between the incoming charge and the electron already present in the orbital. Specifically, in the $F_{16}ZnPc/Si(111)-B$ system, the

HOMO orbital of $F_{16}ZnPc$ is expected to be split into the SOMO/SUMO since electrons are transferred from molecules to the substrate. Another terminology for describing the split orbitals are HOMO and HOMO-U, which correspond to the SUMO and SOMO, respectively. The spatial variation of the SOMO/HOMO-U peak that is observed on the negative sample bias seems linked to the inhomogeneous screening effect from the subsurface boron distribution, whereas the SUMO/HOMO is likely positioned within the Si bandgap which prevents its observation due to the lack of resonant tunneling..[296,297]

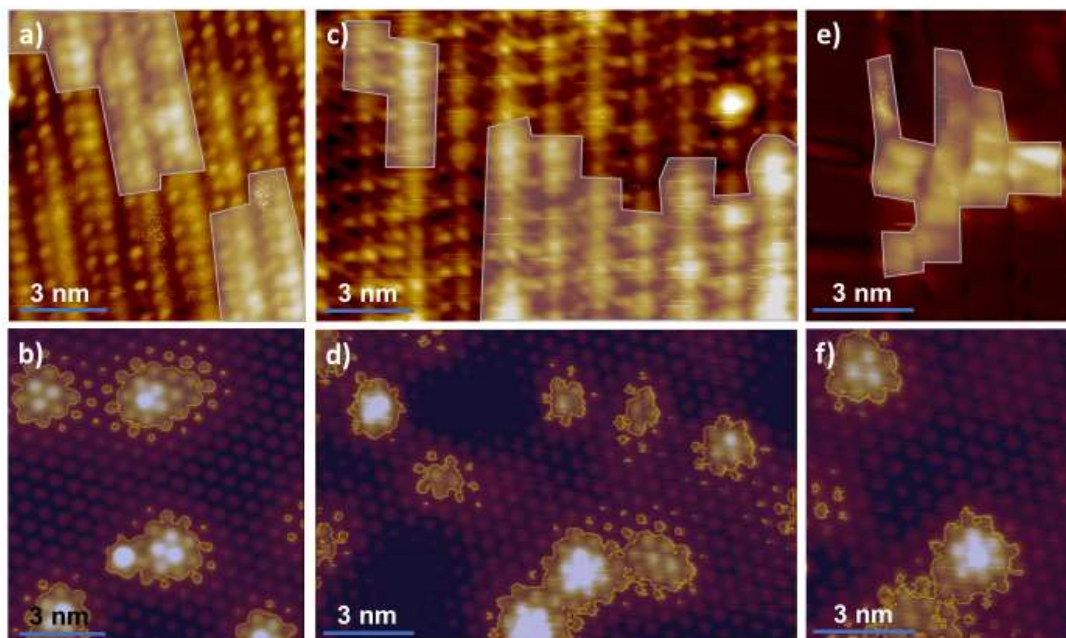


Figure 7-10: Comparison of Subsurface Boron Distribution to Filled-State Images of $F_{16}ZnPc$

STM topography images obtained at 77K of $F_{16}ZnPc$ ($V_S = -2.5V$; a) and c) on the top panels) and Si(111)-B ($V_S = -0.5 V$; b), d), and f) on the bottom panels). Significant contrast variation can be observed in the filled state images of both $F_{16}ZnPc$ and Si. Bright areas of Si indicative of close-lying boron dopants near the surface are shaded for clarity. (e) dI/dV map of $F_{16}ZnPc$ at the setpoint of $V_S = -2.3 V$, $I_t = 50 pA$. Inhomogeneous variation of the filled state images translates to variation in the dI/dV maps as well.

As has been described before, charging energy, U , will be attenuated by a variety of factors such as the substrate screening and polarization of neighboring molecules. The image charge

screening is one such effect and is dependent on the dielectric and image charge position of the particular substrate as described in Section 3.1. Note that the latter two are both substrate dependent. And in our system, areas of higher subsurface boron density are likely correlated to a more protruding image plane[178], resulting in a greater screening effect on the intra-orbital Coulomb interaction which moves the SOMO/HOMO-U peak closer to the Fermi level (see Figure 7-10). However, this inhomogeneous substrate screening should also perturb intramolecular charging energy, and thus the apparent band gap of the molecular overlayer, which is contradictory to the experimental observation of the stationary position of the F₁₆ZnPc LUMO as well as the unperturbed ZnPc band gap. Different from the probing of SOMO/HOMO-U which changes the charge state of the F₁₆ZnPc molecule from +1 to +2, the screening modulation is expected to be weaker on the ZnPc molecular levels and F₁₆ZnPc's own LUMO due to the smaller charge pre-factor in the image-charge equation. In addition, the polarization response of molecular adsorbates to the image-charge field is expected to reduce the magnitude of the substrate screening.[170] The more delocalized nature of F₁₆ZnPc's LUMO and ZnPc's molecular orbitals will result in a greater polarizability[268,298-300], as compared to the F₁₆ZnPc's HOMO, leading to a larger correction term. We speculate that the combination of these two effects is responsible for the overall smaller modulation of the substrate screening on the aforementioned orbitals, which renders SOMO/HOMO-U of the F₁₆ZnPc overlayer the only observed energetically varied orbital. Nevertheless, the precise determination of location-dependent q', z_o , as well as the polarization response which collectively impacts the screening reduction on U, will require extensive theoretical investigations in the future.[34,42,170,301]

7.5 Conclusion

In conclusion, we have demonstrated that $F_{16}ZnPc$ molecular assemblies exhibit charge transfer with the Si(111)-B substrate, as corroborated by the downward band bending in the bulk Si. When the electronic structures of the $F_{16}ZnPc$ and $ZnPc$ monolayers are compared, a noticeable variation in the energy level of occupied molecular orbital is observed across the $F_{16}ZnPc$ overlayer, which is in sharp contrast to the constant energy levels of the $ZnPc$ orbitals and $F_{16}ZnPc$'s own LUMO. This is hypothesized to originate from the subsurface boron distribution in the Si(111)-B substrate, which causes an inhomogeneous electrostatic screening of the intra-orbital Coulomb interaction in $F_{16}ZnPc$ due to the partially filled HOMO born from the interfacial charge transfer process.

In terms of integrating organic molecular systems with mainstream inorganic semiconductors in device architectures, this observation puts a strong emphasis on the homogeneity of semiconducting substrates. Although molecular thin films can be grown into long-range ordered structures with a high crystallinity on Si(111)-B owing to the deactivated surface with low defect density, variations in the subsurface dopant concentration, even a few atomic layers deep, can have drastic impact on the molecular electronic structures and thereby the charge injection/collection behaviors that are of paramount importance to the operation of organic and molecular electronic devices.

8 Interfacial Charge Transfer Enhancement via Molecular Heterostructures Formation on Electronically Corrugated Boron Nitride

Studies of interfacial energetics between organic (O) molecules and inorganic (I) substrate, as well as between molecular donor and acceptor identities, have raised enormous interest from both the fundamental perspectives and the technological relevance. In Chapter 3, we discussed how these heterointerfaces play a critical role in determining the efficiency of a variety of organic electronic devices such as organic light emitting diodes (OLEDs), organic photovoltaics (OPV), and organic field effect transistors (OFETs). Additionally, (bulk) molecular solids of donor-acceptor charge transfer complexes could exhibit rich physical properties with complex phase diagram and/or high carrier mobility originating from the intermolecular charge transfer as noted in Chapter 4.[233-237] For thin film applications of this class of material, it is crucial to address the energy level alignment and charge transfer behaviors at the O-O and O-I heterointerfaces. [43,44,95,203,208,302-304] These donor-acceptor binary heterostructures are of particular concern when considering strongly interacting surfaces such as metal substrates, as hybridized interface states could dominate the properties of these systems.[305] On the other hand, molecules on weakly interacting substrates can undergo integer charge transfer (ICT) with a dynamic charging configuration as noted in Section 3.3.2 with the electrostatics of the system playing a critical role in determining the percentage of charged molecules in the film, where the charge state of each individual molecule is strongly dependent on the arrangement of neighboring molecules at any given moment in time.[202]

In this work, using scanning tunneling microscopy/spectroscopy (STM/STS) and finite element analysis, we investigate the charge transfer behavior and interfacial energetics in molecular structures composed of zinc phthalocyanine (ZnPc) and/or its fluorinated counterpart,

hexadecafluorinated zinc phthalocyanine ($F_{16}ZnPc$), on monolayer hexagonal boron nitride (h-BN) grown on Cu(111). Due to its insulating nature, h-BN serves to decouple the molecular overlayer from the metallic substrate, which prevents strong hybridization at the interface and confines the system to the ICT regime.[156,205,306-308] $ZnPc$ and $F_{16}ZnPc$ are chosen as the donor and acceptor molecular species of interest due to their geometric similarity, the inert metal center which further reduces possible interaction pathways with the substrate, and their predicted ability to exhibit donor-acceptor intermolecular charge transfer characteristics when packed edge-to-edge. We show that these two molecules can both form weakly interacting self-assembled structures on h-BN/Cu(111) surface (Section 8.1) with minimal interfacial charge transfer (Section 8.2), and the co-deposition of the two molecular species onto the substrate yields a checkerboard binary structure that is adopted to minimize the F-F repulsion between $F_{16}ZnPc$ molecules. (Section 8.1) In comparison to those of the pure phases, the electronic structure of $F_{16}ZnPc$ in the binary system, discussed in Section 8.3, is shifted down in energy, whereas the energy levels of $ZnPc$ are upshifted toward the vacuum level. This observation is attributed to the formation of interface dipoles arising from the enhanced charge transfer between the $F_{16}ZnPc$ constituents and the substrate in the binary blend, which leads to an overall vacuum level shift of the entire molecular layer. In Section 8.4, we combined our data in conjunction with finite element analysis, to conclude that the increased charge transfer interaction originates from the greater Madelung energy analog of the binary superstructure, which stabilizes the charged $F_{16}ZnPc$ molecules against the intermolecular coulomb repulsion. This study contributes to a better understanding of the charge transfer processes in donor-acceptor molecular superstructures in the presence of a weakly interacting substrate. Parts of this chapter are adapted This chapter is adapted from the References *A. Tan et al., Physical Review B (2019, under review)*.

8.1 Growth of ZnPc and F₁₆ZnPc on h-BN/Cu(111)

Self-assembly of single-component or binary molecular monolayers on the surface of a clean metal has been extensively explored in the past. [55,94,195,305,309-315] As discussed previously, often, chemical interaction with the formation of chemical bonds or weak hybridization between molecular orbitals and the continuum states of the metallic substrate emerges at the hetero-interface, leading to the complex sharing of electrons and/or hybridized interface states which can dominate the characteristics of molecular thin films. [43,94,195,196,199,202,305] Furthermore, the ‘push-back’ or Pauli repulsion effect where the electron tails of the clean metal surface are pushed back into the metal by molecular adsorbates effectively reducing the metal work function and thus modulates the positions of the frontier molecular orbitals relative to the substrate Fermi level.[40,43,179] Since the ‘push-back’ effect is highly sensitive to the adsorption height of molecular adsorbates, any perturbation of the height or the charge reorganization in the binary blend is expected to notably modify the interfacial energy level alignment.[312] Thus, to confine the system to the weakly interacting regime and to largely preserve the intrinsic properties of molecular structures, a decoupling layer will be desirable. Inorganic salts and 2D materials, such as sodium chloride, has been exploited for this purpose.[164,202,313] More recently, h-BN monolayer has also demonstrated its capabilities in decoupling molecular adsorbates from the metallic substrate, yet it offers the additional advantage of imposing periodic electronic modulations to the molecular overlayer through Moiré patterns.[156,205,306,307,316,317]

Figure 8-1a shows the Moiré pattern of h-BN on Cu(111), which is hexagonal in nature but the exact periodicity of the pattern depends on the specific azimuthal rotation of the h-BN domain with respect to the Cu(111) surface.[306,307] The growth of molecular species on h-BN/Cu(111) proceeds with preferential nucleation on the hill locations of the Moiré pattern at low coverage,

which eventually expands outwards to form a molecular overlayer (Figure 8-2). Figure 8-1b-d show the zoomed in STM images of the single-component ZnPc assembly, F₁₆ZnPc assembly, and the ZnPc-F₁₆ZnPc binary heterostructure, respectively. The pure F₁₆ZnPc overlayer on h-BN/Cu(111) proves to be less ordered with defects and vacancies more readily formed in comparison to ZnPc assemblies, along with the coexistence of two different azimuthal molecular orientations termed as α - and β -orientations and denoted by the blue and red arrows, respectively. The alternative molecular orientations can help minimize the repulsive interaction between the fluorine groups of adjacent F₁₆ZnPc molecules, as has been reported in F₁₆CuPc assemblies formed on various substrates including Cu(111) and HOPG.[71,77,121,302,318,319] In the heterostructure, molecules adopt a checkerboard pattern where F₁₆ZnPc occupy alternating sites within the ZnPc lattice. This geometric configuration arises from the hydrogen bonding interaction between ZnPc and F₁₆ZnPc molecules, which also suppresses the F-F repulsion between F₁₆ZnPc molecules as compared to that of the pure F₁₆ZnPc film as seen in Figure 8-2. Like the single-component molecular layers, packing within the binary structures is not perturbed by the h-BN/Cu(111) Moiré pattern which is geometrically flat resulting from the weak interaction at the interface of h-BN and Cu substrate.[156,306,307,316,317]

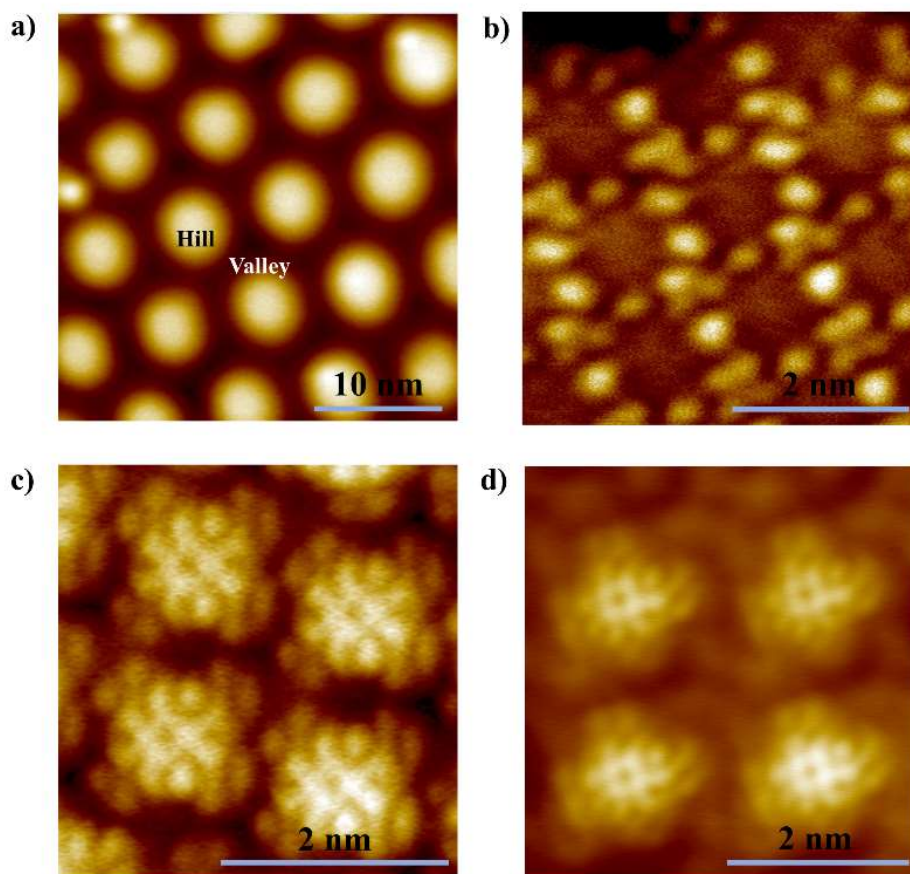


Figure 8-1: STM Images of h-BN and Pristine Orbitals of ZnPc, F₁₆ZnPc and the Binary ZnPc/F₁₆ZnPc Structure.

STM topography images taken on (a) h-BN/Cu(111) with the hill and valley locations of the Moiré pattern labelled ($V_s = 4$ V, $I_t = 2$ pA), (b) ZnPc ($V_s = -2$ V, $I_t = 3$ pA) and (c) F₁₆ZnPc ($V_s = 2$ V, $I_t = 2$ pA) and (d) ZnPc/F₁₆ZnPc heterojunction ($V_s = 0.15$ V, $I_t = 75$ pA). Pristine molecular orbital-like features are observed, demonstrating the weak interaction between the organic molecules and the underlying h-BN/Cu(111) substrate. The lattice parameters of the molecular overlayers are listed in Table 3.

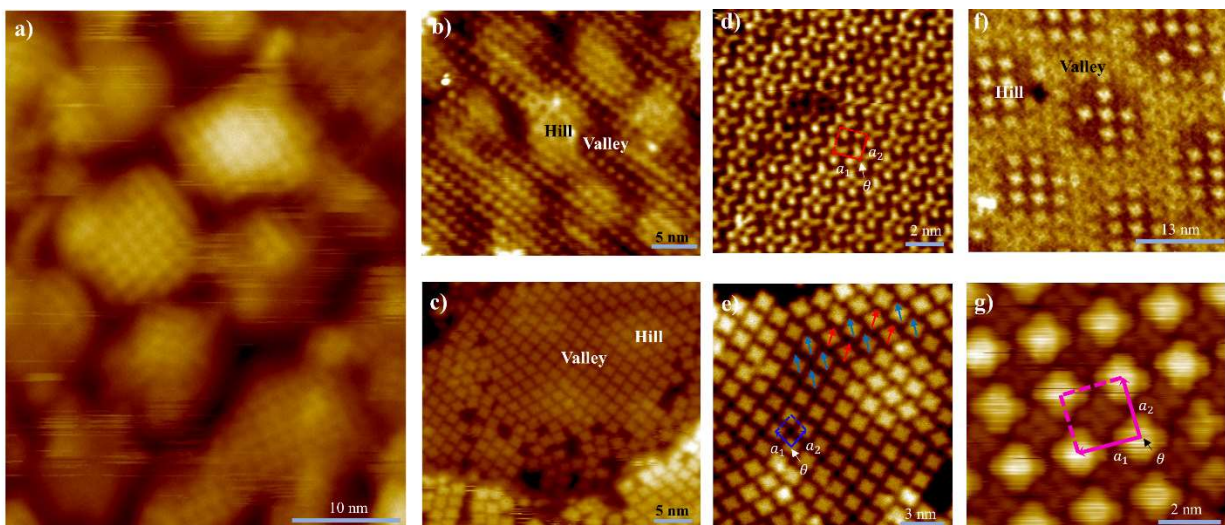


Figure 8-2: Growth of ZnPc and F₁₆ZnPc Organic Assemblies

(a) STM topography images taken on ZnPc at low coverage ($V_s = 4$ V, $I_t = 1$ pA) demonstrating nucleation preference of the molecules on h-BN hill locations. STM topography images taken on (b) ZnPc ($V_s = 4$ V, $I_t = 2$ pA) and (c) F₁₆ZnPc ($V_s = 2$ V, $I_t = 1$ pA) assemblies on h-BN/Cu(111), where the electronic perturbations of the h-BN Moiré patterns are observed. Zoomed-in STM topography images of (d) ZnPc ($V_s = -1$ V, $I_t = 5$ pA) and (e) F₁₆ZnPc ($V_s = 2$ V, $I_t = 2$ pA) showing the flower-petal structure of the Pc molecules and their orientation within the molecular layer. (f) STM topography image ($V_s = 2$ V, $I_t = 1$ pA) taken on the ZnPc/F₁₆ZnPc heterojunction, showing the periodic electrostatic modulation from the underlying h-BN/Cu(111) Moiré pattern. Bright molecules correspond to F₁₆ZnPc. (g) Zoomed-in STM topography image ($V_s = 4$ V, $I_t = 10$ pA) of the heterostructure showing the flower-petal structure of ZnPc and F₁₆ZnPc molecules and their orientation within the molecular layer. The unit cells of the molecular overlayers are labeled in (d), (e) and (g), with the lattice parameters listed in Table 3.

8.2 Electronic Structure of ZnPc and F₁₆ZnPc on h-BN/Cu(111)

While molecular packing is relatively uniform across the surface, electronic variations due to the Moiré perturbation can be observed across all three assemblies as seen in Figure 8-2 and Figure 8-3. Figure 8-3a,c shows the STS spectra taken on the ZnPc monolayer, F₁₆ZnPc monolayer, and above the ZnPc and F₁₆ZnPc constituents within the binary heterostructure, respectively. In all these spectra, well-defined density of states (DOS) features at positive bias are identified. Gaussian deconvolution of these DOS features (Figure 8-4) reveals molecular peaks associated

with the lowest unoccupied molecular orbitals (LUMOs), as evidenced by the pristine molecular orbital-like features observed in both the STM images and the differential conductance maps taken at the corresponding biases (Figure 8-1b-d, Figure 8-2 and Figure 8-3), accompanied by additional satellite peaks.[261,298,302,318,320,321] These spectral features lie at higher energies and are associated with vibrational modes of Pc molecules as discussed in Section 5.2.3. The average spacing between adjacent Gaussian peaks across all spectra is determined to be 0.21 ± 0.02 eV. ZnPc and F₁₆ZnPc spectra are combined for the purpose of this average due to the similarity between the vibrational energies of these molecules, particularly with regards to the relevant energy range.[322,323] To accurately determine the vibrational mode energy in the presence of the h-BN layer requires the consideration of the potential drop over the molecule leading to a corrected energy spacing using Equation (5-25) where $\alpha = 0.093$.[321] The actual energy spacing is therefore 0.19 ± 0.02 eV. The likely vibrational mode associated with this energy is the C=N aza + C=C pyrrole + C=C benzene mode which corresponds to 1528 cm^{-1} or 0.189 eV.[324] Furthermore, the existence of the negative differential resistance (NDR) regime following the DOS features further proves the weak interaction between the molecular overlayers and the substrate, suggesting that h-BN has functioned as a decoupling layer which effectively suppresses the hybridization between molecular moieties and the Cu(111) substrate as described earlier in Section 5.2.3. Nevertheless, when the spectra taken on the hill and valley locations of the Moiré pattern are compared within each individual assembly, ~ 0.25 eV difference in the onset of the DOS feature can be depicted. This is in agreement with the expected local work function modulation arising from the Moiré pattern of the h-BN/Cu(111) substrate, which correspondingly perturbs the positions of the frontier molecular orbitals with respect to the substrate Fermi level.[156,205]

Theoretical calculations of the CuPc-F₁₆CuPc heterostructure, a close approximation to the ZnPc variant, suggests the existence of intermolecular charge transfer when donor and acceptor molecules are packed side-to-side.[186] Consequently, the local vacuum level above the positively/negatively charged donor/acceptor molecular identities is expected to shift with respect to that exhibited in the single-component pure layers (without the donor-acceptor intermolecular charge transfer), leading to the LUMO of the donor shifting closer to the substrate Fermi level whereas the LUMO of acceptor, further away.[40,284] Nevertheless, our STS data taken on the heterostructures illustrate a different picture: ZnPc molecular orbitals (Figure 8-3) are consistently observed at higher energies (by up to ~0.5V) relative to the substrate Fermi level as compared to that of the pure layer, while the F₁₆ZnPc positive peak feature has migrated even closer to the Fermi level. This observation indicates that the intermolecular charge transfer either does not exist or does not play a dominant role in the band structure alignment of the binary heterostructure on h-BN/Cu(111). It is worth noting that Moiré pattern of the substrate simply serves as a work function modulating template, which does not seem to alter the baseline behavior of donor-acceptor heterojunctions (Figure 8-3). As a result, we focus the discussion using the representative STS spectra taken on the valley sites of the substrate.

Similar trend of orbital shifts with respect to the single-component pure layers has been observed in various donor-acceptor binary blends adsorbed on clean metal substrates.[305,309-315] This has been largely attributed to the Pauli repulsion effects coupled with the perturbations of the adsorption height of each molecular constituents and the involved charge reorganization in the binary blend, as discussed earlier.[309,312,314,315] In these studies, it was assumed that the induced density of interface states arising from the (weak) hybridization of molecular adsorbates and the metal substrate are positioned away from the Fermi level, thus not contributing

significantly to the interfacial energy level alignment. Nevertheless, the Pauli repulsion effects should have been greatly suppressed by the h-BN decoupling layer in our studies.[42] Furthermore, different from the ensemble-averaged UPS and core-level x-ray photoelectron spectroscopy (XPS) techniques where the donor-acceptor ratio dictates the averaged work function of the blend, STS exploited in this study is a local probe technique. Thus, the opposite shifts of the donor and acceptor molecular orbitals with respect to the substrate Fermi level owing to the work function averaging can be minimized.[312,315,325]

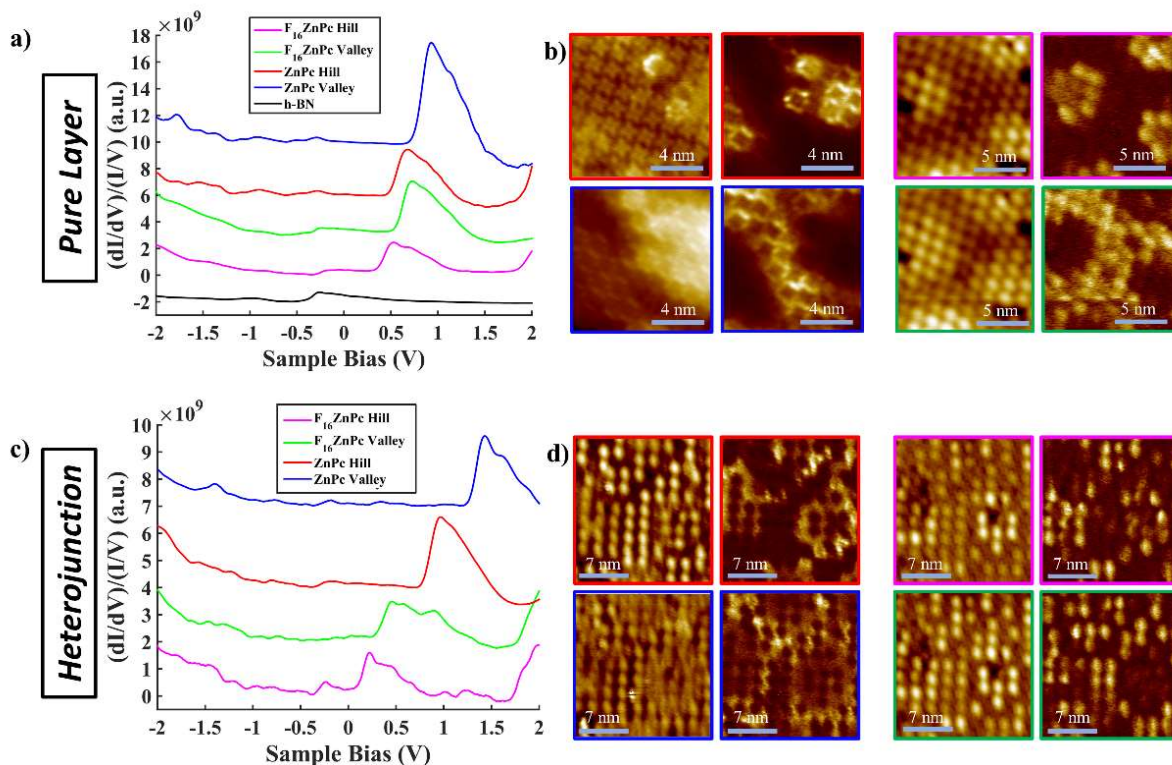


Figure 8-3: Electronic Perturbation of h-BN Moiré Pattern on Organic Assemblies

(a) STS data taken on h-BN/Cu(111) (setpoint: $V_s = 2$ V, $I_t = 100$ pA), and on the ZnPc ($V_s = 2$ V, $I_t = 100$ pA) and F_{16} ZnPc ($V_s = 2$ V, $I_t = 50$ pA) assemblies above the hill and valley locations within the Moiré patterns of the h-BN/Cu(111) substrate. The curves are vertically offset for clarity. As shown in (a), the STS curve (black) taken on h-BN/Cu(111) displays only a small step function arising from the electron tunneling directly between the tip and the Cu(111) surface state at ~ -0.4 V.[326,327] Simultaneously taken STM topography images (left columns) and dI/dV differential conductance maps (right columns) on (b) the ZnPc molecular overlayer ($I_t = 100$ pA) at $V_s = 0.6$ V (top, red frames) and $V_s = 0.9$ V (bottom, blue frames) and the F_{16} ZnPc molecular overlayer ($I_t = 30$ pA) at $V_s = 0.4$ V (top, pink frames) and $V_s = 0.6$ V (bottom, green frames), corresponding to the LUMO peak levels of the individual molecular layers above the hill and valley locations of the Moiré pattern, respectively. (c) STS data (setpoint: $V_s = 2$ V, $I_t = 100$ pA) of the two molecular constituents in the ZnPc/ F_{16} ZnPc heterojunction on various Moiré locations. The curves are vertically offset for clarity. (d) Simultaneously taken STM topography images and dI/dV maps ($I_t = 30$ pA) on the ZnPc/ F_{16} ZnPc heterojunction, at $V_s = 0.1$ V, corresponding to the LUMO peak of F_{16} ZnPc at Moiré hills (top, pink frames), at $V_s = 0.3$ V, corresponding to the F_{16} ZnPc peak at Moiré valleys (bottom, green frames), at $V_s = 1$ V, corresponding to the ZnPc peak at Moiré hills (top, red frames), and at $V_s = 1.2$ V, corresponding to the ZnPc peak at Moiré valleys (bottom, blue frames).

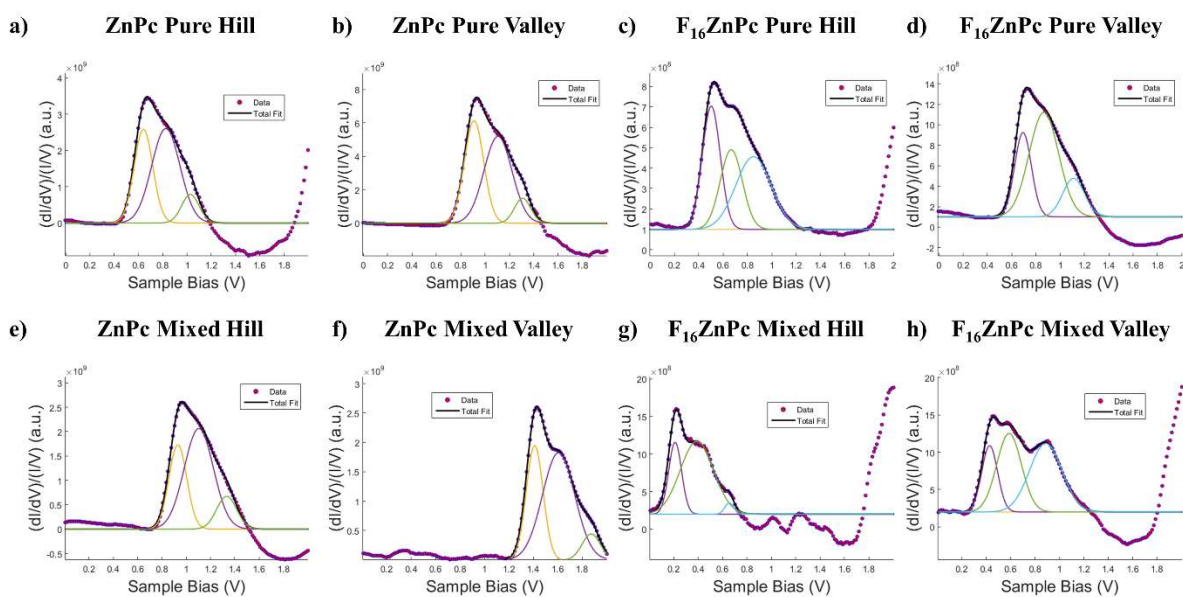


Figure 8-4: Gaussian Fits of pure and mixed ZnPc/F₁₆ZnPc STS Spectra

Gaussian Peak fitting of the (a, b) pure ZnPc spectrum, (c, d) pure F₁₆ZnPc spectrum, (e, f) mixed layer ZnPc spectrum and (g, h) mixed layer F₁₆ZnPc spectrum, was done using the fitting function in MATLAB. The spectra used here are reproduced from Figure 8-3 for the pure and mixed layers, respectively. The first peak of the fitting is attributed to the molecular LUMO.

Other factors that could possibly impact the positions of the molecular orbitals in the binary donor-acceptor blend as compared to the pure layers include i) intermolecular hybridization and charge redistribution via formation of hydrogen bonding between ZnPc and F₁₆ZnPc, ii) electrostatic screening by the supramolecular environment, and iii) interfacial (integer) charge transfer.[41,302,309-313] As shown in Figure 8-1d, pristine looking molecular orbitals of F₁₆ZnPc is exhibited in the binary blend, indicating that no significant hybridization has occurred between the donor and acceptor molecules. When introducing a different molecular species into the matrix of a thin film, the polarizability of the different organic molecules can result in the change in the local electrostatic environment as discussed in Section 3.1.[39,164,313] From a purely electrostatic consideration, barring changes to the molecule-substrate interaction and additional molecule-molecule interaction, the contribution of molecule polarization to the screening of excess charges

(such as is created in an electronic structure measurement technique such as STS) can be calculated using Equation (3-3). Using the dielectric constant of the two molecular species as an appropriate analogue for the purpose of this calculation, we find that the contribution of the molecular polarization to the electrostatic screening is roughly equivalent in the pure molecular layers. The higher dielectric constant of F₁₆ZnPc (4.8) compared to ZnPc (4) is offset by the slightly larger unit cell that is adopted.[302,328,329] When considering the binary heterostructure, F₁₆ZnPc molecules are surrounded by ZnPc molecules and vice versa. The overall change in the screening effect results in a ~7% increase in polarization energy for ZnPc molecules and a ~10% decrease for F₁₆ZnPc molecules. This suggests that the LUMO of ZnPc molecules, upon heterojunction formation, should shift towards the Fermi level while the LUMO of F₁₆ZnPc molecules should shift away from the Fermi level. This back-of-envelope calculation therefore suggests that our experimental observation is not the result of the different polarizabilities of ZnPc and F₁₆ZnPc. By ruling out (i) and (ii) as the primary cause for the shift, we focus the following discussion on interfacial charge transfer and the associated interfacial behaviors in the single-component molecular overlayers and the binary blend.

A comparison of the LUMO energy level of the ZnPc monolayer revealed in our STS measurements with those derived from the literature reported molecular electron affinity (EA) and work function of h-BN/Cu(111) suggests that ZnPc on h-BN/Cu(111) is vacuum level aligned and that charge transfer between the molecular adsorbates and the substrate is minimal. [27,156] The case of F₁₆ZnPc molecular overlayer is a bit more puzzling. Due to the more electronegative nature of F₁₆ZnPc, its LUMO is expected to sit ~0.5eV closer to the substrate Fermi level than that of ZnPc.[27] Although this trend is observed in our experiment, the difference between the ZnPc and F₁₆ZnPc LUMO peak positions (~0.2eV) is much smaller, suggesting that a finite amount of charge

has been transferred into the F₁₆ZnPc LUMO resulting in the formation of an interface dipole that shifts the vacuum level and the F₁₆ZnPc LUMO away from the substrate Fermi level by ~0.3eV as. This energy level alignment is illustrated in Figure 8-5. To estimate the size of the interfacial charge transfer between F₁₆ZnPc and the substrate, finite element electrostatics simulations were conducted as described in Section 5.3.3 with the structure set up as shown in Figure 5-10 and . In this simple model, all F₁₆ZnPc molecules are charged with a uniform charge density, and the degree of charge transfer is fine-tuned to match the upshift of ~0.3eV extrapolated from the experimental observation. This yields a ~0.27e charge transfer per molecule. This charging process increases the electrostatic potential energy of electrons above the molecular adsorbates, thereby shifting the vacuum level, and correspondingly the LUMO orbitals, upwards. It should be noted that in weakly interacting physisorbed systems, such as the case of F₁₆ZnPc on h-BN, interfacial charge transfer is mediated via electron tunneling between molecular orbitals and substrate states. As discussed previously, this process is generally described by the ICT model, where the dynamic coexistence of charged and neutral molecules often render the average amount of charge transfer per molecule fractional.[202,209] In this case, it can be expected that at any instance of time, one out of every four F₁₆ZnPc molecules is charged.

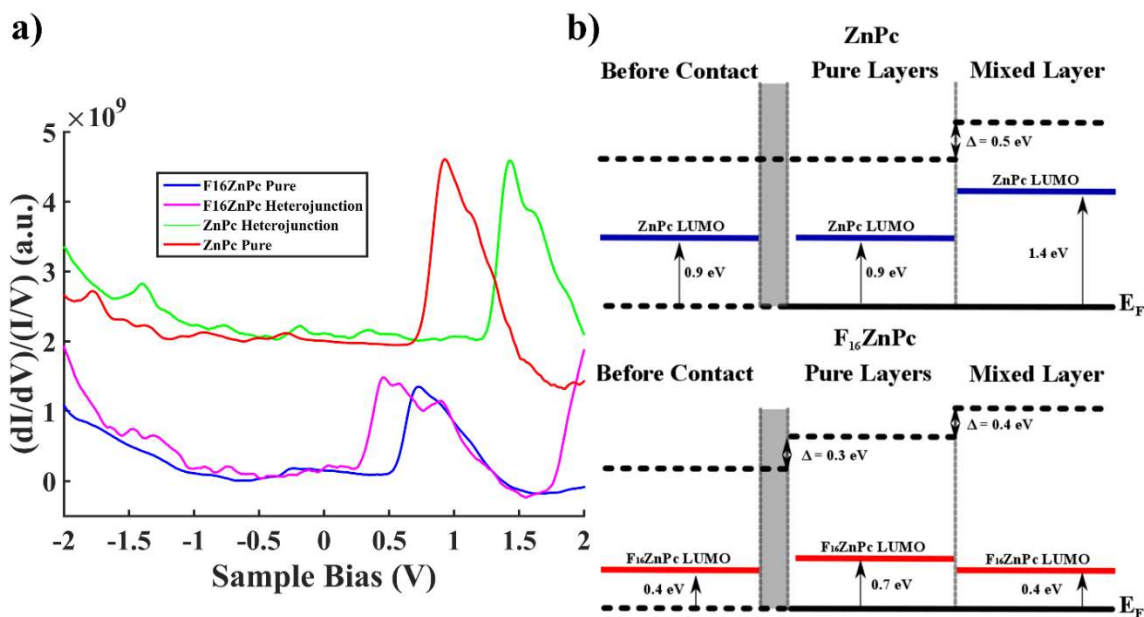


Figure 8-5: Energy-band diagrams illustrated for ZnPc (right) and F₁₆ZnPc (left) at valley locations.

(a) Combined STS data taken on valley locations of the pure ZnPc (setpoint: $V_s = 2\text{V}$, $I_t = 100\text{pA}$), pure F₁₆ZnPc ($V_s = 2\text{V}$, $I_t = 50\text{pA}$) and on the ZnPc/F₁₆ZnPc heterojunction ($V_s = 2\text{V}$, $I_t = 100\text{pA}$) from the curves shown in Figure 8-3. (b) Schematic diagram illustrating the energy level alignment and shifts of molecular orbitals between the pure layers and the binary heterojunction. Furthermore, upon heterojunction formation, the increased charge transfer between F₁₆ZnPc and h-BN/Cu(111), as predicted by COMSOL simulations and the upshift of the ZnPc LUMO, suggests that the vacuum level shift resulting from the interfacial dipole located at F₁₆ZnPc sites increases to 0.7 eV (Figure 8-7). This increased dipole is a localized effect and the increased EA is likely attributed to the increased local vacuum level similar to the effect of the orientation-dependent molecule quadrupole field.[284]

8.3 Electronic Structure of the binary ZnPc/F₁₆ZnPc layer on h-BN/Cu(111)

Upon understanding the interfacial behavior in single-component molecular overlayers, we revisit the binary heterostructure. The upshift of the ZnPc LUMO observed in the heterojunction as compared to the pure layer could be a direct consequence of the overall negatively charged film via interfacial charge transfer. However, it is unlikely that ZnPc becomes charged while F₁₆ZnPc, a more electronegative molecule that has already been demonstrated to charge transfer with the

substrate, remains charge neutral. This leads us to hypothesize that $F_{16}ZnPc$ molecules in the heterojunction have charge transferred with the substrate more than what was suggested in the pure layer, and the resulting interfacial dipole is responsible for the observed upshift in the $ZnPc$ LUMO. To verify this hypothesis, the system is, once again, recreated in COMSOL. In this model, $F_{16}ZnPc$ molecules are charged in a checkerboard pattern that approximates the heterojunction system where the $ZnPc$ molecules occupy every other site and remain neutral (Figure 8-6b). The electrostatic potential energy of electrons above the molecular adsorbates, specifically $ZnPc$, is calculated and the amount of charge transferred between $F_{16}ZnPc$ molecules and the substrate is tuned to match the $\sim 0.5\text{eV}$ upshift of the $ZnPc$ LUMO in the heterojunction. Based on these parameters, we find that a $\sim 1e$ charge transfer is required to produce a similar magnitude upshift, as seen in Figure 8-6c. The population of the $F_{16}ZnPc$ LUMO explains the shift of this orbital towards the Fermi level in the blend. Further refinement could be done by adjusting the image plane position of the $Cu(111)$ surface or by modulating the net charge transferred from the substrate to the $F_{16}ZnPc$ molecules or even the overall size of the charged matrix as noted in Figure 8-7.[42,170,178]

This now defines a clear difference in regime between the charging behavior of $F_{16}ZnPc$ in its pure layer, where charge transfer is fractional and dynamic, and in the $ZnPc/F_{16}ZnPc$ heterojunction, where the charging is complete and static. An intriguing question remains to be addressed, i.e., why $F_{16}ZnPc$ molecules charge more in the heterojunction than in its pure layer. In the ICT model involving interfaces between organic molecules and inorganic substrates, charge transfer can typically be categorized into three separate regimes.[40,41,186,202] Two of these regimes are straightforward where the LUMO of molecular adsorbates either sits very far above the Fermi level of the substrate, thereby prohibiting direct interfacial charge transfer, or far beneath

the Fermi level where the charge transfer is strongly favored. The third regime is when the LUMO lies slightly above the Fermi level of the substrate, typically within $\sim 0.5\text{eV}$ from E_F .^[43,186] Interfacial charge transfer has been demonstrated in this scenario, and different mechanisms including Fermi level pinning by polaron states associated with the nuclear relaxation of charged molecules or as a natural consequence of the Fermi-Dirac statistics coupled with the DOS distribution of organic molecular systems, particularly, the tail states that extend into the molecular gap, have been proposed.^[40,330,331] Nevertheless, the relaxation energy in conjugated small organic molecules are typically much smaller than 0.5eV , and DOS broadening, relating to imperfect molecular structures, may not be the main reason for the enhanced interfacial charge transfer in the binary blend due to the comparable degree of molecular ordering exhibited in the pure layer and the heterostructure as well as the localized nature of the STM probing.^[43,159]

Table 3: Lattice parameters and averaged Gaussian-fit peak positions of the unoccupied density of state features in the STS spectra taken on the pure and mixed molecular layers.

Note that the $F_{16}\text{ZnPc}$ unit cell refers to the $\alpha\alpha$ -orientation unit cell. For the LUMO levels, error bars are derived from the standard deviation of peak positions from multiple data sets and the modulation voltage (26mV) is used as a lower bound.

Material	$a_1(\text{nm})$	$a_2(\text{nm})$	$\theta(\text{degrees})$	Moiré Location	LUMO (eV)
ZnPc	1.36 ± 0.04	1.37 ± 0.05	87.5 ± 1.9	Hill	0.68 ± 0.08
				Valley	0.90 ± 0.04
F₁₆ZnPc	1.49 ± 0.05	1.39 ± 0.05	79.9 ± 4.3	Hill	0.46 ± 0.11
				Valley	0.72 ± 0.09
Heterojunction	2.03 ± 0.04	1.94 ± 0.04	88.2 ± 1.8	ZnPc Hill	0.93 ± 0.03
				ZnPc Valley	1.36 ± 0.03
				F ₁₆ ZnPc Hill	0.23 ± 0.03
				F ₁₆ ZnPc Valley	0.42 ± 0.03

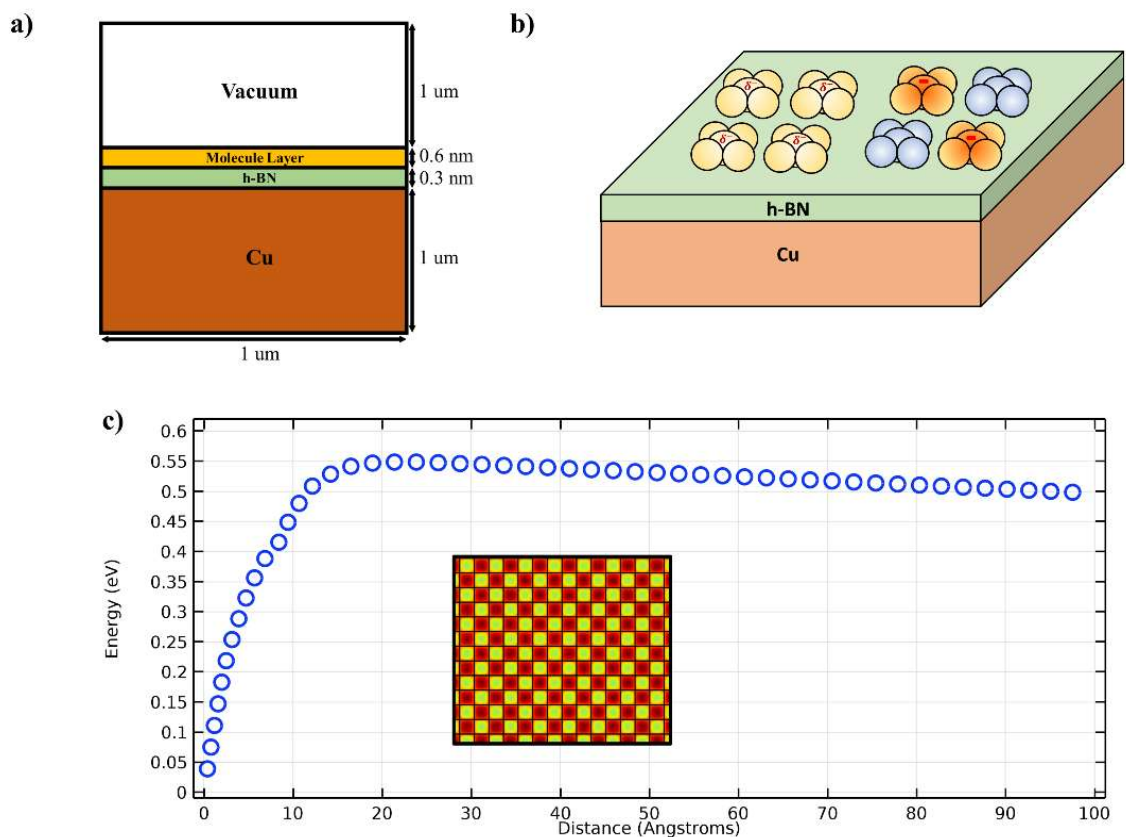


Figure 8-6: Finite element electrostatic simulations using COMSOL.

(a) 2D representation of the geometric setup of the simulation reproduced from Figure 5-10. (b) Schematic illustration of the charge state of $F_{16}ZnPc$ molecules in its pure layer (left) and the mixed binary heterostructure (right), respectively. (c) Electrostatic potential energy for electrons is plotted from the image charge plane of the metal up to 100 angstroms directly above the $ZnPc$ molecule near the center of the binary molecular assembly. The potential energy for electrons reaches the maximum a couple of nanometers beyond the image charge plane, corresponding to the upshift of the local vacuum level (above the $ZnPc$ constituents), which then decays to a saturation value with increasing distance. Inset shows a portion of the 100×100 checkerboard matrix used in the calculation, where $F_{16}ZnPc$ molecules are charged by $1e$ (red) and $ZnPc$ remain neutral (yellow).

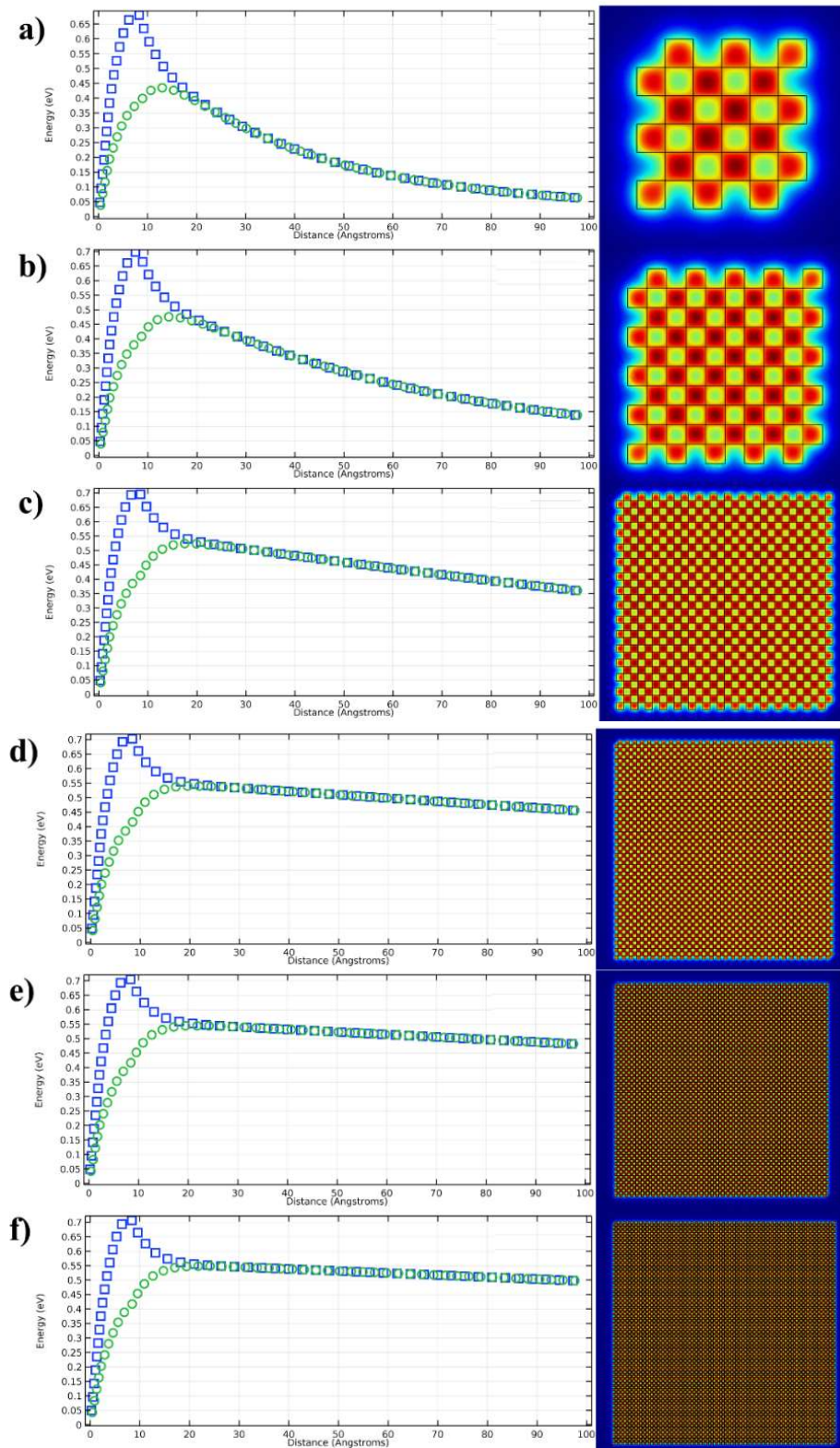


Figure 8-7: COMSOL Simulation of the dependence of the vacuum level shift on the size of the molecular layer relative to the distance probed.

Figure 8-7 (cont'd)

Finite element electrostatic simulation using COMSOL at (a) $N=6$, (b) $N=10$, (c) $N=30$, (d) $N=60$, (e) $N=80$, (f) $N=100$ molecules across, with the electrostatic potential energy for electrons plotted (left) from the image charge plane to 100 angstroms directly above ZnPc (green squares) and F_{16} ZnPc (blue squares) near the center of the molecular assembly. Molecules are arranged in a $N \times N$ grid where each square represents a 1.44 nm x 1.44 nm Pc molecule (right). While N is small, i.e. when the radius of the molecular assembly is comparable to the distance from the molecular layer where the electrostatic potential energy for electrons is sought, small changes in the assembly size will lead to a sizable alteration in the potential energy. This probing distance, which is comparable to the position of the STM tip, is around 10-20 angstroms from the surface corresponding to a tip-sample distance of under 1 nm. A maximum in the electrostatic potential energy can be seen directly above ZnPc which represents the local vacuum level shift, originating from the charge transfer between the F_{16} ZnPc and the underlying Cu substrate. A change in the maximum of about 0.1 eV can be observed when scaling from $N=6$ to $N=60$. Red areas represent areas with higher electrostatic potential energy compared to blue areas.

8.4 Discussion

We speculate that the interfacial charge transfer can be enabled/enhanced in molecular assemblies when the resulting electrostatic energy of the system consisting of the charged molecular lattice and the substrate is sufficient to compensate for the LUMO-Fermi level offset. The electrostatic energy of the system is the sum-total of the two separate energy terms, i.e., the stabilizing energy between the charged molecules and their corresponding image charges in the substrate, typically known as the polarization energy, and the destabilizing energy between adjacent charged molecules. This sum-total electrostatic energy in the molecular overlayer on h-BN/Cu(111) is analogous to the Madelung energy, i.e., the energy gained by the formation of an ionic matrix from its charged constituents, in organic charge transfer complexes or ionic systems. [233-235] Therefore, for ease of discussion, it is referred to as, simply, the Madelung energy in the following analysis.

Considering the heterojunction system, ZnPc molecules do not appear to directly interact with the F_{16} ZnPc molecules, therefore their role within this estimation of the Madelung energy is

simply that of a dielectric spacer. In this context, the Madelung energy of the heterojunction is anticipated to be larger than that of the pure system due to the weaker electron-electron repulsion between the more widely spaced charged F₁₆ZnPc molecules. To provide a more quantitative estimation, we calculate the Madelung energy per F₁₆ZnPc molecule in the heterojunction and in its pure layer. As just discussed, to first approximation, this energy can be described by the equation:

$$E_M = P - E_{ee} \quad (8-1)$$

where P is the polarization energy and E_{ee} is the destabilizing energy arising from the e-e repulsion.[239,332] The polarization energy is calculated by taking the difference between the charging energy of a molecule in free space and within the system with molecular layers treated as continuum dielectric medium.[333] P amounts to 0.78eV in both the heterojunction and the pure layer, whereas the destabilizing energy acting on individual F₁₆ZnPc molecules should differ between the two structures due to the stronger e-e repulsion involved in the latter. This destabilizing energy can be estimated in a 50 × 50 matrix with the F₁₆ZnPc molecules either charged in a checkerboard pattern (inset of Figure 8-6c) mimicking the heterojunction or in the complete pattern for the pure layer. In comparison to the model system consisting of continuum molecular dielectric layers, the additional electrostatic energy associated with charging a molecule in the charged matrix is, therefore, E_{ee}, which amounts to be 0.07 eV and 0.27 eV in the checkerboard and fully charged matrix respectively. Thus, the Madelung energy is approximated to be 0.71 eV for the heterostructure and 0.51 eV for the pure layer. The larger Madelung energy provides a greater driving force for interfacial charge transfer to occur, which lends quantitative evidence to the more negatively charged heterostructure as opposed to the pure layer. It should be emphasized again that the discussion of a Madelung energy analog should strictly be treated as

only an analog. A typical calculation of the Madelung energy involves treating the positive and negative charges of an ionic lattice as point charges with well-defined inter-charge distance. It should be noted that applying equations for the Madelung constant and Madelung energy as described by equations (4-1) and (4-2), can be significantly more complicated due to the substrate's image charge screening, both from the Cu and the dielectric spacer, h-BN, and their corresponding effects on the l_{ij} distance. Determination of a true Madelung energy for this system goes beyond the scope of this body of work.

It should be noted that the $\sim 1e$ occupation of the $F_{16}ZnPc$ that is predicted by COMSOL simulations poses an interesting complication when considering STS data. During STS data acquisition of the unoccupied molecular state of $F_{16}ZnPc$, electrons are tunneled into the molecule directly below the STM tip. For the scenario of the heterojunction, the $1e$ occupation of the $F_{16}ZnPc$ LUMO suggests that the molecular orbital is now situated near or directly at the substrate Fermi level. As a result, the localized single electron occupation of the LUMO leads to a splitting of its STS feature into a singly unoccupied molecular orbital (SUMO) and a singly occupied molecular orbital (SOMO) which are separated by the intra-orbital Coulomb repulsion.[164,175,202,211,212] This, therefore, suggests that the positive feature that is observed in the $F_{16}ZnPc$ heterojunction STS could potentially not be the molecular LUMO but rather the SUMO. In the case of the pure $F_{16}ZnPc$ layer, though the coexistence of the charged and neutral molecules in similar systems have been directly approved by ultraviolet photoemission spectroscopy (UPS) and x-ray photoemission spectroscopy (XPS) measurements owing to the timescale of the photoemission process (~ 1 fs), probing of dynamically charged molecules by STS is rather complicated.[207-210] Due to the technique's lack of temporal resolution and the strong local electric field between the tip and sample, which can perturb the initial charge state of the

molecule directly underneath the tip, all molecules appear similar in the STS measurements. However their LUMO energy levels are still susceptible to the vacuum level shift induced by the interfacial charge transfer, which is in agreement with what we observed in the pure F₁₆ZnPc layer.[208]

8.5 Conclusion

In conclusion, we have demonstrated that ZnPc and F₁₆ZnPc, in their pure phase, form weakly interacting organized structures that are electronically but not geometrically perturbed by the Moiré patterns of the h-BN/Cu(111) substrate. Co-deposition of these two molecules yields a checkerboard structure that is adopted to minimize the F-F repulsion between F₁₆ZnPc molecules. The energy levels of molecular orbitals in the heterostructures are observed to upshift for ZnPc and downshift for F₁₆ZnPc with respect to those of the pure phase, regardless of the location of the h-BN Moiré pattern. This trend is opposite to that expected if donor-acceptor intermolecular charge transfer has dominated. Instead, it is the result of the enhanced charging of F₁₆ZnPc molecules in the heterostructure via interfacial charge transfer with the substrate. The emergence of this charge transfer interaction in the heterostructure is hypothesized to originate from the greater Madelung energy analog of the heterostructure in contrast to that of the pure phase. This phenomenon brings forth a significant complication as well as a great opportunity in the design of thin film molecular heterojunctions on substrates as the presence of the substrate, even a weakly interacting one, such as h-BN/metal which does not perturb the pristine molecular orbitals and characteristics, can still promote interfacial charge transfer and inhibit intermolecular charge transfer. On one hand, steps will need to be taken to further decouple the heterojunctions from the substrate to keep their intrinsic properties. On the other hand, interfacial charge transfer may act

as an additional knob to engineer the properties of molecular heterojunctions which could enrich the potential (opto)electronic applications of the hybrid system.

9 Growth and Electronic Structure of TCNQ and K-TCNQ Charge Transfer Complexes on Cu(111)

Based on the understanding developed with regards to the growth and electronic structure characteristics of donor/acceptor molecules in their pure and mixed phases in Chapter 6 through Chapter 8, the next step in the process is the development and understanding of thin film CTCs. Unfortunately, the phthalocyanine molecular systems that we have been working with thus far is not known for exhibiting the more exotic properties of CTCs such as metallic conductivity or ferroelectricity. Thus, it is necessary to choose a combination of molecules whose properties go beyond the typical semiconducting properties exhibited in the donor-acceptor binary layer of ZnPc and F₁₆ZnPc. In collaboration with Professor Shenqiang Ren's group, we investigated properties of K-TCNQ whose bulk measurements showed that this compound was capable of a metal-to-insulator (MI) transition under laser irradiation or electric pulse. Some of the P-E loops measured by Shen's group, showed curious behavior that could be linked to ferroelectricity. We are interested in the characterization of TCNQ and K-TCNQ assemblies and further develop the understanding of the influence of the incorporation of K atoms into the TCNQ lattice on the growth and electronic structure.

Cu(111) was chosen as the initial template of choice to determine the basic growth conditions for K-TCNQ. K-TCNQ powder, provided by Shen's group, was loaded into the low-temperature effusion cell and mounted in the preparation chamber itself. The sublimation temperature of TCNQ is ~120° C, significantly lower than the 450°C of Pc molecules which could lead to a significant vapor pressure at room temperature.[334] However, the coordination of K and TCNQ forms a compound that does not sublime significantly at 120° C, allowing the compound to be loaded into the chamber safely without compromising UHV pressures. The growth and

electronic structure of TCNQ deposited on Cu(111) will be discussed in Section 9.1. It should be noted that the deposition of TCNQ was carried out using the K-TCNQ source. The strong agreement of the experimental data discussed in Section 9.1 with literature results, strongly suggest that K atoms are not being released from the K-TCNQ source in significant quantities even at 175 °C. Therefore, in order to study K-doped TCNQ, a separate potassium dispenser from SAES was used to controllably dope pre-grown TCNQ samples with K atoms. The growth and electronic structure of K-TCNQ will be discussed in Section 9.2.

9.1 Growth and Electronic Structure of TCNQ on Cu(111)

TCNQ molecules deposited on Cu(111) at room temperature, exhibit a strong preference for nucleation at Cu step edges. A disordered phase tends to grow outwards from step edge, likely as a result of a strong binding energy to the bottom of the Cu step. When the disordered phase grows larger and passivates most of the Cu steps, ordered islands of TCNQ begin to emerge on the terrace of Cu substrates or from the edges the disordered phase. as can be seen in Figure 9-1a. This structure is characterized by a one-dimensional mesh of TCNQ molecules of two orthogonal mutual molecular orientations spaced by a row of single molecules. A 5-molecule unit cell can then be constructed with lattice parameters: $a_1 = 2.71 \pm 0.04 \text{ nm}$, $a_2 = 2.76 \pm 0.03 \text{ nm}$ $\alpha = 39.27 \pm 0.38^\circ$ as see in Figure 9-1b. STM studies of TCNQ on Cu(111) have shown that the assembly adopts a commensurate epitaxial registration with regards to the substrate, indicative of a strong molecule-substrate interaction.[335]

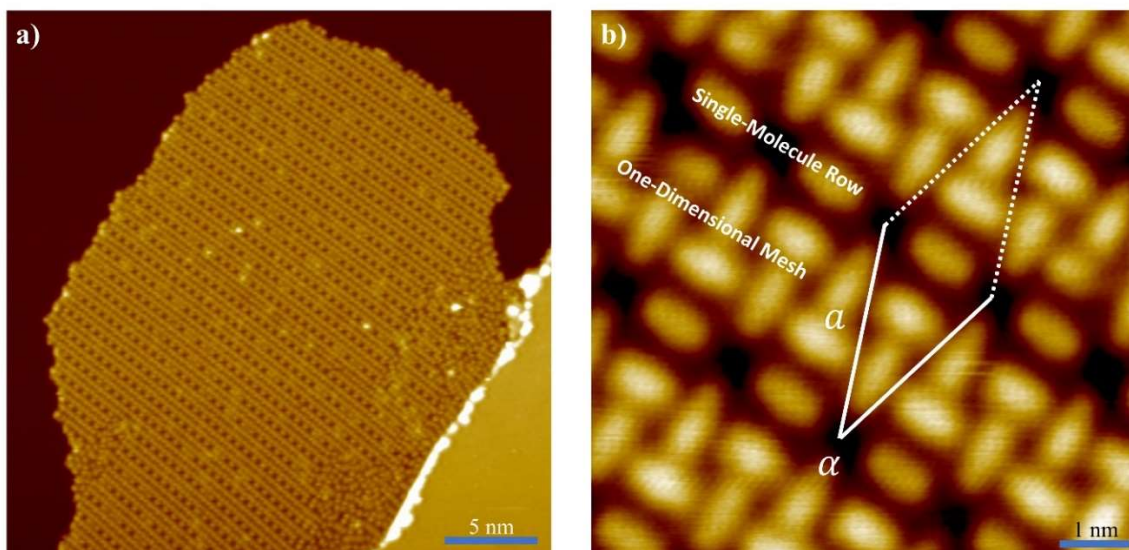


Figure 9-1: STM Image of TCNQ on Cu(111)

(a) Zoomed-out image of TCNQ ($V_s = 2$ V, $I_t = 5$ pA) showing the coexistence of an ordered and disordered phase of TCNQ. Disordered structures tend to nucleate outward from the step edge of Cu(111) before transitioning to ordered TCNQ outside the influence of the step edge. (b) Zoomed-in image of TCNQ lattice ($V_s = 2$ V, $I_t = 5$ pA) with the 5-molecule unit cell marked. Structure is characterized by a one-dimensional mesh spaced by single molecule rows as noted in the image.

Electronic structure measurements of TCNQ reveal a complicated STS pattern. The main spectral features of interest here are observed at ~ 0.6 V and ~ 0.25 V. In order to ascertain the nature of these peak features, differential conductance mapping (dI/dV mapping) is used to probe the spatial distribution of the DOS. Maps taken at 0.6 V reveal a delocalized structure along the one-dimensional mesh while maps taken at 0.25 V show localized structures associated with the single molecule rows. The correlation of the dI/dV maps to the molecular lattice leads us to conclude that these spectral features are associated with the molecular orbitals. No internal features of the molecular orbitals can be distinguished due to the strong degree of hybridization between the Cu(111) surface and the TCNQ molecules.[335] The exact nature of the two unoccupied states is a notable question. Based on literature measurements, the LUMO and LUMO+1 of TCNQ lies at 3.38 eV and 3.1 eV.[336] While the work function of Cu(111) is reported as 4.94 eV, the

adsorption of molecules on a metal will result in the push-back of the metal's electron cloud, resulting in a lowering of the work function as noted in Chapter 3.[156] This effect could account for the energy level alignment of TCNQ's unoccupied orbitals on Cu(111). However, why does the LUMO and LUMO+1 orbitals localize on different molecule sites within the TCNQ lattice? Alternatively, the two spectral features could be the result of different degrees of charge transfer interaction with the substrate with single-row molecules due to the lower molecular coordination, and therefore lower e-e repulsion, charge transferring more with the substrate, a phenomenon noted in Chapter 8. This increased charge transfer could lead to a LUMO that is positioned closer to the Fermi level in accordance with the Fermi-Dirac distribution. However, Bader analysis of the degree of charge transfer indicates a charge transfer of 1.3 electrons per molecule and no unique distinction between the two types of molecules.[335] On the other hand, the significant degree of charge transfer between TCNQ molecules and Cu(111) coupled with the strong molecule-substrate interaction which forces TCNQ molecules to conform to the Cu(111)'s lattice very likely leads to the formation of distinct interface states with energy levels that are specific to molecule's adsorption geometry.[305,335] Molecules in the mesh associated with the 0.6 V spectral feature appear more delocalized compared to the single molecule rows could be the result of the formation of a confined hybrid band between TCNQ and Cu though the exact nature of these states will likely require density functional theory (DFT) calculations.[305]

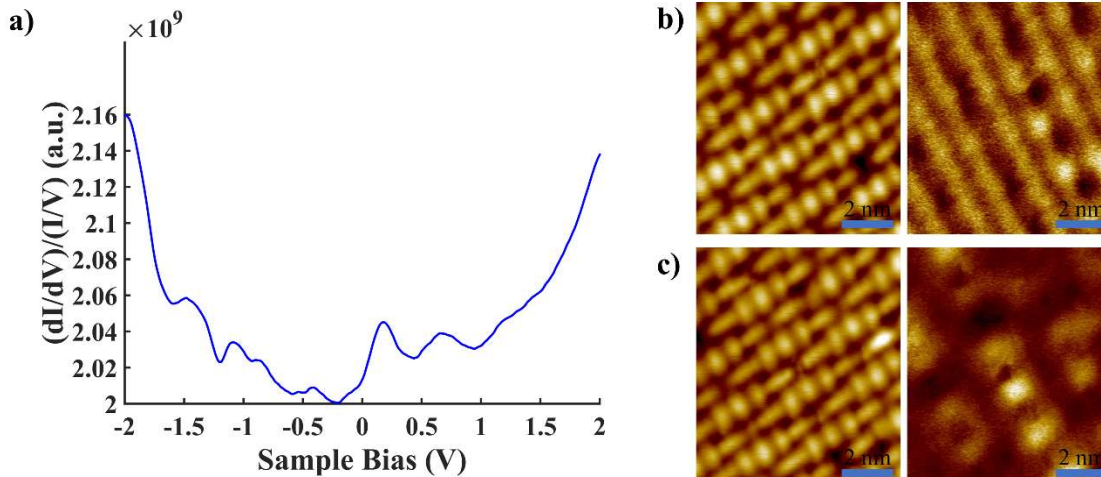


Figure 9-2: Electronic Structure and dI/dV maps of TCNQ on Cu(111)

(a) STS data taken on the ordered TCNQ structure ($V_s = 2$ V, $I_t = 200$ pA). The presence of two unoccupied state peaks are observed. dI/dV maps of TCNQ measured at (b) ($V_s = 0.6$ V, $I_t = 200$ pA) where the DOS seems to be along the one-dimensional mesh and (c) ($V_s = 0.25$ V, $I_t = 200$ pA) where the DOS is localized along the single molecule rows.

9.2 Growth and Electronic Structure of K-TCNQ on Cu(111)

With the characterization of TCNQ on Cu(111) complete, we turn our attention to K-doped TCNQ. The doping of K atoms to TCNQ results in a variety of different possible structures that depend on the initial conditions of the molecular overlayer and the local doping concentration. Initial indication of K doping at low concentrations occur at the edges of ordered TCNQ structures as seen in Figure 9-3a. Doped areas appear significantly brighter resulting from the increased DOS introduced by K atoms. K atoms in this lightly doped regime seem to prefer to adsorb into the one-dimensional mesh of TCNQ structures before perturbing the single molecule rows. In rare cases, a two-dimensional mesh emerges from the doped-TCNQ edges whose unit cell is expanded from an elevated temperature structure of TCNQ which also assumes a two-dimensional mesh, as seen in Figure 9-3b. [335,337,338] The unit cell of this structure is given by the parameters: $b_1 = 1.36 \pm 0.04$ nm, $b_2 = 1.26 \pm 0.07$ nm, $\beta = 91.1 \pm 0.4^\circ$. This structure is in good agreement

with the unit of K-TCNQ grown on Ag(111) and correlates to the b-c plane of bulk K-TCNQ. [337,338] K atoms occupy the center sites of the mesh and drawn out along with the unit cell in Figure 9-3b. This structure forms a 1:1 ratio between K and TCNQ and likely results in significantly enhanced electrostatically stabilized lattice due to the ionic attraction between ionized K and TCNQ species. The difficulty in locating this phase likely results from the inability for TCNQ molecules to easily transition between different structures on Cu(111) on a large scale due to the existence of a large activation energy of 0.63 eV that exists between the room temperature and elevated temperature structures of TCNQ on Cu(111).[335] This means that in order for the two-dimensional mesh structure of K-TCNQ to form, the elevated temperature form of TCNQ (which also assumes a two-dimensional mesh) must first form which is suppressed by the large activation energy which explains why this structure is so rarely observed.[335]

Further increase of the local doping concentration of K leads to the formation of an entirely different structure of K-TCNQ, characterized by irregularly spaced dark stripes running through the assembly as seen in Figure 9-3c. It should be noted that this phase of K-TCNQ is also observed for lower doping concentrations of K but seems to grow from the disordered phase of TCNQ. Closer inspection of this structure suggests the presence of a similar mesh-type structure. However, unlike the two-dimensional mesh, this mesh is truncated along the \vec{b}_1 direction of the two-dimensional mesh's unit cell by dark boundaries as seen in Figure 9-3b. We hypothesize that this phase emerges as a result of the large activation energy for TCNQ to transition between structures. This leads to the formation of grain boundaries where the K concentration and TCNQ orientations are perturbed and a dark stripe that possesses a structure different from that of either the oval TCNQ molecules or the spherical K atoms.

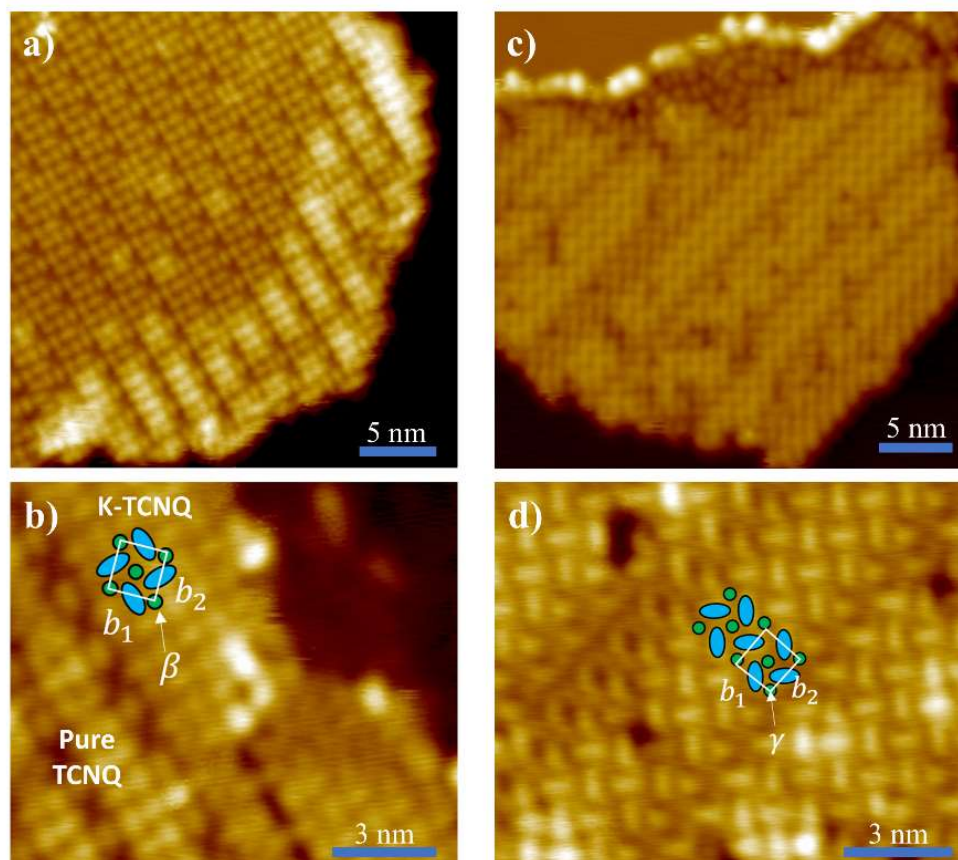


Figure 9-3: STM images showing the growth of K-TCNQ on Cu(111) at low and moderate K doping.

STM image of (a) lightly K-doped TCNQ structure ($V_s = 2$ V, $I_t = 5$ pA) where K doping is primarily localized on the edges of the TCNQ assembly, (b) the two-dimensional mesh structure ($V_s = -0.01$ V, $I_t = 30$ pA) with the unit cell outlined, (c) moderately K-doped TCNQ structure, typically referred to as the stripe phase ($V_s = 2$ V, $I_t = 5$ pA) where two-dimensional mesh structures are truncated along the \vec{b}_1 direction by dark boundaries (d) zoomed-in image of the striped phase of K-TCNQ ($V_s = -0.01$ V, $I_t = 200$ pA) shows a similar lattice as observed in (b).

The precise configuration of this dark stripe structure is difficult to glean from the stripe structures shown in Figure 9-3cd but a rare, more uniform phase of this structure that occurs at higher doping concentration, shown in Figure 9-4 could provide more insight. This more uniform structure consists of a one-dimensional row of single mesh units along the same \vec{b}_2 direction and shall be known as the condensed stripe phase. This structure appearing to be a distorted version of the two-dimensional mesh with the appearance of a dark trench that separates the mesh units.

Based on a combination of bias-dependent imaging and a functionalized tip, the positions of the K atoms and TCNQ molecules are assigned as per Figure 9-4b-d. Based on this assignment, two K atoms approximately occupy the very edge of the dark trenches with one K atom occupying the center of each mesh center with an overall unit cell given by: $c_1 = 2.4 \text{ nm}$, $c_2 = 1.34 \text{ nm}$, $\gamma = 72.09^\circ$ and a stoichiometry ratio of 1:1. This might suggest that a combination of insufficient potassium doping and/or the high TCNQ inter-structure conversion energy is the cause of the formation of the stripe phase of K-TCNQ.

Finally, upon significant increase in the doping concentration, K_2 -TCNQ is formed, adopting a similar head-to-tail structure observed in studies of K_2 -TCNQ on Ag(111) as seen in Figure 9-5. [338] The lattice constant of this phase is given by: $d_1 = 1.32 \pm 0.09 \text{ nm}$, $d_2 = 1.02 \pm 0.07 \text{ nm}$, $\delta = 107 \pm 8^\circ$. An intriguing effect of the formation of the K_2 -TCNQ structure is the emergence of a distinct two-dimensional moiré pattern suggesting a significantly weaker molecule-substrate interaction noted in Figure 9-5a. By applying the phase coherence model described by the Equation (5-28), it can be noted that the K-TCNQ structure could easily reach a POL coincidence structure by using the lattice parameters $b_1 = 1.363 \text{ nm}$, $b_2 = 1.261 \text{ nm}$, $\beta = 89.82^\circ$ with the azimuthal rotation, $\phi = 29.08^\circ$ which are within experimental error.[339] The distinct reduction in the degree of epitaxial registration of the molecular overlayer as the result of K doping leads us to conclude that the incorporation of K atoms into the TCNQ lattice results in reduction of the molecule-substrate interaction in favor of interaction between the TCNQ molecules and K atoms. [338]

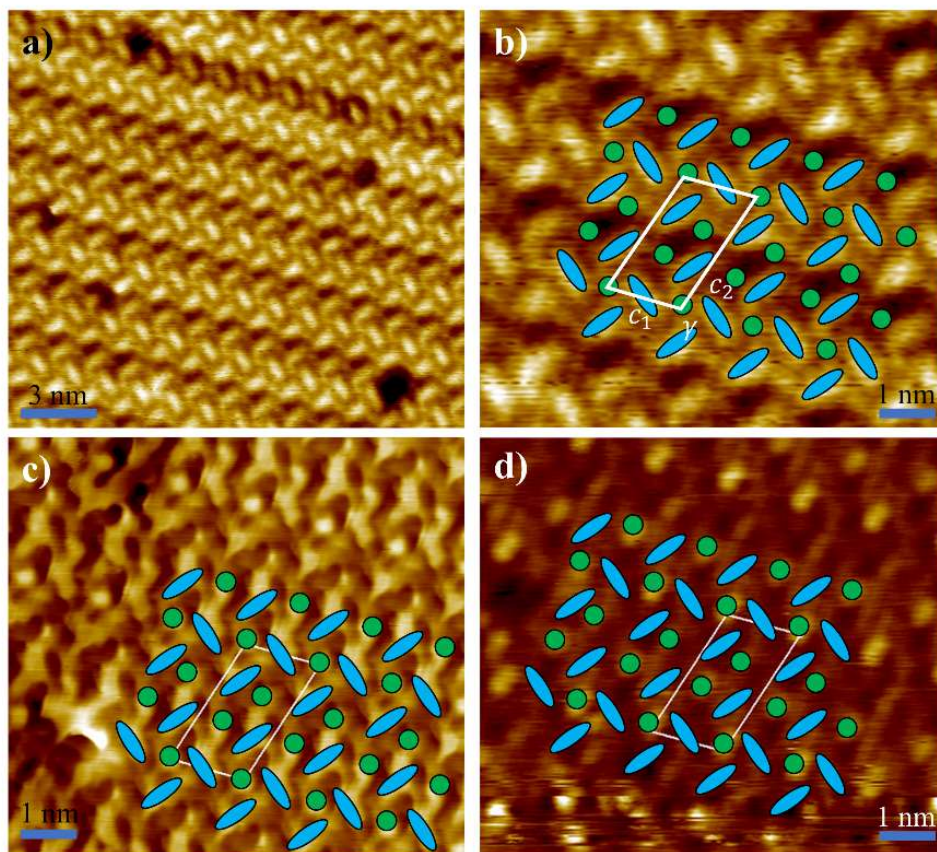


Figure 9-4: Assignment of the condensed stripe phase of K-doped TCNQ

(a) Zoomed-out STM image of the condensed stripe phase. Unit cell assignment and position of TCNQ and K atoms are determined from zoomed-in STM images of the condensed version of the stripe phase of K-TCNQ taken with a functionalized tip at different biases: (b) ($V_s = 1$ V, $I_t = 30$ pA) (c) ($V_s = 0.1$ V, $I_t = 30$ pA) (d) ($V_s = -1.5$ V, $I_t = 30$ pA) noSting that TCNQ molecules are observed at empty-state imaging conditions while K atoms are observed in filled-state imaging conditions. The unit cell is marked in (b) with the outline shown in (c) and (d).

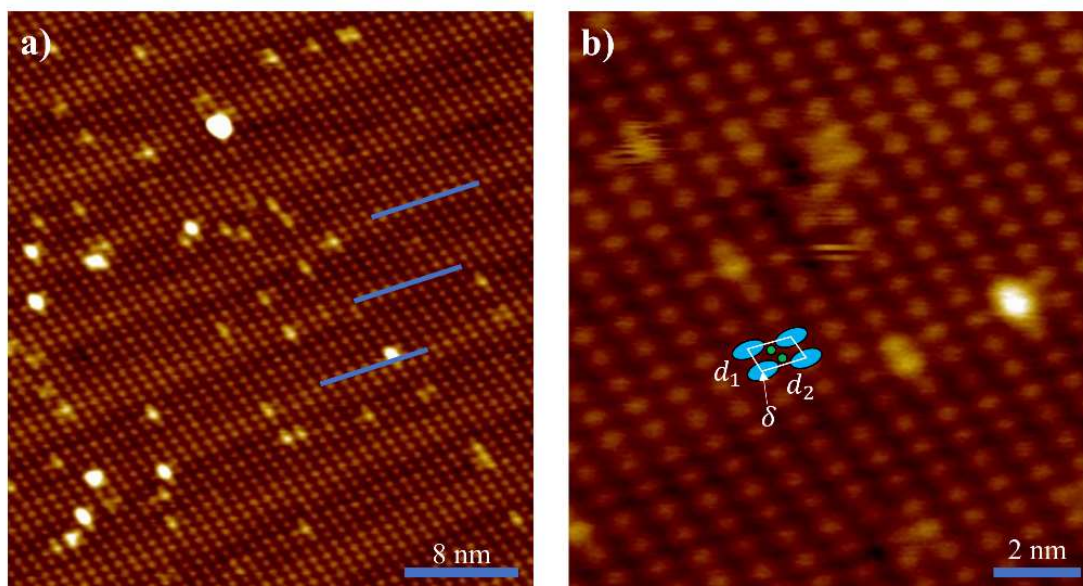


Figure 9-5: Structure of K₂-TCNQ at high K doping.

(a) large scale and (b) zoomed-in STM images taken of K₂-TCNQ ($V_s = 2$ V, $I_t = 5$ pA). Significant doping of K onto TCNQ results in the formation of the head-to-tail phase of K₂-TCNQ and the emergence of a two-dimensional moiré pattern marked by blue lines. This pattern is outlined by blue lines in (a) while the unit cell of the head-to-tail phase is shown in (b).

9.3 Electronic Structure of K-TCNQ on Cu(111)

The decreased molecule-substrate interaction is beneficial to the study of K-TCNQ and its interesting MI transition under laser irradiation or electric pulse as it implies that the TCNQ molecules are now interacting strongly with doped K atoms as they would in the bulk. Bulk K-TCNQ, due to the strong electron donating capabilities of K atoms is expected to result in a fully ionic complex where TCNQ molecules are fully ionized to the -1 charge state. Naturally, this would be highly detrimental to metallic like conduction as noted earlier in Chapter 4 due to the existence of a strong intra-orbital Coulomb repulsion. A theory put forth by Shen's group was that a mixed valence state is somehow formed when bulk K-TCNQ transitions into a metallic state. It was speculated that this mixed valency is created by the formation of pure TCNQ regions within

the K-TCNQ crystal upon laser irradiation or electric pulse. Naturally, one might expect the missing K atoms to lead to the formation of a K_2 TCNQ region as well. Thus, the interface between the electrically neutral TCNQ, the -1 charge state of TCNQ in K-TCNQ and the -2 charge state of TCNQ in K_2 -TCNQ regions, could satisfy one of the necessary conditions for metallic conduction in an organic CTC. Fortunately, a heterojunction of pure TCNQ and K-TCNQ can be formed as was shown in Figure 9-3.

STS spectra taken around or at the heterojunction of TCNQ and K-TCNQ are shown in Figure 9-6. STS taken on TCNQ sites show the characteristic twin peak feature of TCNQ/Cu(111). By tracking the movement of the spectral feature located further away from the Fermi level, we find that this peak broadens as we go from pure TCNQ to the interface of K-TCNQ to the bright mesh of K-TCNQ. It should also be noted that the lower energy interface state of TCNQ remains roughly constant in energy across all spectra which is not surprising due to the presence of nearby TCNQ molecules occupying the relatively unperturbed single molecule rows. As expected, this feature is not present in the stripe phase of K-TCNQ as seen in Figure 9-7a. In order to understand the shift and perturbation observed near the heterojunction, a discussion of the electronic structure of pure K-TCNQ must be had.

The general striped phase structure of K-TCNQ will be the focus of discussion as it is by far the more dominant and reproducible structure of K-TCNQ on Cu(111). STS taken on these structures reveal the presence of a broad DOS ranging between 0 and ~ 1 V as seen in Figure 9-7a which is correlated to the structure of K-TCNQ as observed in dI/dV maps taken at 0.8 V as seen in Figure 9-7bc. The shift from the two fairly well-defined unoccupied interface states observed in TCNQ to the single broad unoccupied state of K-TCNQ could arise from a number of different mechanisms. The most prominent of which is the hybridization of the TCNQ LUMO with a broad

DOS distribution, such as the Cu surface state. This would imply that the molecule-substrate interaction is increased as a result of K doping which we have disproved in our structural studies. Bias dependent images taken on areas that show both TCNQ and the stripe phase of K-TCNQ, as seen in in Figure 9-7d, show an unusual behavior of the K-TCNQ structure. Despite having good resolution of the shape and orientation of TCNQ molecules, K-TCNQ areas prove significantly harder to resolve at 2 V. This is further illustrated when imaging K-TCNQ at 1 V, showing a significant delocalization along the direction of the stripe as seen in Figure 9-7e. This smearing of the molecule's shape could be associated with a delocalization of the molecule's DOS which could be for metallic conductivity.[305] Studies conducted on pure K deposited on Cu detail the formation of an unoccupied state with a broad DOS distribution, resulting from the charge donation between K and Cu.[340,341] However, it should be noted that this unoccupied state exists without the need for K-Cu bond formation and that the interaction between K and Cu is purely electrostatic in nature.[341] It is therefore likely that this broad unoccupied DOS interacts with the TCNQ's LUMO to yield the broadened unoccupied spectral feature observed in pure K-TCNQ layers. Returning to the heterojunction, the gradual broadening effect observed at the interface of TCNQ and K-TCNQ is therefore the result of the interaction between TCNQ molecules and the K unoccupied states where early signs of the molecular smearing can already be seen in the meshes of K-TCNQ in Figure 9-6.

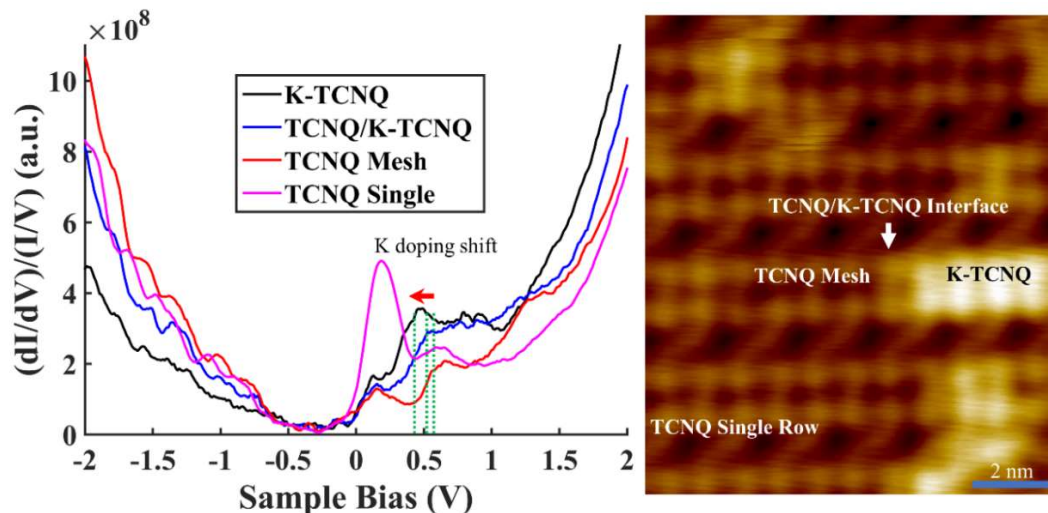


Figure 9-6: Heterojunction of TCNQ/K-TCNQ

STS data ($V_s = 2$ V, $I_t = 30$ pA) taken on TCNQ or K-TCNQ molecules shown in the STM image (right). An overall broadening and shift towards the Fermi level is observed for the unoccupied state peak situated at ~ 0.6 eV as a result of increasing K concentration. The peak associated with the TCNQ single molecule rows is present in all curves.

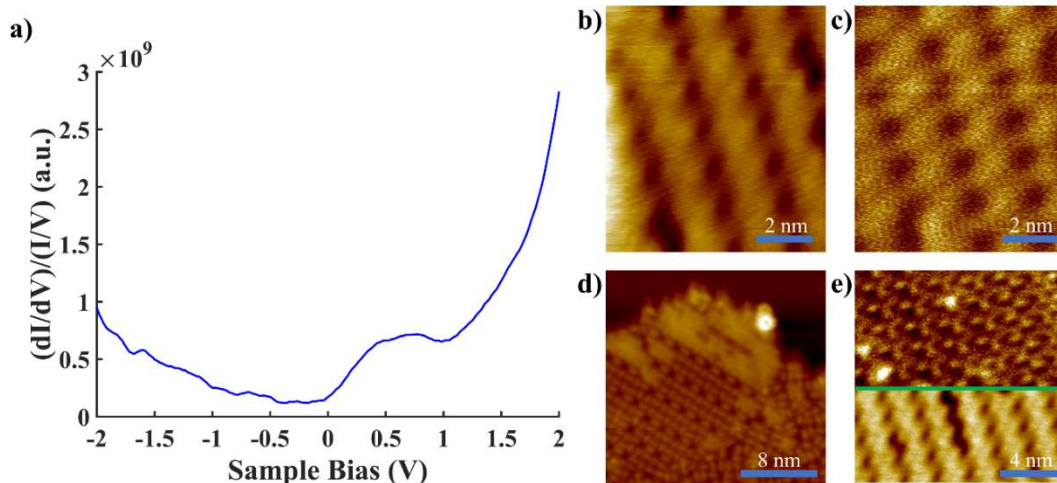


Figure 9-7: Electronic Structure of stripe phase K-TCNQ

(a) STS taken on the K-TCNQ structure ($V_s = 2$ V, $I_t = 200$ pA) reveals the presence of a broad unoccupied state peak. Simultaneously taken STM (b) and dI/dV maps (c) on the K-TCNQ structure taken at ($V_s = 0.8$ V, $I_t = 100$ pA) reveal further correlation between the geometric structure and the DOS distribution of K-TCNQ. (d) STM image ($V_s = 2$ V, $I_t = 5$ pA) of an area where the disordered and ordered phase of TCNQ and the two dimensional mesh phase of K-TCNQ. Despite having a sharp tip, K-TCNQ areas are hard to make out. (e) Bias-dependent STM images taken on the stripe phase of K-TCNQ at (top) ($V_s = -2$ V, $I_t = 200$ pA) and (bottom) ($V_s = 1$ V, $I_t = 5$ pA) reveals a strong electronic signature.

9.4 Conclusion and Future Studies

Based on the results of the different phases of K-TCNQ on Cu(111), it can be concluded that the Cu(111) substrate plays a significant role in perturbing the geometric and electronic structure of K-TCNQ as evidenced by the two-dimensional mesh structure of K-TCNQ which correlates to the bulk b-c plane and the observation of a broad unoccupied state that possibly originates from the hybridization/interaction between TCNQ molecules and the unoccupied state of K which resulted from K-Cu charge transfer. The introduction of K atoms into the TCNQ/Cu(111) system results in the reduction of the TCNQ-Cu interaction culminating in the formation of an incommensurate K_2 -TCNQ structure with an observed moiré pattern.

Further study on the K-TCNQ/Cu(111) system is complicated by the existence of the stripe phase of K-TCNQ on Cu(111) due to its structural inhomogeneity except in rare cases such as the condensed stripe phase structure. In order to circumvent the activation energy needed to reorder the K-TCNQ assembly, deposition of K atoms directly onto the elevated temperature phase of TCNQ might prove insightful. The K-TCNQ on Cu(111) system has demonstrated the initial signs of conductive behavior as observed from the delocalized DOS in STM imaging which sets the stage for developing a correlation between the thin film structures and the bulk properties of K-TCNQ. In order to further illuminate the properties of the thin-film phase of K-TCNQ, additional experiments targeted at studying the conducting $\pi - \pi$ stacking direction of K-TCNQ or the inter-stack coupling of K-TCNQ will need to be completed. By leveraging the large lattice constant of the deactivated Si(111)-B surface, a tilted or standing up phase of K-TCNQ could be formed which would allow for experiments to be conducted in the stacking direction of bulk K-TCNQ. On the other hand, deposition of K-TCNQ on h-BN passivated Cu(111) might prove more insightful due

its decoupling effects which would allow for a more pristine study of the inter-stack coupling of K-TCNQ.

10 Conclusion and Future Prospects

10.1 TTF-CA: A Novel Organic Ferroelectric

10.1.1 Introduction to TTF-CA

TTF-CA bulk crystal possesses a sizable ferroelectric polarization of $6.3\mu\text{C cm}^{-2}$ and a reasonably small coercive field of 5.4 kV cm^{-1} comparable to some inorganic ferroelectrics like barium titanate.[244,342]. Furthermore, this system is characterized by a valence instability resulting from a delicate balance between the electrostatic energy gain from ionic lattice formation (Madelung energy) and the energy cost of molecular ionization (energy offset between donor and acceptor levels) leading to the existence of a neutral ($\sim 0.34e$) to ionic ($\sim 0.52e$) (NI) transition as seen in Figure 10-1a.[242,244] This transition can be triggered by cooling TTF-CA crystals to 81K or subjecting it to 8kbar of pressure.[241,242,343]

The transition between neutral and ionic phases is a first order transition where a sudden increase in the degree of charge transfer between donor TTF molecules and acceptor CA molecules as well as the lattice parameters as shown in Figure 10-1a. The first order transition is likely the result of the litany of different interactions that occur in the TTF-CA lattice. Formation of O—H, C—Cl and S—Cl result in enhanced coupling throughout the molecular crystal, allowing for long-range ferroelectric domains to be formed.[344,345] The combined influence of these intermolecular bonds manifest in a similar first order transition in the lattice parameters in the b and c directions, outside of the principal stacking, a , direction which is also the direction $\pi - \pi$ interaction.[344] The fact that strong intermolecular interaction in the flat-lying b - c plane of TTF-CA makes it an enticing compound to study on h-BN. Within this system, the large degree of charge transfer is the result of strong hybridization observed between the HOMO of TTF and the LUMO of CA in its ionic phase.[241-243]

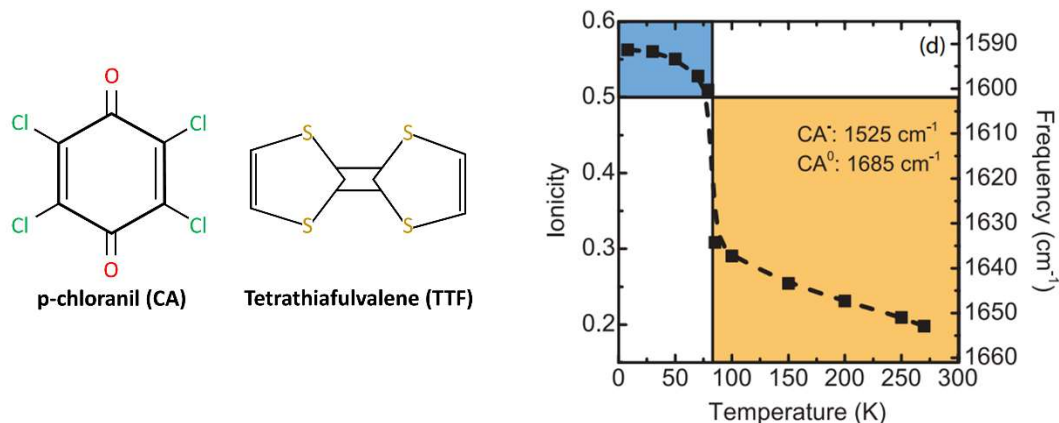


Figure 10-1: Properties of TTF-CA

(a) Schematic diagram of CA and TTF molecules. (b) Ionicity and Frequency vs Temperature of TTF-CA. The ionicity of the TTF-CA crystal increasing from $\sim 0.2e$ with decreasing temperature until a transition temperature of 81K is reached where a sudden increase in the ionicity to $0.5e$ is observed. Reproduced with permission from [245].

It is clear at this point that there is a strong interconnection between the molecular packing, intermolecular interaction, the degree of charge transfer and the properties of the CTC itself. Due to the ever pressing need to produce thinner and thinner devices, it is inevitable that organic CTCs will need to be applied in their thin film phase which requires the interfacing of the CTC with a supporting substrate. As noted from earlier discussion, the influence of the substrate cannot be ignored and could significantly alter the electronic and morphological properties of the CTC, and correspondingly, its physical properties. Thus far, TTF-CA represents a very promising organic ferroelectric material, however, the discussion of the properties of TTF-CA is limited to its bulk phase and a highly relevant question rests on whether the ferroelectric properties of a bulk organic CTC can survive in the highly altered electrostatic environment of a substrate-supported thin film phase.

10.1.2 Preliminary Data on the Growth of TTF-CA

The deposition of TTF-CA can be quite tricky due to the low sublimation temperatures and high vapor pressures of the parent molecules. Both molecules evaporate readily at room

temperature which prevents us from using the same methodology used to deposit ZnPc, F₁₆ZnPc and K-TCNQ as TTF-CA cannot be loaded into the UHV without severely compromising the vacuum. To circumvent this issue, the valved evaporators described in Section 5.4.3 was designed and installed. Preliminary growth experiments of TTF on the Cu(111) and deactivated Si(111)-B surface showed that the deposition via these evaporators was indeed possible. Deposition of CA forms an organized assembly on the surface of Cu(111), while deposited TTF molecules does not seem to readily order on Cu(111) as shown in Figure 10-2ab. Co-deposition of TTF-CA, on the other hand, forms an intriguing structure as shown Figure 10-2c Four lobes are observed that seem correlated to each other. Furthermore, these four-lobes are flanked by two additional lobes which delocalize into stripes at higher scanning bias. These structures are suspected to be the four Cl groups and the two O groups of CA, respectively. The row of seeming darker orbs are then suspected to be TTF molecules that could either lie flat or tilted with respect to the substrate. Further study could be undertaken to determine the exact molecular configuration of these structures. However, as concluded from the K-TCNQ study in Chapter 9, growth of CTC systems on metal are unlikely to produce the exotic electronic effects that we are seeking. Therefore, future studies should be focused on the growth of TTF-CA on h-BN/Cu(111) and the deactivated Si(111)-B surfaces.

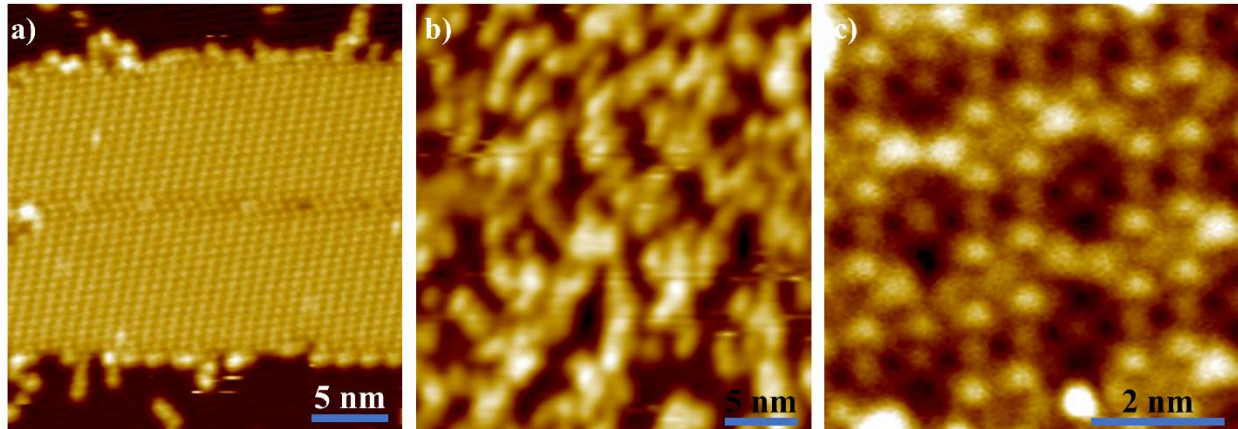


Figure 10-2: Growth of pure CA and TTF molecules grown on Cu(111)

(a) STM image of pure CA deposited on Cu(111) ($V_s = 2$ V, $I_t = 5$ pA) show the growth of an organized assembly in addition to scattered molecular clusters across the surface. (b) STM image of TTF deposited on Cu(111) ($V_s = 2$ V, $I_t = 5$ pA) show the lack of organized structures even at high molecular coverage. (c) Zoomed in STM image of the TTF-CA structure ($V_s = 0.1$ V, $I_t = 2$ pA). The four-lobed structures are suspected to be CA molecules with TTF molecules lying tilted with respect to the substrate in the dark trenches separating the CA molecules.

10.2 Summary of Results and Future Work

To develop a new generation of thin and efficient organic molecular electronics with unique physical properties, the nature of the molecule-substrate interaction and the different energy level alignment mechanisms should be carefully considered. In this dissertation, we have discussed the different aspects in tailoring the growth and electronic structures of organic molecular assemblies on weakly interacting substrates and how they might influence the overall energy level alignment that dictate critical contact properties for molecular electronics. Arising from the progress in establishing long-range ordered molecular thin films on weakly-interacting substrates, understanding and predicting the interfacial energy-level alignment in such systems becomes crucial. The accurate description of the density of states distribution of the frontier molecular orbitals will be instrumental in determining the charge injection barriers and the resulting contact resistance of organic electronic devices. However, due to the host of physical phenomena that can

affect both the geometric and electronic structures of organic molecular thin films, it is naturally difficult to control the organic molecular systems as the different aspects are often intertwined together in determining their properties. From a fundamental perspective, it is not surprising that a wide range of energy level alignment schemes and contact properties have been observed and argued in literature. Thorough characterization of the interfacial molecular morphology is indispensable for understanding the interfacial phenomena and for rationally controlling the interface. Stringent requirements need to be placed on the electrostatic environment of the molecules through not only the precise tailoring of the growth of the film, its interaction with neighboring molecules and the underlying substrate but also through the careful control and/or consideration of the substrate's subsurface as well.

Studies focusing on the electronic structure of ZnPc and F₁₆ZnPc on the deactivated Si(111)-B surface revealed the presence of interfacial charge transfer between F₁₆ZnPc monolayer and Si evidenced by the downward band bending in the bulk Si. Inhomogeneous electrostatic screening of the intra-orbital Coulomb interaction arising from the substrate boron distribution in the deactivated Si(111)-B substrate gives rise to a pronounced spatial variation of the occupied molecular state across the molecular assembly in contrast to constant energy levels of the molecular states of electrically neutral ZnPc assemblies. This observation puts a strong emphasis on the homogeneity of both the surface and near-surface regimes of semiconducting substrates as modulation in dopant concentration in the subsurface regime can drastically alter the molecular orbital energies and therefore, the charge injection/collection barriers.

Studies of ZnPc and F₁₆ZnPc on the geometrically flat but electronically corrugated h-BN/Cu(111) showed the growth of weakly-interacting organized pure and binary assemblies. 1:1 mixtures of ZnPc/F₁₆ZnPc yielded a checkerboard pattern that were adopted to minimize the F-F

repulsion between adjacent $F_{16}ZnPc$ molecules. Regardless of the molecules' location relative to the h-BN moiré pattern, the energy levels of molecular orbitals in the mixed structure are observed to upshift for ZnPc and downshift for $F_{16}ZnPc$ with respect to those of the pure phase. This trend runs contrary to the expected intermolecular charge transfer, instead leading to the conclusion that the enhanced charging of $F_{16}ZnPc$ molecules in the heterostructure is the result of interfacial charge transfer with the substrate. This is the result of the greater Madelung energy analog in the heterostructure compared to the pure phase due to the dielectric screening of ZnPc molecules. These results bring forth a troublesome complication as well as a fantastic opportunity for the design of thin film molecular heterojunctions on a supporting substrate. The presence of the substrate, even a weakly interacting one, such as h-BN/metal which does not perturb the pristine molecular orbitals and characteristics, can still lead to interfacial charge transfer and suppress intermolecular charge transfer. Steps will need to be taken to further isolate the donor-acceptor heterostructure from the substrate in order to preserve their intrinsic properties. The influence of the substrate could also serve as an additional tuning knob to aid the engineering of donor-acceptor heterostructure properties which could expand the scope of their potential (opto)electronic applications.

Since only preliminary results have been shown of both the K-TCNQ and the TTF-CA systems, more investigation will need to be carried out to further explore the properties of these unique organic CTC systems. The controlled growth and assembly of these systems on weakly-interacting substrates such as h-BN or the deactivated Si(111)-B could open the door to studying the metallic properties of K-TCNQ or the ferroelectric properties of TTF-CA in their thin film phases by STM/STS. Furthermore, the structural and electronic instabilities found by the geometric and electronic transitions in these systems could allow for the selection or alteration of

their fundamental CTC properties by the application of STM electric fields or substrate-induced electrostatic and geometric modulations which could lead to a better isolation of the fundamental physical mechanisms that dictate the properties of organic CTCs.

BIBLIOGRAPHY

BIBLIOGRAPHY

- [1] Nat Mater **12**, 591 (2013).
- [2] A. Facchetti, Chemistry of Materials **23**, 733 (2011).
- [3] W. Zhao, S. Li, H. Yao, S. Zhang, Y. Zhang, B. Yang, and J. Hou, J Am Chem Soc **139**, 7148 (2017).
- [4] L. Dou, Y. Liu, Z. Hong, G. Li, and Y. Yang, Chem Rev **115**, 12633 (2015).
- [5] S. E. Root, S. Savagatrup, A. D. Printz, D. Rodriguez, and D. J. Lipomi, Chem Rev **117**, 6467 (2017).
- [6] F. Yang, M. Shtein, and S. R. Forrest, Nature Materials **4**, 37 (2004).
- [7] W. G., Journal of Materials Research **19**, 1889 (2004).
- [8] S. R. Forrest, Nature **428**, 911 (2004).
- [9] Y. Yuan *et al.*, Nat Commun **5**, 3005 (2014).
- [10] J. Lewis, Materials Today **9**, 38 (2006).
- [11] F. Schreiber, physica status solidi (a) **201**, 1037 (2004).
- [12] C. G. Claessens, U. Hahn, and T. Torres, The Chemical Record **8**, 75 (2008).
- [13] M. Brendel *et al.*, Advanced Functional Materials **25**, 1565 (2015).
- [14] J. A. A. W. Elemans, R. van Hameren, R. J. M. Nolte, and A. E. Rowan, Advanced Materials **18**, 1251 (2006).
- [15] K. K. McGrath, K. Jang, K. A. Robins, and D. C. Lee, Chemistry **15**, 4070 (2009).
- [16] K. Takimiya, S. Shinamura, I. Osaka, and E. Miyazaki, Adv Mater **23**, 4347 (2011).
- [17] A. Gerlach, S. Sellner, S. Kowarik, and F. Schreiber, physica status solidi (a) **205**, 461 (2008).
- [18] J. E. Goose, E. L. First, and P. Clancy, Physical Review B **81**, 205310 (2010).
- [19] F. J. Meyer zu Heringdorf, M. C. Reuter, and R. M. Tromp, Nature **412**, 517 (2001).
- [20] G. Hlawacek, P. Puschnig, P. Frank, A. Winkler, C. Ambrosch-Draxl, and C. Teichert, Science **321**, 108 (2008).

- [21] J. Rivnay, L. H. Jimison, J. E. Northrup, M. F. Toney, R. Noriega, S. Lu, T. J. Marks, A. Facchetti, and A. Salleo, *Nat Mater* **8**, 952 (2009).
- [22] A. Shehu, S. D. Quiroga, P. D'Angelo, C. Albonetti, F. Borgatti, M. Murgia, A. Scorzoni, P. Stoliar, and F. Biscarini, *Physical Review Letters* **104**, 246602 (2010).
- [23] A. B. Chwang and C. D. Frisbie, *Journal of Applied Physics* **90**, 1342 (2001).
- [24] M. Tello, M. Chiesa, C. M. Duffy, and H. Sirringhaus, *Advanced Functional Materials* **18**, 3907 (2008).
- [25] V. Kalihari, E. B. Tadmor, G. Haugstad, and C. D. Frisbie, *Advanced Materials* **20**, 4033 (2008).
- [26] S. Kowarik, A. Gerlach, and F. Schreiber, *Journal of Physics: Condensed Matter* **20**, 184005 (2008).
- [27] W. Chen, S. Chen, S. Chen, Y. Li Huang, H. Huang, D. C. Qi, X. Y. Gao, J. Ma, and A. T. S. Wee, *Journal of Applied Physics* **106**, 064910 (2009).
- [28] W. Chen, H. Huang, S. Chen, Y. L. Huang, X. Y. Gao, and A. T. S. Wee, *Chemistry of Materials* **20**, 7017 (2008).
- [29] S. Duhm, G. Heimel, I. Salzmann, H. Glowatzki, R. L. Johnson, A. Vollmer, J. P. Rabe, and N. Koch, *Nat Mater* **7**, 326 (2008).
- [30] W. N. Han *et al.*, *Applied Physics Letters* **103**, 253301 (2013).
- [31] G. Heimel, I. Salzmann, S. Duhm, and N. Koch, *Chemistry of Materials* **23**, 359 (2011).
- [32] I. Avilov, V. Geskin, and J. Cornil, *Advanced Functional Materials* **19**, 624 (2009).
- [33] S. Verlaak, D. Beljonne, D. Cheyngs, C. Rolin, M. Linares, F. Castet, J. Cornil, and P. Heremans, *Advanced Functional Materials* **19**, 3809 (2009).
- [34] J. B. Neaton, M. S. Hybertsen, and S. G. Louie, *Physical Review Letters* **97**, 216405 (2006).
- [35] M. Linares *et al.*, *J Phys Chem C* **114**, 3215 (2010).
- [36] S. R. Yost, L. P. Wang, and T. Van Voorhis, *J Phys Chem C* **115**, 14431 (2011).
- [37] X. Lu, M. Grobis, K. H. Khoo, S. G. Louie, and M. F. Crommie, *Physical Review B* **70**, 115418 (2004).
- [38] J. D. Sau, J. B. Neaton, H. J. Choi, S. G. Louie, and M. L. Cohen, *Physical Review Letters* **101**, 026804 (2008).
- [39] I. Fernández Torrente, K. J. Franke, and J. Ignacio Pascual, *Journal of Physics: Condensed Matter* **20**, 184001 (2008).

- [40] S. Braun, W. R. Salaneck, and M. Fahlman, *Advanced Materials* **21**, 1450 (2009).
- [41] S. Braun, W. Osikowicz, Y. Wang, and W. R. Salaneck, *Organic Electronics* **8**, 14 (2007).
- [42] Y. J. Zheng *et al.*, *Acs Nano* **10**, 2476 (2016).
- [43] J. Hwang, A. Wan, and A. Kahn, *Materials Science and Engineering: R: Reports* **64**, 1 (2009).
- [44] D. Cahen, A. Kahn, and E. Umbach, *Materials Today* **8**, 32 (2005).
- [45] A. Tan and P. Zhang, in *Encyclopedia of Interfacial Chemistry* (Elsevier, 2018), pp. 267
- [46] A. Tan and P. Zhang, *Journal of Physics: Condensed Matter* (2019).
- [47] G. M. Whitesides, Mathias, J.P. , Seto, C.T., *Science*, 1312 (1991).
- [48] J. A. Theobald, N. S. Oxtoby, M. A. Phillips, N. R. Champness, and P. H. Beton, *Nature* **424**, 1029 (2003).
- [49] M. E. Canas-Ventura, W. Xiao, D. Wasserfallen, K. Mullen, H. Brune, J. V. Barth, and R. Fasel, *Angewandte Chemie* **46**, 1814 (2007).
- [50] S. Furukawa, K. Tahara, F. C. De Schryver, M. Van der Auweraer, Y. Tobe, and S. De Feyter, *Angewandte Chemie* **46**, 2831 (2007).
- [51] M. de Wild, S. Berner, H. Suzuki, H. Yanagi, D. Schlettwein, S. Ivan, A. Baratoff, H.-J. Guentherodt, and T. A. Jung, *ChemPhysChem* **3**, 881 (2002).
- [52] Y. Wakayama, *Japanese Journal of Applied Physics* **55**, 1102AA (2016).
- [53] T. Yokoyama, S. Yokoyama, T. Kamikado, Y. Okuno, and S. Mashiko, *Nature* **413**, 619 (2001).
- [54] C. Ratsch and J. A. Venables, *Journal of Vacuum Science & Technology A: Vacuum, Surfaces, and Films* **21**, S96 (2003).
- [55] A. Kühnle, *Current Opinion in Colloid & Interface Science* **14**, 157 (2009).
- [56] J. V. Barth, G. Costantini, and K. Kern, *Nature* **437**, 671 (2005).
- [57] A. Kubono and R. Akiyama, *Journal of Applied Physics* **98**, 093502 (2005).
- [58] H. Sitter, R. Resel, G. Koller, M. G. Ramsey, A. Andreev, and C. Teichert, **101**, 3 (2008).
- [59] I. V. Markov, *Crystal Growth for Beginners: Fundamentals of Nucleation, Crystal Growth, and Epitaxy* (World Scientific Publishing Co. Pte. Ltd., 2003), 2nd edn.

- [60] K. Byrappa, T. Ohachi, W. Michaeli, H. Warlimont, and E. Weber, in *Crystal Growth Technology* (William Andrew Inc., 2003), pp. 25.
- [61] D. E. Savage, F. Liu, V. Zielasek, and M. G. Lagally, in *Germanium Silicon: Physics and Materials* (1998), pp. 49.
- [62] T. A. Witten and L. M. Sander, *Physical Review Letters* **47**, 1400 (1981).
- [63] Z. Zhang, *Science* **276**, 377 (1997).
- [64] X. N. Zhang, E. Barrena, D. G. de Oteyza, and H. Dosch, *Surface Science* **601**, 2420 (2007).
- [65] R. L. Schwoebel and E. J. Shipsey, *Journal of Applied Physics* **37**, 3682 (1966).
- [66] S.-C. Li, Y. Han, J.-F. Jia, Q.-K. Xue, and F. Liu, *Physical Review B* **74**, 195428 (2006).
- [67] H. Zheng, M. H. Xie, H. S. Wu, and Q. K. Xue, *Physical Review B* **77**, 045303 (2008).
- [68] J. Krug, P. Politi, and T. Michely, *Physical Review B* **61**, 14037 (2000).
- [69] A. C. Mayer, R. Ruiz, H. Zhou, R. L. Headrick, A. Kazimirov, and G. G. Malliaras, *Physical Review B* **73**, 205307 (2006).
- [70] X. Zhang, E. Barrena, D. Goswami, D. G. de Oteyza, C. Weis, and H. Dosch, *Physical Review Letters* **103**, 136101 (2009).
- [71] A. Tan, S. Wagner, and P. Zhang, *The Journal of Chemical Physics* **146**, 052809 (2017).
- [72] G. E. Thayer, J. T. Sadowski, F. Meyer zu Heringdorf, T. Sakurai, and R. M. Tromp, *Phys Rev Lett* **95**, 256106 (2005).
- [73] T. J. Z. Stock and J. Nogami, *Surface Science* **637-638**, 132 (2015).
- [74] D. Käfer, L. Ruppel, and G. Witte, *Physical Review B* **75**, 085309 (2007).
- [75] Y. Zheng, D. Qi, N. Chandrasekhar, X. Gao, C. Troadec, and A. T. Wee, *Langmuir* **23**, 8336 (2007).
- [76] D. G. de Oteyza, E. Barrena, H. Dosch, and Y. Wakayama, *Phys Chem Chem Phys* **11**, 8741 (2009).
- [77] Y. Wakayama, *J Phys Chem C* **111**, 2675 (2007).
- [78] K. Glöckler, C. Seidel, A. Soukopp, M. Sokolowski, E. Umbach, M. Böhringer, R. Berndt, and W. D. Schneider, *Surface Science* **405**, 1 (1998).
- [79] H. Glowatzki, S. Duhm, K. F. Braun, J. P. Rabe, and N. Koch, *Physical Review B* **76**, 125425 (2007).

- [80] B. Krause, F. Schreiber, H. Dosch, A. Pimpinelli, and O. H. Seeck, *Europhysics Letters (EPL)* **65**, 372 (2004).
- [81] B. Krause, A. C. Dürr, K. Ritley, F. Schreiber, H. Dosch, and D. Smilgies, *Physical Review B* **66**, 235404 (2002).
- [82] S. Kowarik, A. Gerlach, S. Sellner, F. Schreiber, L. Cavalcanti, and O. Konovalov, *Physical Review Letters* **96**, 125504 (2006).
- [83] R. R. Lunt, J. B. Benziger, and S. R. Forrest, *Applied Physics Letters* **90**, 181932 (2007).
- [84] A. C. Mayer, R. Ruiz, R. L. Headrick, A. Kazimirov, and G. G. Malliaras, *Organic Electronics* **5**, 257 (2004).
- [85] R. Ruiz *et al.*, *Chemistry of Materials* **16**, 4497 (2004).
- [86] S. Kowarik, A. Gerlach, W. Leitenberger, J. Hu, G. Witte, C. Wöll, U. Pietsch, and F. Schreiber, *Thin Solid Films* **515**, 5606 (2007).
- [87] R. Banerjee, J. Novak, C. Frank, C. Lorch, A. Hinderhofer, A. Gerlach, and F. Schreiber, *Phys Rev Lett* **110**, 185506 (2013).
- [88] S. R. Wagner and P. P. Zhang, *J Phys Chem C* **118**, 2194 (2014).
- [89] T. Wang, T. R. Kafle, B. Kattel, Q. Liu, J. Wu, and W. L. Chan, *Sci Rep* **6**, 28895 (2016).
- [90] F. Sellam, T. Schmitz-Hübsch, M. Toerker, S. Mannsfeld, H. Proehl, T. Fritz, K. Leo, C. Simpson, and K. Müllen, *Surface Science* **478**, 113 (2001).
- [91] L. Kilian, E. Umbach, and M. Sokolowski, *Surface Science* **573**, 359 (2004).
- [92] A. Franco-Cañellas *et al.*, *Physical Review Materials* **1**, 013001 (2017).
- [93] A. Tan, S. R. Wagner, and P. P. Zhang, *Physical Review B* **96**, 035313 (2017).
- [94] M. Toader, T. G. Gopakumar, P. Shukrynau, and M. Hietschold, *J Phys Chem C* **114**, 21548 (2010).
- [95] W. H. Soe, C. Manzano, H. S. Wong, and C. Joachim, *J Phys Condens Matter* **24**, 354011 (2012).
- [96] A. Mugarza, R. Robles, C. Krull, R. Korytár, N. Lorente, and P. Gambardella, *Physical Review B* **85**, 155437 (2012).
- [97] S. R. Forrest and M. E. Thompson, *Chemical Reviews* **107**, 923 (2007).
- [98] G. Chen, Z. Ling, B. Wei, J. Zhang, Z. Hong, H. Sasabe, and J. Kido, *Front Chem* **6**, 412 (2018).

- [99] Y. Diao, L. Shaw, Z. Bao, and S. C. B. Mannsfeld, *Energy Environ. Sci.* **7**, 2145 (2014).
- [100] M. Chang, G. T. Lim, B. Park, and E. Reichmanis, *Polymers (Basel)* **9** (2017).
- [101] L. Shaw and Z. Bao, *Israel Journal of Chemistry* **54**, 496 (2014).
- [102] L. Grill, I. Stass, K.-H. Rieder, and F. Moresco, *Surface Science* **600**, L143 (2006).
- [103] Y. Terada, B.-K. Choi, S. Heike, M. Fujimori, and T. Hashizume, *Nano Letters* **3**, 527 (2003).
- [104] A. Piqué *et al.*, *Thin Solid Films* **355-356**, 536 (1999).
- [105] S. R. Forrest, *Chemical Reviews* **97**, 1793 (1997).
- [106] A. Hinaut *et al.*, *Nanoscale* **10**, 1337 (2018).
- [107] A. Hinaut, R. Pawlak, E. Meyer, and T. Glatzel, *Beilstein J Nanotechnol* **6**, 1927 (2015).
- [108] R. R. Lunt, B. E. Lassiter, J. B. Benziger, and S. R. Forrest, *Applied Physics Letters* **95**, 233305 (2009).
- [109] S. Iannotta and T. Toccoli, *Journal of Polymer Science Part B: Polymer Physics* **41**, 2501 (2003).
- [110] T. V. Desai, A. R. Woll, F. Schreiber, and J. R. Engstrom, *J Phys Chem C* **114**, 20120 (2010).
- [111] S. R. Wagner and P. Zhang, *Surf. Sci.* **630**, 22 (2014).
- [112] S. R. Wagner, B. Huang, C. Park, J. Feng, M. Yoon, and P. Zhang, *Physical Review Letters* **115**, 096101 (2015).
- [113] S. R. Wagner, R. R. Lunt, and P. Zhang, *Physical Review Letters* **110**, 086107 (2013).
- [114] B. Baris, V. Luzet, E. Duverger, P. Sonnet, F. Palmino, and F. Cherioux, *Angewandte Chemie* **50**, 4094 (2011).
- [115] B. Baris, J. Jeannoutot, V. Luzet, F. Palmino, A. Rochefort, and F. Cherioux, *Acs Nano* **6**, 6905 (2012).
- [116] Y. Makoudi, F. Palmino, M. Arab, E. Duverger, and F. Cherioux, *Journal of the American Chemical Society* **130**, 6670 (2008).
- [117] G. Copie, Y. Makoudi, C. Krzeminski, F. Chérioux, F. Palmino, S. Lamare, B. Grandidier, and F. Cleri, *J Phys Chem C* **118**, 12817 (2014).
- [118] I. I. Lyo, E. Kaxiras, and P. Avouris, *Phys Rev Lett* **63**, 1261 (1989).

- [119] D. Jariwala *et al.*, *Nano Lett* **16**, 497 (2016).
- [120] A. Kumar, K. Banerjee, and P. Liljeroth, *Nanotechnology* **28**, 082001 (2017).
- [121] H. Z. Tsai *et al.*, *Acs Nano* **9**, 12168 (2015).
- [122] T. Tian and C.-J. Shih, *Industrial & Engineering Chemistry Research* **56**, 10552 (2017).
- [123] Y. Zhang *et al.*, *Nano Lett* **14**, 5547 (2014).
- [124] Y. Liu, N. O. Weiss, X. Duan, H.-C. Cheng, Y. Huang, and X. Duan, *Nature Reviews Materials* **1**, 16042 (2016).
- [125] G.-H. Lee *et al.*, *APL Materials* **2**, 092511 (2014).
- [126] K. L. Kim *et al.*, *Nano Lett* **16**, 334 (2016).
- [127] J. Cervenka *et al.*, *Nanoscale* **7**, 1471 (2015).
- [128] P. Jarvinen, S. K. Hamalainen, K. Banerjee, P. Hakkinen, M. Ijas, A. Harju, and P. Liljeroth, *Nano Lett* **13**, 3199 (2013).
- [129] A. Tarasov, S. Zhang, M. Y. Tsai, P. M. Campbell, S. Graham, S. Barlow, S. R. Marder, and E. M. Vogel, *Adv Mater* **27**, 1175 (2015).
- [130] E. J. G. Santos, D. Scullion, X. S. Chu, D. O. Li, N. P. Guisinger, and Q. H. Wang, *Nanoscale* **9**, 13245 (2017).
- [131] S. Bettis Homan, V. K. Sangwan, I. Balla, H. Bergeron, E. A. Weiss, and M. C. Hersam, *Nano Lett* **17**, 164 (2017).
- [132] D. Jariwala, T. J. Marks, and M. C. Hersam, *Nat Mater* **16**, 170 (2017).
- [133] T. Roy, M. Tosun, J. S. Kang, A. B. Sachid, S. B. Desai, M. Hettick, C. C. Hu, and A. Javey, *Acs Nano* **8**, 6259 (2014).
- [134] S. Das, R. Gulotty, A. V. Sumant, and A. Roelofs, *Nano Lett* **14**, 2861 (2014).
- [135] M. Gobbi, E. Orgiu, and P. Samori, *Adv Mater* **30**, e1706103 (2018).
- [136] S. J. Kang *et al.*, *Advanced Functional Materials* **24**, 5157 (2014).
- [137] Y. L. Huang, Y. J. Zheng, Z. Song, D. Chi, A. T. S. Wee, and S. Y. Quek, *Chem Soc Rev* **47**, 3241 (2018).
- [138] W. Xia, L. Dai, P. Yu, X. Tong, W. Song, G. Zhang, and Z. Wang, *Nanoscale* **9**, 4324 (2017).
- [139] D. He *et al.*, *Applied Physics Letters* **107**, 183103 (2015).

- [140] L. Yu, A. Zubair, E. J. Santos, X. Zhang, Y. Lin, Y. Zhang, and T. Palacios, *Nano Lett* **15**, 4928 (2015).
- [141] M. Gobbi *et al.*, *Nat Commun* **8**, 14767 (2017).
- [142] A. J. Samuels and J. D. Carey, *Acs Nano* **7**, 2790 (2013).
- [143] J. Park *et al.*, *Adv Mater* **24**, 407 (2012).
- [144] W. J. Yu, L. Liao, S. H. Chae, Y. H. Lee, and X. Duan, *Nano Lett* **11**, 4759 (2011).
- [145] D. He *et al.*, *Nat Commun* **5**, 5162 (2014).
- [146] F. Yang, S. Cheng, X. Zhang, X. Ren, R. Li, H. Dong, and W. Hu, *Adv Mater* **30**, 1702415 (2018).
- [147] S. Liu, R. He, Z. Ye, X. Du, J. Lin, H. Jiang, B. Liu, and J. H. Edgar, *Crystal Growth & Design* **17**, 4932 (2017).
- [148] Y. Ji *et al.*, *Acs Nano* **11**, 12057 (2017).
- [149] Y. Bleu, F. Bourquard, T. Tite, A. S. Loir, C. Maddi, C. Donnet, and F. Garrelie, *Front Chem* **6**, 572 (2018).
- [150] J. H. Lee *et al.*, *Science* **344**, 286 (2014).
- [151] J. S. Lee *et al.*, *Science* **362**, 817 (2018).
- [152] D. He *et al.*, *Sci Adv* **3**, e1701186 (2017).
- [153] B. Lussem, C. M. Keum, D. Kasemann, B. Naab, Z. Bao, and K. Leo, *Chem Rev* **116**, 13714 (2016).
- [154] C. Liu, Y. Xu, and Y.-Y. Noh, *Materials Today* **18**, 79 (2015).
- [155] M. T. Greiner, M. G. Helander, W. M. Tang, Z. B. Wang, J. Qiu, and Z. H. Lu, *Nat Mater* **11**, 76 (2011).
- [156] S. Joshi *et al.*, *Nano Lett* **12**, 5821 (2012).
- [157] K. Akaike, *Japanese Journal of Applied Physics* **57**, 03ea03 (2018).
- [158] J.-P. Yang *et al.*, *Organic Electronics* **48**, 172 (2017).
- [159] M. Oehzelt, N. Koch, and G. Heimel, *Nat Commun* **5**, 4174 (2014).
- [160] A. Fahlman, C. Nordling, and K. Siegbahn, *ESCA : atomic, molecular and solid state structure studied by means of electron spectroscopy* (Uppsala : Almqvist and Wiksell, 1967).

- [161] H. Yamane and N. Kosugi, *Journal of Electron Spectroscopy and Related Phenomena* **204**, 61 (2015).
- [162] F. Bussolotti, J. Yang, A. Hinderhofer, Y. Huang, W. Chen, S. Kera, A. T. S. Wee, and N. Ueno, *Physical Review B* **89**, 115319 (2014).
- [163] A. Mugarza, C. Krull, R. Robles, S. Stepanow, G. Ceballos, and P. Gambardella, *Nat Commun* **2**, 490 (2011).
- [164] K. A. Cochrane, A. Schiffrin, T. S. Roussy, M. Capsoni, and S. A. Burke, *Nat Commun* **6**, 8312 (2015).
- [165] F. Haidu, G. Salvan, D. R. T. Zahn, L. Smykalla, M. Hietschold, and M. Knupfer, *Journal of Vacuum Science & Technology A: Vacuum, Surfaces, and Films* **32**, 040602 (2014).
- [166] S. M. Ryno, C. Risko, and J. L. Bredas, *J Am Chem Soc* **136**, 6421 (2014).
- [167] S. M. Ryno, C. Risko, and J. L. Bredas, *ACS Appl Mater Interfaces* **8**, 14053 (2016).
- [168] S. Soubatch, C. Weiss, R. Temirov, and F. S. Tautz, *Phys Rev Lett* **102**, 177405 (2009).
- [169] J. M. Garcia-Lastra, C. Rostgaard, A. Rubio, and K. S. Thygesen, *Physical Review B* **80**, 245427 (2009).
- [170] P. Puschnig, P. Amiri, and C. Draxl, *Physical Review B* **86**, 085107 (2012).
- [171] D. A. Egger, Z. F. Liu, J. B. Neaton, and L. Kronik, *Nano Lett* **15**, 2448 (2015).
- [172] Y. Kang, S. H. Jeon, Y. Cho, and S. Han, *Physical Review B* **93**, 035131 (2016).
- [173] J. Kerfoot *et al.*, *J Chem Phys* **149**, 054701 (2018).
- [174] R. Hesper, L. H. Tjeng, and G. A. Sawatzky, *Europhysics Letters (EPL)* **40**, 177 (1997).
- [175] M. Hollerer *et al.*, *Acs Nano* **11**, 6252 (2017).
- [176] M. G. Helander, M. T. Greiner, Z. B. Wang, and Z. H. Lu, *Physical Review B* **81**, 153308 (2010).
- [177] L.-H. Zhao, R.-Q. Peng, C. C. H. Chiam, H. Guo, J.-M. Zhuo, L.-L. Chua, A. T. S. Wee, and P. K. H. Ho, *Applied Physics Letters* **101**, 053304 (2012).
- [178] S. Ossicini, C. M. Bertoni, and P. Gies, *Europhysics Letters (EPL)* **1**, 661 (1986).
- [179] N. Koch, A. Vollmer, S. Duhm, Y. Sakamoto, and T. Suzuki, *Advanced Materials* **19**, 112 (2007).
- [180] I. Salzmann, S. Duhm, G. Heimel, M. Oehzelt, R. Kniprath, R. L. Johnson, J. P. Rabe, and N. Koch, *J Am Chem Soc* **130**, 12870 (2008).

- [181] L. Zhang, S. S. Roy, R. J. Hamers, M. S. Arnold, and T. L. Andrew, *J Phys Chem C* **119**, 45 (2014).
- [182] G. D'Avino, L. Muccioli, F. Castet, C. Poelking, D. Andrienko, Z. G. Soos, J. Cornil, and D. Beljonne, *J Phys Condens Matter* **28**, 433002 (2016).
- [183] A. Opitz *et al.*, *Sci Rep* **6**, 21291 (2016).
- [184] P. Lang, M. E. Ardhaoui, J. C. Wittmann, J. P. Dallas, G. Horowitz, B. Lotz, F. Garnier, and C. Straupe, *Synthetic Metals* **84**, 605 (1997).
- [185] J. Q. Zhong, H. Y. Mao, R. Wang, D. C. Qi, L. Cao, Y. Z. Wang, and W. Chen, *J Phys Chem C* **115**, 23922 (2011).
- [186] D. Çakir, M. Bokdam, M. P. de Jong, M. Fahlman, and G. Brocks, *Applied Physics Letters* **100**, 203302 (2012).
- [187] M. M. Byranvand, T. Kim, S. Song, G. Kang, S. U. Ryu, and T. Park, *Advanced Energy Materials* **8**, 1702235 (2018).
- [188] B. P. Rand *et al.*, *Advanced Functional Materials* **22**, 2987 (2012).
- [189] M. Willenbockel, D. Luftner, B. Stadtmuller, G. Koller, C. Kumpf, S. Soubatch, P. Puschnig, M. G. Ramsey, and F. S. Tautz, *Phys Chem Chem Phys* **17**, 1530 (2015).
- [190] D. G. de Oteyza *et al.*, *J Chem Phys* **133**, 214703 (2010).
- [191] M. Alemani, S. Selvanathan, F. Ample, M. V. Peters, K.-H. Rieder, F. Moresco, C. Joachim, S. Hecht, and L. Grill, *J Phys Chem C* **112**, 10509 (2008).
- [192] R. J. Maurer, V. G. Ruiz, J. Camarillo-Cisneros, W. Liu, N. Ferri, K. Reuter, and A. Tkatchenko, *Progress in Surface Science* **91**, 72 (2016).
- [193] O. Bauer *et al.*, *Physical Review B* **86**, 235431 (2012).
- [194] C. Uhlmann, I. Swart, and J. Repp, *Nano Lett* **13**, 777 (2013).
- [195] M. Takada and H. Tada, *Japanese Journal of Applied Physics* **44**, 5332 (2005).
- [196] T. Frederiksen, K. J. Franke, A. Arnau, G. Schulze, J. I. Pascual, and N. Lorente, *Physical Review B* **78**, 233401 (2008).
- [197] M. Stöhr, M. Wahl, C. H. Galka, T. Riehm, T. A. Jung, and L. H. Gade, *Angewandte Chemie* **117**, 7560 (2005).
- [198] D. J. Lavrich, S. M. Wetterer, S. L. Bernasek, and G. Scoles, *The Journal of Physical Chemistry B* **102**, 3456 (1998).

- [199] P. Amsalem, G. Heimel, and N. Koch, in *Encyclopedia of Interfacial Chemistry* (Elsevier, 2018), pp. 50.
- [200] M. N. Faraggi, N. Jiang, N. Gonzalez-Lakunza, A. Langner, S. Stepanow, K. Kern, and A. Arnau, *J Phys Chem C* **116**, 24558 (2012).
- [201] F. S. Tautz, M. Eremtchenko, J. A. Schaefer, M. Sokolowski, V. Shklover, and E. Umbach, *Physical Review B* **65**, 125405 (2002).
- [202] O. T. Hofmann, P. Rinke, M. Scheffler, and G. Heimel, *Acs Nano* **9**, 5391 (2015).
- [203] T. R. Umbach, I. Fernandez-Torrente, J. N. Ladenthin, J. I. Pascual, and K. J. Franke, *J Phys Condens Matter* **24**, 354003 (2012).
- [204] S.-A. Savu, G. Biddau, L. Pardini, R. Bula, H. F. Bettinger, C. Draxl, T. Chassé, and M. B. Casu, *J Phys Chem C* **119**, 12538 (2015).
- [205] S. Joshi *et al.*, *Acs Nano* **8**, 430 (2014).
- [206] M. Gruenewald *et al.*, *J Phys Chem C* **119**, 4865 (2015).
- [207] S. Winkler, P. Amsalem, J. Frisch, M. Oehzelt, G. Heimel, and N. Koch, *Materials Horizons* **2**, 427 (2015).
- [208] A. Della Pia, M. Riello, A. Floris, D. Stassen, T. S. Jones, D. Bonifazi, A. De Vita, and G. Costantini, *Acs Nano* **8**, 12356 (2014).
- [209] P. Amsalem, J. Niederhausen, A. Wilke, G. Heimel, R. Schlesinger, S. Winkler, A. Vollmer, J. P. Rabe, and N. Koch, *Physical Review B* **87**, 035440 (2013).
- [210] H. Wang, P. Amsalem, G. Heimel, I. Salzmann, N. Koch, and M. Oehzelt, *Adv Mater* **26**, 925 (2014).
- [211] J. Repp, G. Meyer, S. Paavilainen, F. E. Olsson, and M. Persson, *Science* **312**, 1196 (2006).
- [212] U. Ham and W. Ho, *J Chem Phys* **138**, 074703 (2013).
- [213] C. Krull, R. Robles, A. Mugarza, and P. Gambardella, *Nat Mater* **12**, 337 (2013).
- [214] S. Braun and W. R. Salaneck, *Chemical Physics Letters* **438**, 259 (2007).
- [215] A. D. Pia *et al.*, *ChemPhysChem* **19**, 2405 (2018).
- [216] A. Kumar, K. Banerjee, M. Dvorak, F. Schulz, A. Harju, P. Rinke, and P. Liljeroth, *Acs Nano* **11**, 4960 (2017).
- [217] J. Wang, L. Xu, Y. J. Lee, M. De Anda Villa, A. V. Malko, and J. W. Hsu, *Nano Lett* **15**, 7627 (2015).

- [218] R. Steim, F. R. Kogler, and C. J. Brabec, *Journal of Materials Chemistry* **20**, 2499 (2010).
- [219] R. Q. Png, M. C. Ang, M. H. Teo, K. K. Choo, C. G. Tang, D. Belaineh, L. L. Chua, and P. K. Ho, *Nat Commun* **7**, 11948 (2016).
- [220] L. Ley, Y. Smets, C. I. Pakes, and J. Ristein, *Advanced Functional Materials* **23**, 794 (2013).
- [221] Y.-Y. Du *et al.*, *AIP Advances* **9**, 045122 (2019).
- [222] Q. Bao, S. Fabiano, M. Andersson, S. Braun, Z. Sun, X. Crispin, M. Berggren, X. Liu, and M. Fahlman, *Advanced Functional Materials* **26**, 1077 (2016).
- [223] T. Matsushima, Y. Kinoshita, and H. Murata, *Applied Physics Letters* **91**, 253504 (2007).
- [224] N. B. Kotadiya, H. Lu, A. Mondal, Y. Ie, D. Andrienko, P. W. M. Blom, and G. A. H. Wetzelaer, *Nat Mater* **17**, 329 (2018).
- [225] M. Oehzelt, K. Akaike, N. Koch, and G. Heimel, *Sci Adv* **1**, e1501127 (2015).
- [226] E. K. Lee, M. Y. Lee, C. H. Park, H. R. Lee, and J. H. Oh, *Adv Mater* **29** (2017).
- [227] S. Sinha, C. H. Wang, M. Mukherjee, T. Mukherjee, and Y. W. Yang, *Langmuir* **30**, 15433 (2014).
- [228] Q. Bao, X. Liu, S. Braun, J. Yang, Y. Li, J. Tang, C. Duan, and M. Fahlman, *ACS Appl Mater Interfaces* **10**, 6491 (2018).
- [229] Y. Yin, D. A. Lewis, and G. G. Andersson, *ACS Appl Mater Interfaces* **10**, 44163 (2018).
- [230] J. Q. Zhong, H. Y. Mao, R. Wang, J. D. Lin, Y. B. Zhao, J. L. Zhang, D. G. Ma, and W. Chen, *Organic Electronics* **13**, 2793 (2012).
- [231] H. Klauk, in *Handbook of Visual Display Technology* (Springer Berlin Heidelberg, Berlin, Heidelberg, 2014), pp. 1.
- [232] D. Yu, Y.-Q. Yang, Z. Chen, Y. Tao, and Y.-F. Liu, *Optics Communications* **362**, 43 (2016).
- [233] J. B. Torrance, *Annals of the New York Academy of Sciences* **313**, 210 (1978).
- [234] G. Saito and Y. Yoshida, *Top Curr Chem* **312**, 67 (2012).
- [235] K. P. Goetz, D. Vermeulen, M. E. Payne, C. Kloc, L. E. McNeil, and O. D. Jurchescu, *J. Mater. Chem. C* **2**, 3065 (2014).
- [236] J.-P. Pouget, P. Alemany, and E. Canadell, *Materials Horizons* **5**, 590 (2018).
- [237] R. Rösslhuber, E. Rose, T. Ivek, A. Pustogow, T. Breier, M. Geiger, K. Schrem, G. Untereiner, and M. Dressel, *Crystals* **8**, 121 (2018).

- [238] K. Ragavendran, D. Vasudevan, A. Veluchamy, and B. Emmanuel, *The Journal of Physical Chemistry B* **108**, 16899 (2004).
- [239] L. Glasser, *Inorg Chem* **51**, 2420 (2012).
- [240] G. Saito and Y. Yoshida, *Bulletin of the Chemical Society of Japan* **80**, 1 (2007).
- [241] R. Takehara, K. Sunami, F. Iwase, M. Hosoda, K. Miyagawa, T. Miyamoto, H. Okamoto, and K. Kanoda, *Physical Review B* **98** (2018).
- [242] M. Dressel and T. Peterseim, *Crystals* **7**, 17 (2017).
- [243] S. Horiuchi, K. Kobayashi, R. Kumai, and S. Ishibashi, *Chemistry Letters* **43**, 26 (2014).
- [244] K. Kobayashi, S. Horiuchi, R. Kumai, F. Kagawa, Y. Murakami, and Y. Tokura, *Phys Rev Lett* **108**, 237601 (2012).
- [245] S. Tomic and M. Dressel, *Rep Prog Phys* **78**, 096501 (2015).
- [246] K. Chang *et al.*, *Science* **353**, 274 (2016).
- [247] H. Lüth, *Solid Surfaces, Interfaces and Thin Films* (Springer, 2010), Graduate Texts in Physics.
- [248] R. Wilson, in *Surface Analysis– The Principal Techniques* (2009), pp. 613.
- [249] G. Binnig, H. Rohrer, C. Gerber, and E. Weibel, *Physical Review Letters* **49**, 57 (1982).
- [250] G. Binnig, H. Rohrer, C. Gerber, and E. Weibel, *Applied Physics Letters* **40**, 178 (1982).
- [251] J. Stroscio and W. Kaiser, in *Methods of Experimental Physics* (Academic Press, 1993), pp. 1.
- [252] C. J. Chen, *Introduction to Scanning Tunneling Microscopy* (Oxford Science Publications, 2008), 2 edn., Monographs on the Physics and Chemistry of Materials, 64.
- [253] G. J. Leggett, in *Surface Analysis– The Principal Techniques* (2009), pp. 479.
- [254] J. Tersoff and D. R. Hamann, *Physical Review Letters* **50**, 1998 (1983).
- [255] J. Tersoff and D. R. Hamann, *Physical Review B* **31**, 805 (1985).
- [256] N. Krane, C. Lotze, and K. J. Franke, *Surface Science* **678**, 136 (2018).
- [257] K. J. Franke, G. Schulze, N. Henningsen, I. Fernandez-Torrente, J. I. Pascual, S. Zarwell, K. Ruck-Braun, M. Cobian, and N. Lorente, *Physical Review Letters* **100**, 036807 (2008).
- [258] M. Grobis, A. Wachowiak, R. Yamachika, and M. F. Crommie, *Applied Physics Letters* **86**, 204102 (2005).

- [259] H. J. Lee, J. H. Lee, and W. Ho, *Chemphyschem* **6**, 971 (2005).
- [260] G. V. Nazin, S. W. Wu, and W. Ho, *Proc Natl Acad Sci U S A* **102**, 8832 (2005).
- [261] N. A. Pradhan, N. Liu, and W. Ho, *J Phys Chem B* **109**, 8513 (2005).
- [262] A. C. Hillier and M. D. Ward, *Physical Review B* **54**, 14037 (1996).
- [263] D. E. Hooks, T. Fritz, and M. D. Ward, *Advanced Materials* **13**, 227 (2001).
- [264] G. Copie, Y. Makoudi, C. Krzeminski, F. Cherioux, F. Palmino, S. Lamare, B. Grandier, and F. Cleri, *Journal of Physical Chemistry C* **118**, 12817 (2014).
- [265] B. Baris, V. Luzet, E. Duverger, P. Sonnet, F. Palmino, and F. Cherioux, *Angew. Chem. Int. Ed.* **50**, 4094 (2011).
- [266] E. J. Spadafora, J. Berger, P. Mutombo, M. Telychko, M. Švec, Z. Majzik, A. B. McLean, and P. Jelínek, *J Phys Chem C* **118**, 15744 (2014).
- [267] P. R. Kidambi, R. Blume, J. Kling, J. B. Wagner, C. Baecht, R. S. Weatherup, R. Schloegl, B. C. Bayer, and S. Hofmann, *Chem Mater* **26**, 6380 (2014).
- [268] M. Gorgoi, W. Michaelis, T. U. Kampen, D. Schlettwein, and D. R. T. Zahn, *Applied Surface Science* **234**, 138 (2004).
- [269] S. R. Wagner, R. R. Lunt, and P. Zhang, *Phys Rev Lett* **110**, 086107 (2013).
- [270] E. Bauer, *Surface Science* **7**, 351 (1967).
- [271] E. G. Mcrae, *Surface Science* **11**, 492 (1968).
- [272] L. Kilian, U. Stahl, I. Kossev, M. Sokolowski, R. Fink, and E. Umbach, *Surface Science* **602**, 2427 (2008).
- [273] M. Meissner, M. Gruenewald, F. Sojka, C. Udhardt, R. Forker, and T. Fritz, *Surface Science* **606**, 1709 (2012).
- [274] M. Klimenkov, S. Nepijko, H. Kuhlenbeck, and H. J. Freund, *Surface Science* **385**, 66 (1997).
- [275] L. Meng, R. T. Wu, L. Z. Zhang, L. F. Li, S. X. Du, Y. L. Wang, and H. J. Gao, *J Phys-Condens Mat* **24** (2012).
- [276] S. R. Wagner and P. P. Zhang, *Surface Science* **630**, 22 (2014).
- [277] D. Çakir, M. Bokdam, M. P. de Jong, M. Fahlman, and G. Brocks, *Applied Physics Letters* **100**, 203302 (2012).

- [278] C. Tournier-Colletta, B. Kierren, Y. Fagot-Revurat, and D. Malterre, *Physical Review B* **87**, 075427 (2013).
- [279] H. Q. Shi, M. W. Radny, and P. V. Smith, *Physical Review B* **66**, 085329 (2002).
- [280] A. B. McLean, L. J. Terminello, and F. J. Himpsel, *Physical Review B* **41**, 7694 (1990).
- [281] E. Kaxiras, K. C. Pandey, F. J. Himpsel, and R. M. Tromp, *Physical Review B* **41**, 1262 (1990).
- [282] S.-H. Chang, S. Kuck, J. Brede, L. Lichtenstein, G. Hoffmann, and R. Wiesendanger, *Physical Review B* **78**, 233409 (2008).
- [283] T. Sonnleitner, I. Swart, N. Pavliček, A. Pöllmann, and J. Repp, *Physical Review Letters* **107**, 186103 (2011).
- [284] G. Heimel, I. Salzmann, S. Duhm, and N. Koch, *Chemistry of Materials* **23**, 359 (2011).
- [285] H. Ishii, K. Sugiyama, E. Ito, and K. Seki, *Advanced Materials* **11**, 605 (1999).
- [286] M. H. Andrews, A. H. Marshak, and R. Shrivastava, *Journal of Applied Physics* **52**, 6783 (1981).
- [287] S. Ristić, A. Prijić, and Z. Prijić, *Serbian Journal of Electrical Engineering* **1**, 237 (2004).
- [288] R. M. Feenstra, J. M. Woodall, and G. D. Pettit, *Physical Review Letters* **71**, 1176 (1993).
- [289] G. Mahieu, B. Grandidier, D. Deresmes, J. P. Nys, D. Stiévenard, and P. Ebert, *Physical Review Letters* **94**, 026407 (2005).
- [290] L. Liu, J. Yu, and J. W. Lyding, *Applied Physics Letters* **78**, 386 (2001).
- [291] Y. D. Kwon, *Physical Review B* **73**, 165210 (2006).
- [292] S. R. Wagner and P. P. Zhang, *Surface Science* **630**, 22 (2014).
- [293] S. R. Wagner and P. P. Zhang, *J. Phys. Chem. C* **118**, 2194 (2014).
- [294] A. Bendounan, F. Forster, A. Schöll, D. Batchelor, J. Ziroff, E. Umbach, and F. Reinert, *Surface Science* **601**, 4013 (2007).
- [295] M. Hollerer *et al.*, *ACS Nano* (2017).
- [296] K. W. Hipps, D. E. Barlow, and U. Mazur, *The Journal of Physical Chemistry B* **104**, 2444 (2000).
- [297] M. Lackinger, T. Müller, T. G. Gopakumar, F. Müller, M. Hietschold, and G. W. Flynn, *The Journal of Physical Chemistry B* **108**, 2279 (2004).

- [298] J. Ren, S. Meng, Y. L. Wang, X. C. Ma, Q. K. Xue, and E. Kaxiras, *J Chem Phys* **134**, 194706 (2011).
- [299] Y.-Z. Lan, H.-L. Kang, and T. Niu, *International Journal of Quantum Chemistry* **113**, 949 (2013).
- [300] D. A. Smith and M. E. Mura, *The Journal of Physical Chemistry* **98**, 6903 (1994).
- [301] D. A. Egger, Z. F. Liu, J. B. Neaton, and L. Kronik, *Nano Lett* **15**, 2448 (2015).
- [302] J. Q. Zhong, X. Qin, J. L. Zhang, S. Kera, N. Ueno, A. T. Wee, J. Yang, and W. Chen, *Acs Nano* **8**, 1699 (2014).
- [303] W. Gao and A. Kahn, *Organic Electronics* **3**, 53 (2002).
- [304] F. Jackel, U. G. Perera, V. Iancu, K. F. Braun, N. Koch, J. P. Rabe, and S. W. Hla, *Physical Review Letters* **100**, 126102 (2008).
- [305] N. Gonzalez-Lakunza, I. Fernandez-Torrente, K. J. Franke, N. Lorente, A. Arnau, and J. I. Pascual, *Phys Rev Lett* **100**, 156805 (2008).
- [306] M. Schwarz *et al.*, *Acs Nano* **11**, 9151 (2017).
- [307] Q. Li *et al.*, *Nano Lett* **15**, 5804 (2015).
- [308] J. I. Urgel, M. Schwarz, M. Garnica, D. Stassen, D. Bonifazi, D. Ecija, J. V. Barth, and W. Auwärter, *J Am Chem Soc* **137**, 2420 (2015).
- [309] A. El-Sayed *et al.*, *Acs Nano* **7**, 6914 (2013).
- [310] N. Gonzalez-Lakunza, M. E. Canas-Ventura, P. Ruffieux, R. Rieger, K. Mullen, R. Fasel, and A. Arnau, *Chemphyschem* **10**, 2943 (2009).
- [311] J. L. Cabellos, D. J. Mowbray, E. Goiri, A. El-Sayed, L. Floreano, D. G. de Oteyza, C. Rogero, J. E. Ortega, and A. Rubio, *J Phys Chem C* **116**, 17991 (2012).
- [312] E. Goiri, P. Borghetti, A. El-Sayed, J. E. Ortega, and D. G. de Oteyza, *Adv Mater* **28**, 1340 (2016).
- [313] K. A. Cochrane, T. S. Roussy, B. Yuan, G. Tom, E. Mårzell, and S. A. Burke, *J Phys Chem C* **122**, 8437 (2018).
- [314] B. Stadtmüller *et al.*, *Nat Commun* **5**, 3685 (2014).
- [315] J. Rodríguez-Fernández *et al.*, *J Phys Chem C* **121**, 23505 (2017).
- [316] J. Gómez Díaz, Y. Ding, R. Koitz, A. P. Seitsonen, M. Iannuzzi, and J. Hutter, *Theoretical Chemistry Accounts* **132** (2013).

- [317] R. Koitz, A. P. Seitsonen, M. Iannuzzi, and J. Hutter, *Nanoscale* **5**, 5589 (2013).
- [318] Y.-L. Wang *et al.*, *Physical Review B* **82**, 245420 (2010).
- [319] Y. L. Huang, W. Chen, S. Chen, and A. T. S. Wee, *Applied Physics A* **95**, 107 (2008).
- [320] Y. Zhang *et al.*, *Nature* **531**, 623 (2016).
- [321] L. Liu, T. Dienel, R. Widmer, and O. Groning, *Acs Nano* **9**, 10125 (2015).
- [322] O. I. Arillo-Flores, M. M. Fadlallah, C. Schuster, U. Eckern, and A. H. Romero, *Physical Review B* **87**, 165115 (2013).
- [323] F. C. Wu, H. L. Cheng, C. H. Yen, J. W. Lin, S. J. Liu, W. Y. Chou, and F. C. Tang, *Phys Chem Chem Phys* **12**, 2098 (2010).
- [324] R. Aroca, Z. Q. Zeng, and J. Mink, *Journal of Physics and Chemistry of Solids* **51**, 135 (1990).
- [325] M. Schwarze *et al.*, *Science* **352**, 1446 (2016).
- [326] F. E. Olsson, M. Persson, A. G. Borisov, J. P. Gauyacq, J. Lagoute, and S. Folsch, *Physical Review Letters* **93**, 206803 (2004).
- [327] E. Zupanič, R. Žitko, H. Midden, I. Mušević, and A. Prodan, *Croatica Chemica Acta* **82**, 485 (2009).
- [328] A. M. Saleh, S. M. Hraibat, R. M. L. Kitaneh, M. M. Abu-Samreh, and S. M. Musameh, *Journal of Semiconductors* **33**, 082002 (2012).
- [329] W. Tress, *Organic Solar Cells* (Springer, 2014), Vol. 208, Springer Series in Materials Science.
- [330] R. Schlesinger, in *Energy-Level Control at Hybrid Inorganic/Organic Semiconductor Interfaces* (2017), pp. 7.
- [331] I. G. Hill, A. Kahn, Z. G. Soos, and J. R. A. Pascal, *Chemical Physics Letters* **327**, 181 (2000).
- [332] E. I. Izgorodina, U. L. Bernard, P. M. Dean, J. M. Pringle, and D. R. MacFarlane, *Crystal Growth & Design* **9**, 4834 (2009).
- [333] S. Sharifzadeh, A. Biller, L. Kronik, and J. B. Neaton, *Physical Review B* **85**, 125307 (2012).
- [334] K. Yase, Y. Takahashi, Norihiko Arakato, and A. Kawazu, *Japanese Journal of Applied Physics* **34**, 636 (1995).
- [335] D. Stradi *et al.*, *RSC Advances* **6**, 15071 (2016).

- [336] G. Z. Zhu and L. S. Wang, *J Chem Phys* **143**, 221102 (2015).
- [337] P. J. Blowey, L. A. Rochford, D. A. Duncan, D. A. Warr, T. L. Lee, D. P. Woodruff, and G. Costantini, *Faraday Discuss* **204**, 97 (2017).
- [338] P. J. Blowey, University of Warwick, 2018.
- [339] T. Chanier and L. Henrard, *The European Physical Journal B* **88** (2015).
- [340] J. Kliewer and R. Berndt, *Physical Review B* **65** (2001).
- [341] J. Zhao *et al.*, *Physical Review B* **78**, 085419 (2008).
- [342] B. Ertug, *AJER* **02**, 01 (2013).
- [343] A. Dengl, R. Beyer, T. Peterseim, T. Ivek, G. Untereiner, and M. Dressel, *J Chem Phys* **140**, 244511 (2014).
- [344] M. Le Cointe *et al.*, *Phys Rev B Condens Matter* **51**, 3374 (1995).
- [345] P. García, S. Dahaoui, C. Katan, M. Souhassou, and C. Lecomte, *Faraday Discuss.* **135**, 217 (2007).